



UNIVERSITÀ
DEGLI STUDI
DI BRESCIA

**DOTTORATO DI RICERCA IN INGEGNERIA
MECCANICA E INDUSTRIALE**

XXXIII CICLO

Settore concorsuale ING-IND/14

**NUMERICAL AND SEMI-ANALYTICAL
MODELS APPLIED TO WHEEL-RAIL
CONTACT PROBLEMS**

RELATORE

PROF. ANGELO MAZZÙ

DOTTORANDO

ING. NICOLA ZANI

COORDINATRICE

PROF.SSA LAURA ELEONORA DEPERO



UNIVERSITÀ
DEGLI STUDI
DI BRESCIA

DOTTORATO DI RICERCA IN
INGEGNERIA MECCANICA E INDUSTRIALE

Settore scientifico disciplinare ING-IND/14

CICLO XXXIII

**NUMERICAL AND SEMI-ANALYTICAL MODELS APPLIED TO
WHEEL-RAIL CONTACT PROBLEMS**

Dottorando:
Ing. Nicola Zani

Relatore:
Prof. Angelo Mazzù

Coordinatore:
Prof.ssa Laura Eleonora Depero

To my family

Table of contents

List of figures	IV
List of tables	IX
Abstract	1

PART I

Chapter 1 - Introduction

1.1	Rail transport	3
1.2	Thesis structure	9
1.3	References	10

Chapter 2 - Review of wheel/rail materials and damage phenomena

2.1	Wheel materials	11
2.2	Rail materials	13
2.3	Phenomena in the wheel–rail interface	14
2.4	References	20

PART II

Chapter 3 - Effect of solid contaminants on wheel/rail material couplings

3.1	State of the art and motivation	25
3.2	Finite element models	28

3.3	Results	32
3.4	Comparison with experimental results	44
3.5	Concluding remarks	46
3.6	References	47

PART III

Chapter 4 - Effect of traces of bainite in railway wheels

4.1	State of the art and motivation	53
4.2	Experimental evidence	57
4.3	Model of analysis	59
4.4	Semi-analytical model results (SAM)	65
4.5	Finite Element model results (FEM)	66
4.6	Discussion of the results	75
4.7	Concluding remarks	76
4.8	References	77

PART IV

Introduction to the semi-analytical model	85
---	----

Chapter 5 - Contact mechanics

5.1	Hertzian theory	87
5.2	Distributed normal and tangential tractions	91
5.3	Post-processing	93
5.4	References	95

Chapter 6 - Constitutive models

6.1	Some notes on tensor calculus	97
6.2	General remarks on constitutive modelling	100
6.3	Plasticity	100
6.4	Chaboche plastic model	105
6.5	References	108

Chapter 7 - Multiaxial fatigue criteria

7.1	High cycle fatigue criteria	111
7.2	Low cycle fatigue criteria	114
7.3	Ratcheting	116

7.4	References	116
-----	------------	-----

Chapter 8 - Wear

8.1	Modelling wear	118
8.2	References	119

Chapter 9 - Simulations

9.1	Hertzian contact and elastic stress quantities	120
9.2	Cyclic plasticity	138
9.3	Convergence in the wear model	144
9.4	Multiaxial fatigue: Dang Van and Crossland	145
9.5	Multiaxial fatigue: Jiang-Sehitoglu	147
9.6	Conclusions and ongoing activities	149
9.7	References	150

Chapter 10 - Conclusions and perspectives

10.1	Conclusions	153
10.2	Perspectives	154

List of figures

PART I

Chapter 1 - Introduction

Figure 1.1 – Route length (km) in European countries participating in the survey in 2018	6
Figure 1.2 – Top speed train records and maximum operating speeds (Maglev trains are not considered)	7

Chapter 2 - Review of wheel/rail materials and damage phenomena

Figure 2.1 – Regions of contact between the rail head and wheel flange (1)	15
Figure 2.2 – Wear map BS11 rail steel versus AAR CLASS D (7)	16
Figure 2.3 – Example of Ty approach plot (5)	16
Figure 2.4 – Different types of contact loading and resulting crack formation	17
Figure 2.5 – Shelling in a railway wheel (courtesy of Lucchini RS)	17
Figure 2.6 – Micrographs showing shelling in railway wheels (courtesy of Lucchini RS)	18
Figure 2.7 – Surface-initiated RCF causing surface pitting (8)	18
Figure 2.8 – Thermal cracks extending in an axial/radial direction (8)	19
Figure 2.9 – Material response to cyclic loading (σ is stress, ϵ is the deformation)	20
Figure 2.10 – Shakedown map defined by current friction force and normalised contact pressure (5)	20

PART II

Chapter 3 - Effect of solid contaminants on wheel/rail material couplings

Figure 3.1 – Finite element model of the solid-contaminated contact	29
--	----

Figure 3.2 – Finite element model of the clean contact	29
Figure 3.3 – Correlation between cyclic yield strength and Brinell hardness in rail and wheel steels	30
Figure 3.4 – Equivalent line contact pressure distributions compared with correspondent point contact distributions along the longitudinal axis of the contact ellipse (22)	31
Figure 3.5 – Pressure distribution in clean contact in compression loading, with $P = 8 \text{ kN/mm}$ (curve condition): a) European couplings; b) American couplings	32
Figure 3.6 – Pressure distribution in contaminated contact, with $P = 3 \text{ kN/mm}$ (a) and $P = 8 \text{ kN/mm}$ (b)	33
Figure 3.7 - Pressure distribution in clean contact in rolling condition with $P = 8 \text{ kN/mm}$ (curve condition): a) European couplings; b) American couplings	34
Figure 3.8 – Map of the Mises equivalent plastic strain in the contact zone with rail $C.YSR = 685 \text{ MPa}$, wheel $C.YSW = 505 \text{ MPa}$, $p_0 = 490 \text{ MPa}$ in clean (a) and contaminated contact (b,c)	35
Figure 3.9 – Map of the Mises equivalent plastic strain in the contact zone with rail $C.YSR = 685 \text{ MPa}$, wheel $C.YSW = 505 \text{ MPa}$, $p_0 = 490 \text{ MPa}$ in clean contact: (a) compressive loading; (b) rolling condition	36
Figure 3.10 – Maximum von Mises equivalent plastic strain in clean contact in curve ($p_0 = 800 \text{ MPa}$) and in straight line ($p_0 = 490 \text{ MPa}$) as a function of the wheel cyclic yield strength $C.YSW$ for various rail cyclic yield strength $C.YSR$ in: a) wheels; b) rails	37
Figure 3.11 – Maximum von Mises plastic strain $\varepsilon_{p \text{ Mises}}$ in contaminated contact in curve ($p_0 = 800 \text{ MPa}$) and in straight line ($p_0 = 490 \text{ MPa}$) as a function of the wheel cyclic yield strength $C.YSW$ for various values of the rail cyclic yield strength $C.YSR$; a) in wheels; b) in rails	38
Figure 3.12 – Maximum von Mises equivalent plastic strain in clean contact in rolling condition in curve ($p_0 = 800 \text{ MPa}$) and in straight line ($p_0 = 490 \text{ MPa}$) as a function of the wheel cyclic yield strength $C.YSW$ for various rail cyclic yield strength $C.YSR$ in: a) wheels; b) rails	39
Figure 3.13 – Von Mises equivalent plastic strain in contaminated contact in straight line ($p_0 = 490 \text{ MPa}$) as a function of the wheel cyclic yield strength $C.YSW$ for various rail cyclic yield strength $C.YSR$ in wheels: a) wheels; b) rails	40
Figure 3.14 – Von Mises equivalent plastic strain in contaminated contact in curve ($p_0 = 800 \text{ MPa}$) as a function of the wheel cyclic yield strength $C.YSW$ for various rail cyclic yield strength $C.YSR$ in rails: a) wheel; b) rail	41
Figure 3.15 – Gradient of the Mises stress below the location of the particle closest to the contact centre, with rail $C.YSR = 489 \text{ MPa}$, wheel $C.YSW = 505 \text{ MPa}$, $p_0 = 490 \text{ MPa}$; a) overall; b) zoom on layer with $z < 0.2 \text{ mm}$	42
Figure 3.16 – Variation of the depth of influence of the local particle-body contact normalized with the particle radius as a function of the wheel $C.YSW$, for various rail $C.YSR$ and contact pressure, compared with the case of fully elastic materials: a) in wheels; b) in rails	43
Figure 3.17 – Micrographs of the sections of wheel and rail steels tested in (2) in clean condition: a) EN ER8 wheel steel ($C.YSW = 470 \text{ MPa}$); b) R350HT rail steel ($C.YSR = 691 \text{ MPa}$), tested against the EN ER8; c) SANDLOS® S wheel steel ($C.YSW = 660 \text{ MPa}$); d) R350HT rail steel tested against the SANDLOS® S	45

Figure 3.18 – Micrographs of the sections of wheel and rail steels tested in (2) in sand contaminated condition: a) EN ER8 wheel steel (*C.YSW*); b) R350HT rail steel (*C.YSR* = 691 MPa), tested against the EN ER8; c) SANDLOS® S wheel steel (*C.YSW* = 660 MPa); d) R350HT rail steel, tested against the SANDLOS® S

45

PART III

Chapter 4 - Effect of traces of bainite in railway wheels

Figure 4.1 – Location of the specimens analysed to calculate the bainitic spots dimensions (unit: mm)	57
Figure 4.2 – Equivalent radius" distribution in six railway wheels	58
Figure 4.3 – Micrographs showing the bainitic structure in the ferritic-pearlitic matrix with different amount of bainitic spots:	58
Figure 4.4 – Semi-analytical model used for the comparison with SAM	62
Figure 4.5 – Finite element model used for the comparison with SAM	63
Figure 4.6 – Stress-strain curves for Swift and Ramberg-Osgood constitutive laws	63
Figure 4.7 – Von Mises stress along the depth at the centre of the contact in presence of a circular inhomogeneity	64
Figure 4.8 – Plastic strain along the depth at the centre of the contact in presence of a circular inhomogeneity	64
Figure 4.9 – a) Rolling contact problem in SAM, b) Von Mises stress field in the rolling plane when the contact load is above the cluster of bainite	65
Figure 4.10 – Von Mises stress profile in presence of three phases along the depth varying the radius dimension	66
Figure 4.11 – Finite element model: on the right, the global model; on the left, the sub-model	67
(below) Figure 4.12 – Von Mises plastic strain distribution around the bainitic spots according to phase size ($z/a = 0.78$)	69
Figure 4.13 – Von Mises equivalent plastic strain evolution according to radius dimensions after one cycle: (a) circular bainitic spots centred at 2.5 mm depth ($z/a = 0.6$); (b) circular bainitic spots centred at 3.3 mm ($z/a = 0.78$)	69
Figure 4.14 – Von Mises equivalent plastic strain profile according to ellipse dimension, major axis inclination and depth after one cycle loading (b = major semi-axis in mm)	71
Figure 4.15 – Residual equivalent von Mises plastic strain (PEEQ) according to axis bainitic phase slope (major axis set to 100 μm)	72
Figure 4.16 – Plastic strain profile after one cycle loading for circular section bainite spots according to different interaxis and radius	74

PART IV

Chapter 5 - Contact mechanics

Figure 5.1 – Schematic representation of the cylindrical (line) contact	90
Figure 5.2 – Elastic half-space loaded by a normal pressure $p(x)$ and a tangential traction distributed in an arbitrary manner	91
Figure 5.3 – Stresses acting on a plane in a three-dimensional coordinate system	94

Figure 5.4 – Rotating coordinate system in the half-space model	94
--	----

Chapter 6 - Constitutive models

Figure 6.1 – Types of constitutive models	101
Figure 6.2 – Basic elastic-plastic response in uniaxial case	102
Figure 6.3 – Isotropic hardening: deviatoric plane and stress-strain curve (linear hardening)	104
Figure 6.4 – Kinematic hardening: deviatoric plane and stress-strain curve (linear hardening)	104
Figure 6.5 – Mixed hardening: deviatoric plane and stress-strain curve (linear hardening)	104
Figure 6.6 – Stress-strain curve for mixed non-linear hardening	104
Figure 6.7 – Rheological model for multiaxial plastic with hardening	105

Chapter 7 - Multiaxial fatigue criteria

Figure 7.1 – Normal stress and shear stress acting on a material plane. O is the application point of the vector \mathbf{t}	113
Figure 7.2 – Definition of shear strain amplitude through the construction of the minimum circumscribed circle to curve Ψ	113
Figure 7.3 – Evaluation of shear stress range $\Delta\tau$. Example with stresses evaluated at four instants in time. The shear strain range is evaluated in the same way.	115

Chapter 9 - Simulations

Figure 9.1 – Schematic representation of the general and the line contact	121
Figure 9.2 – Hertzian pressure distribution in the line contact problem	122
Figure 9.3 – Hertzian pressure distribution in the elliptical contact problem: (a) contact loading in direction x in MPa; (b) contact loading in direction y in MPa; (c) 3D pressure plot and contour plot.	123
Figure 9.4 – Elastic stresses and von Mises contours in the plane $y = 0$ (friction coefficient $f = 0$, $pH = 1100$ MPa (line contact))	124
Figure 9.5 – Principal stresses and deviatoric stresses contours in the plane $y = 0$ (friction coefficient $f = 0$, $pH = 1100$ MPa (line contact))	125
Figure 9.6 – Elastic stresses and von Mises contours in the plane $y = 0$ (friction coefficient $f = 0.3$, $pH = 1100$ MPa (line contact))	126
Figure 9.7 – Principal stresses and deviatoric stresses contours in the plane $y = 0$ (friction coefficient $f = 0.3$, $pH = 1100$ MPa (line contact))	127
Figure 9.8 – Elastic stresses and von Mises contours in the plane $y = 0$ (friction coefficient $f = 0.5$, $pH = 1100$ MPa (line contact))	128
Figure 9.9 – Principal stresses and deviatoric stresses contours in the plane $y = 0$ (friction coefficient $f = 0.5$, $pH = 1100$ MPa (line contact))	129
Figure 9.10 – Elastic stresses and von Mises contours in the plane $y = 0$ (friction coefficient $f = 0$, $pH = 1100$ MPa (elliptical contact))	130
Figure 9.11 – Principal stresses and deviatoric stresses contours in the plane $y = 0$ (friction coefficient $f = 0$, $pH = 1100$ MPa (elliptical contact))	131
Figure 9.12 – Elastic stresses and von Mises contours in the plane $y = 0$ (friction coefficient $f = 0.3$, $pH = 1100$ MPa (elliptical contact))	132
Figure 9.13 – Principal stresses and deviatoric stresses contours in the plane $y = 0$ (friction coefficient $f = 0.3$, $pH = 1100$ MPa (elliptical contact))	133

Figure 9.14 – Elastic stresses and von Mises contours in the plane $y = 0$ (friction coefficient $f = 0.5$, $pH = 1100$ MPa (elliptical contact))	134
Figure 9.15 – Principal stresses and deviatoric stresses contours in the plane $y = 0$ (friction coefficient $f = 0.5$, $pH = 1100$ MPa (elliptical contact))	135
Figure 9.16 – Elastic stresses along the rolling direction x at $za = 0.15$ and $za = 0.5$ (line contact)	136
Figure 9.17 – <i>Elastic stresses along the rolling direction x at $za = 0.15$ and $za = 0.5$ (elliptical contact)</i>	137
Figure 9.18 – Shear plastic strain versus number of cycles (left) and dimensionless depth z/a (right) according to the friction coefficient	139
Figure 9.19 – Shear plastic stain versus number of cycles according to the geometry contact type	140
Figure 9.20 – Shear plastic strain versus number of cycles and dimensionless depth z/a according to the contact pressure (1100 MPa on the left, 1800 MPa on the right) when the friction coefficient is set to 0.3	141
Figure 9.21 – Shear plastic strain versus number of cycles and dimensionless depth z/a according to the contact pressure (1100 MPa on the left, 1800 MPa on the right) when the friction coefficient is set to 0.5	142
Figure 9.22 – (following page) Shear plastic strain versus number of with and without the effect of wear. The first row refers to contact pressure equal to 1100 MPa, the second one to 1800 MPa	143
Figure 9.23 – Schematic representation of the layers	144
Figure 9.24 – Shear plastic strain along the depth according to different Δz size	144
Figure 9.25 – Dang Van and Crossland equivalent stress according to the dimensionless depth z/a for line and elliptical contact	146
Figure 9.26 – Plastic shear strain evolution at four depths	147
Figure 9.27 – $\Delta\tau$, $\Delta\gamma$ and FP parameter by varying the depth and the angle ϑ	148

List of tables

PART I

Chapter 2 – Review of wheel/rail materials and damage phenomena

Table 2.1 – (top) Minimum and maximum content of the alloy elements in European and American steel grades, according to EN 13262 and AAR M-107/M-208 codes; (bottom) common applications of AAR and ER wheel steel grades (1)	12
Table 2.2 – Typical rail steel grades in Europe, according to EN 13674-1:2009 (1)	13
Table 2.3 – Main rail steel grades in the USA (1)	14

PART II

Chapter 3 - Effect of solid contaminants on wheel/rail material couplings

Table 3.1 – Main steel grades for wheel/rail couplings used in Europe (above) and America (below) in straight line and curve	26
Table 3.2 – Main mechanical properties for improved UPLOS® and SANDLOS® family steels. UPLOS® A.CL.C and UPLOS® A.CL.D are the steel grades developed by Lucchini RS in compliance with AAR standards	27

PART III

Chapter 4 - Effect of traces of bainite in railway wheels

Table 4.1 – Mechanical properties for MICRALOS and AAR C wheel steels (23)	55
Table 4.2 – Mechanical properties for ER7 (ferritic-pearlitic steel) and HYPERLOS® (ferritic-pearlitic with traces of bainite) (29)	56
Table 4.3 – Details about the semi-analytic and the finite element models adopted for the comparison	60
Table 4.4 – Mechanical properties for materials employed in the simulations for FEM and SAM comparison	62
Table 4.5 – Details about the FE model and computing time	68
Table 4.6 – Plastic properties of the bainitic spots in FEM simulations	68

Table 4.7 – Interaxis adopted with respect to bainite size according to different radius dimension	73
Table 4.8 – Average amount of bainitic phases according to different radius dimension	73

PART IV

Chapter 9 - Simulations

Table 9.1 – Geometrical properties of the adopted models. elastic properties and results of the Hertzian problem	121
Table 9.2 – Plastic properties of the material (1)	138
Table 9.3 – Multiaxial fatigue material parameters	145
Table 9.4 – Von Mises shear stress threshold for elastic response according to the shakedown maps	145

Abstract

La presente tesi, sviluppata in collaborazione con l'azienda Lucchini RS (Lovere, Italia), è incentrata sullo sviluppo di modelli numerici e semi-numerici per applicazioni ferroviarie, in particolare il contatto ruota-rotaia. Tre diverse aree di ricerca sono oggetto di analisi.

La prima di queste riguarda lo studio dell'effetto di contaminanti solidi interposti tra la ruota e la rotaia, come per esempio la sabbia negli ambienti desertici. Nonostante in particolari circostanze la sabbia venga utilizzata per migliorare l'adesione tra ruota e rotaia, i granelli di sabbia così come i detriti di rocce possono drammaticamente peggiorare il comportamento ad usura; inoltre, le pressioni localizzate sui componenti sono fonte di deformazioni plastiche di intensità maggiore rispetto ad un contatto asciutto. Il corretto abbinamento dei materiali di ruote e rotaie risulta di fondamentale importanza per migliorare l'efficienza e la vita utile di questi componenti. Simulazioni numeriche agli elementi finiti sono state eseguite per valutare come il campo delle deformazioni plastiche cambia al variare dell'accoppiamento dei materiali.

Il secondo tema trattato è di natura metallurgica e riguarda la microstruttura delle ruote monoblocco. La microstruttura è tipicamente ferritico-perlitica e tale struttura rimane la migliore dal punto di vista della resistenza ad usura e a fatica. Tuttavia, la formazione della bainite è inevitabile durante il raffreddamento continuo degli acciai ipoeutetoidici e la presenza di bainite potrebbe compromettere il comportamento meccanico della ruota, poiché la bainite presenta una velocità di usura maggiore della perlite. Inoltre, è risaputo che fasi metallurgiche di diversa natura vicine tra loro possono generare sovrasollecitazioni e, di conseguenza, maggiori deformazioni a causa delle diverse proprietà meccaniche. Lucchini RS ha individuato la velocità di raffreddamento da adottare durante il trattamento termico di *rim chilling* che permette di contenere il più possibile le tracce di isole bainitiche nella corona di rotolamento della ruota e di ottenere la durezza e la tenacità richiesta dalle normative. Obiettivo di questa tesi è individuare la massima quantità di isole bainitiche nella microstruttura ferritico-perlitica che non compromette il comportamento della ruota dal punto di vista della deformazione plastica. Per raggiungere

questo obiettivo, si è ricorso a modelli numerici agli elementi finiti e ad un modello semi-analitico scritto dai ricercatori francesi dell'*Institute National des Sciences Appliquées* di Lione (INSA-Lyon).

Nella terza parte viene proposto un modello semi-analitico, mirato a risolvere problemi di contatto non conforme, come quello ruota-rotaia. L'utilizzo di un modello semi-analitico anziché uno numerico presenta come principale vantaggio la riduzione del tempo di calcolo. Il modello si propone principalmente di trovare la risposta ciclica del materiale, partendo dalla risoluzione del problema del contatto Hertziano, dal calcolo del campo degli sforzi elastici e dal modello costitutivo plastico di Chaboche. Infine, sono proposti alcuni criteri di verifica a fatica multiassiale ad alto e basso numero di cicli. Questa parte è stata realizzata in collaborazione con la *Chalmers University of Technology* di Göteborg in Svezia.

Parole chiave: teoria del contatto non conforme, metodo agli elementi finiti, modello semi-analitico, contaminanti solidi, fatica per contatto ciclico, fatica ad alto/basso numero di cicli, usura, deformazioni plastiche, microstruttura, bainiti.

Key words: non-conforming contact mechanics theory, finite element models, semi-analytical models, solid contaminants, rolling contact fatigue, high/low cycles fatigue, wear, plastic deformation, microstructure, bainite.



Part I

Chapter 1 - Introduction

Chapter 2 - Review of wheel/rail materials and damage phenomena

Introduction

1

1.1 Rail transport

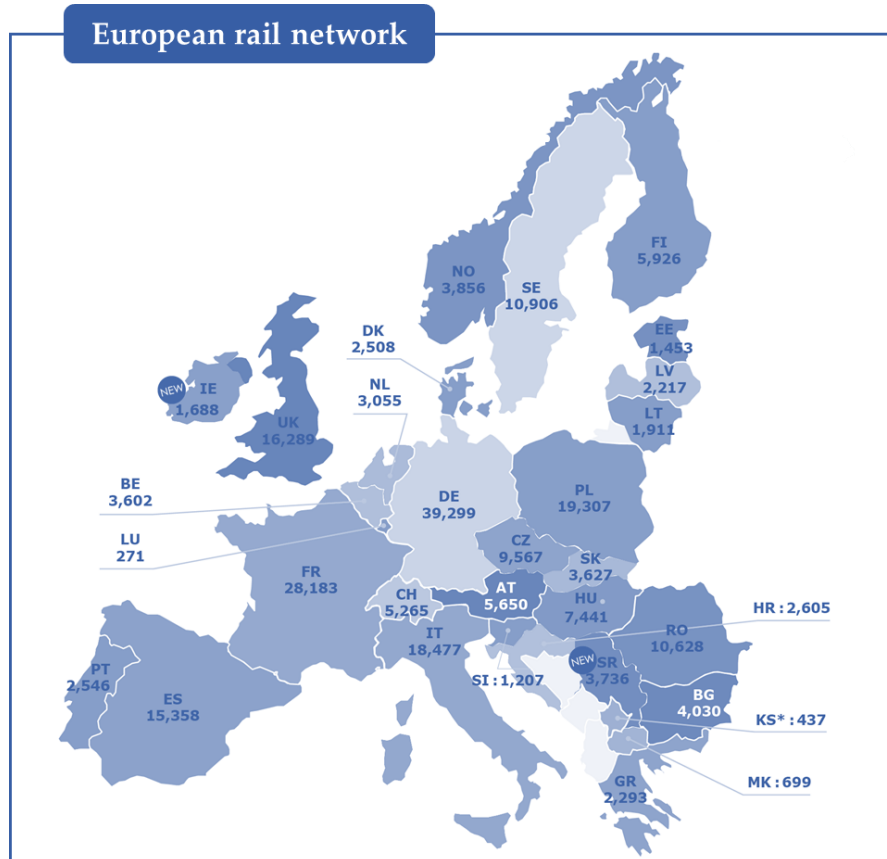
The railway is considered a means of fast and secure transportation. The constant development of this sector has led to an improvement in the performance of rail transport; nevertheless, this does not prevent conditions limiting the optimum efficiency and performance.

Railway transport has comparative advantages (noticeably, speed and comfort for passengers and economies of scale for freight) with medium to long distances over other means of transportation. According to the *Independent Regulators Group – Rail (IRG-Rail)*, the route length for the monitored European countries is over 234,000 km (1). Furthermore, over 50% of this total is from only five countries: Italy, Germany, France, Poland and the United Kingdom. FIGURE 1.1 illustrates the route length in 2018. Across the countries that participated in the IGR-Rail survey in 2018, 55% of the total route is electrified. Since 2014, the length of electrified tracks has been slowly increasing at an average rate of 0.6% per year. On the other hand, the non-electrified route tracks have been decreasing since 2014 by about 0.7% (1).

If we focus on the European rail traffic from 2014 to 2018, the rate of distribution between passenger and freight has been substantially unchanged. Over a total of 4.5 billion train-km reported, freight traffic only contributed 19%, while passenger traffic accounted for the remaining 81%. The difference in freight and passenger traffic volumes is due to the rail freight services suffering from reliability and low quality, as a result of the lack of traffic management and the absence of coordination in the cross-border capacity (2).

The situation in the United States of America (USA) differs completely, where freight traffic is more diffused than passenger services. USA had about 222,900 railroad route-km in 2017 (1), whereas the route length of passenger rails service operated over about 34,500 km. The next chapter elaborates on how this opposite trend with respect to Europe implies a different choice in the railway wheels material.

Figure 1.1 – Route length (km) in European countries participating in the survey in 2018



The history of the wheel–rail systems has mirrored the industrial revolution started in the second half of the 18th century and the technological advances achieved. Flanged wheels running on a cast-iron rail have been in use since the 18th century. Coned wheels with a flangeway clearance, enabling the wheels to run on a straight track without flange–rail contact, were established in the 1830s. The spread of the industrial revolution throughout Europe in the first half of the 19th century lead to massive railway projects. In 1825, the first railway line with locomotives and regular traffic opened in England. A decade later, the first Italian train line was launched.

The maximum speed has been increasing over the years. In 1830, the Rocket steam locomotive designed by Robert Stephenson reached a speed of approximately 50 km/h. In 1903, Siemens & Halske designed the first experimental electric rail car, which exceeded 200 km/h.

The 1960s saw a rise in high-speed trains. In 1964, the Japanese *Shinkansen*, or *bullet train*, was introduced, travelling at a maximum speed of 210 km/h. In 1981, the French TGV (*Train à Grande Vitesse*) was introduced at 260 km/h and now runs at 300–320 km/h in regular traffic. FIGURE 1.2 shows the maximum operating speed and top speed records of trains worldwide (3).

Unlike the conventional trains that use wheels, the Maglev train is based on magnetic levitation. This kind of train is costly to construct, with only three operational Maglev systems in existence, in South Korea, China and Japan. The Chinese Maglev has the highest run speed of 431 km/h, while, in 2015, the Japanese Maglev hit a record of 603 km/h.

Axle loads have been increasing significantly over the years, reaching values of 30, 35 and 40 tonnes per axle for heavy-haul applications (especially in the USA and Australia).

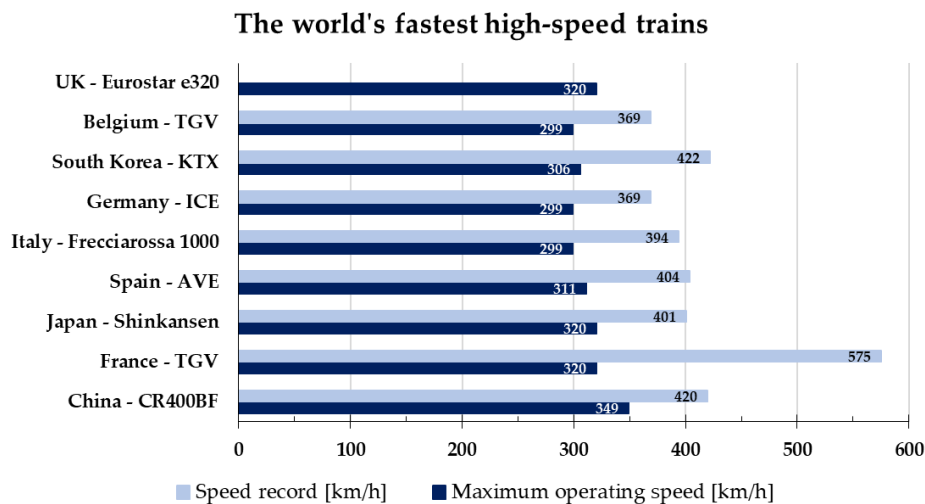


Figure 1.2 – Top speed train records and maximum operating speeds (Maglev trains are not considered)

Lucchini RS

Lucchini RS S.p.A. (RS stands for *rolling stock*) is an Italian company specialized on steel products such as railway products (wheelsets, axles, wheels), tool steels, forge ingots, steel casting and forgings. The company headquarters is in Brescia, but the main plant located in Lovere (Bergamo) on the west shore of the Iseo Lake. Typical of this company is its ability to house on site all phases of production from the initial design to the finished product.



Figure 1.3 – A short description of Lucchini RS company;
<https://lucchinirs.com/it/>

1.2 Thesis structure

The trend to heavier axle loads and higher speeds has increased the demand for more defined mechanical properties and geometries. Inefficiently designed railway components (rails, wheels, axles, etc.) and materials can lead to a dramatic increase in maintenance costs, train delays and personal injuries. The optimal design may even contribute to reducing CO₂ emissions and energy consumption. With this goal in mind, many railway companies and universities have been carrying out research activities in this field.

This thesis was financed by the Lucchini RS company, and it examines some railway challenges from a numerical point of view using finite element methods (FEM) and semi-analytical models. FEM models were carried out with the commercial software Abaqus®. The current work contains four parts.

Part 1 includes this introductory chapter (*Chapter 1*) and *Chapter 2*. The first section of *Chapter 2* gives a brief overview of the wheel and rail steels, focusing on European and American materials. In addition, the main phenomena occurring at the wheel-rail interface are proposed: contact, wear and fatigue.

Part 2 examines the effect of solid contaminants in wheel–rail contact (*Chapter 3*). After a short literature review about this topic, the finite element models are illustrated. The main task of this chapter is to investigate how the changing of wheel and rail material couplings influences the plastic deformation in wheels and rails. The numerical results are then compared to the experimental outcomes obtained through a twin-disk testing machine.

The effect of non-homogeneous microstructure in railway wheels is analysed in *Part 3*. *Chapter 4* first illustrates the possible microstructures of railway wheels (ferritic-pearlitic, bainitic and ferritic-pearlitic with traces of bainite), highlighting the qualities and the defects of each alternative. Numerical models and semi-analytical models will be proposed to study the effect of small traces of bainite in ferritic-pearlitic wheel steels. Determining the amount of bainite that does not compromise wheel behaviour is the goal. This chapter was carried out in partnership with the French university INSA-Lyon.

Part 4 is concerned with a semi-analytical model coded in Matlab®, whose aim is to investigate the cyclic response in non-conformal contact problems. This part is organised in four theoretical chapters and the final chapter illustrating the results. *Chapter 5* explains the contact mechanics theory, focusing on the Hertzian theory applied to cylindrical and elliptical contact. *Chapter 6* shows how to solve the elastic problem to obtain the elastic stress of the bodies in contact. The plastic constitutive law is presented in *Chapter 7*. *Chapter 8* shows how wear is handled in the model. Lastly, *Chapter 9* analyses the results of the simulations. This part was carried out in partnership with Chalmers University of Technology in Gotheborg (Sweden).

Finally, the conclusion gives a brief summary and critique of the findings.

1.3 References

1. Independent Regulators Group – Rail. Eight annual market monitoring report, Mar 2020. <https://www.irg-rail.eu/irg/documents/market-monitoring/260,2020.html>
2. Transport in the European Union, Current Trends and Issues, Mar 2019. <https://ec.europa.eu/transport/sites/transport/files/2019-transport-in-the-eu-current-trends-and-issues.pdf>
3. U.S. Department of Transportation. Transport statistics annual report 2018. <https://www.bts.gov/sites/bts.dot.gov/files/docs/browse-statistical-products-and-data/transportation-statistics-annual-reports/TSAR-Full-2018-Web-Final.pdf>
4. <https://www.statista.com/chart/10792/the-worlds-fastest-high-speed-trains/>
5. <https://lucchinirs.com/portfolio/residual-stress-measurement-on-wheels-and-axles/>

Review of wheel–rail materials and damage phenomena

2

2.1 Wheel materials

The traditional approach to railway solid-wheel materials uses carbon steel for almost every application; however, the standards followed in North America (AAR), Russia (GOST), Japan (JIS) and Europe (EN) may vary. In this work, we only focus on EN and AAR.

According to EN 136262, the European solid wheels are mainly based on grade C steels, with carbon content in the range of 0.45–0.60%, lower than that of the North American solid wheels. For example, the C content of AAR Class B and C solid wheels ranges from 0.57 to 0.77%. Another main difference between the American and European chemical composition relies on the content of Si: the European range being lower (maximum 0.40%) compared to AAR range (0.15–1.00%). Si limits the formation of martensite and promotes the formation of pearlite. If pearlite formation is rapid, the austenite will form pearlite before it reaches the martensite transformation start temperature. The AAR standard also demands a calibrated content of sulfur to improve machinability; this requirement is rarely found in the European standards.

Solid wheels made of these materials can be produced in two main different heat treatment conditions: total quenching, that is rarely adopted, and rim chilling. The latter creates circumferential compressive residual stresses in the wheel rim, which suppress propagation of transverse cracks. Rim chilling also promotes a good combination of strength, toughness and resistance to wear.

TABLE 2.1 shows the chemical composition of the European and American solid wheel steel grades and their common applications.

As previously stated, most solid wheels have been produced from carbon steel grades, with the appropriate content of Si and Mn. The resulting microstructure consists of two elements:

- soft ferrite generally generated around the prior austenite grain boundaries

- hard pearlite comprising lamellae of the softer ferrite and the harder cementite.

Table 2.1 – (top) Minimum and maximum content of the alloy elements in European and American steel grades, according to EN 13262 and AAR M-107/M-208 codes; (bottom) common applications of AAR and ER wheel steel grades (1)

Grade	Min. and max. content in European and North American steel grades (%)														
		C	S	P	Mn	Cr	Ni	Mo	Cu	Si	V	Al	Nb	Ti	Cr+Ni+Mo
EN ER6	Max	0.48	0.015	0.020	0.75	0.30	0.30	0.08	0.25	0.40	0.060	-	-	-	0.50
EN ER7	Max	0.52	0.015	0.020	0.80	0.30	0.30	0.08	0.25	0.40	0.060	-	-	-	0.50
EN ER8	Max	0.56	0.015	0.020	0.80	0.30	0.30	0.08	0.25	0.40	0.060	-	-	-	0.50
EN ERS8	Max	0.57	0.015	0.020	1.10	0.30	0.30	0.08	0.25	1.10	0.060	-	-	-	0.50
EN ER9	Max	0.60	0.015	0.020	0.80	0.30	0.30	0.08	0.25	0.40	0.060	-	-	-	0.50
AAR CLASS L	Min	-	-	-	0.60	-	-	-	-	0.15	-	-	-	-	-
AAR CLASS L	Max	0.47	0.015	0.020	0.90	0.25	0.25	0.10	0.25	1.00	0.040	0.060	0.050	0.030	-
AAR CLASS A	Min	0.47	-	-	0.60	-	-	-	-	0.15	-	-	-	-	-
AAR CLASS A	Max	0.57	0.015	0.020	0.90	0.25	0.25	0.10	0.25	1.00	0.040	0.060	0.050	0.030	-
AAR CLASS B	Min	0.57	-	-	0.60	-	-	-	-	0.15	-	-	-	-	-
AAR CLASS B	Max	0.67	0.015	0.020	0.90	0.25	0.25	0.10	0.25	1.00	0.040	0.060	0.050	0.030	-
AAR CLASS C	Min	0.67	-	-	0.60	-	-	-	-	0.15	-	-	-	-	-
AAR CLASS C	Max	0.77	0.015	0.020	0.90	0.25	0.25	0.10	0.25	1.00	0.040	0.060	0.050	0.030	-
AAR CLASS D	Min	0.67	-	-	0.60	-	-	-	-	0.15	-	-	-	-	-
AAR CLASS D	Max	0.77	0.015	0.020	0.90	0.25	0.25	0.10	0.25	1.00	0.040	0.060	0.050	0.030	-

EN 13262 or AAR M107/M108	Common applications
EN 13262 ER6 AAR CLASS L	Generally applied in low-axle load simulations, for some underground applications or regional and suburban passenger carriages and locomotives
EN 13262 ER7	Suitable for a wide range of applications in Europe, as it gives a good balance between toughness and hardness on the tread; mostly used for carriages and locomotives in passenger service
EN 13262 ER8	Commonly applied for heavy-duty applications; increasing demand in Europe in the last decade for applications requiring improved wheel wear, RCF (rolling contact fatigue) and out-of-roundness resistance
EN 13262 ER9	Seldom used in Europe, except for heavy-duty applications, high-contact stress in special locomotives and carriages
AAR CLASS A	Rarely used in Europe, suitable for heavy-duty wheel application, high contact stress in special locomotives or rapid transit carriages
AAR CLASS B	Seldom used in Europe, but very common in Japan and the USA mass transit transportation. Suitable for heavy-duty applications, special suburban and urban vehicles, rapid transit carriages, heavily loaded locomotives with high diameter driving wheels with light braking conditions
AAR CLASS C	
AAR CLASS D	Suitable for locomotives and carriages under extreme load and service conditions

This microstructure has shown an excellent combination of the mechanical properties required for the railway application. In these steels, the mechanical properties are mainly governed by the grain size, thickness of

the cementite lamellae and distance between the cementite lamellae. Fracture toughness, impact tests and area reduction are determined largely by the grain size and the thickness of the cementite lamellae. The mechanical properties improve when the thickness of the lamellae and the grain size decrease. Furthermore, when the interlamellar spacing decreases, the yield strength and the ultimate tensile stress increase.

The pearlitic microstructure can be altered in several ways, for example, by subjecting the steel to special heat treatment and accelerating cooling processes, changing the thickness of the lamellae, changing the proportion of the lamellae in the pearlite, precipitating fine carbides within the ferrite and so on. Increasing the content of C and introducing special alloying elements (Ni, Nb, V, Cr, Al, Ti and Mo) can alter the chemical composition.

To achieve a sufficient level of toughness, pearlitic steels grades can be replaced with tempered bainitic and martensitic steel grades. These steels exhibit a different microstructure consisting of harder iron carbide laths embedded in softer acicular ferrite. Tempered bainitic martensitic steels are a good alternative to high-C steels when traditional requirements of microstructure and chemical analysis are not mandatory.

In Europe, forged solid wheels, or rolled tyres mounted on a wheel centre, are used almost exclusively. Manufacturing a forged railway wheel includes forging, rolling, heat treatment, machining and ultrasonic testing.

2.2 Rail materials

At present, most of the rail steels are made of carbon steel, with a C content ranging between 0.7 and 0.8%. The microstructure is typically pearlitic.

EN13674-1:2011 is the European standard generally accepted by most railway companies. TABLE 2.2 shows the different options proposed in Europe (2):

- standard carbon steel grade steels not heat-treated or “naturally cooled”
- alloyed rail steels not heat-treated or “naturally cooled”
- traditional heat-treated rail steels
- R370CrHT and R400HT that are heat-treated steels with increased levels of hardness

Table 2.2 – Typical rail steel grades in Europe, according to EN 13674-1:2009 (1)

Rail steel grade	Hardness [HB]	Naturally cooled		Heat-treated		
		C, Mn steels	Alloyed steels	C, Mn steels	Alloyed steels	Ultra-high C
R200	200–240	X				
R220	220–260	X				
R260	260–300	X				
R260Mn	260–300	X				
R320Cr	320–360		X (1% Cr)			
R350HT	350–390			X		
R350LHT	350–390			X		
R370CrHT	370–410				X	
R400HT	400–440					X

In North America, most rails comply with the AREMA (American Railway Engineering and Maintenance-of-Way Association) standard (TABLE 2.3). 25% are not heat-treated, while 75% are quenched and tempered.

Table 2.3 – Main rail steel grades in the USA (1)

Rail steel grade	Hardness [HB]
AREMA 325	325–385
AREMA 370	370–410
AREMA 400	400–440

The heat-treated rail steels are beneficial for curves with radii less than 300 m or in unfavourable environmental conditions, like deserts. In the past twenty years, heat treatment has become a more standard product, especially in high normal axle load, in systems with very sharp curves, for heavy-haul applications and in turnouts. The heat treatment can be applied to the whole rail section or to a portion of the railhead.

Hyper-eutectoid steels have been recently produced as an improvement of the first eutectoid heat-treated carbon steels. The carbon level of these steels is roughly 0.8–0.9%, with a small addition of chromium, resulting in higher hardness values.

Similarly to wheels, pearlitic rails have been replaced by bainitic rails for applications that require higher yield strength, ultimate tensile strength, fracture toughness and hardness. Austenitic rails were manufactured as well.

Rails are produced from continuously cast blooms. During manufacturing, rails are checked for defects by automatic and continuous ultrasonic testing.

2.3 Phenomena in the wheel–rail interface

Wheel–rail contact is an extremely complex problem to solve that requires knowledge in various disciplines to understand and model. Furthermore, the lack of any analogies with other engineering components adds to the challenge. The main issue is the changing nature of the wheel–rail system: the continuous variations of the contact area and the stresses, which are different for each wheel, leading to different worn profiles. Another complexity of the wheel–rail contact is the fact that all the critical issues are interlinked. Consider, for example, rolling contact fatigue (RCF) and wear: if wear is reduced, cracks can grow to the point that RCF failure occurs; on the other hand, if crack growth is truncated, wear is more likely to be the problem. Friction modifiers are often used to control wear damage, but they may influence crack growth.

2.3.1 Wheel–rail contact

The position of the wheel–rail contact varies continuously as the train follows its path, with a typical contact patch of 1 cm². The position depends on the wheel and rail profiles, the degree of curvature of the track and whether the wheel is the leading or trailing wheelset on a bogie. Three

possible regions can be identified (3,4). In straight track or high-radius curves, the railhead and wheel tread are likely to be in contact (Region A in FIGURE 2.1), while the wheel flange and rail gauge corner will be in contact along tighter curves (Region B in FIGURE 2.1). The contact may also occur, but is least likely, between the field sides of the rail and wheel (Region C). In Region A, the lowest contact stresses and lateral forces occur; Region B yields to higher wear rates and contact stresses and two-point contacts may even occur; finally, Region C results in wear problems causing incorrect steering of the system.

Numerous mathematical solutions have been proposed over the years to solve the contact problem. The most straightforward approach was in the second half of the 19th century by Heinrich Hertz, considered the pioneer of the contact mechanics. Further details about his approach can be found in CHAPTER 5.

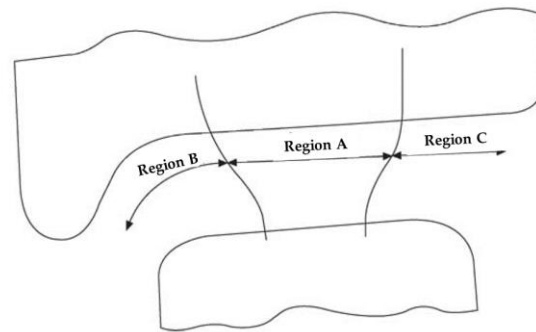


Figure 2.1 – Regions of contact between the rail head and wheel flange (1)

2.3.2 Wear

Wear is the displacement or loss of material from a contacting surface. The wear mechanism depends on several factors, among which are the nature of the material and other elements of the tribo-system, including environmental conditions and the presence of other contaminants (sand, leaves, wear debris, friction modifiers, etc.) (4,5,6).

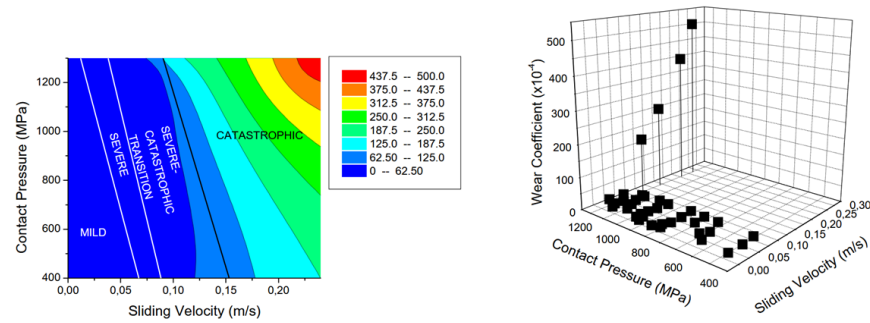
In wheel–rail contact, there are two areas of interest, sliding and rolling. Sliding motion (motion tangential to the surface) is more severe than motion perpendicular to the surface, occurring with rolling or impact. Sliding may result in *oxidative wear* in the mild contact condition (Region A, low sliding velocity and load) and in *adhesive* or *galling wear* (Region B). If particles are present in the contact, abrasive wear may also occur. In very severe sliding conditions, high *heat generation* may result in the contact leading to a thermal breakdown of the material.

Fatigue dominates the wear mechanisms during rolling motion. Typically referred to as *fatigue wear*, this kind of wear is created with the formation of cracks and separation of material due to repeated forces. These cracks seldom initiate below the surface and then propagate to the surface. However, if the traction force is significant, cracks initiate at the surface. Another critical kind of wear is *abrasive wear*, classified as *three-body abrasive wear* when hard particles are trapped between the surfaces and *two-body*

abrasive wear where the asperities of the harder body remove portions of the softer body.

Wear is often classified as *mild* or *severe*. For any pair of materials, increasing either the normal load, sliding speed or temperature leads to a sudden jump in wear rate. Increasing temperature leads to the transition to a *catastrophic* wear regime. Mild wear results in smooth surfaces, and the debris is minimal (100 nm diameter), while severe wear in rough and torn surfaces has large debris (up to 0.01 mm diameter) (5). FIGURE 2.2 (7) shows two example data from twin-disk testing using BS11 rail steel versus AAR CLASS D (data are available in (8)).

Figure 2.2 – Wear map
BS11 rail steel versus AAR
CLASS D (7)



The most common wear models are the following:

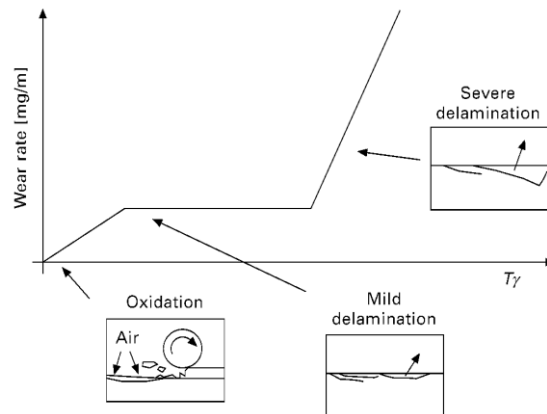
- *Archard model*: It asserts that the wear volume V is directly proportional to the sliding distance l , the contact load P , but inversely proportional to the surface hardness H of the wearing material:

$$V = k \frac{P l}{H}, \quad (2.1)$$

where k is the wear coefficient

- *T γ approach*: T is the tractive force given by the normal force multiplied by the friction in the contact, and γ is the slip in the contact (FIGURE 2.3). This method is widely applied in the railway field.

Figure 2.3 – Example of $T\gamma$
approach plot (5)



2.3.3 Fatigue

RCF and wear are the main damage phenomena in rails and wheels. RCF is caused by cyclic loading of the material and results in cracks. These cracks can further propagate, causing the fracture of the component.

FIGURE 2.4 illustrates the crack formation and propagation that can occur from contact loading under different conditions (9). FIGURE 2.4A shows the case of pulsating vertical force, that can lead to surface or sub-surface cracks; in this case, the cracks will be arrested when they have grown out the contact stress zone (unless a bulk stress exists). In FIGURE 2.4B, the vertical load (pulsating or constant) is combined with an oscillating lateral load (fretting fatigue), and cracks may form at the surface. In FIGURE 2.4C, the rolling condition is combined with interfacial shear and slip; this results in plastic deformation and crack initiation and growth.

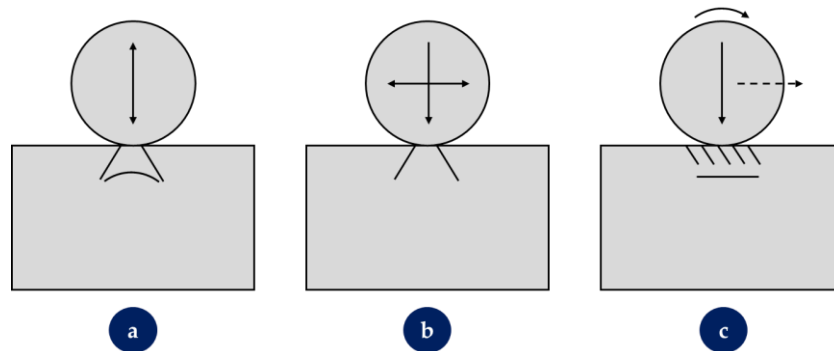


Figure 2.4 – Different types of contact loading and resulting crack formation

Sub-surface-initiated rolling contact fatigue

Sub-surface-initiated RCF is relatively rare; however, when it occurs, it is potentially dangerous. The cracks initiate below the contact surface and, in the wheel, can branch towards the hub or the wheel surface (10). The crack formation is a result of low material resistance and high stress. Material cleanliness assumes a vital role since material defects may lead to intensified stresses (11,12). FIGURE 2.5 and FIGURE 2.6 illustrate examples of sub-surface-initiated RCF cracks in railway wheels.



Figure 2.5 – Example of sub-surface-initiated RCF in a railway wheel (courtesy of Lucchini RS)

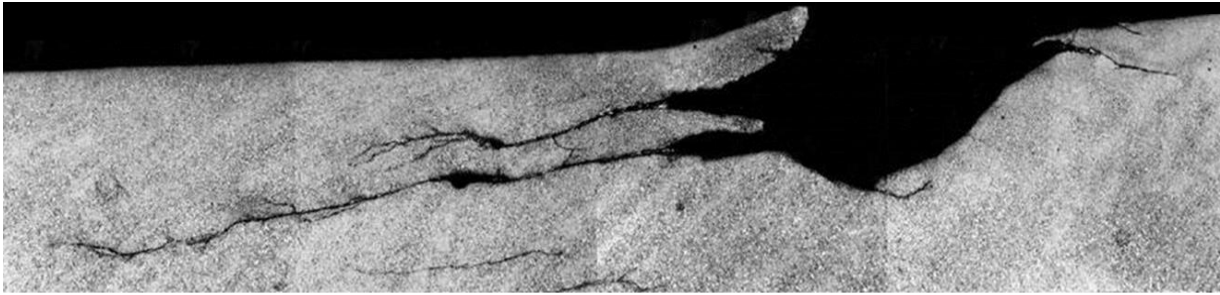
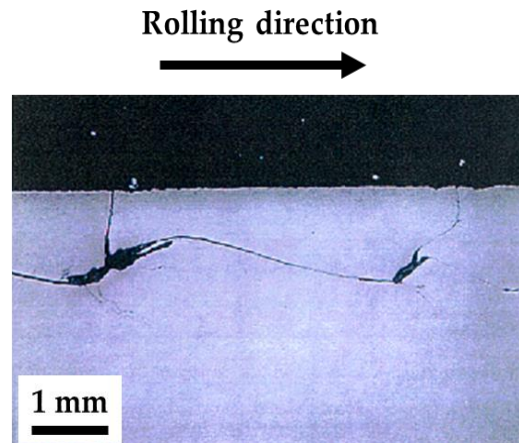


Figure 2.6 –
Micrographs showing
sub-surface RCF cracks
in railway wheels
(courtesy of Lucchini
RS)



Surface initiated rolling contact fatigue

Surface-initiated RCF cracks are more common but less severe than sub-surface ones. These cracks initiate because of frictional rolling/sliding contact leading to plastic deformation. The crack forms when plastic deformations exceed the plastic strain and propagate owing to the rolling contact loading and the hydro-pressurisation (caused by fluids trapped in the crack) (13). In wheels, surface-initiated cracks typically branch towards the surface and cause surface pitting (FIGURE 2.7), while cracks in rails may propagate downwards leading to transversal rail breaks.

Figure 2.7 – Surface-
initiated RCF causing
surface pitting (8)



The remedy for surface cracks is re-profiling, which is a costly approach requiring trains to be taken out of traffic. Surface cracks may even be worn away by wear itself if slip is high enough; the balance between crack initiation and wear is referred to as the “magic wear rate” (14).

Thermal cracks

Thermal damage occurs when the outer layer of the wheel is severely heated (through the tread braking or, simply, the friction between wheel and rail). Thermal cracks initiate when the material plastically deforms from the restrained thermal expansion during heating; the tensile residual stresses induced by the cooling may promote crack propagation (15). Thermal damage is also related to material transformation. An example of thermal cracks in the wheels is shown in FIGURE 2.8.

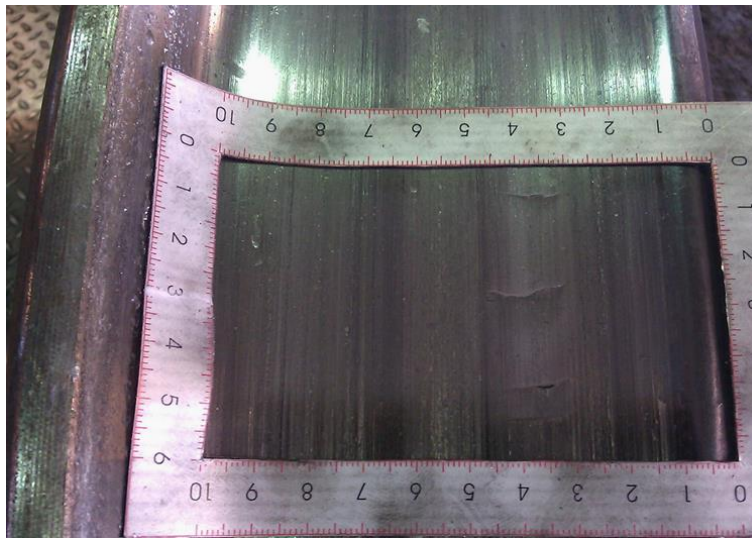


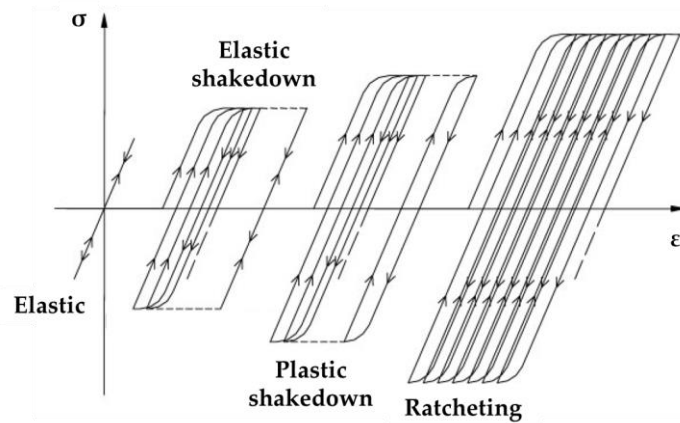
Figure 2.8 – Thermal cracks extending in an axial/radial direction (8)

Cyclic stress response

In general, four possible scenarios to cyclic response are known (FIGURE 2.9) (5,16):

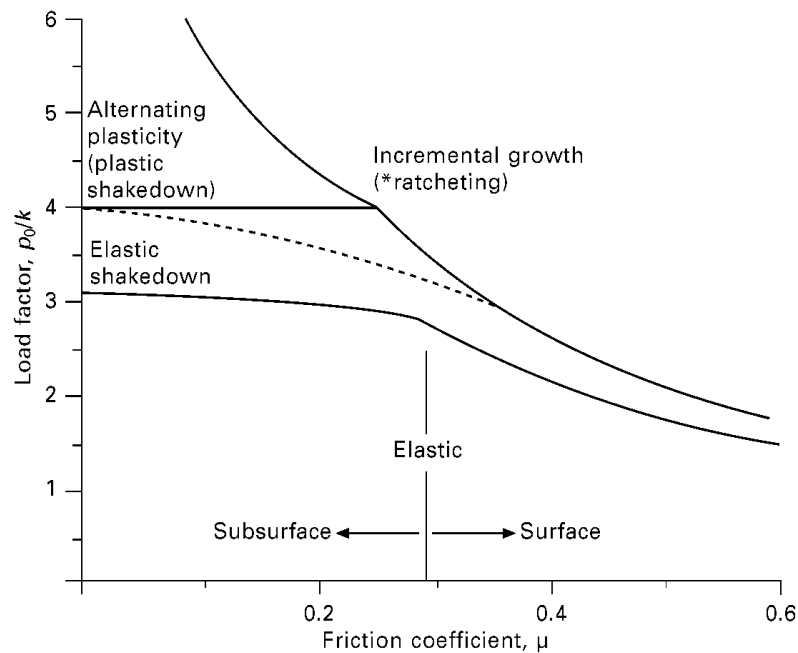
- *elastic response* – no plastic deformation
- *elastic shakedown* – some plastic strains admitting in the early, but the material reverting to elastic behaviour owing to material hardening and residual stresses
- *plastic shakedown* – plastic strains following a hysteric cycle with no strain accumulation
- *ratcheting* – cyclic plastic strain accumulation

Figure 2.9 – Material response to cyclic loading (σ is stress, ϵ is the deformation)



Shakedown maps are a useful tool to predict the cyclic response. FIGURE 2.10 (5) illustrates an example of a shakedown map for contact between coaxial cylinders; it shows the limit of the material behaviour in terms of the friction coefficient and a non-dimensional load factor, obtained by dividing the contact pressure by the shear yield strength. For friction coefficients above about 0.3, plastic flow is greatest on the surface.

Figure 2.10 – Shakedown map defined by current friction force and normalised contact pressure (5)



2.4 References

1. Ghidini A, Diener M, Schneider J. Special wheels for mass transit, Lucchini RS, Lovere (Italy), 2014.
2. Ghidini A, Faccoli M., Mazzù A. SANDLOS® wheels for desert environments, Lucchini RS, Lovere (Italy), 2017.

3. Tournay, H., 2001, Supporting technologies vehicle track interaction, in Guidelines to Best Practice for Heavy Haul Railway Operations: Wheel and Rail Interface Issues, International Heavy Haul Association, Virginia Beach, VA, USA, 2-1-2.73.
4. Soleimani H, Moavenian M. Tribological Aspects of Wheel–Rail Contact: A Review of Wear Mechanisms and Effective Factors on Rolling Contact Fatigue. *Urban Rail Transit* 3, 227–237 (2017). <https://doi.org/10.1007/s40864-017-0072-2>.
5. Lewis R, Olofsson U. Wheel-rail interface handbook, 1st edition. Woodhead Publishing Limited. September 2009. ISBN: [9781845694128](https://doi.org/10.1007/9781845694128).
6. Faccoli M, Petrogalli C, Lancini M, Ghidini A, Mazzù A. Effect of desert sand on wear and rolling contact fatigue behaviour of various railway wheel steels. *Wear*. 15 Feb 2018; 396–397:146–61. <https://doi.org/10.1016/j.wear.2017.05.012>.
7. Lewis R, Olofsson U. Mapping rail wear regimes and transitions. *Wear*. Oct 2004; 257(7–8): 721–729. <https://doi.org/10.1016/j.wear.2004.03.019>.
8. Bolton PJ, Clayton P. Rolling–sliding wear damage in rail and tyre steels. *Wear*. 16 Jan 1984; 92(2):145–165. [https://doi.org/10.1016/0043-1648\(84\)90066-8](https://doi.org/10.1016/0043-1648(84)90066-8).
9. Ekberg A, Åkesson B, Kabo E. Wheel/rail rolling contact fatigue – Probe, predict, prevent. *Wear*. 15 Jun 2014; 314(1–2):2–12. <https://doi.org/10.1016/j.wear.2013.12.004>.
10. Ekberg A, Marais J. Effects of imperfections on fatigue initiation in railway wheels. *Proc Inst Mech Eng Part F J Rail Rapid Transit*. 2000; 214(1):45–54. <https://doi.org/10.1243%2F0954409001531234>.
11. Kabo E, Ekberg A. Material defects in rolling contact fatigue of railway wheels—the influence of defect size. *Wear*. 2005 Mar; 258(7–8):1194–200. <https://doi.org/10.1016/j.wear.2004.03.070>.
12. Sandström J, De Maré J. Probability of subsurface fatigue initiation in rolling contact. *Wear*. 18 May 2011; 271(1–2):143–7. <https://doi.org/10.1016/j.wear.2010.10.018>.
13. Mazzù A, Petrogalli C, Lancini M, Ghidini A, Faccoli M. Effect of Wear on Surface Crack Propagation in Rail–Wheel Wet Contact. *J Mater Eng Perform*. 2018 Feb 25; 27(2):630–9. <https://doi.org/10.1007/s11665-018-3185-1>.
14. Magel EE, Rolling Contact Fatigue: A Comprehensive Review, US Department of Transportation, Federal Railroad Administration, Technical Report, November 2011. <http://www.fra.dot.gov/>.
15. Caprioli S, Vernersson T, Handa K, Ikeuchi K. Thermal cracking of

railway wheels: Towards experimental validation. Tribol Int. 2016 Feb 1; 94:409–20. <https://doi.org/10.1177%2F0954409712452347>.

16. Mazzù A. A simplified non-linear kinematic hardening model for ratchetting and wear assessment in rolling contact. J Strain Anal Eng Des. 2008; 43(5):349–60. <https://doi.org/10.1243%2F03093247JSA405>.

Part II



Chapter 3 - Effect of solid contaminants on wheel/rail material couplings

(right image) Rail track in Namibia <https://unsplash.com/s/photos/desert-train>

(left image) Desert railway track in Morocco <https://www.youtube.com/watch?v=7EEEu2HF8es>

List of symbols

Symbol	Description
a	Semi-contact length
$C.YS$	Cyclic yield strength
$C.YS_R$	Rail yield cyclic yield strength
$C.YS_W$	Wheel yield cyclic yield strength
E	Young's modulus
FE	Finite Element
HB	Brinell hardness
N	Hardening exponent in Ramberg-Osgood law
P	Contact force per unite length
p^0	Hertzian pressure
R_P	Particle radius
s	Slip ratio
z_P	Depth below which the effect of the particle is negligible
α	Conventional cyclic yield deformation
ε	Strain
ε_P	Plastic strain
ε_{VM}	Von Mises equivalent plastic strain
ϑ	Rotation set in the Finite Element model
σ	Stress

Effect of solid contaminants on wheel/rail material couplings

3

This chapter is based on the paper:

Mazzù, A. Ghidini, N. Zani, M. Faccoli. A simplified numerical study of wheel/rail material coupling in presence of solid contaminants. Tribology – Materials, Surfaces & Interfaces. 2020. <https://doi.org/10.1080/17515831.2020.1829877>

3.1 State of the art and motivation

The choice of the correct material coupling is decisive to optimise the life of both the railway wheels and rails. FIGURE 3.1 shows the results of an enquiry about the typical wheel-rail material couplings in Europe and North America, published in (1). At a first sight, the following observations can be done:

1. The rails are generally harder than the wheels.
2. In general, the wheel materials preferred in America are harder than the ones preferred in Europe, what implies higher yield strength and, consequently, lower plastic deformation.
3. For each group, the rail materials are harder in curve than in straight line.

This highlights the tendency to consider the wheel as the sacrificial element, as it can be reprofiled or replaced with lower impact on the maintenance costs if compared with the rails.

However, the demand of steels with higher performance is increasing for both the wheels and the rails, due to the new challenges linked to higher speeds, higher freights and harsher environmental conditions. An interest arose about the effects of solid contaminants at the wheel-rail interface, which is a crucial topic for new high-speed lines that are planned or under construction in desert environments (1,2).

It is commonly thought that increasing the hardness of one of the contacting elements, while reducing wear on itself, will increase wear on the other body. However, in his review of recent studies on this topic, Burstow (3) argued that this belief is not always justified. Indeed, in a clean and dry environment, a hardness change of one of the bodies is expected to slightly

change the size and shape of the contact patch, with a limited effect on the stress field of the other body.

Table 3.1 – Main steel grades for wheel/rail couplings used in Europe (above) and America (below) in straight line and curve

		Rail	
		Straight line	
Steel grade	Typical hardness [HB]	Steel grade	Typical hardness [HB]
EN ER7	235÷285	EN R260	260÷300
EN ER8	248÷302		
EN ER9	255÷311		
AAR CLASS A	300÷340	AREMA 325	325÷365
AAR CLASS B	320÷360		
AAR CLASS D	345÷410		

Wheel		Rail	
		Curve	
Steel grade	Typical hardness [HB]	Steel grade	Typical hardness [HB]
EN ER7	235÷285	R350HT	350÷390
EN ER8	248÷302	R350HT	350÷390
		R370CrHT	370÷410
EN ER9	255÷311	R370CrHT	370÷410
		R410HT	400÷440
AAR CLASS B	300÷340	AREMA 370 AREMA 400	370÷410 400÷440
AAR CLASS C	320÷360		
AAR CLASS D	345÷410		

Lewis et al. (4) investigated the effect of hardness ratio on wear changing the rail and maintaining the same wheel; increasing rail hardness has the effect of lowering its wear rate, whereas wheel wear rate is constant when the rail is harder than the wheel but decreases when the rail gradually softens. Liu et al. (5) investigated the effect of axle load on rail materials, finding that the wheel/rail hardness ratio has an increasing effect on the wear rate as far as the axle load increases.

A considerable amount of literature has been published on the presence of solid contaminants (such as sand, wear debris, crushed ballast, dust, etc.) and the damage process caused by such contaminants on both rails and wheels. The practice of sanding (i.e. the application of sand in at the contact surface) is widely diffused to enhance wheel-rail adhesion, especially when the rails become slippery due to the formation of thin layers of wet chopped leaves on their top. These studies showed that wear dramatically increases in the presence of sand, up to 30 times the wear in clean dry conditions. The worn surface has a frosted appearance, with the formation of indentation and abrasion score marks; the subsurface region is characterised by huge plastic strain, formation of surface cracks and detachment of large material particles that make the surface very rough (6-13).

Recent researches (2,14) identified a damage mechanism related to solid contaminants that is linked to a local ratcheting, involving a layer whose depth is on the dimensional scale of the area of contact between the main bodies (wheel or rail) and the contaminant particles. This thin layer, characterized by huge plastic strain, is clearly distinct from the underlying layer where plastic strain is of lower magnitude order. In the surface layer, the huge plastic flow, coupled with third body indentation, can lead to the incorporation of the contaminant inside the metal substrate, generating subsurface clusters of incoherent material which enhance high rate delamination wear. This damage mechanism, as well as the others previously identified, is strongly influenced by the materials hardness and their coupling.

In the last decade, Lucchini RS has developed a group of steels specifically designed for desert environment, called SANDLOS®. SANDLOS® steels follow the American regulations for railway wheels (AAR) since they represent the upgraded version of AAR steels. In this work, we mainly refer to two versions of SANDLOS®: SANDLOS® S and SANDLOS® H, that are the upgraded versions of AAR CLASS C and AAR CLASS D, respectively. SANDLOS® S is designed for interaction with head hardened rails (R350HT÷R370CrHT) and it is aimed at mass transit transportation and heavy applications (special vehicles, high-speed service and heavily loaded locomotives with light braking conditions). SANDLOS® H is designed for very hard treated rails (R400HT) and is specifically targeted to locomotives and passenger cars in extreme service and loading conditions. TABLE 3.4 shows some typical mechanical properties of SANDLOS® steels compared with the traditional CLASS C and CLASS D steels. Data have been collected by Lucchini RS's Metallurgic Department (14). Many metallurgical investigations on full scale and small scale (2) showed that SANDLOS® materials exhibited excellent performance in terms of resistance to wear in desert environment, thanks to good toughness and ductility. The high mechanical properties confine the extremely huge plasticization layer due to the presence of contaminants to a thin plasticized layer. These steels have also proved to be a good alternative to traditional materials in "clean" environment.

Average results	AAR Class C		AAR Class D	
	UPLOS® A. CL. C	SANDLOS® S	UPLOS® A. CL. D	SANDLOS® H
Monotonic yield strength [MPa]	715	750	770	800
Cyclic yield strength [MPa]	640	660	680	720
Elongation to fracture	0.38	0.37	0.36	0.34
Front rim hardness (HB)	320÷360	325÷360	345÷410	355÷415
Apparent toughness, 20°C [MPa√m]	55	50	45	40

Table 3.4 – Main mechanical properties for improved UPLOS® and SANDLOS® family steels. UPLOS® A.CL.C and UPLOS® A.CL.D are the steel grades developed by Lucchini RS in compliance with AAR standards

Finite Element (FE) analyses can help understanding how contaminants interact with the coupled materials in relation to their hardness. In the

literature, most of FE models have been developed to study the contact problems in clean contact both with elastic and plastic materials (15-16), the crack initiation and propagation (17-18) and the influence of the wheel geometry (19). However, little FE simulations were carried out to study the effects of solid contaminants. In (2,14), this mechanism was simulated by means of two ring sectors in plastic material rolling one on the other with a few entrapped contaminant particles.

In this chapter, the effect of material coupling on the plastic strain of wheels and rails in presence of solid contaminants was analysed by means of finite element simulation, considering some typical material couplings in straight line and curve in indentation loading. In particular, the focus was mainly addressed to the plastic properties of the wheel and rail steels. Analyses with and without contaminants were carried out for comparison. A model concerning rolling condition in clean contact was also proposed. Rolling contact loading in presence of solid contaminants was not considered due to the excessive simulation time and convergence difficulties issues.

As we will see in the next paragraph, these models have not the aim of reproducing the complexity of the interaction between contacting bodies and the solid contaminants: complex phenomena such as abrasion of the contacting surfaces, particles crushing, conglomeration and incorporation of the contaminant particles, irregular particle distribution and size are not included in the FE models. However, they can contribute to understand, at least qualitatively, how hard solid contaminants can affect the contact mechanics of the wheel-rail system in relation to plasticity.

3.2 Finite element models

3.2.1 Geometry and constraints in indentation loading

Two-dimensional plane strain finite elements models were built, simulating both a clean contact and a solid-contaminated contact. The former included a portion of circle representing the wheel and a rectangle representing the rail. The latter, in addition to these, included a number of small equally spaced circles, representing the contaminant particles, between the wheel and the rail, again modelled by plane strain elements. To simplify the model, only a half model was represented and the boundary condition of symmetry was imposed. The dimensions were chosen so that the boundary conditions may not influence the stresses and the strains in the contact area. The bottom of the rail is fixed. The portion of the wheel is tied through beam elements to a reference point, which represents the centre of the wheel itself. The contact load was applied to this point in vertical direction. The geometry of the contaminated contact model is shown in FIGURE 3.1; the model of the clean contact has the same geometry for the wheel and rail bodies. The contaminant radius R_P was set to 20 μm , representative of the average sand fraction that can be transported by the wind (20). Wheel and rail were meshed with CPE4R elements (first-order quadrilateral elements) and CPE3 (first-order triangular elements). The characteristic length of the elements in the global model varies from 0.5 mm to 10 μm in the contact area.

3.2.2 Geometry and constraints in rolling contact loading

Also in rolling contact simulations, two-dimensional plane strain model was built. The model uses portions of the wheel and of the rail. The wheel is a portion of annulus and the rail is a rectangle, fixed at its bottom. The portion of the wheel is tie-constrained to a reference point, like in the previous models. Rolling condition was obtained making this point move towards the horizontal direction. Furthermore, a slip rate of $s = 1\%$ was introduced by forcing the wheel to rotate a quantity equal to:

$$\vartheta = \frac{u}{R(1 - s)} \quad (3.1)$$

where ϑ is the rotation imposed, R the wheel radius, s the slip rate and u the displacement of the wheel. the simulations can be split up into two steps: in the former, the wheel and the rail were brought to contact, in the latter the wheel was made roll over the wheel for 30 mm. This rolling distance ensured that a steady state contact was achieved. FIGURE 3.2 shows the model. Wheel and rail were meshed with CPE4R elements (first-order quadrilateral elements) and CPE3 (first-order triangular elements). The characteristic length of the elements in the global model varies from 0.5 mm to 5 μm in the contact area.

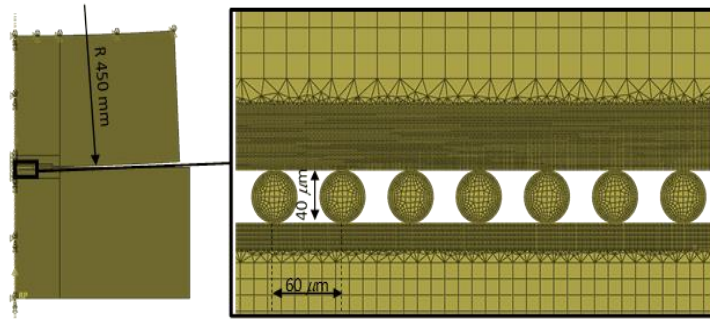


Figure 3.1 – Finite element model of the solid-contaminated contact

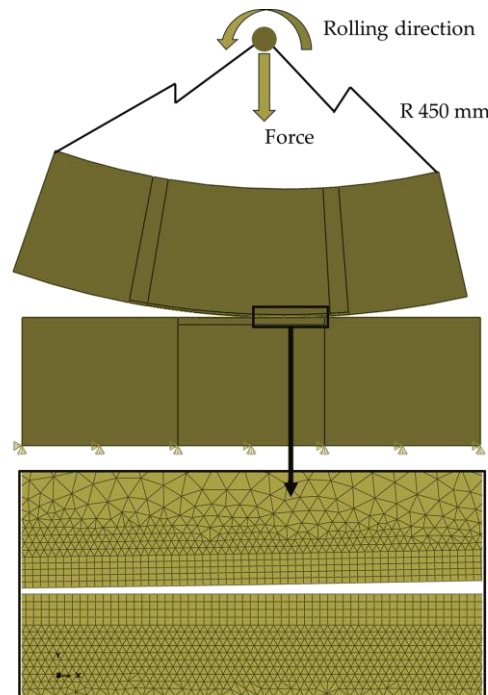


Figure 3.2 – Finite element model of the clean contact

3.2.3 Material models

To determine the material plastic properties to be used in the simulations, the data published in (14) and (20), which contain a review of the main properties of several wheel steels, were considered. In particular, the cyclic yield stress C.YS was considered as representative of the material elastic limit for high number of cycles. In order to estimate this parameter even for the rail steels, a relationship between the Brinell hardness and the cyclic yield stress C.YS was obtained by interpolating the known data of the wheel steels. The trend line shown in FIGURE 3.3 and expressed by Equation 3.1 was obtained; in Figure 3 the black dots correspond to the given wheel steels properties, whereas the red triangles correspond to the estimated rail steel properties.

$$C.YS [MPa] = -0.0121 HB^2 + 10.84 HB - 1389, \text{ with } 250 \leq HB \leq 390 \quad (3.1)$$

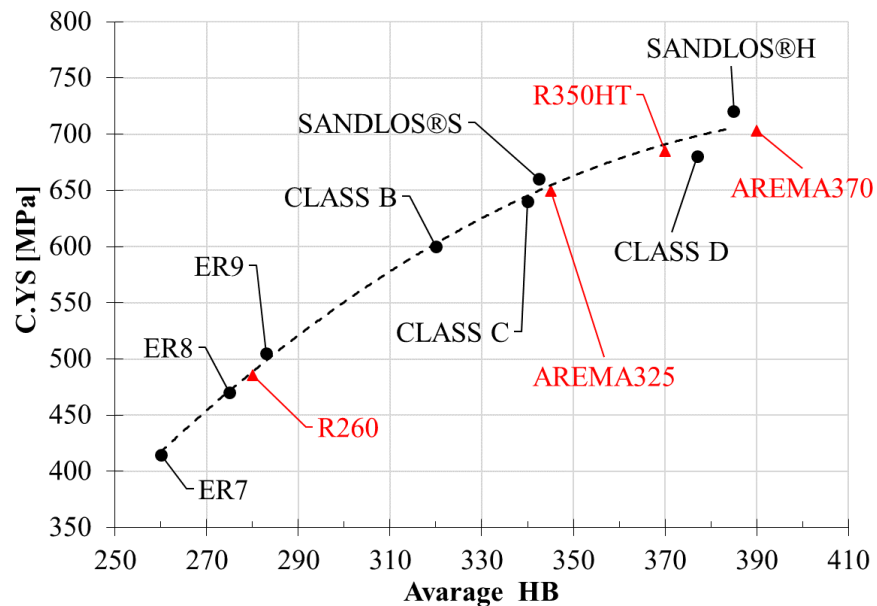
For each steel, once the cyclic yield strength was estimated, the constitutive law was approximated through the Ramberg-Osgood model:

$$\begin{cases} \epsilon = \frac{\sigma}{E} & \text{if } \sigma < C.YS \\ \epsilon = \frac{\sigma}{E} + \alpha \left(\frac{\sigma}{C.YS} \right)^{\frac{1}{n}} & \text{if } \sigma \geq C.YS \end{cases} \quad (3.2)$$

where ϵ and σ are the strain and the stress, respectively, $E = 206$ GPa is the elastic stiffness, $\alpha = 0.002$ is the conventional yield strain and n is the plastic exponent, here set to 5. The plastic part of the strain $\epsilon_p = \alpha \left(\frac{\sigma}{C.YS} \right)^{\frac{1}{n}}$ was introduced into the software only for stress exceeding the elastic limit.

As the contaminant particles are concerned, they were modelled by linear elastic material. In nature, the values of sand and rocks elastic modulus may vary in a wide range, from about 1 GPa till 100 GPa: the highest value (100 GPa) was considered in the simulations as it represents the most deleterious condition.

Figure 3.3 – Correlation between cyclic yield strength and Brinell hardness in rail and wheel steels



3.2.4 Loads

In order to determine the load to be applied in the 2D models, firstly the three-dimensional contact pressure distribution, taking into account a real case of wheel-rail geometry, was estimated according to the Hertz model for elliptical contact. In straight line, a contact load of 70 kN was imposed, typical for high-speed passenger train. The wheel diameter was taken as 900 mm; the transverse radius in the contact zone was set to 330 mm, according to the EPS EN 13715 profile. The rail transverse radius in the contact zone was taken as 300 mm, according to the 60 E1 EN 13674-1 profile. In case of curve, the contact load was set to 80 kN, taking into account the load transfer from the internal to the external wheel due to centrifugal inertia; furthermore, a lower rail transverse radius was considered (240 mm), taking into account a slight lateral displacement of the contact point. Once the pressure distributions were obtained, which were three-dimensional over an elliptical contact area, the Hertz theory of contact between two parallel cylinders was used for determining equivalent two-dimensional pressure distributions, whose profile was similar to the corresponding three-dimensional ones along the longitudinal axis of the elliptical contact area. Such distributions were obtained with a load-per-unit-thickness $P = 3$ kN/mm in straight line and $P = 8$ kN/mm in curve. These loading conditions match to maximum Hertz pressures $p_0 = 490$ MPa and $p_0 = 800$ MPa and semi-amplitude of contact area $a = 3.90$ mm and $a = 6.36$ mm. The value of the pressure in curve is coherent with the one foreseen in (22). The comparison between the equivalent two-dimensional distributions and the sections of the real three-dimensional ones along the longitudinal axis of the elliptical contact area is shown in FIGURE 3.4. The comparison is made under fully elastic strain hypothesis, complying the Hertz theory, just to fix a criterion for determining an equivalent load in plane strain models; the pressure distribution in the FE simulations, as shown below, differ from these due to plastic deformation. In the FE simulations a Coulomb friction law was employed, with coefficient of friction set to 0.5 both for steel-steel and contaminant-steel contact.

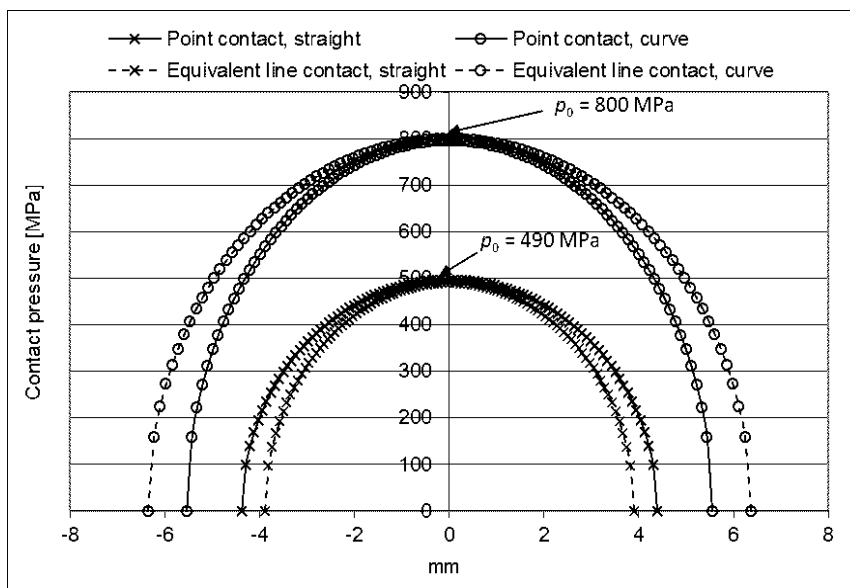
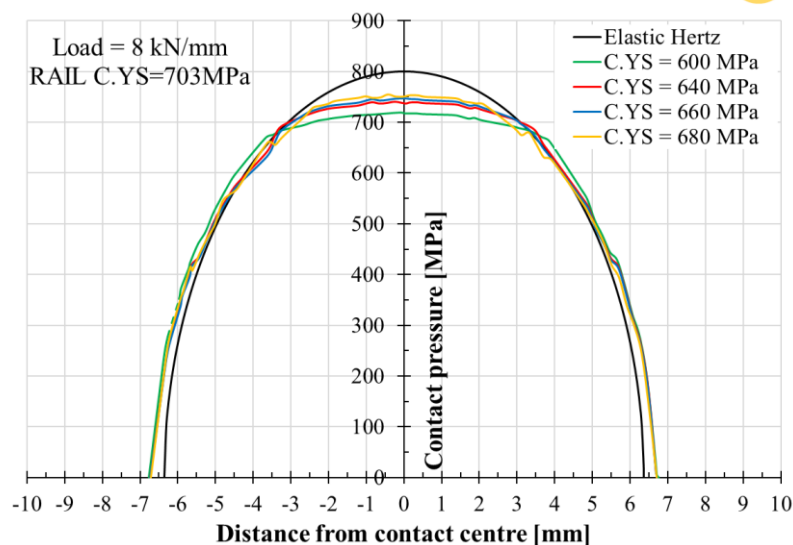
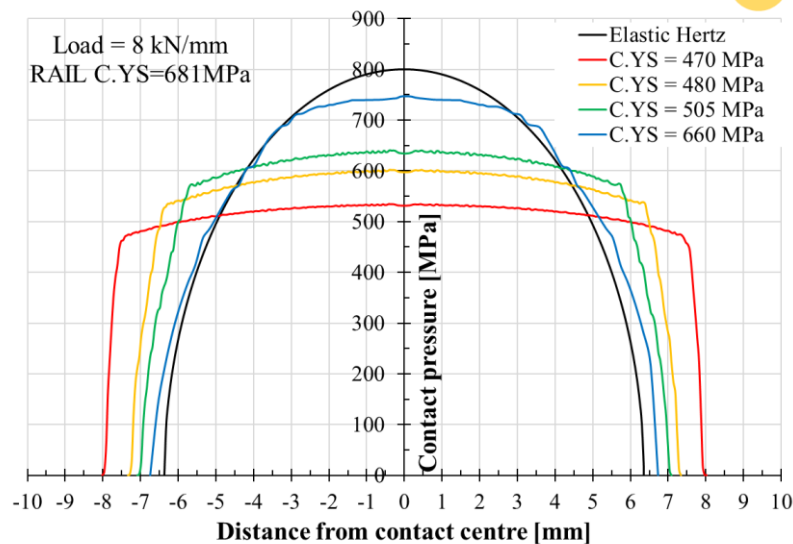


Figure 3.4 – Equivalent line contact pressure distributions compared with correspondent point contact distributions along the longitudinal axis of the contact ellipse (22)

3.3 Results

FIGURE 3.5 and FIGURE 3.6 show the contact pressure distribution on the wheel side in clean and contaminated contact, with the same steel coupling and under the same contact load. The corresponding Hertz pressure distribution was displayed as well for comparison. In clean contact the pressure distribution, which has larger contact area and lower pressure peak with respect to the Hertz case, is likely to be similar to this as far as the cyclic yield strength increases. In contaminated contact the overall pressure is given by a sequence of local distributions over the areas of contact between the contaminant particles and the main body. The peaks of the local distributions, which are of a magnitude order higher with respect to the case of clean contact, are higher at the centre of the overall contact area and decay to zero as far as they approach the borders.

Figure 3.5 – Pressure distribution in clean contact in compression loading, with $P = 8 \text{ kN/mm}$ (curve condition): a) European couplings; b) American couplings



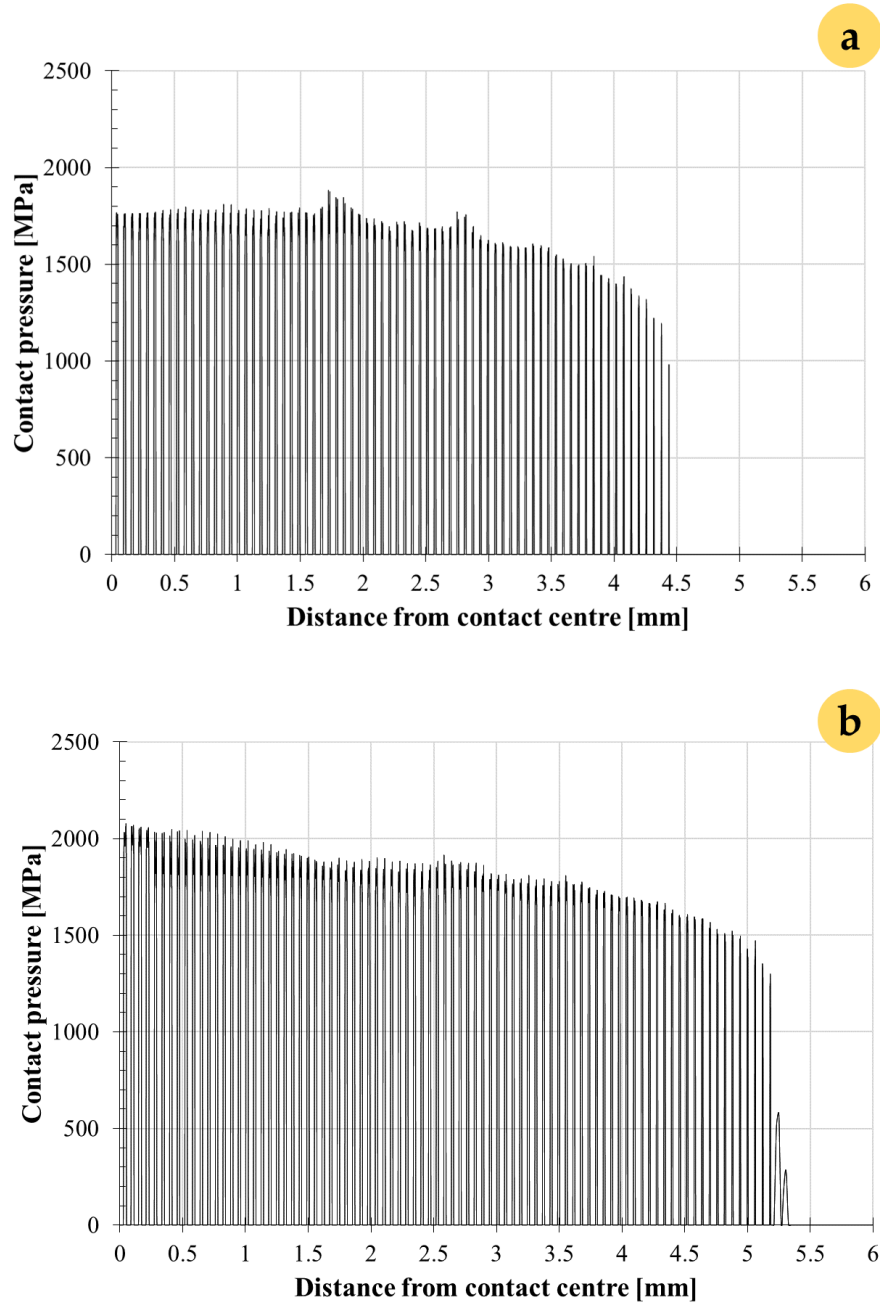


Figure 3.6 – Pressure distribution in contaminated contact, with $P = 3 \text{ kN/mm}$ (a) and $P = 8 \text{ kN/mm}$ (b)

FIGURE 3.7 shows the pressure distribution in the curve condition and in clean contact with European and American couplings compared to the Hertzian pressure when rolling condition is simulated. In plastic regime and in presence of slip rate, the contact area is wider than the Hertzian pressure and the pressure estimated in indentation loading. Also in these conditions, lower C.YS implies lower maximum pressure. Moreover, the pressure distribution is asymmetric, which means the resulting force direction is slightly displaced from the centre of the contact area, generating a momentum due to the friction force on the contact area. The maximum pressure was still much lower than the one estimated in contaminated contact.

Figure 3.7 - Pressure distribution in clean contact in rolling condition with $P = 8$ kN/mm (curve condition): a) European couplings; b) American couplings

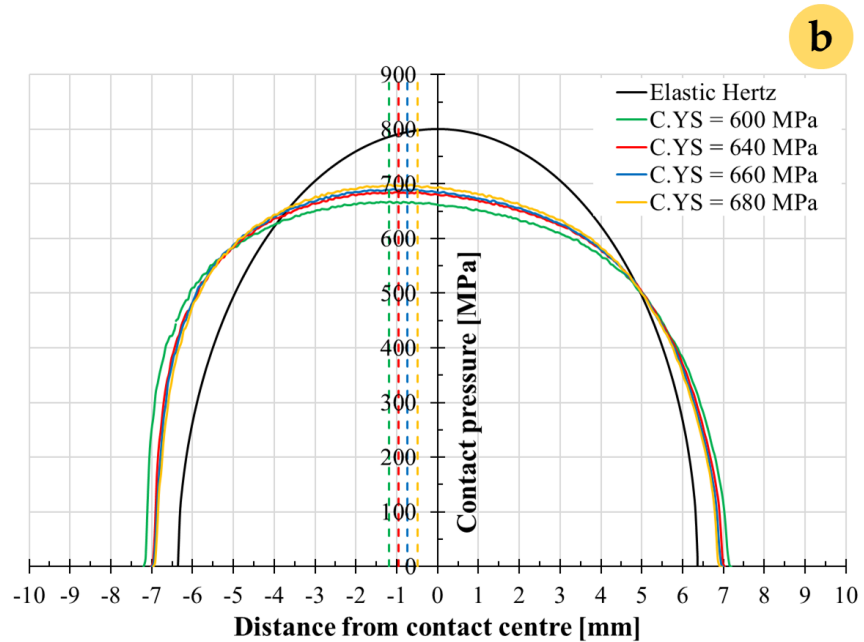
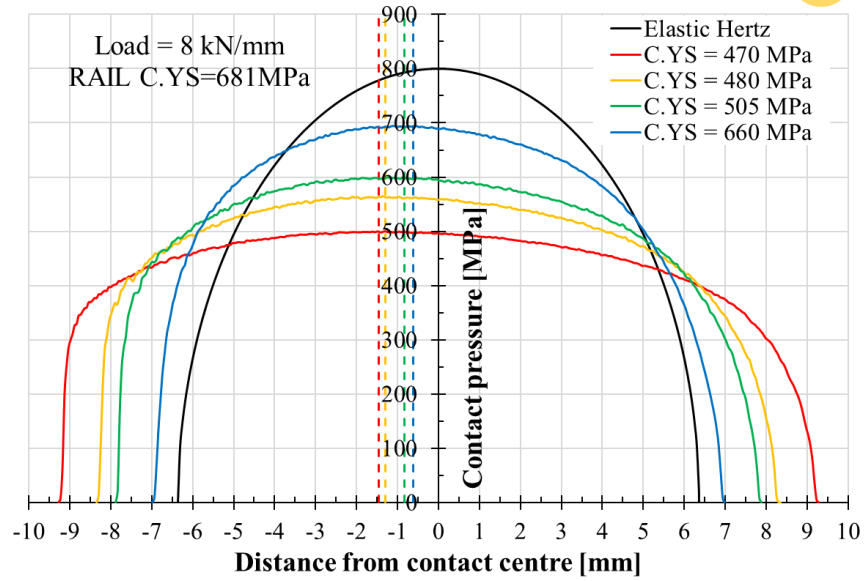


FIGURE 3.8 shows the map of the von Mises stress in clean and contaminated contact with Hertz nominal pressure $p_0 = 490$ MPa, wheel cyclic yield strength $C.YS_w = 505$ MPa and rail cyclic yield strength $C.YS_R = 681$ MPa. In the clean case a stress field involving a region on the dimensional scale of the contact area can be observed under the contact surface. In the contaminated case, an overall stress field similar to the clean contact case is generated, although it appears slightly more elongated in the direction normal to the contact surface. However, zooming the zone of the contaminant particles, a surface layer with local stress distributions related to the contact between the particles and the main bodies can be recognised,

This surface layer is clearly separated from the overall stress field related to the wheel-rail contact.

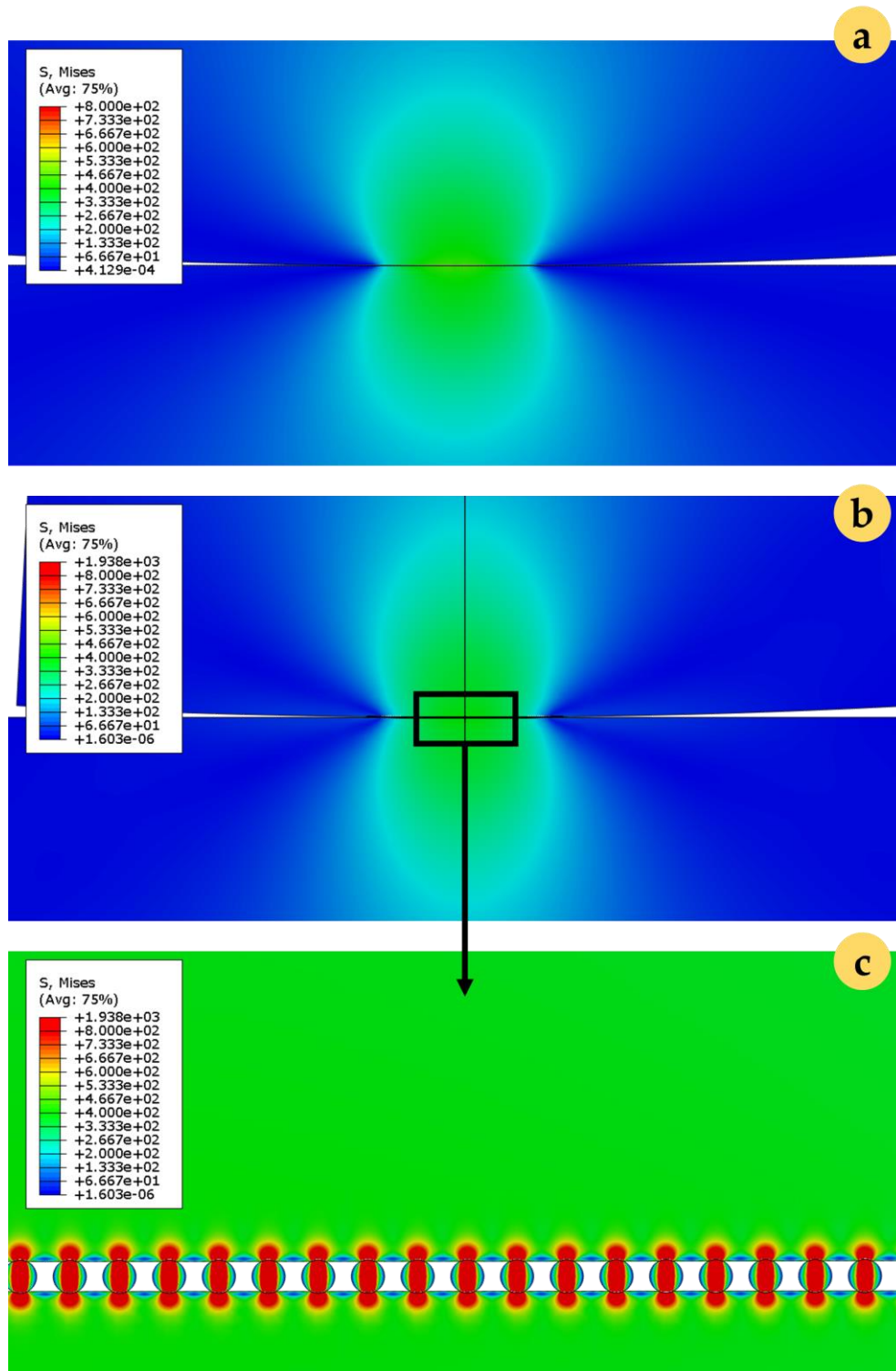


Figure 3.8 – Map of the Mises equivalent stress in the contact zone with rail $C.YS_R = 685$ MPa, wheel $C.YS_W = 505$ MPa, $p_0 = 490$ MPa in clean (a) and contaminated contact (b,c)

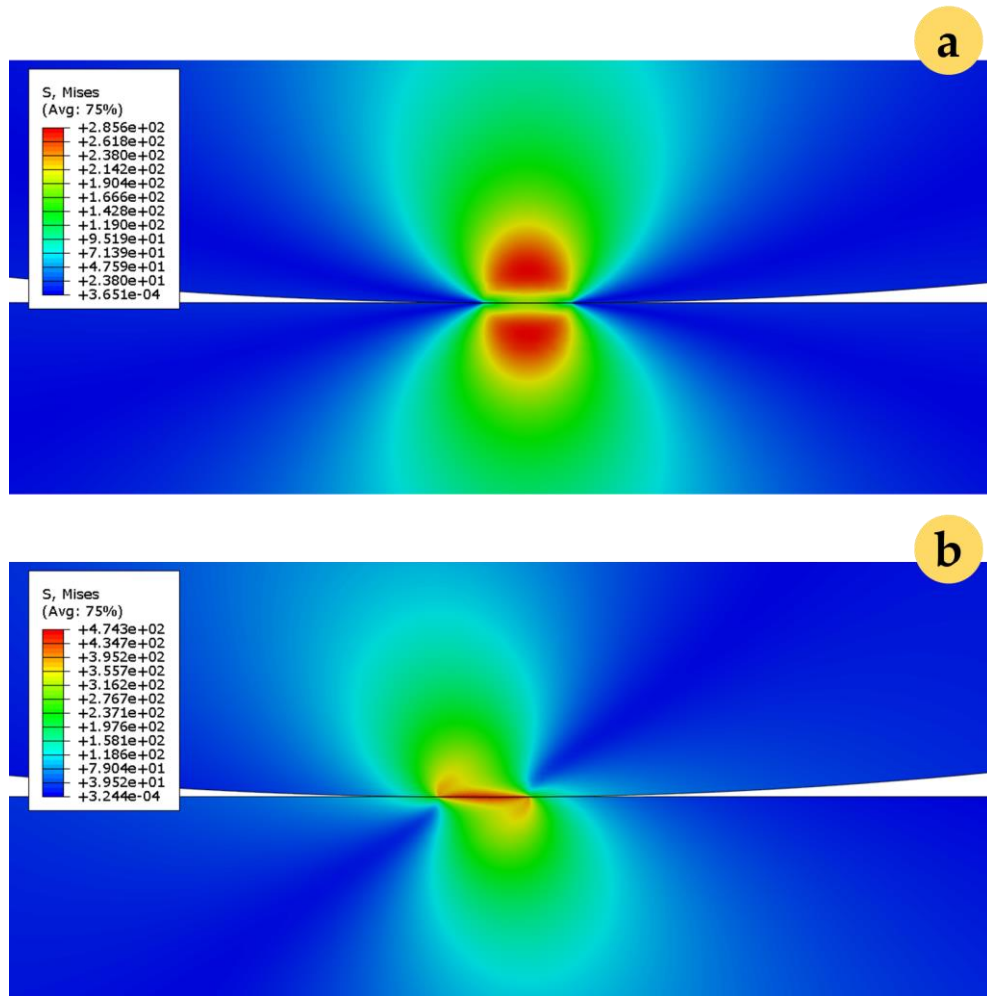


Figure 3.9 – Map of the Mises equivalent stress in the contact zone with rail C. $YS_R = 685$ MPa, wheel C. $YS_W = 505$ MPa, $p_0 = 490$ MPa in clean contact: (a) compressive loading; (b) rolling condition

FIGURE 3.9A and FIGURE 3.9B show the map of the von Mises stress in clean contact for EN ER9 wheel against R350HT rail in indentation loading and in rolling-sliding condition, respectively. As we expect, the maximum von Mises stress in indentation loading is in subsurface. On the other hand, when the wheel rolls over the rail, the maximum shifts towards the surface. As we saw in Chapter 2, the tangential contact force generated during the rolling is responsible of such behaviour, provided that the coefficient of friction is higher than about 0.3. The stress components due to the tangential force give rise to much higher stress values than in the simpler indentation loading (about 40% in the portrayed case). Nevertheless, the maximum von Mises stress is still much lower than the one found in contaminated contact.

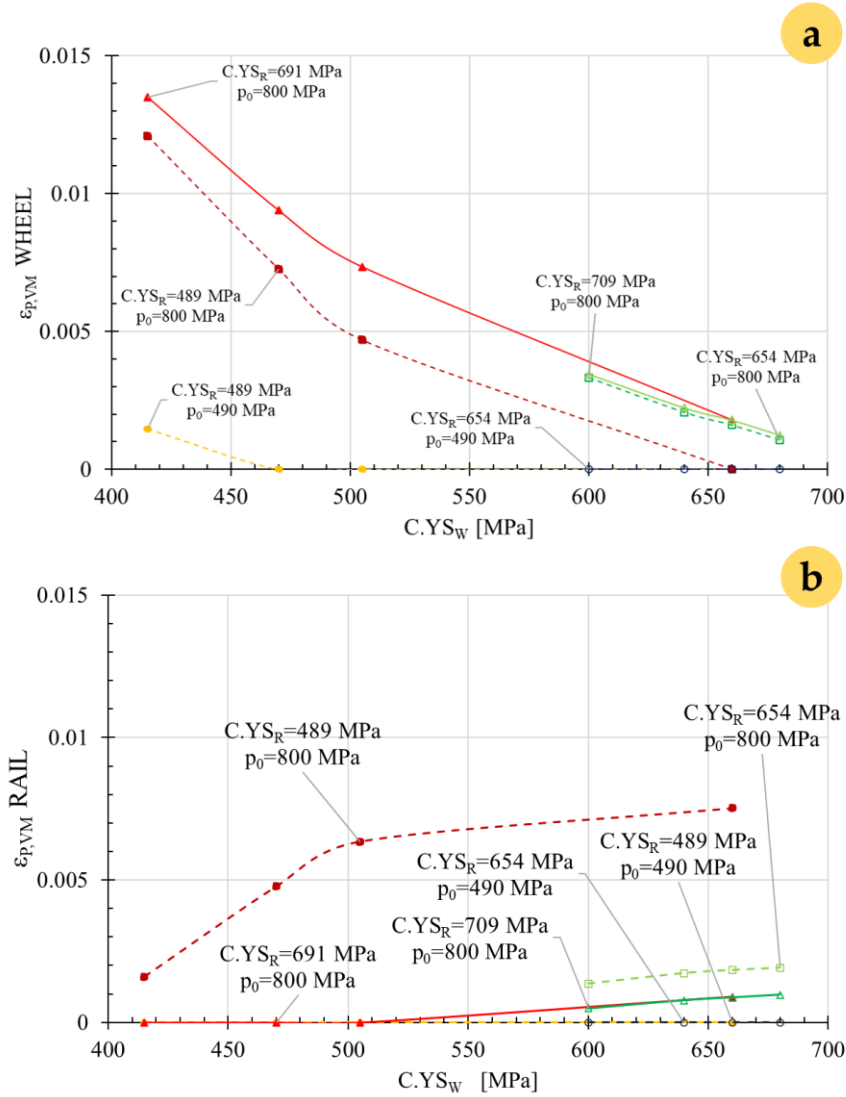


Figure 3.10 – Maximum von Mises equivalent plastic strain in clean contact in curve ($p_0 = 800 \text{ MPa}$) and in straight line ($p_0 = 490 \text{ MPa}$) as a function of the wheel cyclic yield strength $C.YS_W$ for various rail cyclic yield strength $C.YS_R$ in: a) wheels; b) rails

FIGURE 3.10A and FIGURE 3.10B show the trends of the maxima von Mises plastic strain in simulations of clean contact in the wheels and the rails, both in curve ($p_0 = 800 \text{ MPa}$) and in straight line ($p_0 = 490 \text{ MPa}$), as a function of the wheel cyclic yield strength $C.YS_W$ for various rail cyclic yield strength $C.YS_R$. The results with $p_0 = 490 \text{ MPa}$ show that no plastic strain is expected in the rail, whereas plasticization is expected in the wheels only for the lowest $C.YS_W$. With $p_0 = 800 \text{ MPa}$, increasing the rail hardness decreases the plastic strain in the rail itself, but on the other hand it increases the plastic deformation in the wheel. The dependence of the wheel strain on the rail strength $C.YS_R$ is less evident when $C.YS_R$ is higher than the wheel strength $C.YS_W$. This is consistent with the experimental evidence obtained by Lewis et al. [5] in terms of wear rate, which is correlated even to plastic strain. Overall, the results of the simulations in clean contact show that for each of the two contacting bodies the plastic strain depends both on its own cyclic yield strength and on the cyclic yield strength of the coupled body.

Figure 3.11 – Maximum von Mises plastic strain $\varepsilon_{p,Mises}$ in contaminated contact in curve ($p_0 = 800$ MPa) and in straight line ($p_0 = 490$ MPa) as a function of the wheel cyclic yield strength $C.YS_W$ for various values of the rail cyclic yield strength $C.YS_R$; a) in wheels; b) in rails

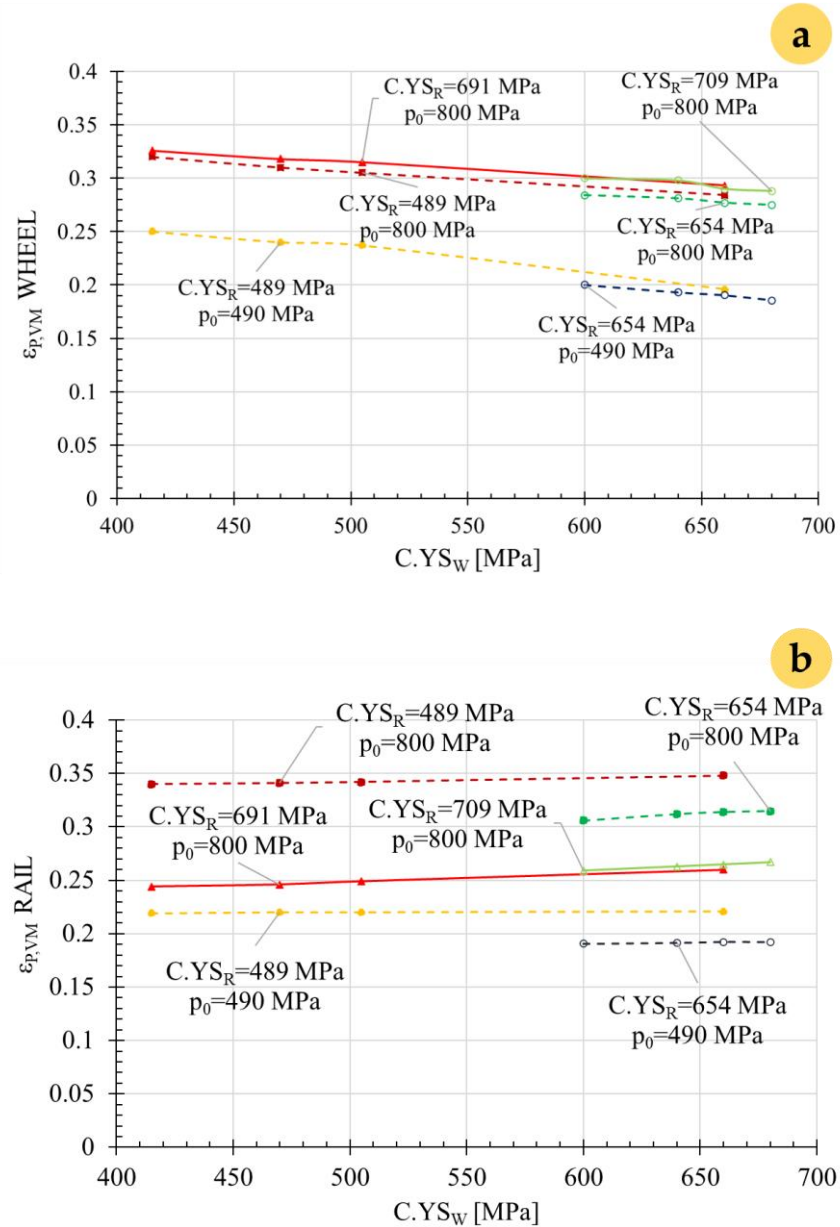


FIGURE 3.11A and FIGURE 3.11B show the same results as FIGURE 3.6 in solid contaminated contact. The diagrams show that when the contaminant is interposed between wheel and rail, the plastic strain in the surface is one order of magnitude higher than in clean condition. Plastic strain in wheels essentially depends on the contact pressure and on the wheel strength $C.YS_W$; the dependence on the rail strength $C.YS_R$ is much slighter. The same goes for the rails: the plastic strain strongly depends on the contact pressure and on the rail $C.YS_R$; the dependence on the wheel $C.YS_W$ is negligible. This means that, contrary to the case of clean contact, in presence of solid contaminant the maximum plastic strain does not depends so much on the properties of the coupled body. The reason is that the maximum plastic deformation is affected mainly by the local contact between the contaminant particles and the body rather than by the overall wheel-rail contact.

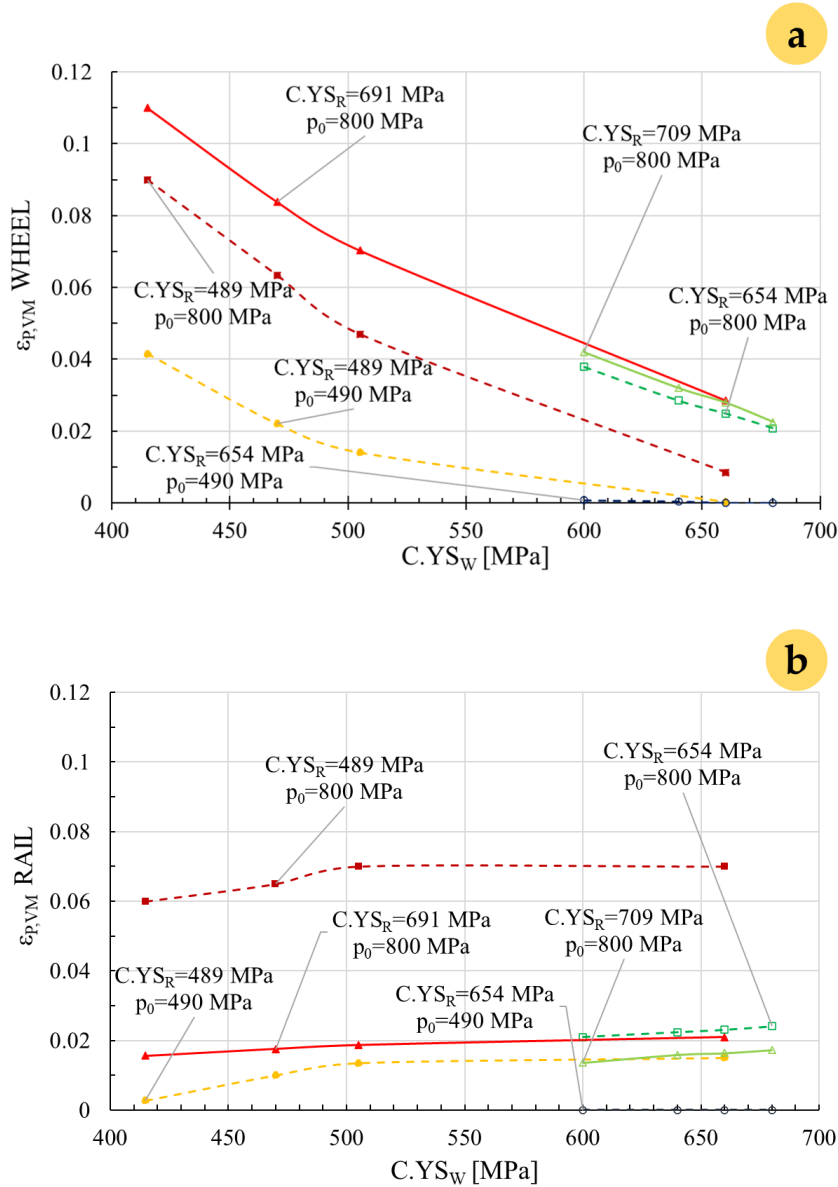


Figure 3.12 – Maximum von Mises equivalent plastic strain in clean contact in rolling condition in curve ($p_0 = 800$ MPa) and in straight line ($p_0 = 490$ MPa) as a function of the wheel cyclic yield strength $C.YS_W$ for various rail cyclic yield strength $C.YS_R$ in: a) wheels; b) rails

FIGURE 3.12A and FIGURE 3.12B show the trends of the maxima von Mises plastic strain in clean contact and rolling conditions. The plastic strain is one order of magnitude higher than in the case of indentation loading due to the action of the friction force generated by the rolling wheel, but the general trend of the curves is the same. When $C.YS_W$ increases, the wheel plastic strain shows a downward trend; on the other hand, the rail plastic strain slightly increases and it seems to reach a steady state when $C.YS_W$ becomes higher than $C.YS_R$. It is also noteworthy that all the rails plasticise, except for the American rail (AREMA 370) when the applied pressure is 490 MPa.

Figure 3.13 – Von Mises equivalent plastic strain in contaminated contact in straight line ($p_0 = 490$ MPa) as a function of the wheel cyclic yield strength $C.YS_W$ for various rail cyclic yield strength $C.YS_R$ in wheels: a) wheels; b) rails

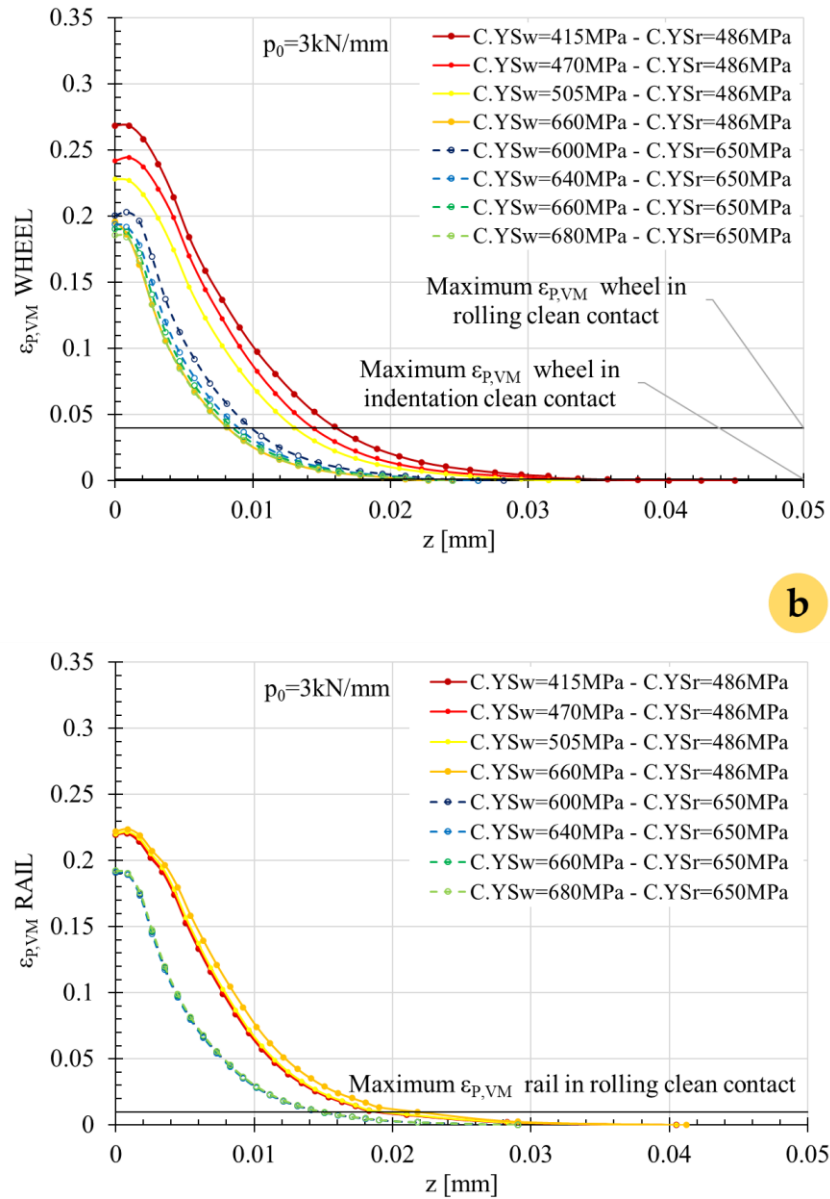


FIGURE 3.13 and FIGURE 3.14 show the equivalent von Mises plastic strain accumulated by the wheels and the rails in straight line ($P = 3$ kN/mm) and curve ($P = 8$ kN/mm). European couplings are identified with coloured solid lines, American couplings with dashed coloured lines. The black solid lines represent the maxima plastic strains found in indentation and rolling conditions in the same loading conditions. SANDLOS®S is considered as well ($C.YS_W = 660$ MPa). In general, the plastic strain in contaminated contact is much higher than in clean contact and even the rails always plasticise, although in clean contact remains in their undeformed state. Once again, the wheels are more affected by the change of rail and load than the rails. The rails are indeed less swayed by the change of wheels, particularly when the contact load is lower. The American railr behave worse than the European one in curve despite the higher cyclic yield strength.

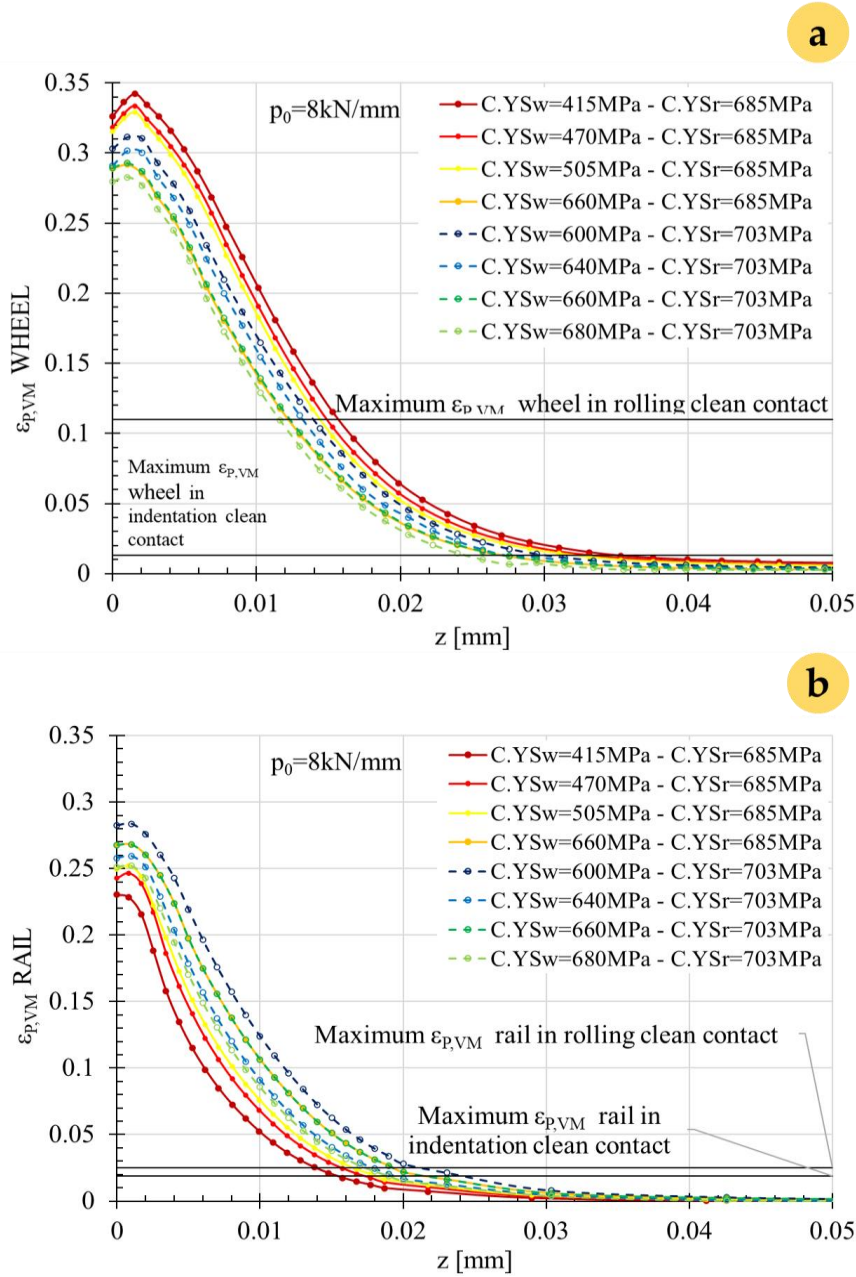


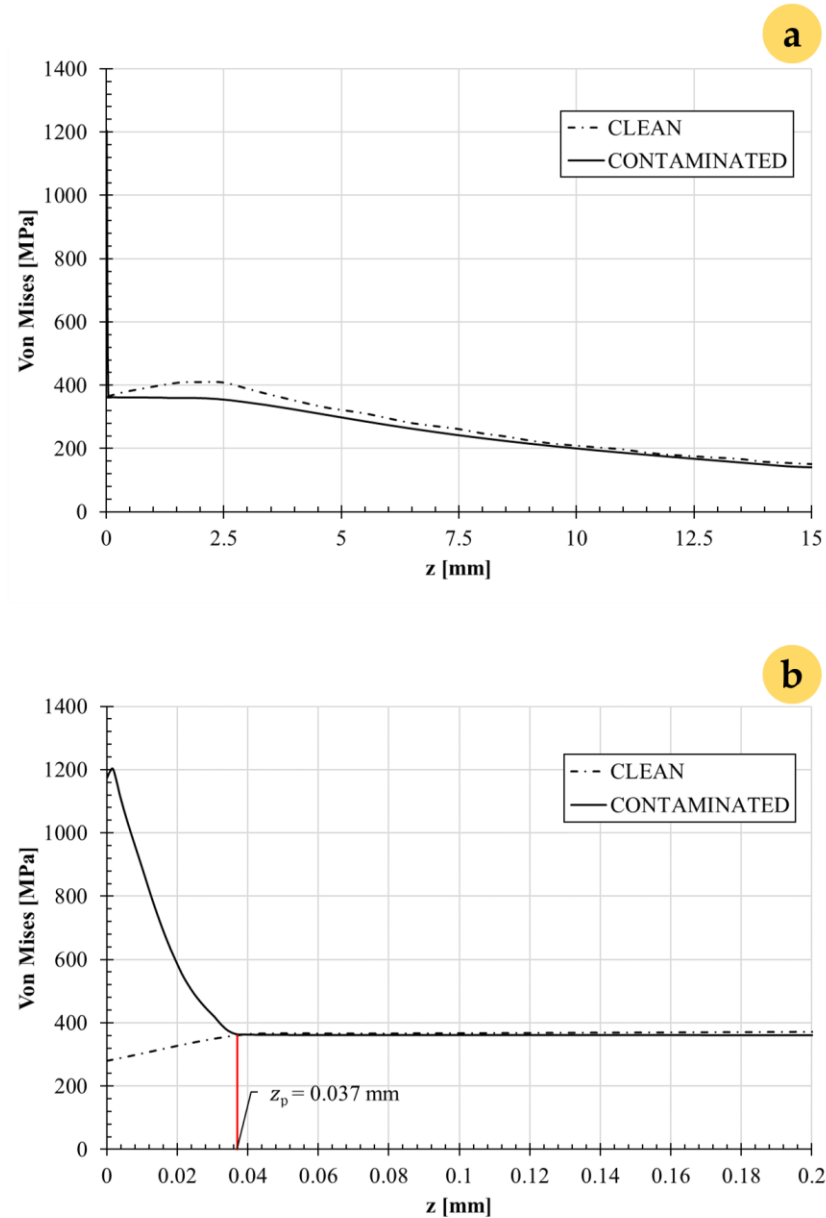
Figure 3.14 – Von Mises equivalent plastic strain in contaminated contact in curve ($p_0 = 800 \text{ MPa}$) as a function of the wheel cyclic yield strength $C.YS_W$ for various rail cyclic yield strength $C.YS_R$ in rails: a) wheel; b) rail

This phenomenon relies on the fact the American wheel-rail couplings have a smaller difference in cyclic yield strength than the European couplings.

These figures are also further evidence of the deleterious effect of solid contaminants between wheel and rail and suggest that there are a subsurface region influenced by such contaminants and a region far enough away the surface only influenced by the “global” wheel-rail contact.

The relation between the stress fields related to local and overall contact respectively can be highlighted by the von Mises plastic strain gradient along the depth shown in FIGURE 3.15. The stress gradient is plotted along a line below the location of the particle closest to the centre of the contact area, both in clean and contaminated contact, with the same steel coupling and under the same load. This line includes the point of maximum equivalent plastic strain. FIGURE 3.15A shows the overall stress field; FIGURE 3.15B is zoomed on the region near the contact surface. Close to the surface, the stresses are much higher in contaminated contact than in clean contact. As far as the depth increases, the two curves tend to overlap. The layer where the two curves tend to diverge can be identified as the zone of influence of the local contact between one of the main bodies (in this case the wheel) and the contaminant particle. The depth z_p which bounds this layer can be taken at the location where the two curves intersect.

Figure 3.15 – Gradient of the Mises stress below the location of the particle closest to the contact centre, with rail $C.YS_R = 489 \text{ MPa}$, wheel $C.YS_W = 505 \text{ MPa}$, $p_0 = 490 \text{ MPa}$; a) overall; b) zoom on layer with $z < 0.2 \text{ mm}$



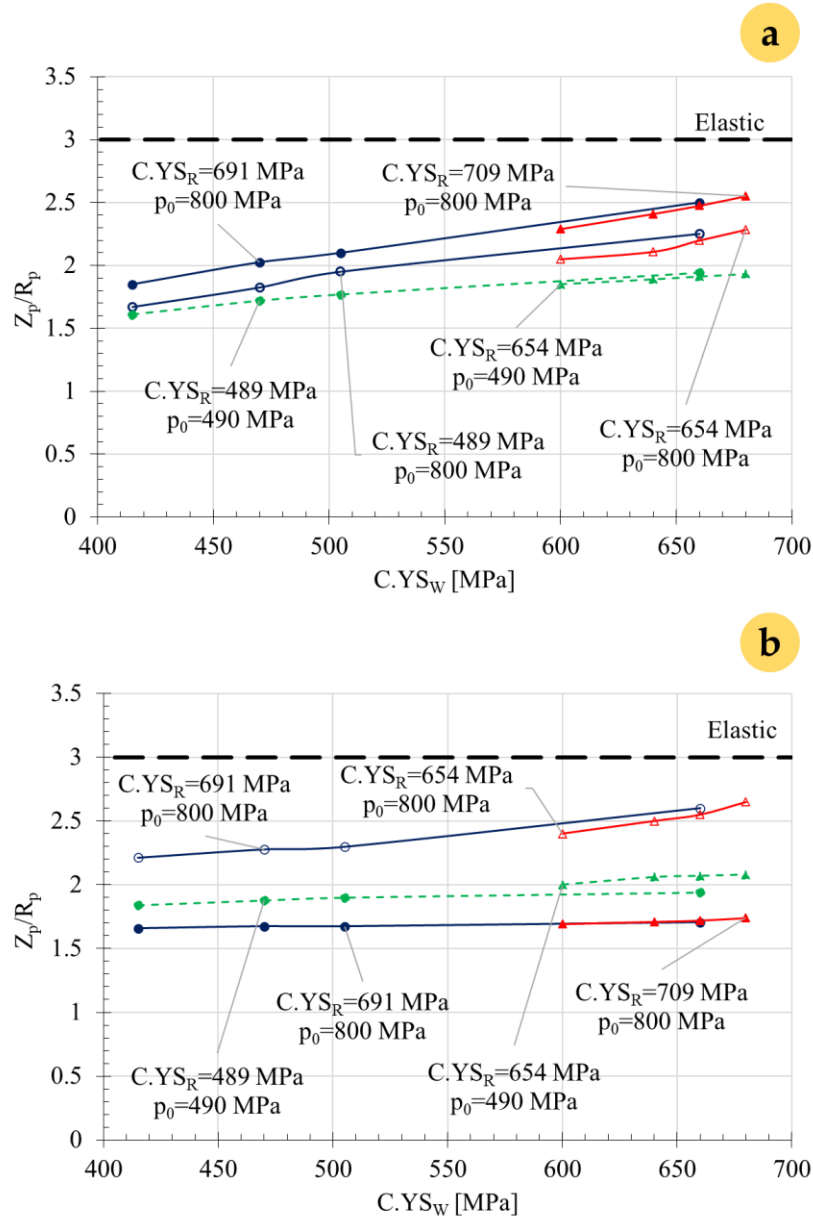


Figure 3.16 – Variation of the depth of influence of the local particle-body contact normalized with the particle radius as a function of the wheel $C.YS_W$, for various rail $C.YS_R$ and contact pressure, compared with the case of fully elastic materials: a) in wheels; b) in rails

FIGURE 3.16 shows the depth of influence of the local contact z_p , normalized with the contaminant particle radius R_p , with varying cyclic yield strengths $C.YS_W$ and $C.YS_R$ and contact pressure p_0 . It is not possible to identify a general univocal law for the dependence of z_p/R_p on the load and material parameters, but it varies around $z_p/R_p = 2$, meaning that the depth of influence of the particles is of the magnitude order of their diameter. Mazzù and Battini (23) elaborated an analytical model to determine the pressure distribution in the presence of solid contaminants with fully elastic contacting material. They also analysed the stress field under such pressure distribution, finding that the depth of influence of the particles is about $z_p/R_p = 3$. The present analysis shows that with plastic materials z_p is always below such limit; therefore $z_p/R_p = 3$ can be taken as the upper bound for the depth of influence of the local particle-body contact. This means that, for a depth $z_p/R_p > 3$ the body can be treated, with good approximation, as the contaminant was not present.

3.4 Comparison with experimental results

In (2) the results of bi-disc experimental tests in clean and sand contaminated contact are published. Such tests were carried out with nominal Hertz pressure set at 1100 MPa, with 500 r.p.m. mean rolling speed and 1% sliding-to-rolling speed ratio, using wheel and rail steel discs of 15 mm thickness and 60 mm diameter. The contaminated contact was obtained adding a continuous sand flow at the contact interface, using calibrated sand with particle size ranging from 0.20 to 0.35 mm. The working condition of such tests were different from those simulated in the present analyses, however the results of these tests provide some feedbacks about the tendency highlighted by the FE simulations.

FIGURE 3.17 shows the sections of two wheel steel specimens, made in ER8 and SANDLOS® S, and of the rail steel specimens that were tested against them, both made with the same rail steel (R350HT). These specimens were tested in clean contact. The layer where plastic strain is visible directly on the microstructure is highlighted. As far as the cyclic yield stress of the wheel increases (from the top to the bottom), the depth of such layer decreases in the wheel specimen (left column) and correspondingly increases in the rail specimen (right column).

FIGURE 3.18 shows the sections of two wheel steel specimens and two rail steel specimens made with the same steels, tested in sand contaminated contact. Whereas the depth of visible strain decreases in the wheel specimen as far as its cyclic yield stress increases, such depth does not change significantly in the rail specimen. This is in agreement with one of the tendencies highlighted by the simulations: in clean contact, the plastic strain of each contacting body depends on the properties of both of the coupled bodies, whereas in solid contaminated contact the plastic strain of each contacting body depends mainly on its own properties.

Other information can be obtained considering the size of the contaminant particles. The particles size passing the contact interface without being crushed is not known, as a post-process analysis of the used sand was not carried out. However, a clue on the size of the passing particles is given by Grieve et al. (24), who measured the particle size distribution before and after tests in sand contaminated contact. Although they were not able to separate the particles passing the contact from those thrown away without being entrapped between the specimens, they observed that the quantity of particles with size up to 146 μm increased after the tests, whereas the quantity of particles of higher size decreased. Therefore, 146 μm can be considered as the upper limit of particle size that can pass the contact without being crushed; roughly, 80-100 μm can be considered the mean size of particles passing the contact and significantly affecting the stress distribution. Therefore, according to the tendency highlighted by the simulations, the maximum depth of influence of the local particle-body contact can be estimated as about 150 μm . Comparing this estimation with the sections of the specimens tested in contaminated contact of FIGURE 3.17, we can observe that for the rail steel and for the harder wheel steel (FIGURE

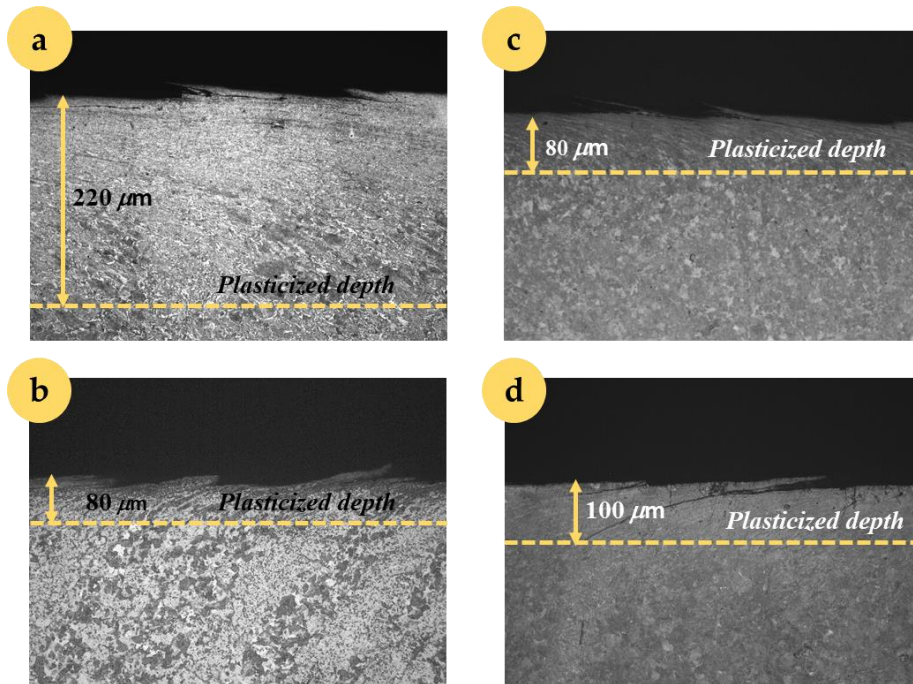


Figure 3.17 – Micrographs of the sections of wheel and rail steels tested in (2) in clean condition: a) EN ER8 wheel steel ($C.YS_W = 470$ MPa); b) R350HT rail steel ($C.YS_R = 691$ MPa), tested against the EN ER8; c) SANDLOS® S wheel steel ($C.YS_W = 660$ MPa); d) R350HT rail steel tested against the SANDLOS® S

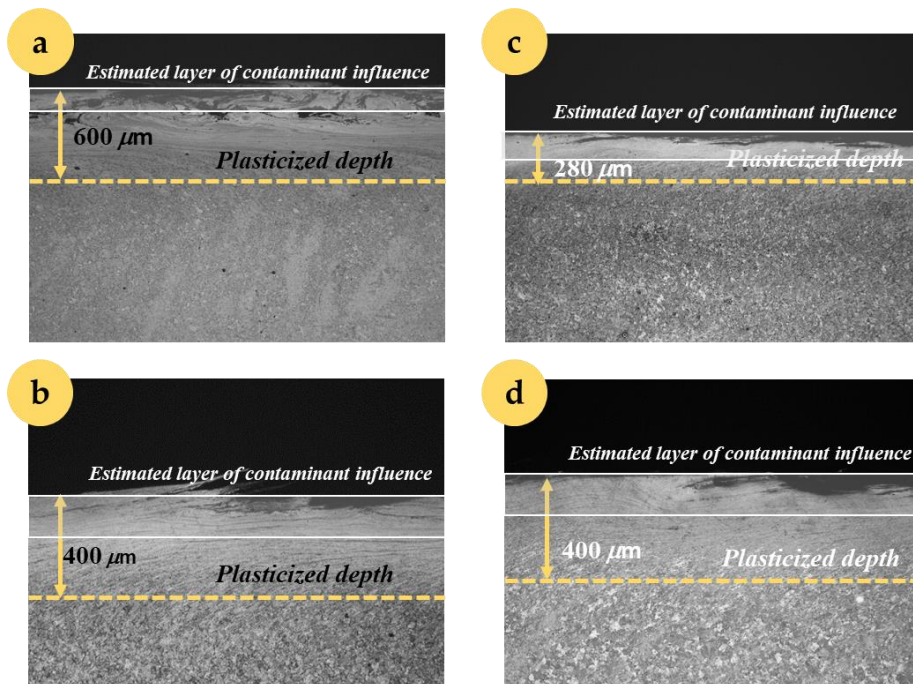


Figure 3.18 – Micrographs of the sections of wheel and rail steels tested in (2) in sand contaminated condition: a) EN ER8 wheel steel $C.YS_W$; b) R350HT rail steel ($C.YS_R = 691$ MPa), tested against the EN ER8; c) SANDLOS® S wheel steel ($C.YS_W = 660$ MPa); d) R350HT rail steel, tested against the SANDLOS® S

18B, FIGURE 18C and FIGURE 18D) the estimated layer of the particle influence is characterized by huge strain, with grain boundaries and cracks oriented parallel to the contact surface. The material laying below this layer exhibits plastic strain as well, but not so severe and progressively decreasing as far as the depth increases, with a pattern similar to the cases of clean contact. On the other hand, in the softest wheel steel (Figure 18a) the layer with huge deformation extends well below the estimated depth of influence of the contaminant. Moreover, sand particles are incorporated in this layer, forming veins of incoherent material below the surface. In this case, reasonably, there wasn't a clear separation between the local and overall strain field, as the latter was severe as well. Therefore, the contaminant

particles were involved in the overall plastic flow process, being even incorporated into the metal bodies.

3.5 Concluding remarks

In this chapter, the effect of changing the cyclic yield strength ratio between wheel and rail in presence of solid contaminants was investigated by means of 2D finite element analyses. Simulations were carried out with two levels of loads, reproducing the contact conditions of a wheel in curve and straight line. Clean contact conditions were simulated as well. The results were discussed mainly in terms of plastic strain and compared with published experimental results.

The main findings are listed in the following points:

- In clean contact, the plastic strain of each contacting body depends on the mechanical properties of both of the coupled components, specifically on the cyclic yield strength. When solid contaminant is added, the plastic strain depends essentially on the local contact between the particles and the body, therefore the influence of the coupled body is low.
- A zone of influence of the local contact between the particles and the body was identified by comparing the stress fields in clean and contaminated contact. Such zone extends in depth up to approximately 2.5 times the radius of the contaminant particles, depending on the load and the mechanical properties of the contacting bodies. An upper bound for the depth of particle influence can be set at 3 times the particle radius, which is obtained in fully elastic contact.
- The comparison with published experimental results of sand contaminated contact revealed that, with hard materials, the damage, in terms of huge ratcheting and crack formation, keeps confined essentially within the zone of influence of the local particle-body contact. On the other hand, if the material of the contacting body is too soft, the local and overall strain field merge and the damage is extended well below the limit of influence of the local contact.

The general conclusion that can be derived is that a key role for improving the performance of wheel and rail steels in solid contaminated environment is played by the cyclic yield strength. By increasing this parameter, it is expected that the most severe damage is limited at a depth comparable to the particle size, without significantly influencing the performance of the coupled element.

3.6 References

1. Ghidini, A, Faccoli M., Mazzù A. SANDLOS® wheels for desert environments, Lucchini RS, Lovere (Italy), 2017.
2. Faccoli M, Petrogalli C, Lancini M, Ghidini A, Mazzù A. Effect of desert sand on wear and rolling contact fatigue behaviour of various railway wheel steels. *Wear*. 2018 Feb 15;396–397:146–61. <https://doi.org/10.1016/j.wear.2017.05.012>.
3. M. Burstow: Wheel/rail hardness and total ‘system’ wear, Report of the Rail Safety and Standards Board, Vehicle/Track System Interface Committee, 2012.
4. Lewis R, Wang WJ, Burstow M, Lewis SR. Investigation of the Influence of Rail Hardness on the Wear of Rail and Wheel Materials under Dry Conditions *Wear and RCF Mechanisms*. 2016;1–17..
5. Liu J, Jiang W, Chen S, Liu Q. Effects of rail materials and axle loads on the wear behavior of wheel/rail steels. *Adv Mech Eng*. 2016;8(7):1–12. <https://doi.org/10.1177%2F1687814016657254>.
6. Kumar S, Krishnamoorthy PK, Prasanna Rao DL. Wheel-rail wear and adhesion with and without sand for a north american locomotive. *J Manuf Sci Eng Trans ASME*. 1986;108(2):141–7. <https://doi.org/10.1115/1.3187049>.
7. Lewis R, Dwyer-Joyce RS. Wear at the wheel/rail interface when sanding is used to increase adhesion. *Proc Inst Mech Eng Part F J Rail Rapid Transit*. 2007;220(1):29–41. <https://doi.org/10.1243%2F095440905X33260>
8. Arias-Cuevas O, Li Z, Lewis R. A laboratory investigation on the influence of the particle size and slip during sanding on the adhesion and wear in the wheel-rail contact. *Wear*. 2011 May 18;271(1–2):14–24. <https://doi.org/10.1016/j.wear.2010.10.050>.
9. Dube NB, Hutchings IM. Influence of particle fracture in the high-stress and low-stress abrasive wear of steel. *Wear*. Elsevier Sequoia SA; 1999. p. 246–56. [https://doi.org/10.1016/S0043-1648\(99\)00297-5](https://doi.org/10.1016/S0043-1648(99)00297-5).
10. Omasta M, Machatka M, Smejkal D, Hartl M, Křupka I. Influence of sanding parameters on adhesion recovery in contaminated wheel–rail contact. *Wear*. 2015 Jan 15;322–323:218–25. <https://doi.org/10.1016/j.wear.2014.11.017>.
11. Cvetkovski K, Ahlström J, Norell M, Persson C. Analysis of wear debris in rolling contact fatigue cracks of pearlitic railway wheels. *Wear*. 2014 Jun 15;314(1–2):51–6. <https://doi.org/10.1016/j.wear.2013.11.049>

12. Gallardo-Hernandez EA, Lewis R. Twin disc assessment of wheel/rail adhesion. *Wear*. 2008 Oct 30;265(9–10):1309–16. <https://doi.org/10.1016/j.wear.2008.03.020>.
13. Lewis R, Wang WJ, Burstow M, Lewis SR. Investigation of the Influence of Rail Hardness on the Wear of Rail and Wheel Materials under Dry Conditions Wear and RCF Mechanisms. *Proc 11th Int Conf Contact Mech Wear Rail/wheel Syst*. 2018;510–7. <https://doi.org/10.1016/j.wear.2019.05.030>
14. Ghidini A, Faccoli M., Mazzù A. SANDLOS® wheels for desert environments, Lucchini RS, Lovere (Italy), 2017.
15. Sebès M, Chollet H, Ayasse J-B, Chevalier L. A multi-Hertzian contact model considering plasticity. *Wear*. 2014 Jun 15;314(1–2):118–24. <https://doi.org/10.1016/j.wear.2013.11.036>.
16. Vasić G, Franklin FJ, Fletcher DI. Influence of partial slip and direction of traction on wear rate in wheel-rail contact. *Wear*. 2011 Jan 12;270(3–4):163–71. <https://doi.org/10.1016/j.wear.2010.10.012>.
17. Krácalík M, Trummer G, Daves W. Application of 2D finite element analysis to compare cracking behaviour in twin-disc tests and full scale wheel/rail experiments. *Wear*. 2016 Jan 15;346–347:140–7. <https://doi.org/10.1016/j.wear.2015.11.013>.
18. Daves W, Kubin W, Scheriau S, Pletz M. A finite element model to simulate the physical mechanisms of wear and crack initiation in wheel/rail contact. *Wear*. 2016 Nov 15;366–367:78–83. <https://doi.org/10.1016/j.wear.2016.05.027>.
19. Srivastava JP, Sarkar PK, Ranjan V. Contact Stress Analysis in Wheel–Rail by Hertzian Method and Finite Element Method. *J Inst Eng Ser C*. 2014 Oct 2;95(4):319–25. <https://doi.org/10.1007/s40032-014-0145-x>.
20. Lancaster N, Nickling W., McKenna Neuman C. Particle size and sorting characteristics of sand in transport on the stoss slope of a small reversing dune. *Geomorphology*. 2002 Mar 1;43(3–4):233–42. [https://doi.org/10.1016/S0169-555X\(01\)00135-0](https://doi.org/10.1016/S0169-555X(01)00135-0).
21. Ghidini. M. Diener, A. Gianni and J. Schneider: SUPERLOS® Innovative steel by Lucchini RS for high-speed wheel application, Lucchini RS, Lovere (Italy), 2012.
22. Iwnicki S. Simulation of wheel – rail contact forces. *Fatigue Fract Eng Mater Struct*. 2003;26(August):887–900. <https://doi.org/10.1046/j.1460-2695.2003.00699.x>.

23. Mazzù A, Battini D. A Model for the Assessment of Wheel–Rail Contact in the Presence of Solid Contaminants. Tribol Trans. 2019 Jan 4; 62-2: 230-238. doi.org/10.1080/10402004.2018.1535104.
24. Grieve DG, Dwyer-Joyce RS, Beynon JH. Abrasive wear of railway track by solid contaminants. Proc Inst Mech Eng Part F J Rail Rapid Transit. 2001 May 21;215(3):193–205. [https://doi.org/ 10.1243% 2F095440 9011531512](https://doi.org/10.1243%2F0954409011531512).

Part III



Chapter 4 - Effect of traces of bainite in railway wheels

(previous page) Micrograph of a railway wheel with ferritic-pearlitic microstructure and presence of traces of bainite.

List of symbols

Symbol	Description
a	Semi-contact length along direction x
B	Material coefficient in Swift's law
b	Major semi-axis dimension of elliptical bainitic spot
C	Material coefficient in Swift's law
C.YS	Cyclic yield strength
c	Semi-contact length along direction y
E	Young's modulus
FEM	Finite Element Model
HB	Brinell hardness
I	Interaxis between two bainitic spots
m	Hardening exponent in Swift's law
n	Hardening exponent in Ramberg-Osgood's law
PEEQ	Von Mises equivalent plastic strain calculated by ABAQUS®
p_0	Hertzian pressure
R_x	Curvature of the contact body along direction x
R_y	Curvature of the contact body along direction y
RCF	Rolling contact fatigue
r	Radius of circular/spherical bainitic spot
SAM	Semi-Analytical Model
x	Cartesian coordinate along the rolling direction (longitudinal direction)
y	Cartesian coordinate along the transverse direction
z	Cartesian coordinate along the depth
z_C	Coordinate of the bainitic spot centre in direction z
α	Conventional cyclic yield deformation
ε	Strain
ε_P	Plastic strain
σ	Stress

Effect of traces of bainite in railway wheels

4

This chapter aims at investigating the presence of bainitic traces in a ferritic-pearlitic microstructure of a railway wheel through finite element models (FEM) and semi-analytical models (SAM). This activity was carried out in partnership with the *Institute National des Sciences Appliquées* in Lyon (INSA-Lyon), whose researchers coded a semi-analytical model for contact problems application.

This chapter is based on the paper:

N. Zani, T. Chaise, A. Ghidini, M. Faccoli, A. Mazzù. *Numerical study about the effect of bainitic traces on plasticity in ferritic-pearlitic railway wheels*. Proceedings of the Institution of Mechanical Engineers, Part F: Journal of Rail and Rapid Transit, 2020. <https://doi.org/10.1177/2F0954409720960888>.

4.1 State of the art and motivation

As anticipated in Chapter 2, the microstructure of railway wheels is typically ferritic-pearlitic. This microstructure has revealed to offer a good compromise between wear response and fatigue behaviour (1-12). The last decades have witnessed an increase in the hardness of the wheel steels and, with this goal in mind, the bainitic steels have been designed. Notwithstanding the number of researches focusing on pearlite and its effect on RCF and wear, there are only a few studies on bainitic microstructure. Pointner (13) discussed the differences between pearlitic and bainitic homogenous microstructures in railway components, especially rails; in his work, he pointed out how the fatigue resistance of bainitic steel is much higher than pearlitic one but, on the other hand, wear rate is higher. Wear resistance in bainitic steels was indeed about half the wear resistance of pearlitic rails with the same hardness. However, the RCF-cracks grow much slower than the cracks in the pearlitic rails.

Despite several works highlighting that the bainitic microstructure offers excellent mechanical properties, its wear performance is still a matter of debate: according to some papers, bainitic steels offer weak wear resistance, ascribed to metallurgical phases, like martensite, retained austenite, allotriomorphic ferrite but also to insufficient strain hardening ability (14-16). Contrary to these studies, many others asserted that the bainitic microstructure showed excellent wear resistance (17-20).

Devanathan et al. (16) published one of the first papers about bainitic rail steels in 1991. In this paper, bainitic steels with different carbon content and, therefore, hardness were compared to traditional eutectoid rail steels. Rolling-sliding tests revealed that the wear rate in the eutectoid steels decreased with increasing the hardness, while the bainitic steels exhibit the opposite behaviour revealing that for hardness value higher than about 300 HB bainitic steels worn out more than traditional rail steels.

Garnham et al. (15) also carried out rolling-sliding dry wear. The main conclusion of this work was that the pearlitic steels are recommended for dry wear applications with rolling. The bainitic steel of the same content of carbon as pearlitic steel showed a little lower wear rate, but at the expenses of the counter-material. The wear resistance of the bainitic steels increased with increasing carbon content, as found by Devanathan et al. (16). Despite better mechanical properties (ultimate tensile strength, yield strength, reduction of area and elongation), the wear rate of the lower carbon bainitic steels was inferior to that of the pearlitic steels.

Hasan et al. (17) investigated the wear behaviour of newly developed carbide-free bainitic with Amsler wear testing machine (bi-disc). The counterpart wheel specimen was pearlitic. The weight loss of the bainitic steels was lower than the pearlitic steel and even the pearlitic wheel steel, despite the lower hardness, had a lower wear rate when coupled with the bainitic steel.

Chen et al. (20) compared pearlitic and bainitic rail steels by means of ring/block wear tester in different cooling conditions. Bainitic steel always possessed better wear resistance than traditional pearlitic steels.

As far as fatigue resistance and ratcheting are concerned, most of the papers agree. Bainitic steels were found to have higher yield strength, fatigue strength and hardness compared to pearlitic steels (21-25); furthermore, the fracture toughness of bainitic steels is almost double than in pearlitic steels (21,26). Bainite may also play a fundamental role in crack propagation. Guan et al. (27) highlighted that, in ferritic-bainitic steels, the harder phase (the bainite) delays the crack propagation or deflects its path and the crack propagation could become unstable later than with ferritic-pearlitic steels.

Yokoyama et al. (25) carried out bi-disk rolling fatigue tests. The wheel steel disc was pearlitic, whereas the rail disc was either bainitic or pearlitic. The tensile strength of the bainitic steels varied from 810 to 1410 MPa, the tensile strength range of the pearlitic rail steel varied in a range from 900-1300 MPa. More details about the loading conditions can be found in the reference. Wear resistance analysis revealed that, at the same tensile strength, the pearlitic steel railways were superior to the bainitic rail steel in wear resistance. Nevertheless, the bainitic steel rail having 1400 MPa of tensile strength performed the same way as the pearlitic steel having 1300 MPa of tensile strength. Such bainitic steel also exhibited higher fracture toughness, fatigue strength and tensile elongation.

In 2006, Aglan et al. (26) investigated the mechanical properties of American rail steels on behalf the U.S. Federal Railway Administration. The fracture

toughness of the bainitic steel was about 27% higher than that of the pearlitic steel and the initiation. The bainitic steel also performed higher crack initiation and propagation lifetime. Moreover, the bainitic steel had higher ultimate strength and elongation to failure, respectively 1500 MPa and 13%, against 1100 MPa and 11% obtained with the pearlitic steel.

Gianni et al. (23) described the MICRALOS® bainitic steel grade, developed by Lucchini RS in the early 2000s. MICRALOS® microstructure is tempered martensite and bainite with a very low content of micro-inclusions. This material was compared with AAR Class C wheel steel in terms of mechanical properties and wear behaviour. MICRALOS® had higher ductility, resistance and toughness properties when compared with AAR Class C. Also, the cyclic yield strength was higher, despite the higher cyclic softening (calculated as the reduction of the yield stress from the monotonic yield stress to the cyclic conditions). The two steels were also compared on-field in the North Scandinavia. The wear of the tread the bainitic steel was slightly higher than that of AAR Class A wheels, but neither surface-initiated rolling contact fatigue cracks nor thermal cracks were found on the bainitic wheels. The properties of the two steels are shown in TABLE 4.1.

	MICRALOS	AAR C
<i>Rim</i>		
Monotonic yield strength [MPa]	1135	700
Ultimate tensile strength [MPa]	1215	1150
Reduction of area [%]	50	32
Elongation to fracture [%]	15	13
Hardness (depth 25 mm from tread) (HB)	386	340
Apparent toughness, 20°C [MPa√m]	135	45
<i>Web</i>		
Monotonic yield strength [MPa]	1040	450
Ultimate tensile strength [MPa]	1160	935
Reduction of area [%]	15	13
Elongation to fracture [%]	50	-

Table 4.1 – Mechanical properties for MICRALOS and AAR C wheel steels (23)

As can be inferred, much work has been carried out on bainitic rails and the results seem very promising. However, little can be drawn about wheel steels made of full bainitic microstructure instead, since little evidence can be found in the literature.

The homogenous bainitic microstructure is not the only solution proposed by the railway companies; in the last few years, there has been a debate about non-uniform microstructure in wheels, mainly traditional ferritic-pearlitic matrix with traces of bainite. Ghidini et al. (28) reported that small spots of bainite are almost inevitable in the external part of the wheel rim (it

is a result of a balance between required mechanical properties and cooling transformation curve) and a small amount of this intermediate phase does not compromise the wheel performance. Faccoli et al. (29,30) investigated the mechanical properties of commercial railway wheel materials produced by Lucchini RS and characterised by a ferritic-pearlitic matrix with bainitic spots, showing that such materials have good properties in terms of ductility, tensile strength and yield strength. TABLE 4.2 shows the mechanical properties of ER7, traditional European wheel steel, and HYPERLOS®, the improved version of ER7 developed by Lucchini RS.

Table 4.2 – Mechanical properties for ER7 (ferritic-pearlitic steel) and HYPERLOS® (ferritic-pearlitic with traces of bainite) (29)

	ER7	HYPERLOS®
Monotonic yield strength [MPa]	555	568
Ultimate tensile strength [MPa]	860	885
Elongation to fracture [%]	17	28
Reduction of area [%]	42	65
Apparent toughness [MPa√m]	89	102

Li et al. (31) investigated the effect of upper bainite in high-speed wheel steels. Two different microstructures were considered: the former wheel steel contains 50% of upper bainite, 40% of pearlite and 10% of ferrite; the latter contains only pearlite and ferrite and the volume fraction of pearlite and bainite was 80% and 20%. Bi-disc tests were performed coupling the wheel specimens with a disc made of U71Mn rail steel. The experiments showed that the upper bainite in the steel worsened the wheel spalling, increasing the weight loss of the wheel.

Shelling: important loss of material due to the rolling contact fatigue. Cracks normally start from the subsurface

Gao et al. (32) and Zhang et al. (33) highlighted that *shelling* and crack initiation are promoted by properties incompatibility at the phases interface; on the other hand, bainite showed low plastic deformation compared to pearlite.

As for crack propagation, bainite should not necessarily be considered as damaging. When bainitic spots are finely distributed in the ferritic-pearlitic matrix, they may arrest propagating cracks initiated at the bainite-matrix interface or in the matrix because of bainite higher fracture toughness. In this regard, Guan et al. (24) observed many crack branching in ferritic-bainitic steels and estimated lower crack propagation speed compared to ferritic-pearlitic steels. On the other hand, macrosegregation generates large areas characterised by bainitic microstructure. In this circumstance, the cracks may even initiate and propagate in bainite, as described in (32) and (34).

This chapter proposes to study the influence of inhomogeneous microstructure in railway wheels (ferritic-pearlitic matrix with bainitic

traces) on the plastic strain with semi-analytical methods (SAM) and finite element methods (FEM), with focus on:

- Effect of the inhomogeneity morphology
- Effect of the inhomogeneity dimension
- Effect of a cluster of inhomogeneities to study the interaction of adjacent bainitic traces.

Multi-parametric studies were carried out and the outcomes were characterised by many stress and plastic strain measures. The essence of this chapter effort is establishing the bainite threshold in the homogenous ferritic-pearlitic microstructure, above which the wheel behaviour may worsen the damage mode and the plastic behaviour.

4.2 Experimental evidence

4.2.1 Dimension and morphology of bainitic spots

Statistical analysis was performed to investigate the morphology and the dimension of the bainitic spots. Wheels in ER8 UPLOS®, a commercial ferritic-pearlitic steel produced by Lucchini RS, were considered. The samples for microstructure examination were taken at 15 mm under the wheel tread of the finished wheels, on the transversal section, on four perpendicular sections of the rim (see FIGURE 4.1). This depth was chosen for two reasons: first, it is the recommended depth for microstructure inspection in the railway wheels standard (EN13262, for example), second, it is representative of the bulk wheel microstructure. The magnification of the optical microscope was 100x. The amount of bainite in the pearlite was measured by software for automatic calculation and analysis LEICA IM 500.

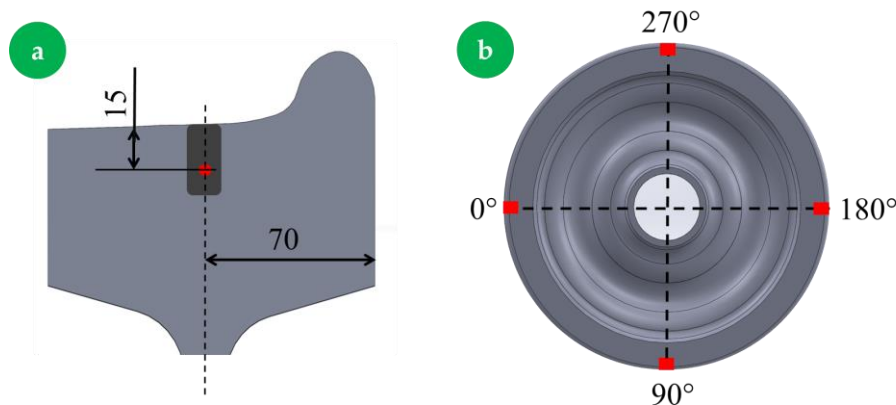


Figure 4.1 – Location of the specimens analysed to calculate the bainitic spots dimensions (unit: mm)

An “equivalent radius” r was introduced to study the dimensions efficiently; this parameter was defined as the radius of a circular section having the same area as the bainitic spot. FIGURE 4.2 shows the boxplots of six wheels: the mean radius ranges from about 65 to 80 μm , while the largest vary 130 from to 206 μm . The maximum amount of bainitic phase in the matrix is about 21%. In this work, the phase dimensions varied from 25 to about 230 μm . FIGURE 4.3 illustrates two examples of ferritic-pearlitic microstructure with different amount of bainitic spots (7.80% in FIGURE 4.3A and 0.62% in FIGURE 4.3B). From these micrographs, we can see that the bainitic islands detected have irregular shapes and only the smaller spots have regular circular section. Furthermore, the bainitic spots are randomly

distributed in the ferritic-pearlitic matrix. To decrease the complexity of the problem and to reduce the number of the geometrical variables, spots with circular and elliptical sections were considered. For the same reason, the bainitic spots distribution problem was investigated by considering nine spots arranged in three rows and columns.

Figure 4.2 – Equivalent radius" distribution in six railway wheels

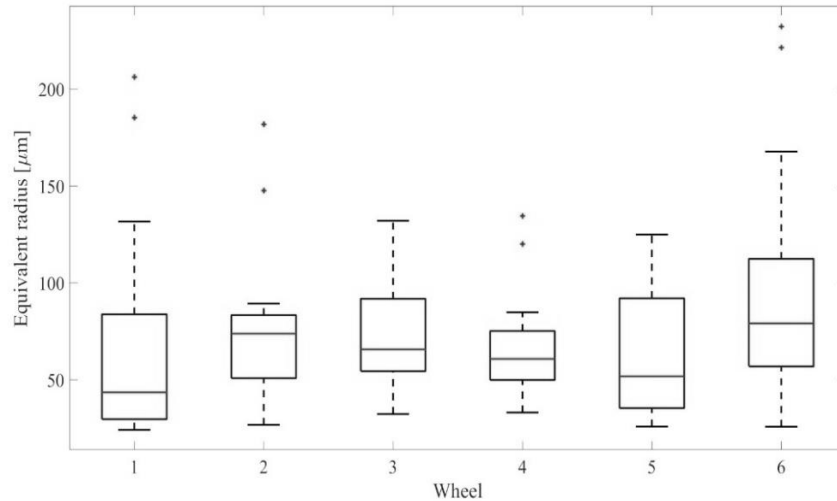
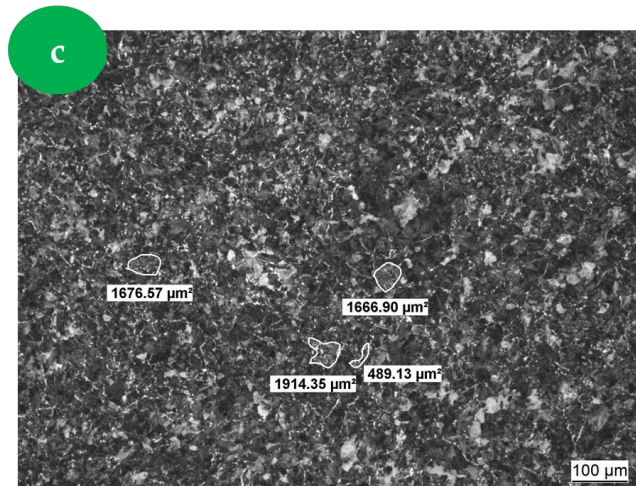
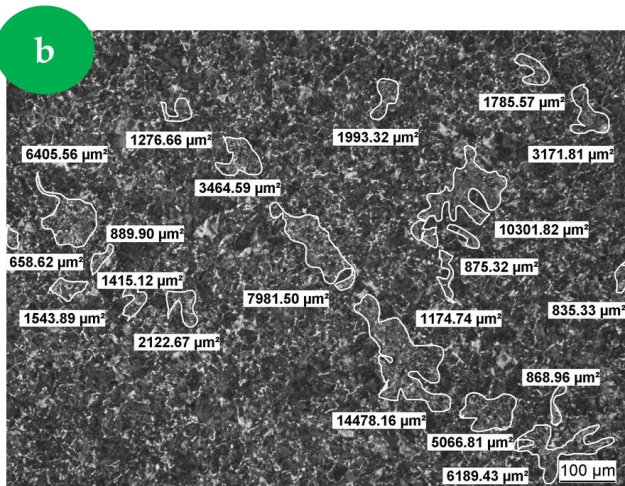
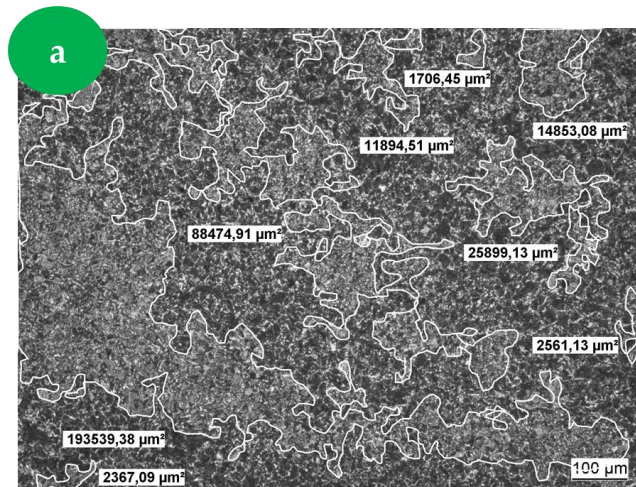


Figure 4.3 – Micrographs showing the bainitic structure in the ferritic-pearlitic matrix with different amount of bainitic spots:

- a) 32.14%
- b) 7.80%
- c) 0.62%



4.2.2 Loading condition

The wheel-rail contact problem in the curve trajectory was considered. Geometries of the bodies in contact were designed to obtain typical dynamic parameters found in curve path (35): Hertzian pressure 1100 MPa, Coulomb friction of about 0.5 and contact patch area 110 mm². The applied normal load was 100 kN, which is equivalent to about 20 t the maximum axle load.

4.2.3 Material properties

ER8 UPLOS® commercial steel was considered as the wheel material. The mechanical properties of the ferritic-pearlitic matrix were assumed to be ER8 UPLOS® properties. As far as the bainitic properties are concerned, the elastic modulus was calculated through a proportion between ferritic-pearlitic Young modulus and hardness and the hardness of bainite; the plastic yield was estimated by means of the relationship (3.2) between the Brinell hardness HB and the cyclic yield strength C.YS proposed in Chapter 3.

Rail steel was considered elastic in all the simulations. This issue is not of concern anyway; indeed, several works show that rails behave better than wheels in terms of plastic deformation, thanks to higher yield strength and hardness (5,12).

Finally, it should be clarified that the ferritic-pearlitic matrix was considered as a single metallurgical phase. This choice relies on the small proportion of grain boundary ferrite in the wheel tread (36), due to thermo-mechanical processing and chemistry. Moreover, the mechanical properties obtained with experimental tests (hardness, tensile tests, fatigue tests and so on) consider the overall behaviour of the two phases.

4.3 Model of analysis

Before dealing with the parametric study of the bainitic phase, a comparison between the two kinds of models adopted is proposed.

The Semi-Analytical Methods (SAM) are a class of computational methods, especially developed for contact problem simulations. The base idea is to use a summation of elementary analytical solutions to describe complex problems. The analytical solutions are described as influence coefficients and based on Green's functions that are solutions to elementary problems used here as kernels in the semi-analytical solution. Typically, the Boussinesq (37) analytical solution describes the surface displacement of a semi-infinite elastic plane subjected to a point force. The summation of those elementary analytical solutions allows solving more complicated problems such as the displacement of the aforementioned plane under a complex pressure distribution. The influence coefficients used in the semi-analytical are the space discretisation of the Green's functions. They have shown a good capability to solve three-dimensional contact problems between materials of complex behaviour (e.g. plasticity (38,39), heterogeneous bodies (40-42) or viscosity (43) among others). Two major advantages of these methods are their robustness in the resolution of contacts (44) and their relative computational speed compared to the Finite Element Method

(FEM). A detailed description of the SAM used in this paper and its validation can be found in (39) and (42).

As far as numerical models are concerned, a two-dimensional plane strain model was implemented using the commercial software ABAQUS®. The finite element method is commonly known to be more versatile than the analytical method; but non-linear 3D simulations involving a high number of elements, like rolling contact in the plastic regime, are tricky to be solved in a reasonable time.

Semi-analytical model (SAM) and finite element model were compared in terms of von Mises equivalent stress and strain. Indentation loading condition was adopted for the comparison. An ellipsoid-plane contact was modelled in the 3D semi-analytical model to obtain the elliptical contact area that characterises the wheel-rail contact. In turn, a 2D cylinder-plane contact was modelled with the finite element method. The dimensions of the ellipsoid and the cylinder were chosen so that the 3D and the 2D models had in common the contact pressure (1100 MPa) and the depth where the maximum Hertzian stress occurs (about 3 mm). TABLE 4.3 describes the geometries of the bodies in contact. FIGURE 4.4 and FIGURE 4.5 shows schematically the contact problems simulated with SAM and FEM.

Table 4.3 – Details about the semi-analytic and the finite element models adopted for the comparison

Finite element model		
Wheel	x	150 mm
	z	50 mm
	Width y	13 mm
Rail	Radius	204 mm
	Width y	13 mm
Bainitic spot	Radius	200 μm
Hertzian Pressure	1100 MPa	
Semi-contact area	a(x)	4.2 mm
	c(y)	L/2 = 6.5 mm
Number of nodes	561554	
Element Type	Second-order plane strain CPE8R	
Number of elements	323115	

Semi-analytical model			
Wheel	Semi-infinite space	x	45 mm
		y	22.5 mm
		z	5 mm
Rail	Indenter	Rx	280 mm
		Ry	670 mm
Bainitic spot		Radius	200 μm
Hertzian Pressure		1100 MPa	
Semi-contact area	a(x)		4.8 mm
	c(y)		8.72 mm
Number of nodes		970200	

As for the bainitic spots, the inhomogeneities in SAM models were represented as equivalent inclusions following Eshelby's formalism. Practical implementation of Eshelby's theory in the semi-analytical method can be found in (45-47) and (40). In this formalism, the inhomogeneities are considered perfectly bounded to the surrounding matrix. In the finite element models, the bainitic spots were simply considered as partitions in the wheel geometry with different mechanical properties with respect to the matrix.

One circular section inhomogeneity was set at $z = 2.5$ mm depth under the contact point ($x = 0$). The inhomogeneity radius was $200 \mu\text{m}$. It should be pointed out that the geometry of the inhomogeneities was not the same, despite the same cross-section; indeed, SAM bainitic spot was spherical, while FEM one was a cylinder. As plastic inhomogeneities cannot be currently implemented in SAM, elastic inhomogeneities were considered. The semi-analytical computation lasted about 2 days and 7 hours when the finite element model took about 6 hours.

When it comes to the matrix material properties, the Ramberg-Osgood model was considered in FEM (Eq. 2) (12). The elastic threshold chosen was the cyclic yield strength C.YS, and the plastic strain component was added to the elastic one for stress value above C.YS:

$$\left\{ \begin{array}{ll} \epsilon = \frac{\sigma}{E} & \text{if } \sigma < C.YS \\ \epsilon = \frac{\sigma}{E} + \alpha \left(\frac{\sigma}{C.YS} \right)^{\frac{1}{n}} & \text{if } \sigma \geq C.YS \end{array} \right. \quad (4.1)$$

where ϵ is the total strain, σ is the stress, E is the Young's Modulus, α is the conventional cyclic yield deformation (0.2%), n is the strain hardening exponent, and C.YS is the cyclic yield strength. TABLE 4.4 summarises the mechanical properties.

Swift plastic constitutive law (42) was implemented in SAM instead:

$$\sigma = B (C + 10^6 \epsilon_p)^m \quad (4.2)$$

where σ and ϵ_p stands for the stress and the plastic strain and B , C and m are material constant. In SAM, the Swift law was considered instead of Ramberg-Osgood since it was the implemented constitutive model that allowed a better convergence. In FIGURE 4.6, the comparison between Swift and Ramberg-Osgood law is shown.

Figure 4.4 – Semi-analytical model used for the comparison with SAM

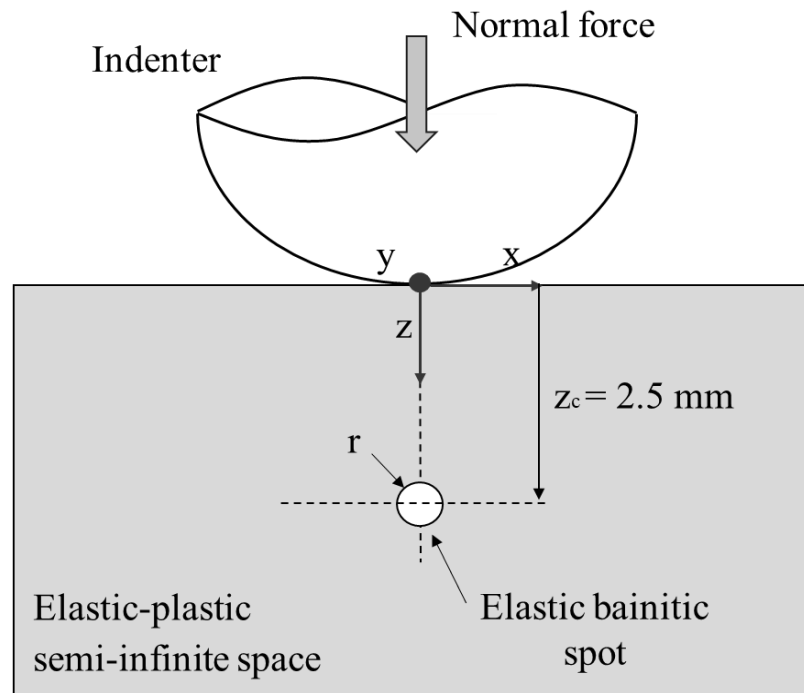


Table 4.4 – Mechanical properties for materials employed in the simulations for FEM and SAM comparison

	ER8 UPLOS®		Rail
Phase	Ferrite-Pearlite	Bainite	-
Subsurface average HB	275	283	-
Elastic Properties			
Poisson ratio	0.3	0.3	0.3
Young Modulus E [GPa]	206	212	206
SAM plastic properties: Swift law coefficients			
m	0.247	-	-
C	300	-	-
B [MPa]	67	-	-
FEM plastic properties: Ramberg-Osgood law coefficients			
Cyclic yield strength C.YS [MPa]	470	-	-
Strain hardening exponent, n	1/5	-	-
Conventional cyclic yield deformation α [%]	0.2	-	-

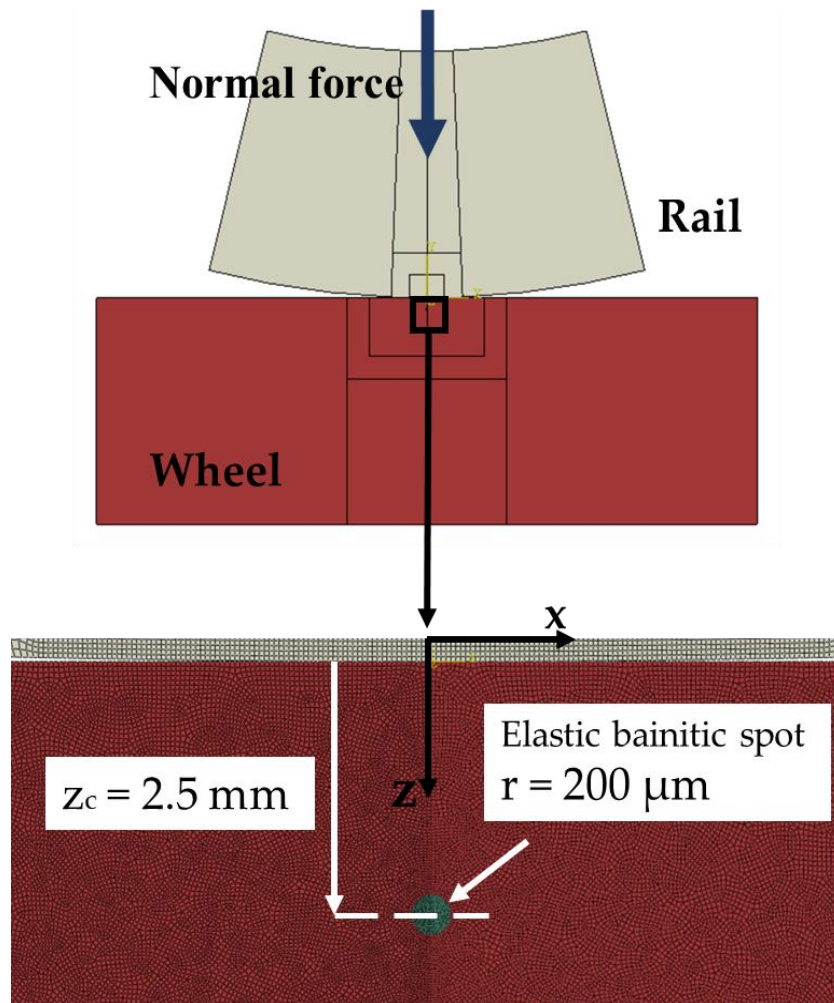


Figure 4.5 – Finite element model used for the comparison with SAM

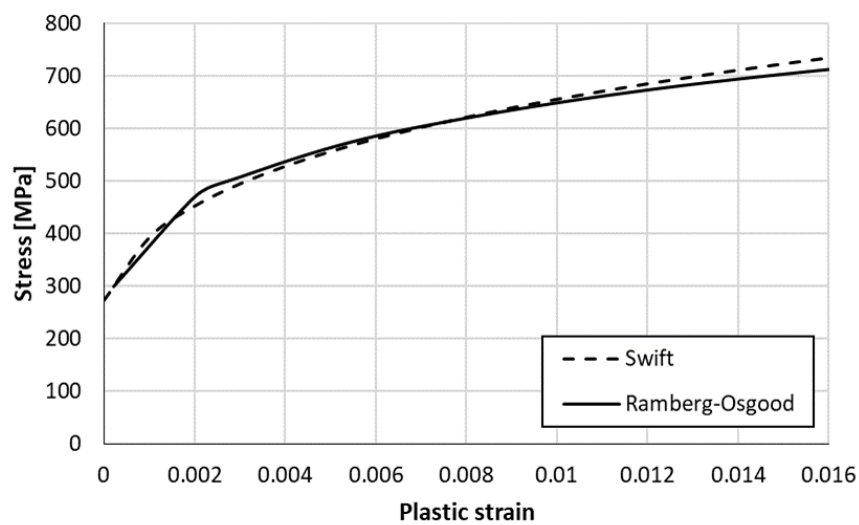


Figure 4.6 – Stress-strain curves for Swift and Ramberg-Osgood constitutive laws

FIGURE 4.7 and FIGURE 4.8 shows von Mises stress and plastic strain along the depth below the contact point ($x = 0$). If we exclude the surface contact, 2D FEM subsurface ferritic-pearlitic von Mises stress was in good agreement with those found with SAM; on the contrary, SAM predicted higher stress in bainite; this effect may be due to SAM limitations in meshing too small phases with respect to the contact area. However, both the models succeeded to predict the overstress at the phase boundary. Finite element plastic strain was more conservative, instead. Discrepancies between the results are a direct result of different pressure distribution in the two geometries: 3D pressure is an ellipsoid with a maximum at the contact centre, and pressure is decreasing moving away from the centre; while 2D pressure is a semi-ellipse projected along the cylinder depth.

Figure 4.7 – Von Mises stress along the depth at the centre of the contact in presence of a circular inhomogeneity

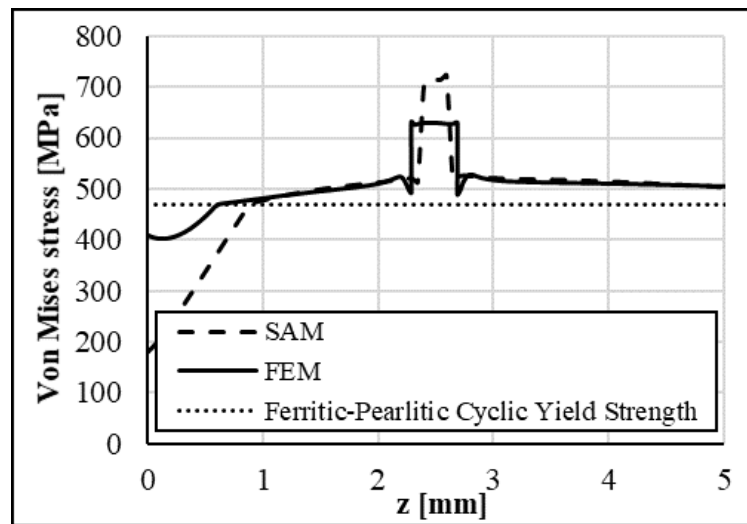
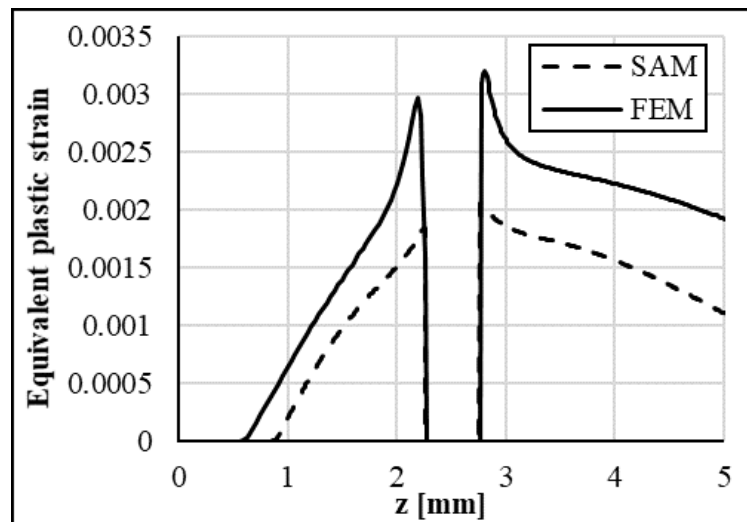


Figure 4.8 – Plastic strain along the depth at the centre of the contact in presence of a circular inhomogeneity



4.4 Semi-analytical model results (SAM)

The bainitic spot distribution problem was solved by applying SAM. Two ellipsoidal geometries were defined to obtain the loading condition described in PARAGRAPH 4.2. Given the difficulties in simulating phases characterised by very small dimensions with respect to the contact patch area in the plastic regime, we limited to consider the scope of consideration to only the elastic regime in both the ferritic-pearlitic matrix and the bainitic spots. A cluster of nine spherical phases with radius r was simulated by changing their radius dimension and fixing the interaxis I to 0.5 mm (FIGURE 4.9A). Elastic-plastic properties were the ones reported in TABLE 4.4. The execution time was about 11 hours.

FIGURE 4.9B illustrates von Mises stress/Hertzian Pressure ratio when the contact load, moving from left to right, is precisely above the bainitic distribution ($z_c = 2.5$ mm, $a = 2.8$ mm and $x = 0$ mm). Figure 7 shows von Mises/Hertzian Pressure ratio along the depth in the homogeneous condition (dot-dash line) and the presence of phases (solid lines), vertical dash lines are also shown to locate the phases easily. A strong influence between the phases was registered when the radius-interaxis ratio is major to 0.2. Indeed, when this parameter is smaller than 0.2, von Mises stress among the phases is not affected by the bainite presence, and it returns to the stress values calculated in the homogeneous condition.

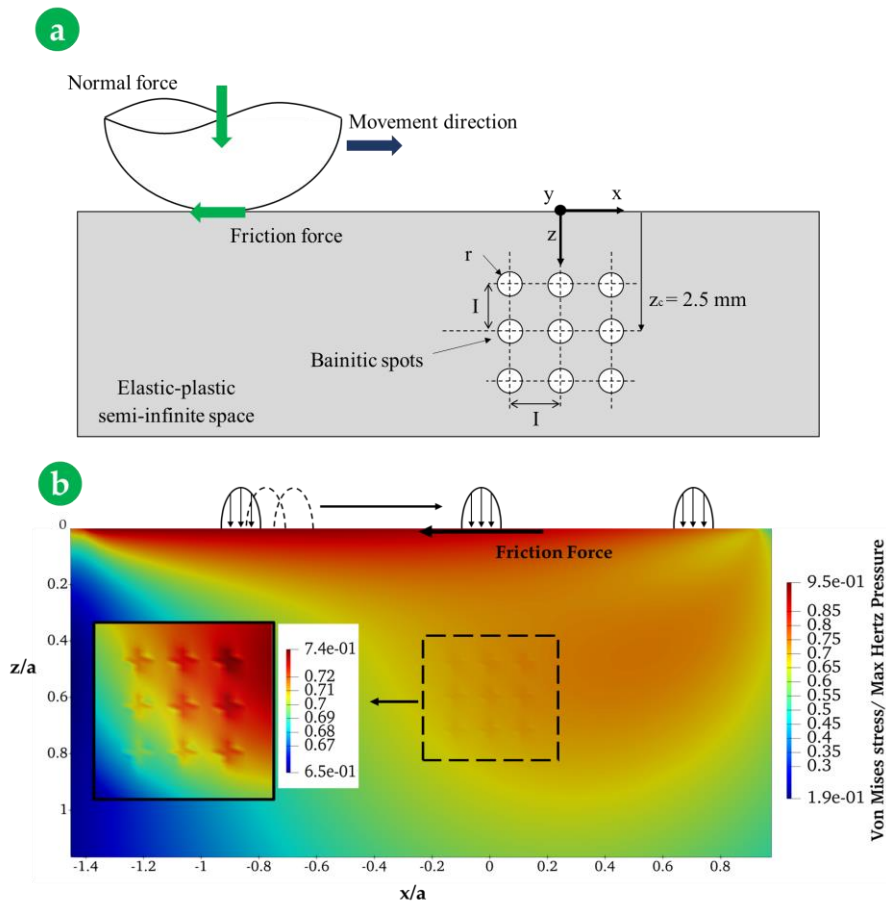
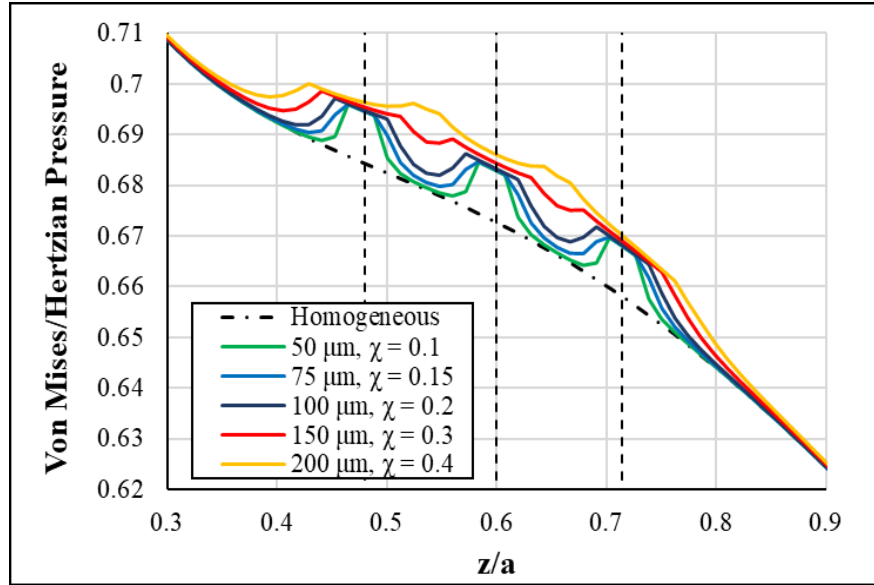


Figure 4.9 –

- a) Rolling contact problem in SAM
- b) Von Mises stress field in the rolling plane when the contact load is above the cluster of bainite

Figure 4.10 – Von Mises stress profile in presence of three phases along the depth varying the radius dimension



4.5 Finite Element model results (FEM)

FEM flexibility concerning meshing and material definition allows to simulate more versatile problems than SAM, including the rolling condition in plastic regime; but, on the other hand, three-dimensional rolling problem in non-linear conditions would require excessive time to be simulated, longer than SAM. For this reason, the sub-modelling technique was adopted to decrease simulation time.

This technique requires a former model, hence forth called “global model”, used to generate a boundary condition for a smaller model. For our purpose the global model represents a full-scale model portraying wheel-rail coupling with homogeneous materials with pearlite properties; whereas the latter model (“the submodel”) represents an area located in the subsurface of the wheel with bainitic spots dispersed in the matrix.

To reproduce the same condition simulated with SAM, where the bottom geometry is the one which can contain the heterogeneities, wheel and rail were exchanged, and the rail component was made roll over the wheel. Furthermore, the stress state and the contact dynamics are the same as the wheel rolling over the rail condition.

FIGURE 4.11 illustrates the model. The wheel was simulated as a flat body, the rail as a portion of a circle. The wheel bottom was fixed, the rail was tie-constrained to a point representing the centre of the circle through the beam elements. The chosen dimensions of the two bodies ensured that the boundary conditions did not affect the outcomes in the contact area.

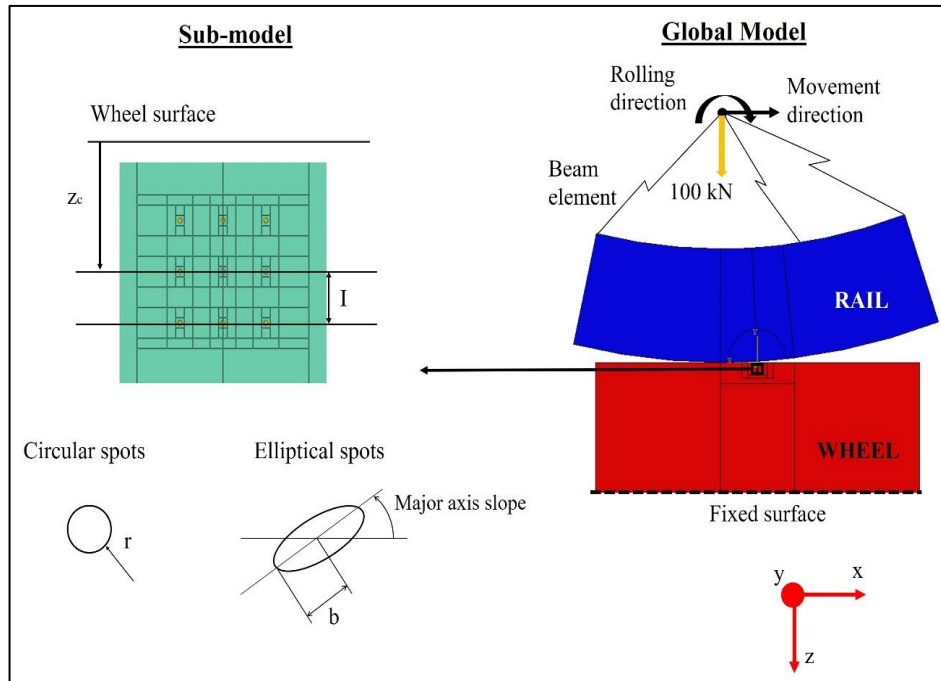


Figure 4.11 – Finite element model: on the right, the global model; on the left, the sub-model

The sub-model area was extracted from the subsurface of the wheel. Sub-model simulations can be classified into two groups:

- *Single phase problem*: these simulations aim to study the role of bainitic spot dimension and shape and the effect on the ferritic-pearlitic matrix. Radius r and semimajor ellipse axis b were set to 25, 50, 100 and 200 μm ; the minor axis was set to half and a quarter the major one; major axis inclination was set to 0, 30, 45, 60 and 90 degrees. Two depths z_c from the contact surface of the wheel were also considered.
- *Spots distribution problem*: this groups of simulations focuses on the bainitic spots interaction with one another and the amount of permittable bainite in the matrix.

The elastic mechanical properties and the plastic properties of ferritic-pearlitic matrix are the ones shown in TABLE 4.4. TABLE 4.6 shows the plastic mechanical properties of the bainitic spots in the wheel. ER8 UPLOS® bainitic Young's modulus and cyclic yield strength of bainite were obtained through interpolation with Brinell hardness HB, as described in PARAGRAPH 5.2.

“Direct (Standard)” constraint enforcement was set to describe the contact and a general contact interaction with a friction coefficient of 0.5 was applied to the assembly. Wheel and rail were meshed with CPE8R elements (second-order quadrilateral plane strain elements). The characteristic length of the elements in the global model varies from 0.5 mm to 10 μm in the contact area. In the submodel, the bainitic spots have a characteristic length of about 1 μm . TABLE 4.5 shows the details on the number of nodes and elements and the simulation time.

Table 4.6 – Plastic properties of the bainitic spots in FEM simulations

Phase	Bainite
Cyclic yield strength, C.YS [MPa]	495
Strain hardening exponent, n	1/5
Conventional cyclic yield deformation, α [%]	0.2

Table 4.5 – Details about the FE model and computing time

	Global model	Submodel	
		One bainitic spot	Bainitic distribution
Computation time	~1 d	~ 3 h	~ 6 h
Number of nodes	372357	126000	251000
Number of elements	363996	125000	250000

4.5.1 Plastic strain according to circular section dimension and depth

FIGURE 4.13 shows the residual von Mises plastic strain (PEEQ) trend after one cycle loading along the depth of the wheel with homogeneous ferritic-pearlitic matrix (dash line) and in the presence of bainite (solid line). The dimensionless depth z/a was obtained by dividing the depth z by the Hertzian semi-contact area $a = 4.2$ mm. It is immediately apparent that the bainitic phase deforms less than the matrix, regardless of the position of the phase. Overstrained regions occur in the matrix areas near the interface with the bainitic spot instead; this phenomenon may be ascribed to the stress intensity factor due to bainite higher hardness. Furthermore, the plastic strain inside the bainitic phase and the overstress values do not appear to be dependent on the dimensions. However, when the phase is set at 3.3 mm depth, the plastic strain in the inferior phase border is even lower than the bainite one. The location of the bainitic spot border with regard to the Hertzian depth and, therefore, to the stress may be a possible explanation. Furthermore, there exist areas with both higher and lower plastic strain than homogeneous conditions at the phase boundary. In this regard, (BELOW) **Figure 4.12** shows that higher plasticized areas alternate to lower deformed ones and that the maximum values occur at about 45-degree angles with respect to the vertical axis. Indeed, stress analysis reveals shear stress to be the component responsible for such behaviour, as it is expected with contact rolling conditions. The order of magnitude of the highest strain seems not to be strongly influenced by the bainitic spots size but increasing the bainite size magnifies the extent of the region affected by the overstrain; this result is in good agreement with the one found by Amuzuga et al. (42).

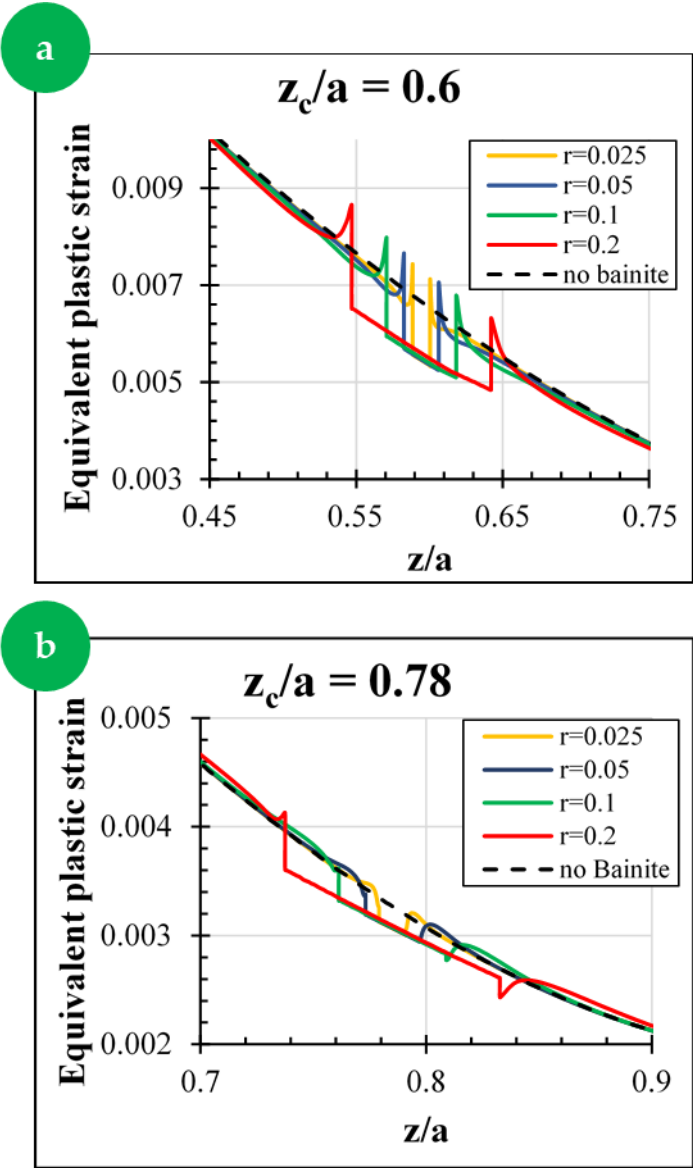
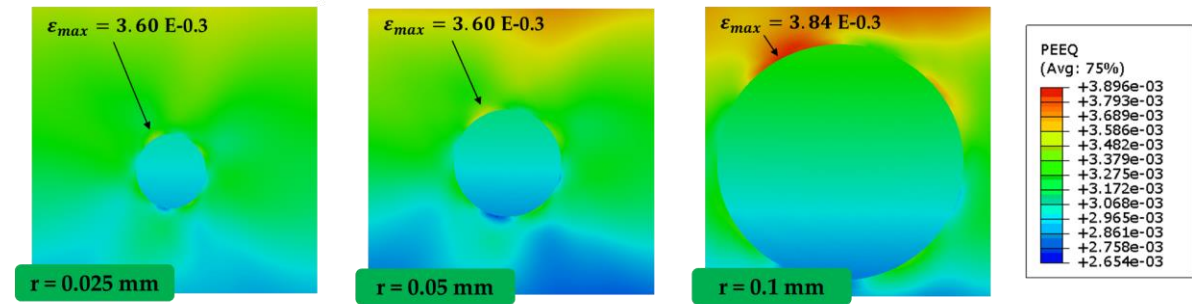


Figure 4.13 – Von Mises equivalent plastic strain evolution according to radius dimensions after one cycle: (a) circular bainitic spots centred at 2.5 mm depth ($z/a=0.6$); (b) circular bainitic spots centred at 3.3 mm ($z/a = 0.78$)

Radius dimension: mm

(below) Figure 4.12 – Von Mises plastic strain distribution around the bainitic spots according to phase size ($z/a = 0.78$)



4.5.2 Plastic strain according to elliptic section dimension, orientation and depth

The elliptic shape effects on plasticity are reported in FIGURE 4.14 and FIGURE 4.15. Simulations considering this geometry were made fixing the major axis dimensions and, then, varying the slope of the axis. FIGURE 4.14 shows the results for the minor axis set to one half the major one. The plots referring to 2.5 mm depth are in good agreement with the ones dealing with circular sections. When deeper phases are considered, one can note that the strain along the depth is affected by the axis inclination and no general trend can be inferred. In each case, bainite spots show lower plastic strain. Further considerations can be derived from observing von Mises equivalent plastic strain in the phase neighbouring. The outcomes referring to the major axis set to 100 μm are shown as an example (FIGURE 4.15). It is noteworthy that the maximum value never occurs at the ellipse apex but on the lateral side. Higher ellipse eccentricity is also considered to simulate a smaller apex radius. As opposed to what we expected, the sharper radius adopted in the simulations does not worsen the mechanical response; indeed, the highest strain value does not still occur at the apex, and its value differs little from previous results.

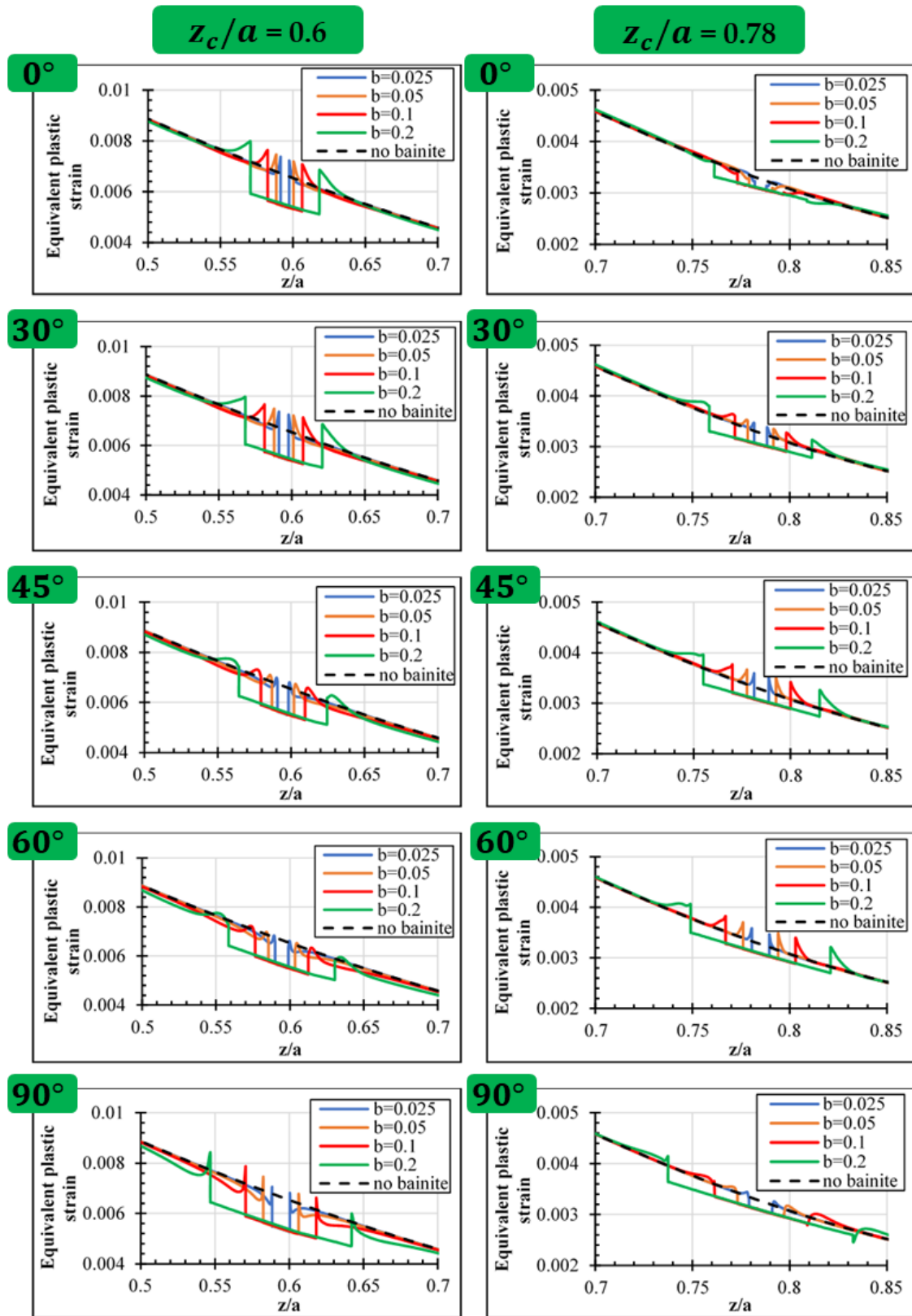


Figure 4.14 – Von Mises equivalent plastic strain profile according to ellipse dimension, major axis inclination and depth after one cycle loading (b = major semi-axis in mm)

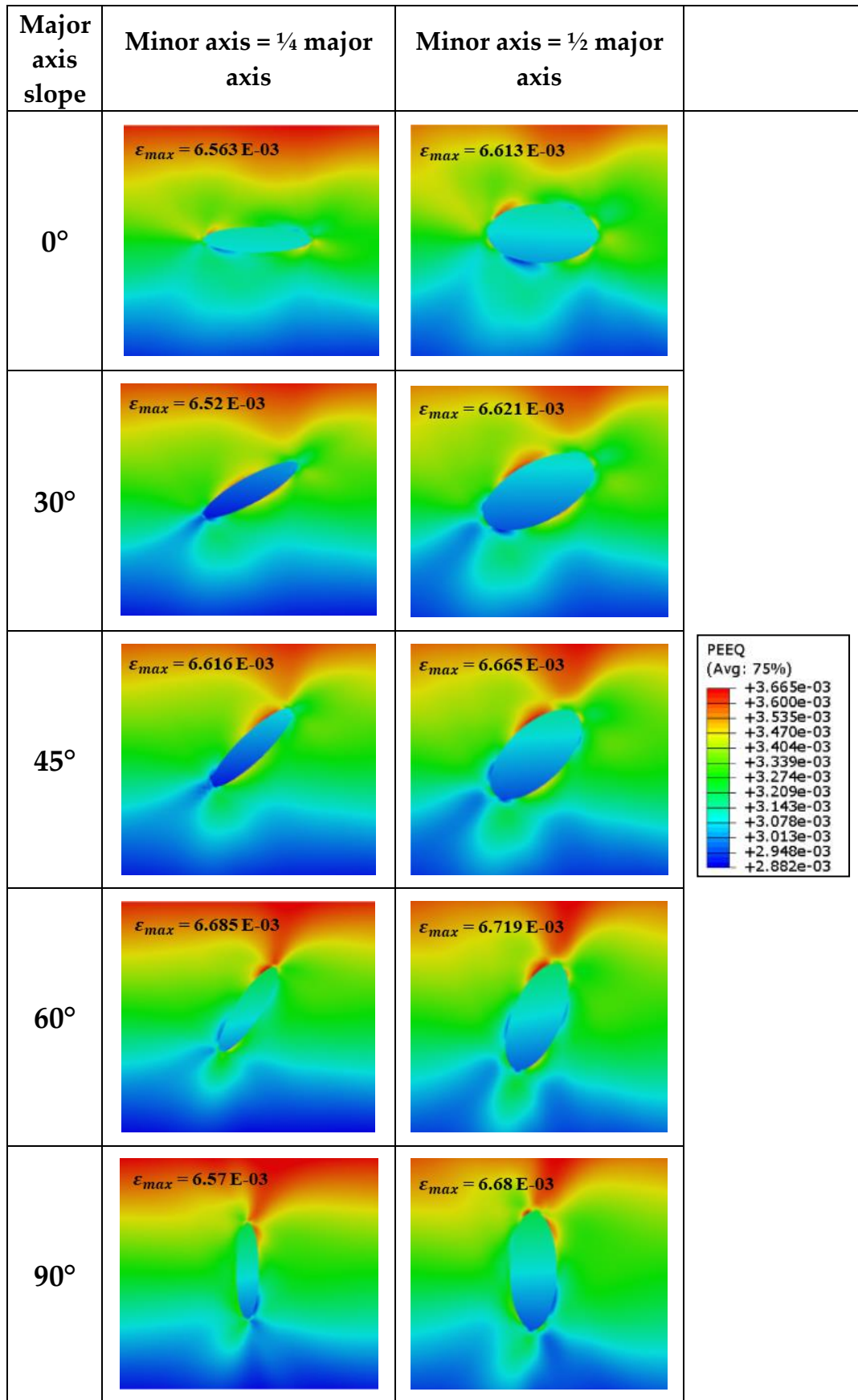


Figure 4.15 – Residual equivalent von Mises plastic strain (PEEQ) according to axis bainitic phase slope (major axis set to 100 μm)

4.5.3 Influence of bainite distribution

The effect of the bainitic spot distribution is investigated in this paragraph. Having regard to the outcome of the previous paragraph, the circular spot section was adopted. TABLE 4.7 shows the analysed cases.

FIGURE 4.16 portrays the equivalent residual plastic strain after one cycle loading along the depth of the middle column of the distribution. When χ (radius/interaxis ratio) major to 0.2, the plastic strain between two neighbouring spots is higher than the one calculated in fully ferritic-pearlitic matrix and the bainitic spots are close enough not to allow the stress and strain field to relax until homogenous values. Consequently, ferritic-pearlitic matrix deforms more compared to the case without bainite and cracks initiation and propagation are expected to become dramatically more likely. The critical χ value is consistent with that one found with the semi-analytical models.

Once the critical parameter was found, the next step is to establish the amount of bainitic phase corresponding to χ equal to 0.2. This value is derived by considering how many circular phases separated from each other by a distance given imposing χ to 0.2 may be contained in an area equal to a micrograph made under 100x magnification. TABLE 4.8 also shows that the average amount corresponds to about 11%.

$\chi = r/I$	$r = 0.025$ [mm]	$r = 0.05$ [mm]	$r = 0.1$ [mm]
0.125	0.2	0.4	0.8
0.165	0.15	0.3	0.6
0.2	0.125	0.25	0.5
0.25	0.1	0.2	0.4

Table 4.7 – Interaxis adopted with respect to bainite size according to different radius dimension

	Radius [mm]					
	0.025	0.05	0.075	0.1	0.125	0.2
Average Amount	12 %	11 %	12 %	9.5 %	11 %	11 %

Table 4.8 – Average amount of bainitic phases according to different radius dimension

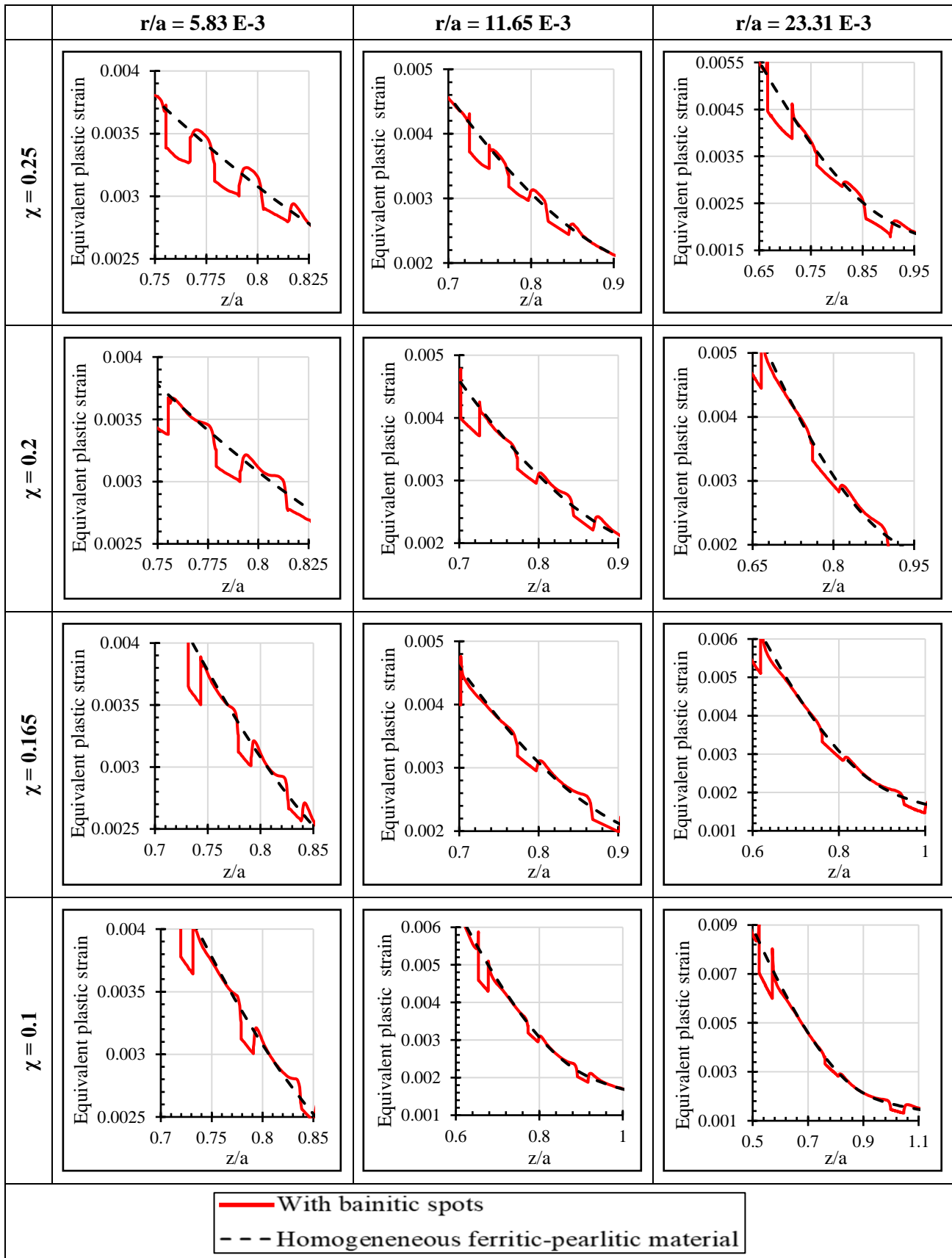


Figure 4.16 – Plastic strain profile after one cycle loading for circular section bainite spots according to different interaxis and radius

4.6 Discussion of the results

As demonstrated in previous research, bainitic microstructure performs better than ferritic-pearlitic one concerning plasticity, thanks to higher yield stress (28,32,48). Nevertheless, traces of bainite in a ferritic-pearlitic matrix generates intensification in stress and strain at the interface with the softer phase (ferrite-pearlite). Experimental evidence showed that localised deformation may easily lead to the initiation of fatigue cracks and that the less resistant region at the boundary between ferrite-pearlite and bainite may become the preferential path of the cracks, causing for example the decohesion at the interface and the spalling failure of the wheel (32,34,49).

The results of the finite element simulations show that the plasticised area is affected by the bainitic spot size (the bigger the spot, the larger the overstrained area is). However, the spot size does not influence the order of magnitude of the plastic strain. As for the ellipse shaped particles, the selected configurations (two geometries in five different orientation) showed that the stress field around the bainitic spots are not too dissimilar between smooth edged and sharp edged particles, leading to the conclusion that the sharper radius is not more detrimental than the smooth one. Anyway, this result must be yet be interpreted with caution as different size/orientation combinations may have a more favourable orientation with the stress field and lead to a different conclusion.

2D and 3D models were in good agreement when it comes to bainitic phase distribution. The simulations predict that, given the bainitic spot size, there is a minimum distance between two neighbouring spots below which the ferritic-pearlitic matrix is fully affected by the stress-strain intensification and plastic strain maximum values may exceed those calculated in the presence of a single spot. Furthermore, as mentioned in the literature review, the plastic strain intensification at the phases interface can accelerate the crack initiation and propagation leading to more severe wear damage (12).

The bainitic amount threshold in the ferritic-pearlitic matrix results to be about 11%. Although this threshold was estimated on a microscopic scale (100x viewed window), this outcome can be transferred to bigger inspection area and, in general, to the wheel tread itself by considering the bigger regions as a merging of the microscopic inspection area.

The proposed models are not able to predict wear as an independent damage phenomenon though, but plastic strain accumulated after each loading cycle (ratcheting) can be related to wear (8,50-55). Ratcheting leads to the exhaustion of material ductility and formation of cracks, which can propagate till part of the material is worn out. For this reason, the overstressed regions must be limited as much as possible.

According to the above observation, a non-homogeneous microstructure is not necessarily negative. Ferritic-pearlitic matrix with traces of bainite characterised by controlled dimensions and distribution may even enhance fatigue strength, (higher fracture toughness and fatigue threshold values) without undermining wear behaviour (ferritic-pearlitic matrix ensures appropriate wear rates).

4.7 Concluding remarks

The following conclusions can be drawn from the analysis of the influence of bainitic phases in the ferritic-pearlitic matrix in rolling contact loading.

- Railway wheels characterised by ferritic-pearlitic matrix and limited bainitic spots uniformly distributed in the matrix can represent a proper compromise among the mechanical properties of the different phases.
- Bainite deforms less than the ferritic-pearlitic matrix; however, both the finite element and the semi-analytical models foresee high strain and stress gradient in the ferritic-pearlitic matrix at the boundary between the two phases. The bainite size magnifies the extent of this affected area.
- Investigation of two simulated bainite morphologies in variable orientations reveals that the maximum plastic deformation not to be strongly influenced by the bainitic spot shape.
- The clustering of bainitic spots is detrimental when the phase radius/interaxis ratio is higher than 0.2 since this condition results in the formation of a highly affected region between the phases. This threshold corresponds to a bainite upper amount of about 11%. Beyond this limit, bainitic spots influence one another and the wheel fatigue strength and wear behaviour may be compromised.

In future studies, the influence of crack propagation in non-homogeneous microstructure should be investigated employing Extended Finite Element Methods.

4.8 References

1. Heyder R, Girsch G. Advanced pearlitic and bainitic high strength rails promise to improve rolling contact fatigue resistance. 7th World Congr Railw Res. 2006;(August):234.
2. Mazzù A, Battini D. A Model for the Assessment of Wheel–Rail Contact in the Presence of Solid Contaminants. *Tribol Trans.* 2019 Jan 4;1–9. <https://doi.org/10.1080/10402004.2018.1535104>.
3. Mazzù A, Provezza L, Zani N, Petrogalli C, Ghidini A, Faccoli M. Effect of shoe braking on wear and fatigue damage of various railway wheel steels for high speed applications. *Wear.* 2019 Sep;434–435:203005. <https://doi.org/10.1016/j.wear.2019.203005>.
4. Faccoli M, Petrogalli C, Lancini M, Ghidini A, Mazzù A. Rolling Contact Fatigue and Wear Behavior of High-Performance Railway Wheel Steels Under Various Rolling-Sliding Contact Conditions. *J Mater Eng Perform.* 2017;26(7):3271–84. <https://doi.org/10.1007/s11665-017-2786-4>.
5. Faccoli M, Provezza L, Petrogalli C, Ghidini A, Mazzù A. Effects of full-stops on shoe-braked railway wheel wear damage. *Wear.* 2019;428–429:64–75. <https://doi.org/10.1016/j.wear.2019.03.006>.
6. Jones K, Fry G. Testing Next Generation High-Performance Wheel Steels. In: XIX International Wheelset Congress, Venice. 2019.
7. Wang WJ, Jiang WJ, Wang HY, Liu QY, Zhu MH, Jin XS. Experimental study on the wear and damage behavior of different wheel/rail materials. *Proc Inst Mech Eng Part F J Rail Rapid Transit.* 2016;230(1):3–14. <https://doi.org/10.1177%2F0954409714524566>.
8. Fletcher DI, Beynon JH. Equilibrium of crack growth and wear rates during unlubricated rolling-sliding contact of pearlitic rail steel. *Proc Inst Mech Eng Part F J Rail Rapid Transit.* 2000;214(2):93–105. <https://doi.org/10.1243%2F0954409001531360>.
9. Christoforou P, Fletcher DI, Lewis R. Benchmarking of premium rail material wear. *Wear.* 2019 Oct 15;436–437:202990. <https://doi.org/10.1016/j.wear.2019.202990>.
10. Tunna J, Sinclair J, Perez J. A review of wheel wear and rolling contact fatigue. *Proc Inst Mech Eng Part F J Rail Rapid Transit.* 2007;221(2):271–89. <https://doi.org/10.1243%2F0954409JRRT72>.
11. Diao G, Yan Q, Shi X, Zhang X, Wen Z, Jin X. Improvement of wear resistance in ferrite-pearlite railway wheel steel via ferrite strengthening and cementite spheroidization. *Mater Res Express.* 2019;6(10):106513. <https://doi.org/10.1088/2053-1591/ab3481>.

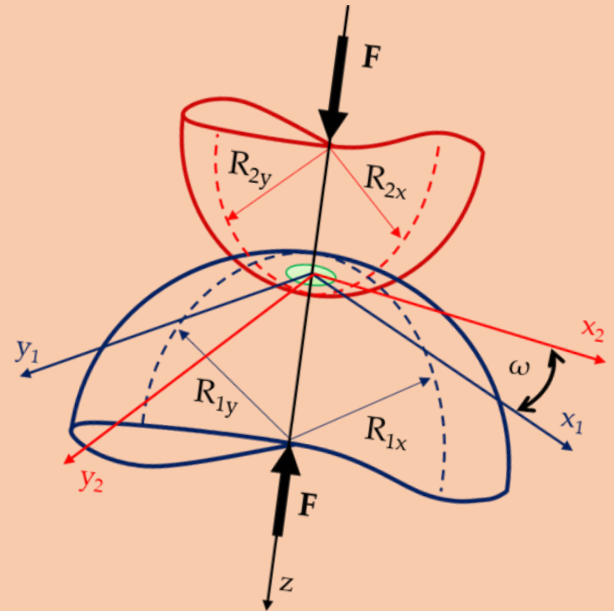
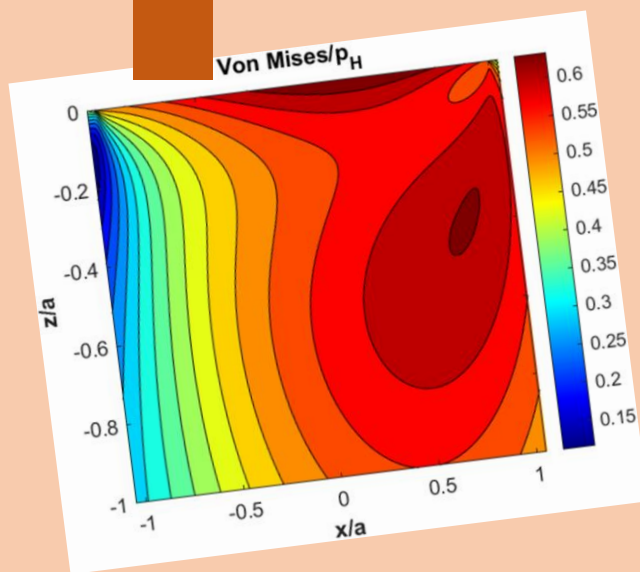
12. Faccoli M, Petrogalli C, Lancini M, Ghidini A, Mazzù A. Effect of desert sand on wear and rolling contact fatigue behaviour of various railway wheel steels. *Wear*. 2018 Feb 15;396–397:146–61.
13. Pointner P. High strength rail steels—The importance of material properties in contact mechanics problems. *Wear*. 2008 Oct 30;265(9–10):1373–9. <https://doi.org/10.1016/j.wear.2008.03.015>.
14. Viáfara CC, Castro MI, Vélez JM, Toro A. Unlubricated sliding wear of pearlitic and bainitic steels. *Wear*. 2005 Jul 1;259(1–6):405–11. <https://doi.org/10.1016/j.wear.2005.02.013>.
15. Garnham JE, Beynon JH. Dry rolling-sliding wear of bainitic and pearlitic steels. *Wear*. 1992 Aug 14;157(1):81–109. <https://doi.org/10.1016/j.wear.2018.05.006>.
16. Devanathan R, Clayton P. Rolling-sliding wear behavior of three bainitic steels. *Wear*. 1991 Dec 20;151(2):255–67. [https://doi.org/10.1016/0043-1648\(91\)90253-Q](https://doi.org/10.1016/0043-1648(91)90253-Q).
17. Hasan SM, Chakrabarti D, Singh SB. Dry rolling/sliding wear behaviour of pearlitic rail and newly developed carbide-free bainitic rail steels. *Wear*. 2018 Aug;408–409:151–9. <https://doi.org/10.1016/j.wear.2018.05.006>.
18. Shipway PH, Wood SJ, Dent AH. The hardness and sliding wear behaviour of a bainitic steel. *Wear*. 1997 Mar 1;203–204:196–205. [https://doi.org/10.1016/S0043-1648\(96\)07411-X](https://doi.org/10.1016/S0043-1648(96)07411-X).
19. Chang LC. The rolling/sliding wear performance of high silicon carbide-free bainitic steels. *Wear*. 2005 Feb 1;258(5–6):730–43. <https://doi.org/10.1016/j.wear.2004.09.064>.
20. Chen Y, Ren R, Pan J, Pan R, Zhao X. Microstructure evolution of rail steels under different dry sliding conditions: A comparison between pearlitic and bainitic microstructures. *Wear*. 2019 Nov 15;438–439:203011. <https://doi.org/10.1016/j.wear.2019.203011>.
21. Sharma S, Sangal S, Mondal K. Wear Behavior of Newly Developed Bainitic Wheel Steels. *J Mater Eng Perform*. 2015 Feb 2;24(2):999–1010. <https://doi.org/10.1007/s11665-014-1328-6>.
22. Liu JP, Li YQ, Zhou QY, Zhang YH, Hu Y, Shi LB, et al. New insight into the dry rolling-sliding wear mechanism of carbide-free bainitic and pearlitic steel. *Wear*. 2019 Aug 15;432–433:202943. <https://doi.org/10.1016/j.wear.2019.202943>.
23. Gianni A, Ghidini A, Karlsson T, Ekberg A. Bainitic steel grade for solid wheels: metallurgical, mechanical and in-service testing for solid

- wheels: metallurgical, mechanical and in-service testing. *Proc Inst Mech Eng Part F J Rail Rapid Transit.* 2008;223(2): 163-171. <https://doi.org/10.1243%2F09544097JRR217>.
24. Zhang MR, Gu HC. Fracture toughness of nanostructured railway wheels. *Eng Fract Mech.* 2008;75:5113–21. <https://doi.org/10.1016/j.engfracmech.2008.07.007>.
 25. Yokoyama H, Mitao S, Yamamoto S, Fujikake M. Effect of the angle of attack on flaking behavior in pearlitic and bainitic steel rails. *Wear.* 2002. [https://doi.org/10.1016/S0043-1648\(02\)00083-2](https://doi.org/10.1016/S0043-1648(02)00083-2).
 26. Aglan H, Fateh M. Fracture and Fatigue Crack Growth of Bainitic and Pearlitic Rail Steels. *Transp Res Board 85th Annu Meet.* 2006;2–5. <https://doi.org/10.1177/1056789506060775>.
 27. Guan M, Yu H. Fatigue crack growth behaviors in hot-rolled low carbon steels: A comparison between ferrite–pearlite and ferrite–bainite microstructures. *Mater Sci Eng A.* 2013 Jan 1;559:875–81. <https://doi.org/10.1016/j.msea.2012.09.036>.
 28. Ghidini A, Diener M, Mazzù A, Zani N, Petrogalli C, Faccoli M. Considerations about microstructure of solid wheels with traces of bainite. *Ing Ferro.* 2020 March 3, 165-178. ISSN: 00200956.
 29. Faccoli M, Ghidini A, Mazzù A. Changes in the Microstructure and Mechanical Properties of Railway Wheel Steels as a Result of the Thermal Load Caused by Shoe Braking. *Metall Mater Trans A Phys Metall Mater Sci.* 2019;50(4):1701–14. <https://doi.org/10.1007/s11661-019-05135-x>.
 30. Faccoli M, Ghidini A, Mazzù A. Experimental and Numerical Investigation of the Thermal Effects on Railway Wheels for Shoe-Braked High-Speed Train Applications. *Metall Mater Trans A Phys Metall Mater Sci.* 2018;49(10):4544–54. <https://doi.org/10.1007/s11661-018-4749-2>.
 31. Li Q, Guo J, Zhao A. Effect of Upper Bainite on Wear Behaviour of High-Speed Wheel Steel. *Tribol Lett.* 2019;67(4):1–9.
 32. Gao B, Tan Z, Liu Z, Gao G, Zhang M, Zhang G, Bai B. Influence of non-uniform microstructure on rolling contact fatigue behavior of high-speed wheel steels. *Eng Fail Anal.* 2019 Jun 1;100:485–91. <https://doi.org/10.1016/j.engfailanal.2019.03.002>.
 33. Zhang G, Ren R. Study on typical failure forms and causes of high-speed railway wheels. *Eng Fail Anal.* 2019 Nov 1;105:1287–95. <https://doi.org/10.1016/j.engfailanal.2019.03.002>.

34. Guanzhen Z, Fangwei Z, Si W, Tao C, Hongxiang Y. Influence of non-uniform microstructure on the tread shelling of High- speed EMU Wheel. In: XIX International Wheelset Congress, Venice. 2019.
35. Iwnicki S. Simulation of wheel – rail contact forces. *Fatigue Fract Eng Mater Struct*. 2003;26(August):887–900. <https://doi.org/10.1046/j.1460-2695.2003.00699.x>.
36. Ghidini A, Diener M, Schneider J, Wheels for freight cars, LRS-Techno Series Vol. 3, Lucchini RS –Lovere, Italy, 2010.
37. Boussinesq J., "Applications des potentiels à l'étude de l'équilibre et du mouvement des solides élastiques." Gauthier-Villars, Paris, 1885.
38. Jacq C, Nélías D, Lormand G, Girodin D. Development of a three-dimensional semi-analytical elastic-plastic contact code. *J Tribol*. 2002;124(4):653–67. <https://doi.org/10.1115/1.1467920>.
39. Chaise T, Nélías D. Contact Pressure and Residual Strain in 3D Elasto-Plastic Rolling Contact for a Circular or Elliptical Point Contact. *J Tribol*. 2011;133(October):1–9. <https://doi.org/10.1115/1.4004878>.
40. Leroux J, Fulleringer B, Nélías D. Contact analysis in presence of spherical inhomogeneities within a half-space. *Int J Solids Struct*. 2010;47(22–23):3034–49. <https://doi.org/10.1016/j.ijsolstr.2010.07.006>.
41. Koumi KE, Zhao L, Leroux J, Chaise T, Nélías D. Contact analysis in the presence of an ellipsoidal inhomogeneity within a half space. *Int J Solids Struct*. 2014;51(6):1390–402. <https://doi.org/10.1016/j.ijsolstr.2013.12.035>.
42. Amuzuga KV, Chaise T, Duval A, Nélías D. Fully Coupled Resolution of Heterogeneous Elastic-Plastic Contact Problem. *J Tribol*. 2016;138(2):1–22. <https://doi.org/10.1115/1.4032072>.
43. Koumi KE, Chaise T, Nélías D. Rolling contact of a rigid sphere/sliding of a spherical indenter upon a viscoelastic half-space containing an ellipsoidal inhomogeneity. *J Mech Phys Solids*. 2015 Jul 1;80:1–25. <https://doi.org/10.1016/j.jmps.2015.04.001>.
44. Gallego L, Nélías D, Deyber S. A fast and efficient contact algorithm for fretting problems applied to fretting modes I, II and III. *Wear*. 2010;268(1):208–22. <https://doi.org/10.1016/j.wear.2009.07.019>.
45. Eshelby JD. The determination of the elastic field of an ellipsoidal inclusion in an anisotropic medium. *Proc R Soc London*, A241. 1957;376–96. <https://doi.org/10.1098/rspa.1957.0133>
46. Eshelby JD. The elastic field outside an ellipsoidal inclusion. *Proc R Soc London*, A252. 1959;(77-WA/APM-29):561–9.

47. Yu AHY, Sanday SC, Chang CI, Mathematical SP, Sciences P. Elastic inclusions and inhomogeneities in transversely isotropic solids. *Proc R Soc London Ser A Math Phys Sci.* 1994;444(1920):239–52. <https://doi.org/10.1098/rspa.1994.0014>
48. Ishikawa N, Yasuda K, Sueyoshi H, Endo S, Ikeda H, Morikawa T, Higashida K. Microscopic deformation and strain hardening analysis of ferrite–bainite dual-phase steels using micro-grid method. *Acta Mater.* 2015 Sep;97:257–68. <https://doi.org/10.1016/j.actamat.2015.06.037>.
49. Qiu C, Cookson J, Mutton P. The role of microstructure and its stability in performance of wheels in heavy haul service. *J Mod Transp.* 2017;25(4):261–7. <https://doi.org/10.1007/s40534-017-0143-9>.
50. Soleimani H, Moavenian M. Tribological Aspects of Wheel–Rail Contact: A Review of Wear Mechanisms and Effective Factors on Rolling Contact Fatigue. *Urban Rail Transit.* 2017 Dec 14;3(4):227–37. <https://doi.org/10.1007/s40864-017-0072-2>.
51. Mazzù A, Petrogalli C, Lancini M, Ghidini A, Faccoli M. Effect of Wear on Surface Crack Propagation in Rail–Wheel Wet Contact. *J Mater Eng Perform.* 2018 Feb 25;27(2):630–9. <https://doi.org/10.1007/s11665-018-3185-1>.
52. Dang Van K. Modelling of damage induced by contacts between solids. *Comptes Rendus Mécanique.* 2008 Jan 1;336(1–2):91–101. <https://doi.org/10.1016/j.crme.2007.10.018>.
53. Ma L, He CG, Zhao XJ, Guo J, Zhu Y, Wang WJ, Liu QY, Jin XS. Study on wear and rolling contact fatigue behaviors of wheel/rail materials under different slip ratio conditions. *Wear.* 2016 Nov 15;366–367:13–26. <https://doi.org/10.1016/j.wear.2016.04.028>.
54. Johnson KL. Contact mechanics and the wear of metals. *Wear.* 1995;190:162–70. [https://doi.org/10.1016/0043-1648\(95\)06665-9](https://doi.org/10.1016/0043-1648(95)06665-9).
55. Donzella G, Mazzù A, Petrogalli C. Competition between wear and rolling contact fatigue at the wheel-rail interface: Some experimental evidence on rail steel. *Proc Inst Mech Eng Part F J Rail Rapid Transit.* 2009;223(1):31–44. <https://doi.org/10.1243%2F09544097JRR161>.

Part IV



Chapter 5 - Contact mechanics

Chapter 6 - Constitutive models

Chapter 7 - Fatigue criteria

Chapter 8 - Wear

Chapter 9 - Simulations

List of the main variables adopted in Part IV

Variable	Description
a	Semi-contact length along direction x
b	Isotropic hardening exponent
c	Semi-contact length along direction y
C	Kinematic hardening parameter
c_{DV}, c_{CR}	Dang Van and Crossland parameters
d	Jiang-Sehitoglu material parameter
E	Young's modulus
F	Contact force
FP, FP_0	Fatigue parameters in Jiang-Sehitoglu's criterion
f	Coulombian friction coefficient
G	Shear elastic modulus
H_i	Elastic equivalent modulus in Hertzian theory
J	Jiang-Sehitoglu material parameter
L	Contact length in line contact
M, N	Hertzian coefficients
N_f	Fatigue number of cycles to failure
m, n	McEwen's coefficients
p_H	Hertzian pressure
R	Actual dragstress for isotropic hardening
R_∞	Isotropic hardening saturation coefficient
$R_{1X}, R_{1Y}, R_{2X}, R_{2Y}$	Curvature of the contact body along direction x (1) and y (2)
SF	Safety factor
X	Actual backstress for kinematic hardening
x, y, z	Cartesian coordinates
w	Wear rate
ϵ, ϵ_{ij}	Strain, strain tensor
ϵ_a	Strain amplitude
ϵ_P	Plastic strain
ϵ_n	Strain component normal to a plane
γ	Kinematic hardening parameter
γ_{ij}	Shear deformation
λ	Plastic Lagrangian multiplier in plastic flow rule
$\sigma_1, \sigma_2, \sigma_3$	Principal stress
σ^{dev}	Deviatoric stress tensor
$\sigma_{eDV}, \sigma_{eCR}$	Dang Van and Crossland material parameter
$\sigma_{eqDV}, \sigma_{eqCR}$	Dang Van and Crossland equivalent stress
σ_h	Hydrostatic pressure
σ_n	Stress component normal to a plane
σ_{y0}, σ_y	Initial/Actual yield stress
σ_{VM}	Von Mises stress
ϑ, φ	Eulerian angles
ν	Poisson's ratio
Φ	Von Mises yield function
ω	Geometric parameter in general contact

Introduction to the semi-analytical model

This section focuses on a semi-analytical model coded in MATLAB® to predict the cyclic response in wheel–rail contact and in bi-disk experimental tests. The proposed activity has been carried out in partnership with *Chalmers University of Technology* in Gotheborg, Sweden.

The code can be divided into five parts (FIGURE 1):

- 1. Contact mechanics problem**

The Hertzian theory is used to find the contact area in point contact and line contact in normal load. The tangential load is implemented as well by considering the full slip condition.

- 2. Elastic stress**

Boussinesq-Cerruti's formulations and McEwen's equations are implemented to calculate the elastic stress in point contact and line contact, respectively. This is an approximation of the real condition since it is common for the wheels and rails to exceed the yield stress.

- 3. Stress-strain response**

Given the stress history, the strain response is calculated by means of plastic constitutive models. The Chaboche model is coded for simulating the non-linear material behaviour.

- 4. Fatigue criteria**

Fatigue damage is evaluated by means of high cycle fatigue and low cycle fatigue criteria, according to the analysed cases. A ratcheting criterion is also proposed.

- 5. Wear**

A wear damage model is also implemented for 2D problems.

Frame of reference

In a rectangular coordinate system, $Oxyz$, the two bodies, lower and upper, are denoted by suffixes 1 and 2. The z -axis is chosen to coincide with the

common normal of the two surfaces, which also coincides with the direction of the contact load. The x- and y-axes are chosen to coincide, where possible, with the axis of symmetry of the body. The xz-plane corresponds with the rolling plane; therefore, the stress history will be taken on this plane. Line contact (cylindrical contact) is a special case; the y-axis lies parallel to the axis of the cylinders, while the x-axis lies in the plane of the cross-section.

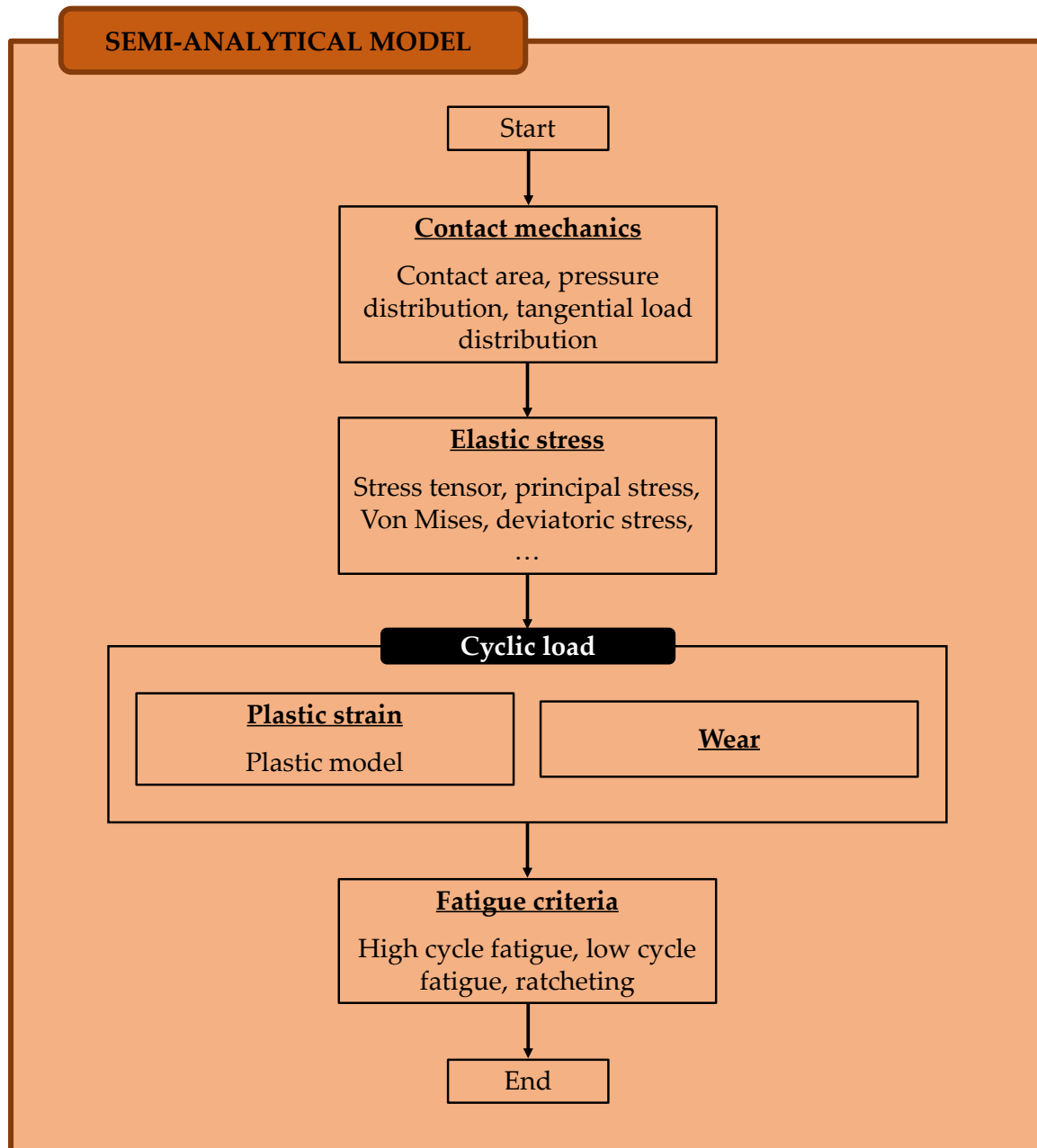


Figure 1 – Flow chart for the semi-analytical model

5.1 Hertzian theory

Dating back to 1882, the Hertzian theory was the first satisfactory analysis of stresses at the contact of two elastic bodies. The hypotheses are the following (1):

- The contact area is, in general, elliptical.
- The bodies in contact can be treated as elastic half-spaces, which are idealised geometry adopted to study non-conforming contact problems. The body of the surface profile is considered semi-infinite in extent and having a plane surface.
- The contact area is smaller than the dimensions of the bodies in contact
- The stress state in the contact area is unaffected by the shape of the bodies far from the contact area
- The surfaces are assumed to be frictionless; this ensures that only a normal pressure is transmitted between them.

5.1.1 General profile

In the general case, the shape of the contact area is unknown in advance. However, the contact area is considered elliptical, having semi-axes a and c .

The pressure distribution is given by the equation

$$p(x, y) = p_H \left(1 - \left(\frac{x}{a} \right)^2 - \left(\frac{y}{c} \right)^2 \right)^{\frac{1}{2}}, \quad (5.1)$$

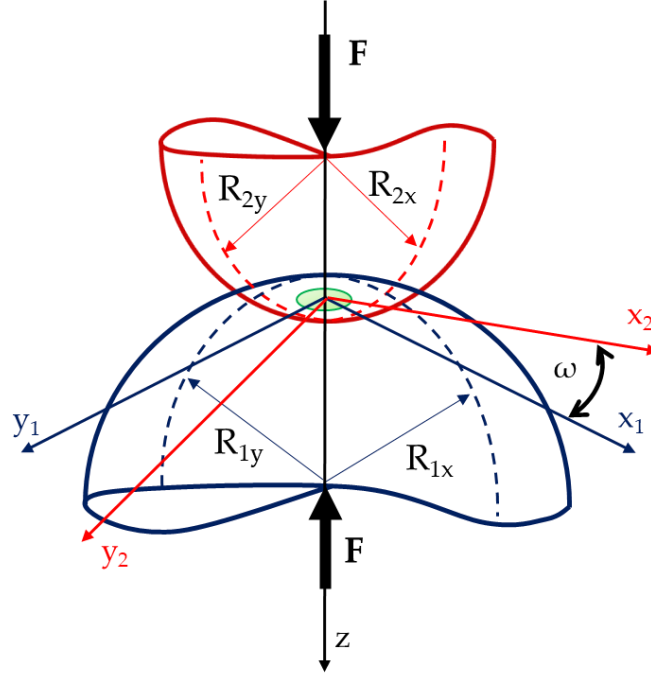
where x, y are the coordinates on the plane contact, $p(x, y)$ is the punctual pressure, and p_H is the Hertzian pressure, which is the maximum pressure.

The contact area and the maximum pressure are the unknowns of the problem. The knowns are the following:

- Geometry, referring to the radii of curvature R_{1x} , R_{1y} , R_{2x} and R_{2y}
- Load F
- Angle of rotation ω between the axis of the two bodies
- The elastic properties of the bodies, Young's modulus E and Poisson's ratio ν .

Planar geometry is characterised by infinite radii. FIGURE 5.1 shows a schematic representation of the geometry in elliptical contact.

Figure 5.1 – Schematic of the general contact



The following scheme determines the contact area:

I. Geometrical parameters (curvatures ρ and geometrical factor κ)

$$\rho_{1x} = \frac{1}{R_{1x}} \quad \rho_{1y} = \frac{1}{R_{1y}} \quad \rho_{2x} = \frac{1}{R_{2x}} \quad \rho_{2y} = \frac{1}{R_{2y}} \quad (5.2)$$

$$\rho_3 = \sqrt{(\rho_{1x} + \rho_{1y})(\rho_{2x} + \rho_{2y}) + (\rho_{1x} - \rho_{1y})(\rho_{2x} - \rho_{2y})(\sin \omega)^2} \quad (5.3)$$

$$\rho_4 = \frac{1}{2} \sqrt{(\rho_{1x} - \rho_{1y})^2 + (\rho_{2x} - \rho_{2y})^2 + 2(\rho_{1x} - \rho_{1y})(\rho_{2x} - \rho_{2y}) \cos(2\omega)} \quad (5.4)$$

$$\rho_5 = \frac{1}{2}(\rho_{1x} + \rho_{1y}) + \frac{1}{2}(\rho_{2x} + \rho_{2y}) \quad (5.5)$$

$$\cos \kappa = \frac{\rho_4}{\rho_5} \quad (5.6)$$

II. Equivalent modulus

$$H_1 = \frac{4}{3} \frac{E_1}{1 - \nu_1^2} \quad (5.7)$$

$$H_2 = \frac{4}{3} \frac{E_2}{1 - \nu_2^2} \quad (5.8)$$

$$H_{12} = [H_1^{-1} + H_2^{-1}]^{-1} \quad (5.9)$$

III. Hertzian parameters (2)

$\cos \kappa$	M	N	$\cos \kappa$	M	N
0	1	1	0.53	1.080377	0.891719
0.01	1.001662	0.998329	0.54	1.081787	0.889021
0.03	1.004963	0.994962	0.55	1.083193	0.886281
0.04	1.006602	0.993264	0.56	1.084595	0.883498
0.05	1.008233	0.991558	0.57	1.085993	0.880668
0.06	1.009857	0.989842	0.58	1.087386	0.877779
0.07	1.011474	0.988117	0.59	1.088776	0.874863
0.08	1.013084	0.986381	0.6	1.090161	0.871882
0.09	1.014686	0.984636	0.61	1.09154	0.868847
0.1	1.016283	0.982879	0.62	1.092915	0.865753
0.11	1.017872	0.981113	0.63	1.094284	0.862599
0.12	1.019456	0.979335	0.65	1.097003	0.856097
0.13	1.021033	0.977546	0.66	1.098352	0.852741
0.14	1.022604	0.975745	0.68	1.101026	0.845801
0.15	1.024169	0.973932	0.69	1.10235	0.842208
0.16	1.025729	0.972107	0.7	1.103663	0.838526
0.17	1.027283	0.97027	0.71	1.104965	0.83475
0.18	1.028831	0.96842	0.73	1.10753	0.826888
0.19	1.030374	0.966556	0.74	1.108789	0.822789
0.2	1.031912	0.964679	0.75	1.110031	0.818566
0.21	1.033445	0.962788	0.76	1.111253	0.814211
0.22	1.034973	0.960883	0.77	1.112453	0.809712
0.23	1.036496	0.958963	0.78	1.113627	0.805059
0.25	1.039528	0.955077	0.79	1.114772	0.800238
0.26	1.041038	0.95311	0.8	1.115884	0.795234
0.27	1.042543	0.951127	0.81	1.116957	0.790029
0.28	1.044043	0.949126	0.82	1.117985	0.784604
0.3	1.047032	0.945073	0.83	1.118961	0.778934
0.31	1.04852	0.943019	0.84	1.119877	0.772994
0.32	1.050005	0.940946	0.85	1.12072	0.766751
0.33	1.051486	0.938853	0.86	1.121478	0.760166
0.35	1.054436	0.934606	0.87	1.122132	0.753193
0.37	1.057371	0.930273	0.88	1.122661	0.745775
0.38	1.058834	0.928073	0.89	1.123035	0.73784
0.39	1.060293	0.925849	0.9	1.123215	0.729298
0.4	1.061749	0.923601	0.91	1.12315	0.720032
0.41	1.063202	0.921327	0.92	1.122765	0.709885
0.42	1.064651	0.919027	0.93	1.121953	0.698641
0.43	1.066097	0.916701	0.94	1.120552	0.68599
0.44	1.067539	0.914346	0.95	1.118301	0.67146
0.45	1.068979	0.911963	0.96	1.114743	0.654282
0.46	1.070415	0.909549	0.97	1.108989	0.633057
0.48	1.073278	0.904628	0.98	1.098938	0.604763
0.5	1.076128	0.899574	0.99	1.077506	0.560295
0.52	1.078964	0.894375	1	0	0

IV. Semi-contact axis

$$a = \sqrt[3]{\frac{F \rho_3^2}{H_{12}}} \sqrt{\frac{\rho_3}{\rho_5 - \rho_4 \rho_3}} \frac{M}{\rho_3} \quad (5.10)$$

$$c = \sqrt[3]{\frac{F \rho_3^2}{H_{12}}} \sqrt{\frac{\rho_3}{\rho_5 + \rho_4 \rho_3}} \frac{N}{\rho_3} \quad (5.11)$$

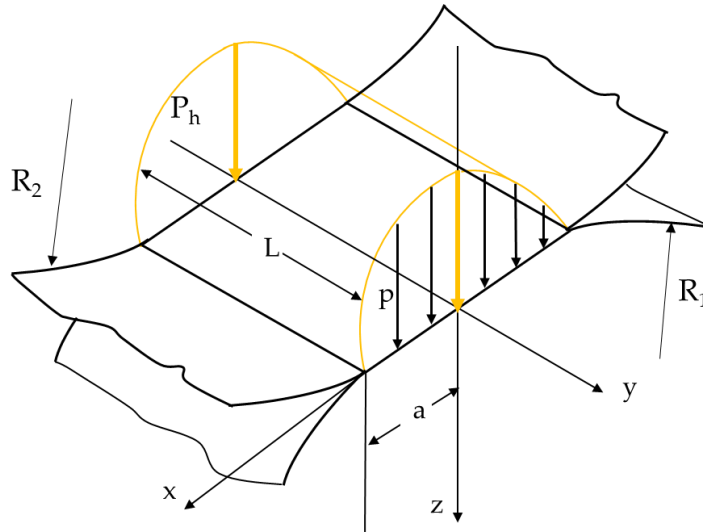
The Hertzian pressure is given by

$$p_H = \frac{3F}{2\pi ac} \quad (5.12)$$

5.1.2 Two-dimensional contact of cylinder bodies

Now, two cylindrical bodies are considered of length L with their axes parallel to the y -axis and are pressed in contact by a force F . The contact area results in a strip of width $2a$ lying parallel to the y -axis. Hertz considered this case as a limit of an elliptical contact when b becomes larger than a . FIGURE 5.2 shows a schematic of the model.

Figure 5.2 – Schematic representation of the cylindrical (line) contact



In this case, the knowns are the following:

- Radii of the two cylinders R_1 and R_2 (set to infinite if planar)
- Applied load F
- Length of the contact L
- Elastic properties E and ν

To determine the semi-contact area, we must first calculate the equivalent modulus H_{12} and the equivalent radius R_{12}

$$H_1 = \frac{E_1}{1 - \nu_1^2} \quad (5.13)$$

$$H_2 = \frac{E_2}{1 - \nu_2^2} \quad (5.14)$$

$$H_{12} = [H_1^{-1} + H_2^{-1}]^{-1} \quad (5.15)$$

$$R_{12} = [R_1^{-1} + R_2^{-1}]^{-1} \quad (5.16)$$

Now, we can calculate the contact area a

$$a^2 = \frac{4FR_{12}}{\pi LH_{12}} \quad (5.17)$$

The pressure distribution is

$$p(x) = p_H \left(1 - \left(\frac{x}{a}\right)^2\right)^{\frac{1}{2}} \quad (5.18)$$

where the Hertzian pressure p_H is given by

$$p_H = \frac{2F}{\pi aL} \quad (5.19)$$

5.2 Distributed normal and tangential tractions

In this paragraph, we introduce the stress field produced in the elastic half-space under the action of distributed normal and tangential forces. The normal force distribution can be associated with the Hertzian pressure studied in the previous paragraph. For the tangential distribution, full slip condition is assumed, i.e. the tangential distribution is proportional to the normal pressure

$$q(x, y) = \mu p(x, y), \quad (5.20)$$

where μ is the friction coefficient.

FIGURE 5.3 shows an elastic half-space loaded over the strip by a normal pressure $p(x, y)$ and tangential traction $q(x, y)$ in an arbitrary manner. The stress at any point in the body of the solid can be calculated. The traction and the tangential loads can be treated as the summation of concentrated forces by discretising the distribution in elemental areas of width ds .

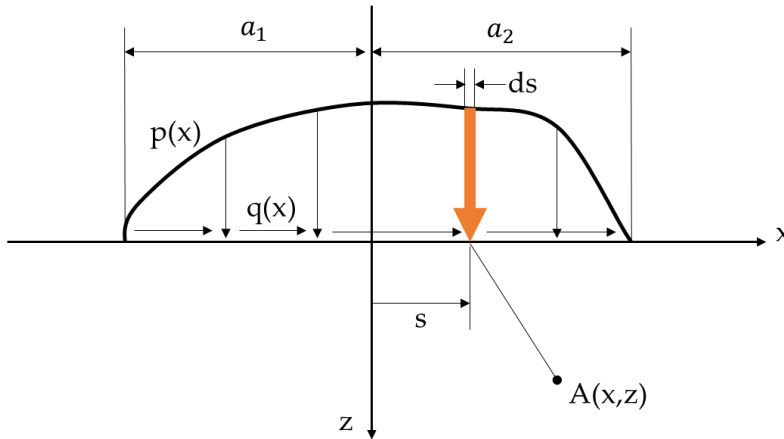


Figure 5.3 – Elastic half-space loaded by a normal pressure $p(x)$ and a tangential traction distributed in an arbitrary manner

After defining a grid of points in the three directions, the stress components at a given point can be found by integrating over the loaded region (1):

$$\sigma_x = -\frac{2z}{\pi} \int_{-a_1}^{a_2} \frac{p(s)(x-s)^2 ds}{\{(x-s)^2 + z^2\}^2} - \frac{2}{\pi} \int_{-a_1}^{a_2} \frac{q(s)(x-s)^3 ds}{\{(x-s)^2 + z^2\}^2} \quad (5.21)$$

$$\sigma_z = -\frac{2z^3}{\pi} \int_{-a_1}^{a_2} \frac{p(s) ds}{\{(x-s)^2 + z^2\}^2} - \frac{2z^3}{\pi} \int_{-a_1}^{a_2} \frac{q(s)(x-s) ds}{\{(x-s)^2 + z^2\}^2} \quad (5.22)$$

$$\tau_{xz} = -\frac{2z^2}{\pi} \int_{-a_1}^{a_2} \frac{p(s)(x-s)ds}{\{(x-s)^2 + z^2\}^2} - \frac{2z}{\pi} \int_{-a_1}^{a_2} \frac{q(s)(x-s)^2 ds}{\{(x-s)^2 + z^2\}^2} \quad (5.23)$$

Since the integration in closed form may be difficult, the stress components can be easily found by the equations obtained from the Boussinesq potential functions (1). For the stress components resulting from the concentrated normal force, we have

$$\sigma_{x,p} = \frac{p}{2\pi} \left[\frac{(1-2\nu)}{r^2} \left\{ \left(1 - \frac{z}{\rho}\right) \frac{x^2 - y^2}{r^2} + \frac{zy^2}{\rho^3} \right\} - \frac{3zx^2}{\rho^5} \right] \quad (5.24)$$

$$\sigma_{y,p} = \frac{p}{2\pi} \left[\frac{(1-2\nu)}{r^2} \left\{ \left(1 - \frac{z}{\rho}\right) \frac{y^2 - x^2}{r^2} + \frac{zx^2}{\rho^3} \right\} - \frac{3zy^2}{\rho^5} \right] \quad (5.25)$$

$$\sigma_{z,p} = -\frac{3pz^3}{2\pi\rho^5} \quad (5.26)$$

$$\tau_{xy,p} = \frac{p}{2\pi} \left[\frac{(1-2\nu)}{r^2} \left\{ \left(1 - \frac{z}{\rho}\right) \frac{xy}{r^2} + \frac{xyz}{\rho^3} \right\} - \frac{3xyz}{\rho^5} \right] \quad (5.27)$$

$$\tau_{xz,p} = -\frac{3pxz^2}{2\pi\rho^5} \quad (5.28)$$

$$\tau_{yz,p} = -\frac{3pyz^2}{2\pi\rho^5} \quad (5.29)$$

While for the tangential force q_x , we have

$$\frac{2\pi\sigma_{x,q}}{q_x} = -\frac{3x^3}{\rho^5} + (1-2\nu) \left\{ \frac{x}{\rho^3} - \frac{3x}{\rho(\rho+z)^2} + \frac{x^3}{\rho^3(\rho+z)^2} + \frac{2x^3}{\rho^2(\rho+z)^3} \right\} \quad (5.30)$$

$$\frac{2\pi\sigma_{y,q}}{q_x} = -\frac{3xy^2}{\rho^5} + (1-2\nu) \left\{ \frac{x}{\rho^3} - \frac{x}{\rho(\rho+z)^2} + \frac{xy^2}{\rho^3(\rho+z)^2} + \frac{2xy^2}{\rho^2(\rho+z)^3} \right\} \quad (5.31)$$

$$\frac{2\pi\sigma_{z,q}}{q_x} = -\frac{3xz^2}{\rho^5} \quad (5.32)$$

$$\frac{2\pi\tau_{xy,q}}{q_x} = -\frac{3xy^2}{\rho^5} + (1-2\nu) \left\{ -\frac{y}{\rho(\rho+z)^2} + \frac{x^2y}{\rho^3(\rho+z)^2} + \frac{2x^2y}{\rho^2(\rho+z)^3} \right\} \quad (5.33)$$

$$\frac{2\pi\tau_{yz,q}}{q_x} = -\frac{3xyz}{\rho^5} \quad (5.34)$$

$$\frac{2\pi\tau_{xz,q}}{q_x} = -\frac{3x^2z}{\rho^5} \quad (5.35)$$

ρ and r are defined as follows

$$\rho^2 = x^2 + y^2 + z^2 \quad (5.36)$$

$$r^2 = x^2 + y^2 \quad (5.37)$$

In the above equations, all the points below the applied load ($\rho = 0$ and $r = 0$) represent singularity points of the second kind. Approaching these points, the stress tends to be infinite. To overcome this issue, we can adopt two grids of points, one to discretise the load distribution, the other to identify the points on which to calculate the stresses. The stress in a point can be calculated as the average value among the stresses generated by the neighbouring point loads. However, even after this expedient, the stresses

calculated near the surface will be higher than actual. Thus, it will be necessary to exclude the surface region during the analysis of the results.

If two cylinders in contact are considered, the stresses acting on the xz -plane can be found by McEwen's equations

$$\sigma_{x,p} = -\frac{p_H}{a} \left[m \left(1 + \frac{n^2 + z^2}{m^2 + n^2} \right) - 2z \right] \quad (5.38)$$

$$\sigma_{z,p} = -\frac{p_H}{a} m \left(1 + \frac{n^2 + z^2}{m^2 + n^2} \right) \quad (5.39)$$

$$\tau_{xz,p} = -\frac{P_H}{a} n \left(\frac{m^2 - z^2}{m^2 + n^2} \right) \quad (5.40)$$

$$\sigma_{x,q} = -\frac{\mu P_H}{a} \left\{ n \left(2 - \frac{z^2 - m^2}{m^2 + n^2} \right) - 2x \right\} \quad (5.41)$$

$$\sigma_{z,q} = -\mu \tau_{xz,p} \quad (5.42)$$

$$\tau_{xz,q} = -\mu \sigma_{z,p} \quad (4.43)$$

$$\sigma_y = -\nu(\sigma_x + \sigma_z), \quad (5.44)$$

where

$$m^2 = 0.5\{[(a^2 - x^2 + z^2)^2 + 4x^2z^2]^2 + (a^2 - x^2 + z^2)\} \quad (5.45)$$

$$n^2 = 0.5\{[(a^2 - x^2 + z^2)^2 + 4x^2z^2]^2 - (a^2 - x^2 + z^2)\} \quad (5.46)$$

The signs of m and n are the same as z and x , respectively. The total stress of each component is obtained by adding the tangential contribution to the normal one.

5.3 Post-processing

Once the elastic stress components are found, we can calculate other useful quantities on the xz -plane:

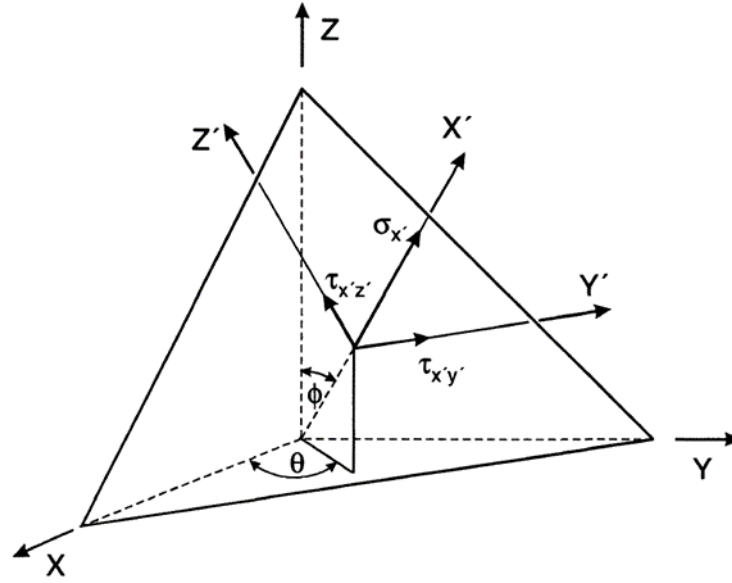
- Hydrostatic and deviatoric components of the stress tensor
- Principal stresses
- Maximum and minimum values of stress components at any depth
- Von Mises equivalent stress

$$\sigma_{VM} = \sqrt{\sigma_1^2 + \sigma_2^2 + \sigma_3^2 - \sigma_1\sigma_2 - \sigma_1\sigma_3 - \sigma_2\sigma_3}, \quad (5.47)$$

where σ_1, σ_2 and σ_3 are the principal stresses.

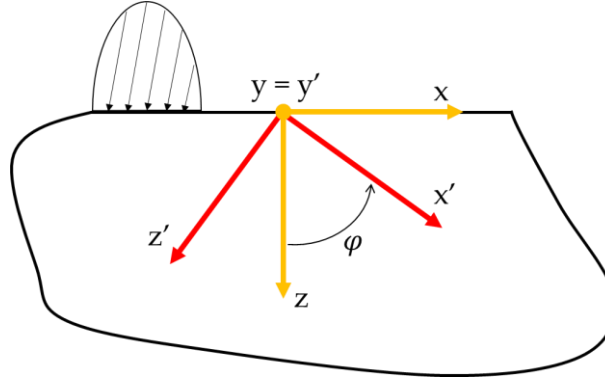
- Normal and shear stresses acting on a plane 45° with respect to the surface. These quantities are useful when applying critical approach fatigue criteria; to define this new tensor, direction cosines are used in terms of angles θ and φ . θ denotes the rotation angle of the xy -plane, while φ is the angle between the old z -axis and the new x -axis (x'). FIGURE 5.4 shows the general case of the coordinate transformation.

Figure 5.4 – Stresses acting on a plane in a three-dimensional coordinate system



In our situation, we can fix the y-axis and rotate the x- and z-axes, varying φ (FIGURE 5.5). Note that the original frame of reference is defined by $\theta = 0^\circ$ and $\varphi = 90^\circ$.

Figure 5.5 – Rotating coordinate system in the half-space model



Below are the equations for the coordinate transformations from the original system xyz to the new one $x'y'z'$ (3):

$$\sigma_{x'} = \sigma_x a_{11}^2 + \sigma_y a_{12}^2 + \sigma_z a_{13}^2 + 2(\tau_{xy} a_{11} a_{12} + \tau_{xz} a_{11} a_{13} + \tau_{yz} a_{12} a_{13}) \quad (5.48)$$

$$\tau_{x'y'} = \sigma_x a_{11} a_{21} + \sigma_y a_{12} a_{22} + \tau_{xy} (a_{11} a_{22} + a_{12} a_{21}) + \tau_{yz} (a_{12} a_{23} + a_{13} a_{22}) + \tau_{xz} (a_{13} a_{21} + a_{11} a_{23}) \quad (5.49)$$

$$\tau_{x'z'} = \sigma_x a_{11} a_{31} + \sigma_y a_{12} a_{32} + \tau_{xy} (a_{11} a_{32} + a_{12} a_{31}) + \tau_{yz} (a_{12} a_{33} + a_{13} a_{32}) + \tau_{xz} (a_{13} a_{31} + a_{11} a_{33}) \quad (5.50)$$

The direction cosines a_{ij} are given by

$$a_{11} = \cos \theta \sin \varphi \quad (5.51)$$

$$a_{12} = \sin \theta \cos \varphi \quad (5.52)$$

$$a_{13} = \cos \varphi \quad (5.53)$$

$$a_{21} = -\sin \theta \quad (5.54)$$

$$a_{22} = \cos \theta \quad (5.55)$$

$$a_{23} = 0 \quad (5.56)$$

$$a_{31} = -\cos \theta \cos \varphi \quad (5.57)$$

$$a_{32} = -\sin \theta \cos \varphi \quad (5.58)$$

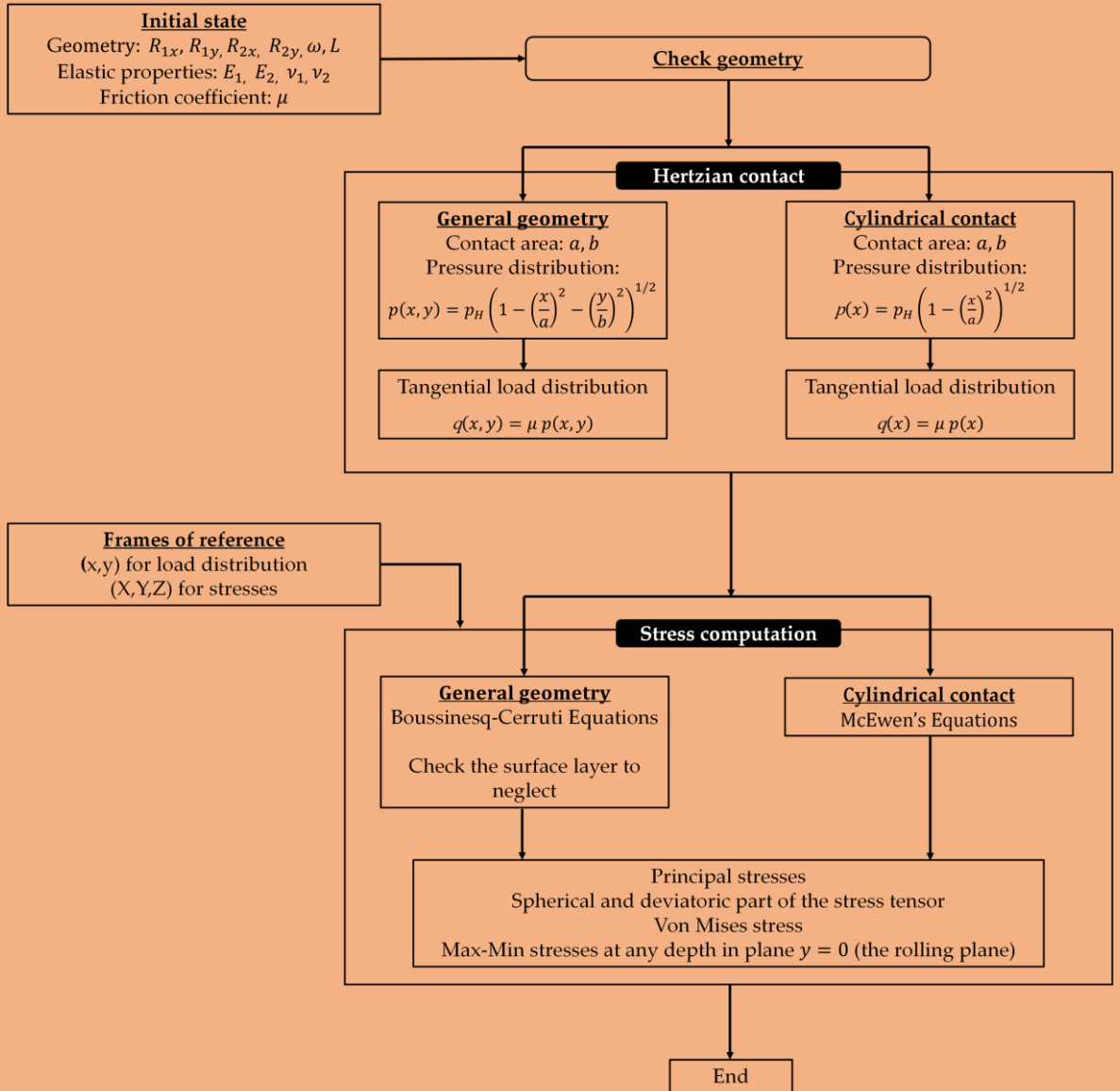
$$a_{33} = \sin \varphi \quad (5.59)$$

Analogous equations can be written for strains by replacing σ with the normal strains ε and the shear stress τ with one-half the shear strain $\gamma/2$.

5.4 References

1. Johnson KL. Contact Mechanics. Cambridge University Press; 1985. <https://doi.org/10.1017/CBO9781139171731>.
2. Cooper DH. Tables of Hertzian Contact-Stress Coefficients. August 1968. <http://hdl.handle.net/2142/74660>.
3. Socie F. Darrel MBG. Multiaxial Fatigue. ASTM Special Technical Publication. S.A.E. Library; 1985. ISBN [0768004535](https://doi.org/10.1520/STP440-1985).

ELASTIC STRESS COMPUTATION



Constitutive models

6

Notation

- i. Lightface Latin and Greek letters denote scalars
- ii. Boldface lowercase Latin and Greek letters denote vectors, but **o**, **x**, **y** and **z** denote points
- iii. Boldface uppercase Latin and Greek denote tensors

6.1 Some notes on tensor calculus

This paragraph covers some basic concepts of tensorial algebra used in the chapter (1,2).

Scalar product and length of a vector

Any vector **v** (first-order tensor) can be represented in an arbitrary Cartesian coordinate system as follows:

$$\mathbf{v} = v_i \mathbf{e}_i \quad (6.1)$$

Given two vectors $\mathbf{u} = u_i \mathbf{e}_i$ and $\mathbf{v} = v_j \mathbf{e}_j$, we define the scalar product as follows (remind the Einstein sum convention $a_j b_j = \sum_{j=1}^3 a_j b_j$):

$$\mathbf{u} \cdot \mathbf{v} = u_i v_i \quad (6.2)$$

The Euclidean norm, or simple length of **u**, denoted $|\mathbf{u}|$, is defined as:

$$u = |\mathbf{u}| = |\mathbf{u} \cdot \mathbf{u}|^{\frac{1}{2}} = [(u_1)^2 + (u_2)^2 + (u_3)^2]^{\frac{1}{2}} \quad (6.3)$$

Second rank tensor

The simplest form of a second order tensor **T** is a dyad, which is defined as the open product (or dyadic) of two vectors **u** and **v**:

$$\mathbf{T} = \mathbf{u} \otimes \mathbf{v} \stackrel{\text{def}}{=} [u_i \mathbf{e}_i] \otimes [v_j \mathbf{e}_j] = u_i v_j \mathbf{e}_i \otimes \mathbf{e}_j \quad (6.4)$$

where \otimes is the “open product” symbol. The matrix format of the dyad $\mathbf{u} \otimes \mathbf{v}$ is:

$$[(\mathbf{u} \otimes \mathbf{v})_{ij}] = \begin{bmatrix} u_1 \\ u_2 \\ u_3 \end{bmatrix} \begin{bmatrix} v_1 & v_2 & v_3 \end{bmatrix} = \begin{bmatrix} u_1 v_1 & u_1 v_2 & u_1 v_3 \\ u_2 v_1 & u_2 v_2 & u_2 v_3 \\ u_3 v_1 & u_3 v_2 & u_3 v_3 \end{bmatrix} \quad (6.5)$$

This defined dyad is a special case of the general representation:

$$\mathbf{T} = T_{ij} \mathbf{e}_i \otimes \mathbf{e}_j \quad (6.6)$$

in this case, the matrix format is the following:

$$\mathbf{T} = \begin{bmatrix} T_{11} & T_{12} & T_{13} \\ T_{21} & T_{22} & T_{23} \\ T_{31} & T_{32} & T_{33} \end{bmatrix} \quad (6.7)$$

Examples of second-order tensors are the stress tensor and the strain tensor.

Second rank tensor: double contraction

The double contraction operator between two base dyads is defined as follows:

$$(\hat{e}_i \hat{e}_j) : (\hat{e}_k \hat{e}_l) = (\hat{e}_i \cdot \hat{e}_k) (\hat{e}_j \cdot \hat{e}_l) = \delta_{ik} \delta_{jl}, \quad (6.8)$$

where δ_{ij} is the Kronecker operator

$$\delta_{ij} = \begin{cases} 1 & i = j \\ 0 & i \neq j \end{cases} \quad (6.9)$$

If we assume bilinearity of that operator, then double contraction between two second-order tensors \mathbf{T} and \mathbf{U} results in a scalar α and is obtained as:

$$\mathbf{T} : \mathbf{U} = T_{ik} U_{jl} = \alpha \quad (6.10)$$

Special second order tensors

The second-order tensor \mathbf{I} defined by the identity $\mathbf{I} \cdot \mathbf{u} = \mathbf{u}$ for any vector \mathbf{u} . the matrix format is

$$\mathbf{I} = [\delta_{ij}] = \begin{bmatrix} 1 & 0 & 0 \\ 0 & 1 & 0 \\ 0 & 0 & 1 \end{bmatrix} \quad (6.11)$$

The deviator of a tensor of as symmetric tensor \mathbf{T} , denoted as \mathbf{T}_{dev} , is defined as

$$\mathbf{T}_{\text{dev}} \stackrel{\text{def}}{=} \mathbf{T} - \frac{1}{3} [\mathbf{I} : \mathbf{T}] \mathbf{I} = \mathbf{T} - T_h \mathbf{I} \quad \text{with} \quad T_h \stackrel{\text{def}}{=} \frac{1}{3} \mathbf{I} : \mathbf{T} = \frac{1}{3} T_{kk} \quad (6.12)$$

T_{vol} is the hydrostatic part of the tensor (note that it is a scalar).

Invariant of second order tensors

Given a tensor \mathbf{T} , we can define three invariant quantities:

$$\text{First invariant} \quad I_1 = \text{tr}(\mathbf{T}) \quad (6.13)$$

$$\text{Second invariant} \quad I_2 = \frac{1}{2} \left[(\text{tr}(\mathbf{T}))^2 - (\text{tr}(\mathbf{T}))^2 \right] \quad (6.14)$$

$$\text{Third invariant} \quad I_3 = \det(\mathbf{T}) \quad (6.15)$$

Special fourth rank tensors

The fourth-order identity tensor \mathbf{I} is defined by the identity $\mathbf{I} : \mathbf{T} = \mathbf{T}$ for any second-order tensor \mathbf{T} . This gives the component representation:

$$\mathbf{I} = \mathbf{I} \otimes \mathbf{I} = \delta_{ik} \delta_{jl} \mathbf{e}_i \otimes \mathbf{e}_j \otimes \mathbf{e}_k \otimes \mathbf{e}_l \quad (6.16)$$

We also define the deviator projection tensor from the fourth-order identity tensor as follows:

$$\mathbf{I}^{dev} \stackrel{\text{def}}{=} \mathbf{I} - \frac{1}{3} \mathbf{I} \otimes \mathbf{I} = \mathbf{I} - \mathbf{I}^{sph} \quad (6.17)$$

Voigt-matrix representation of tensor transformation

Voigt notation uses classical matrix-vector algebra to express tensor operations. To this end, the components of second order tensors are rearranged in a vector. Analogously, the components of fourth-order tensors are rewritten in a matrix. For example, the Voigt format of stress and strain tensors are:

$$\underline{\sigma} = \begin{bmatrix} \sigma_{11} \\ \sigma_{22} \\ \sigma_{33} \\ \sigma_{23} \\ \sigma_{13} \\ \sigma_{12} \end{bmatrix}, \quad \underline{\varepsilon} = \begin{bmatrix} \varepsilon_{11} \\ \varepsilon_{22} \\ \varepsilon_{33} \\ \gamma_{23} \\ \gamma_{13} \\ \gamma_{12} \end{bmatrix} \quad \text{with } \gamma_{ij} = 2\varepsilon_{ij}, \quad i \neq j \quad (6.18)$$

Here we exploited the symmetry of the stress and the strain tensors by considering only the six independent components. However, nothing prevents us from using all nine components.

If we consider the linear transformation between stress and strain:

$$\underline{\sigma} = \underline{E} : \underline{\varepsilon} \quad (6.19)$$

the elastic stiffness matrix \underline{E} is a fourth-order tensor, which becomes a square matrix in Voigt notation: 6×6, if we consider six stress/strain components or 9×9, if we consider full stress/strain tensors. The Voigt format of the elastic stiffness is

$$\underline{E} = \begin{pmatrix} K + \frac{4}{3}G & K - \frac{1}{3}G & K - \frac{1}{3}G & 0 & 0 & 0 \\ K - \frac{1}{3}G & K + \frac{4}{3}G & K - \frac{1}{3}G & 0 & 0 & 0 \\ K - \frac{1}{3}G & K - \frac{1}{3}G & K + \frac{4}{3}G & 0 & 0 & 0 \\ 0 & 0 & 0 & G & G & G \\ 0 & 0 & 0 & G & G & G \\ 0 & 0 & 0 & G & G & G \end{pmatrix} \quad (6.20)$$

where K is the bulk modulus, and G is the shear modulus.

The second order identity and the fourth order identity tensor are:

$$\underline{\mathbf{I}} = \begin{pmatrix} 1 \\ 1 \\ 1 \\ 0 \\ 0 \\ 0 \end{pmatrix} \quad \underline{\mathbf{I}} = \begin{pmatrix} 1 & 0 & 0 & 0 & 0 & 0 \\ 0 & 1 & 0 & 0 & 0 & 0 \\ 0 & 0 & 1 & 0 & 0 & 0 \\ 0 & 0 & 0 & \frac{1}{2} & 0 & 0 \\ 0 & 0 & 0 & 0 & \frac{1}{2} & 0 \\ 0 & 0 & 0 & 0 & 0 & \frac{1}{2} \end{pmatrix} \quad (6.21)$$

Derivatives of a second order tensor

Among the several derivatives, we recall the following:

$$\frac{\partial \mathbf{A}}{\partial \mathbf{A}} = \frac{\partial A_{ij}}{\partial A_{kl}} = \mathbf{I}^{sym} \quad (6.22)$$

$$\frac{\partial |\mathbf{A}_{dev}|}{\partial \mathbf{A}} = \frac{\mathbf{A}_{dev}}{|\mathbf{A}_{dev}|} \quad (6.23)$$

6.2 General remarks on constitutive modelling

Constitutive modelling describes the material responses to mechanical and thermal loading, providing the stress-strain relations. From a mathematical point of view, the constitutive equations are complementary to the kinematic and equilibrium equations. The constitutive models are mathematical simplifications of the complex physical behaviour of the material, and an exact model does not exist. For instance, a material is not considered viscoplastic, but the behaviour of the material can be modelled as viscoplastic.

Constitute models are subjected to constraints, some of which are intuitive but difficult to formulate in a mathematical way through the following (3):

- **Principle of coordinate invariance** – The choice of an arbitrary frame of reference should not affect the relationships between physical entities and the constitutive equations.
- **Principle of material objectivity** – The arbitrary rigid body motion superposed on the actual motion should not affect the constitutive relations.
- **Principle of determinism** – The motion of the body completely defines the stress, meaning future events do not influence the stress state in the body.
- **Constraint of material symmetry** – Response functions are unaffected by certain rotations of the chosen reference configurations owing to material symmetry.
- **Second law of thermodynamics** – Expressed by the Clausius-Duhem inequality, the second law of thermodynamics states that the dissipation of energy is never negative.

FIGURE 6.1 summarises the most relevant types of constitutive models.

6.3 Plasticity

***Plastic** comes from the Greek verb to “form” or “shape”*

Early work about macroscopic and mathematical plasticity dates to 1900 to the 1920s by Huber, von Mises, Prandtl, Hencky and Reuss. In the 1930s, Odqvist first introduced the concept of hardening, later deepened by Melan (1938) and Prager (1947), who coined the term *kinematic hardening*. Plasticity was born as a branch of the mechanics of materials mainly targeted for ductile metals, but this theory has been finding a widespread use also in the modelling of some kinds of polymers and soils.

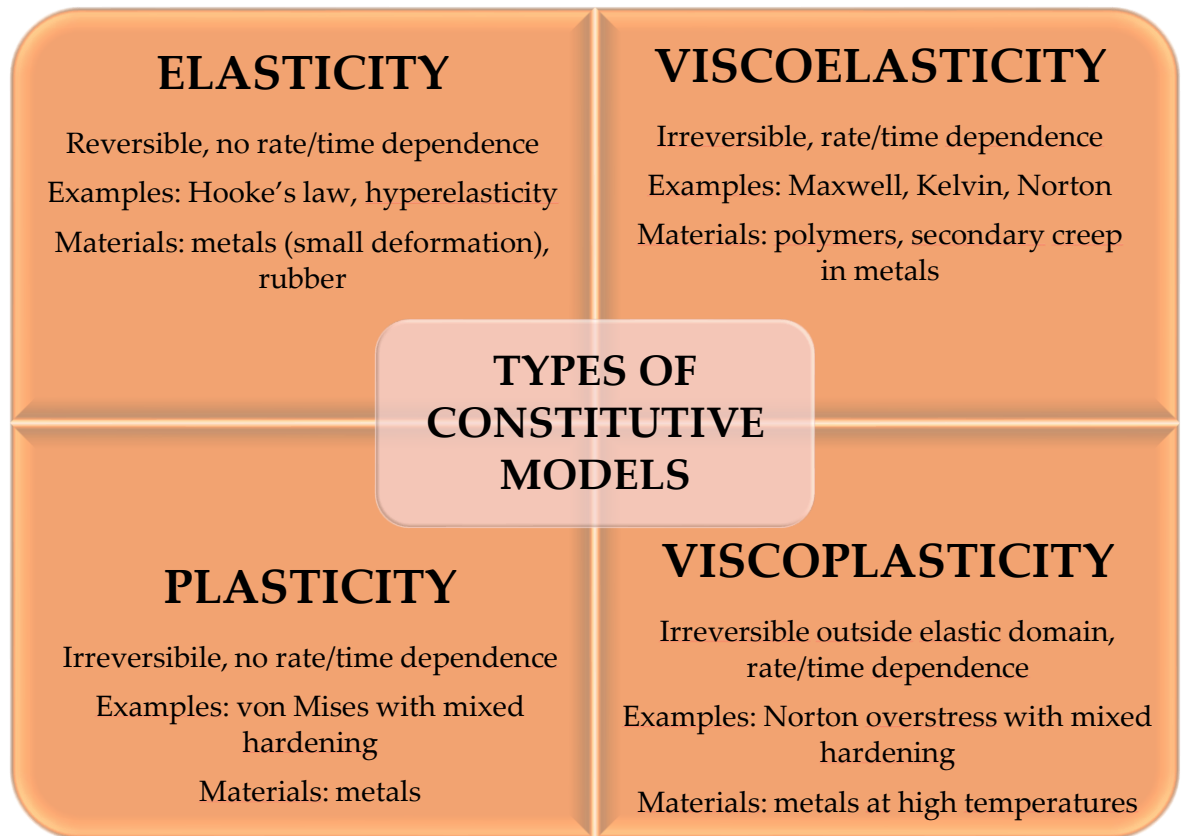


Figure 6.1 – Types of constitutive models

Plasticity is usually related to the irreversible deformations of metals for which the inelastic deformation mostly happens as distortion, while the inelastic volume change is negligible. The plasticity theory concerns time-independent behaviour that is non-linear and where residual strains still exist after that the material is unloaded.

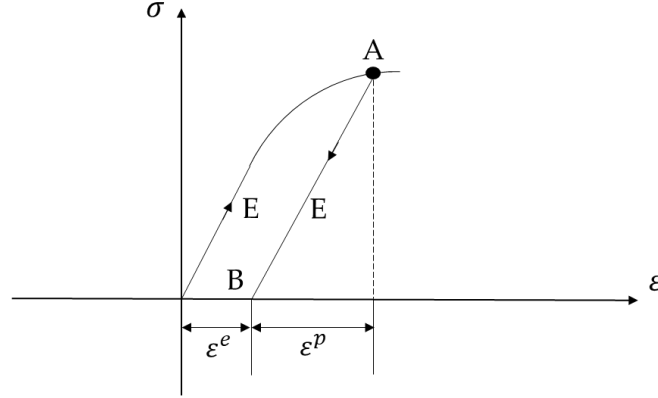
The key point to understanding the plastic, as well as viscoplastic, deformation in metals is in the plastic slip along the crystal plane in the direction of the largest shear stress (3). The motion of the dislocations of atom planes is responsible for this slip. If the crystal structure is perfect, the plastic slip leads to a macroscopic shear deformation without any other distortion of the lattice structure. The plastic strain must be superimposed on the elastic one. However, most metals are polycrystalline, i.e. the grains have different orientations and lattice structure. If the grain orientation is statistically uniform, the macroscopic response can be inferred to be isotropic. Anisotropy induced by the manufacturing process makes this ideal situation difficult to meet (3).

FIGURE 6.2 shows the basic behaviour of an elasto-plastic material. The linear elastic behaviour is defined by the stiffness E . The threshold of the elastic limit is represented by the *initial yield stress* σ_{y0} , after which, plastic strains occur. Unloading from point A occurs elastically with the stiffness E so that, at complete unloading to point B, the residual strain amounts to the plastic strain ε^p developed at point A. Therefore, at point A, the total strain ε consists of the sum of the elastic and plastic strains

$$\varepsilon = \varepsilon^e + \varepsilon^p \quad (6.24)$$

If we reload again from point B, the material behaves elastically until the value σ_y is reached at point A. The value σ_y is denoted as the *current yield stress*. In general, σ_y differs from the initial stress σ_{y0} . The response shown in FIGURE 6.2 is supposedly time-independent; this implies the same response occurs regardless of the loading rate.

Figure 6.2 – Basic elastic-plastic response in uniaxial case



Since the yield stress often changes with the plastic strain, it is clear that the yield surface will vary with the plastic loading. The *hardening rules* describe this change of the yield surface. In general, the *yield surface* is represented by

$$\Phi = \Phi(\sigma_{ij}, K_1, K_2, \dots), \quad (6.25)$$

where K_1, K_2, \dots stand for the *hardening parameters*. Before any plasticity occurs, all the hardening parameters are equal to zero. The hardening parameters can be scalar or tensors. Φ is a non-positive function. In the plasticity theory, $\Phi < 0$ means that the material stays in the elastic field, and when $\Phi = 0$ plastic strain occurs. As an example of a yield function, the von Mises function has the initial yield surface given by

$$\begin{aligned} \Phi &= \sigma_e - \sigma_{y0} = \sqrt{3J_2} - \sigma_{y0} = \\ &= \sqrt{\frac{3}{2}} |\sigma_{dev}| - \sigma_{y0}, \end{aligned} \quad (6.26)$$

where σ_e is the equivalent stress expressed in von Mises terms, J_2 is the second invariant of the stress tensor and σ_{dev} is the deviatoric part of the stress tensor. The yield surface can be represented on the deviatoric plane, as shown in Figure.

Hardening rule is also defined by the *associative plastic flow and hardening rules* that describe how the plastic strain and the hardening parameters evolve in time, i.e. they define $\dot{\varepsilon}_p, \dot{K}_i$. It also must be recalled the *plastic Lagrangian multiplier* λ , a non-negative parameter which acts as a constant of proportionality in the associative rules. The *Kuhn-Tucker relationships* summarise the loading criteria in the plastic field

$$\lambda \geq 0 \quad \Phi(\sigma_{ij}, K_1, K_2, \dots) \leq 0 \quad \lambda \Phi(\sigma_{ij}, K_1, K_2, \dots) = 0 \quad (6.27)$$

Further details about the associative rules can be found in (4).

J_2 Second invariant of stress tensor

$$\sigma_{11}\sigma_{22} + \sigma_{11}\sigma_{33} + \sigma_{22}\sigma_{33}$$

being σ_{11}, σ_{22} and σ_{33} the principal stress

Double contractor tensor product:

$$|\sigma_{dev}| = \sqrt{\sigma_{dev} : \sigma_{dev}}$$

For *isotropic hardening*, the shape and the position of the yield surface remain fixed, whereas the size of the yield surface varies with plastic strain. The yield function is defined as

$$\Phi = \sigma_e - (\sigma_{y0} + R), \quad (6.28)$$

where R is the *dragstress*, a scalar quantity that defines how the yield surface size has changed. The quantity $(\sigma_{y0} + R)$ is the actual yield stress. FIGURE 6.3 shows the stress-strain relationship for the uniaxial case and the deviatoric plane.

For *kinematic hardening*, the shape and the position of the yield surface remain fixed, whereas the position of yield surface varies with plastic strain. In this case, the hardening parameter is a tensorial quantity X_{ij} called *backstress*. To express the yield function, we introduce the *reduced stress* σ^{red} , equal to $\sigma_{dev} - X_{dev}$, with X_{dev} as the deviatoric part of the backstress. The yield function becomes

$$\Phi = \sigma_e^{red} - \sigma_{y0} = \sqrt{\frac{3}{2}} |\sigma^{dev} - \mathbf{X}| - \sigma_{y0} \quad (6.29)$$

More than one backstress can be considered to implement a model that best fits the experimental data. FIGURE 6.4 shows the stress-strain relationship for the uniaxial case and the deviatoric plane.

It is also common to employ a *mixed hardening model*, obtained by combining the isotropic and hardening models. The yield function then becomes

$$\Phi = \sigma_e^{red} - (\sigma_{y0} + R) = \sqrt{\frac{3}{2}} |\sigma^{dev} - \mathbf{X}| - (\sigma_{y0} + R) \quad (6.30)$$

FIGURE 6.5 shows the simplicity linear hardening model, i.e. the slope of the curve in the plastic regime is constant. However, to describe the behaviour of a material in a more realistic fashion, *non-linear laws of hardening* can be adopted. Non-linear laws can model an asymptotic case of perfect plasticity for large plastic strain. This behaviour reflects the saturation of dislocations. The addition of the *saturation coefficients* is needed in the associative flow rules: R_∞ and X_∞ , the isotropic and the kinematic saturation coefficients, respectively. FIGURE 6.6 shows the stress-strain relationship when non-linear hardening is considered.

As an example of mixed hardening, we will consider the Chaboche plasticity model. This model manages to solve many problems relating to non-linear mixed hardening, and it is implemented in finite element software, like Abaqus®. SECTION 6.4 will provide further details about Chaboche equations and numerical implementation.

Figure 6.3 – Isotropic hardening: deviatoric plane and stress-strain curve (linear hardening)

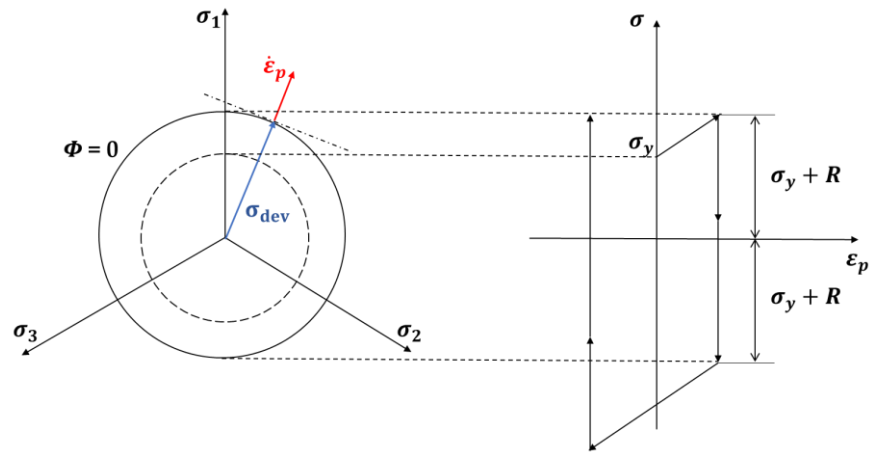


Figure 6.4 – Kinematic hardening: deviatoric plane and stress-strain curve (linear hardening)

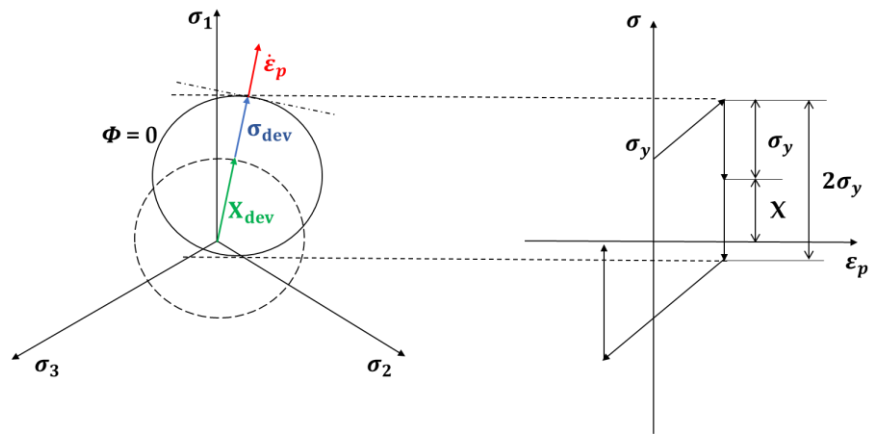


Figure 6.5 – Mixed hardening: deviatoric plane and stress-strain curve (linear hardening)

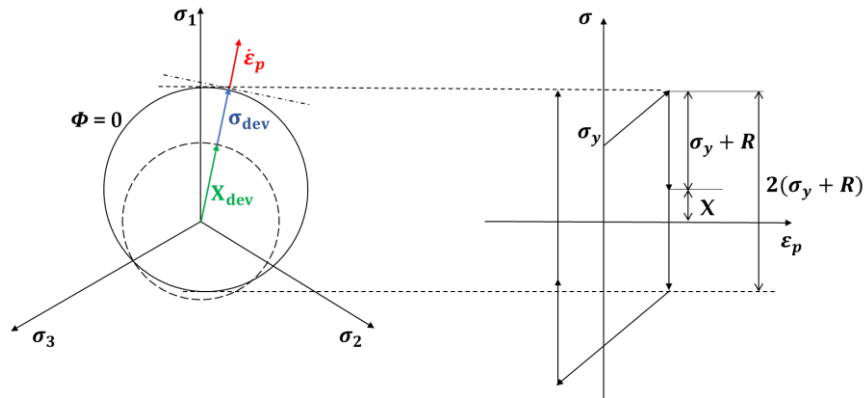
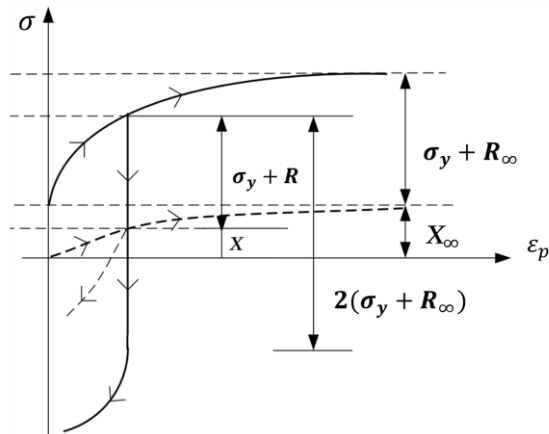


Figure 6.6 – Stress-strain curve for mixed non-linear hardening



Hardening plastic behaviour may be represented by the rheological model shown in FIGURE 6.7. The frictional plastic slider is inactive until $|\sigma| < \sigma_y$, and it increases its resistance because of the amount of slip developed. As anticipated at the beginning of this section, we consider the inelastic deformation to be volume-shear-dominated (or volume-preserving), so the plastic strain is only deviatoric ($\varepsilon_p = \varepsilon_p^{dev}$). The volumetric deformation is governed by the bulk modulus K , whereas the elastic deviatoric strain is controlled by the shear modulus G . H and r represent the hardening modulus and the hardening ratio, respectively, which control the relation between kinematic and isotropic hardening.

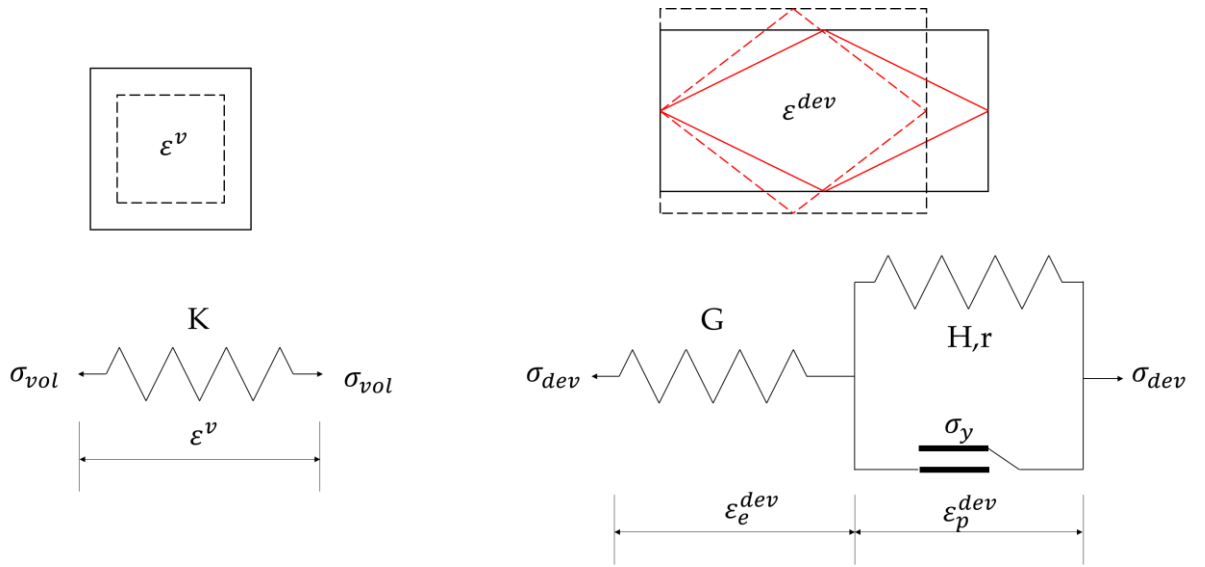


Figure 6.7 – Rheological model for multiaxial plastic with hardening

6.4 Chaboche plastic model

The Chaboche model (5,6) consists of a plastic model with mixed non-linear isotropic and kinematic hardening. In this section, the governing equations and the numerical implementation of the model are shown in the *stress-driven problem*.

The three governing equations are the followings:

I. VON MISES YIELD FUNCTION

$$\Phi = \sqrt{\frac{3}{2}} |\boldsymbol{\sigma}^{dev} - \mathbf{X}| - (\sigma_{y0} + R) \leq 0 \quad (6.31)$$

II. ISOTROPIC NON-LINEAR HARDENING

$$\dot{R} = \lambda b (R_\infty - R), \quad (6.32)$$

where R_∞ is the isotropic saturation coefficient, R is the actual dragstress, b the isotropic coefficient linked to the rapidity with which the saturation limit is reached.

III. KINEMATIC NON-LINEAR HARDENING

The kinematic hardening is supposed to be additively decomposed in several hardening stresses \mathbf{X}_i

$$\mathbf{X} = \sum_{i=1}^n \mathbf{X}_i \quad (6.33)$$

The additive decomposition of the backstress is a concept introduced by Chaboche and yields a better approximation of the stress-strain curve. Nevertheless, it requires more computation time.

The evolution rule, resembling the Armstrong-Frederik equation, is

$$\dot{\mathbf{X}}_i = C_i \dot{\lambda} \frac{\boldsymbol{\sigma}^{dev} - \mathbf{X}}{|\boldsymbol{\sigma}^{dev} - \mathbf{X}|} - \gamma_i \dot{\lambda} \mathbf{X}_i \quad (6.34)$$

The former term denotes the static recovery, the latter the dynamic recovery. We recall here that, since the backstress is a tensor, this equation must be written in terms of components in the numerical implementation.

The parameters b and R_∞ control the isotropic non-linearity of the hardening evolutions, while C_i and γ_i control the kinematic one. The isotropic and kinematic saturation limits are R_∞ and C_i/γ_i , respectively.

The associative rule of the plastic strain is

$$\dot{\boldsymbol{\varepsilon}}^p = \dot{\lambda} \frac{\partial \Phi}{\partial \boldsymbol{\sigma}} = \dot{\lambda} \sqrt{\frac{3}{2}} \frac{\boldsymbol{\sigma}^{dev} - \mathbf{X}}{|\boldsymbol{\sigma}^{dev} - \mathbf{X}|} \quad (6.35)$$

In the evolution equations, $\dot{\lambda}$ denotes the time derivative of the Lagrangian multiplier, related to the equivalent plastic strain

$$\dot{\lambda} = \sqrt{\frac{2}{3}} \dot{\boldsymbol{\varepsilon}}^p : \dot{\boldsymbol{\varepsilon}}^p \quad (6.36)$$

Numerical integration

To integrate the plastic response, let us consider time interval $\mathcal{T} = [0, t]$ subdivided into a finite number of time steps $mtim$

$$\mathcal{T} = \{0, t_1, \dots, t_n, t_{n+1}\}_{n=1, mtim} \quad (6.37)$$

After that, the Backward Euler (BE) finite differences are applied to hardening equations. In so doing, we write the time derivative of a general quantity \mathcal{F} as finite differences, i.e. $\dot{\mathcal{F}} = \frac{\Delta \mathcal{F}}{\Delta t} = \frac{{}^{n+1}\mathcal{F} - {}^n\mathcal{F}}{\Delta t}$. From now on, the quantity ${}^{n+1}\mathcal{F}$ will be simply written as \mathcal{F} .

By applying BE, the equations become

$$\mathbf{X}_i = {}^n\mathbf{X}_i + \Delta \lambda \left(C_i \frac{\boldsymbol{\sigma}^{dev} - \mathbf{X}}{|\boldsymbol{\sigma}^{dev} - \mathbf{X}|} - \gamma_i \dot{\mathbf{X}}_i \right) \quad (6.38)$$

$$R = {}^nR + \Delta \lambda b (R_\infty - R) \quad (6.39)$$

$$\sqrt{\frac{3}{2}} |\boldsymbol{\sigma}^{dev} - \mathbf{X}| - (\sigma_{y0} + R) = 0 \quad (6.40)$$

Given the stress state, the unknowns are the current dragstress R (one unknown), the backstress \mathbf{X}_i (six independent components for each backstress) and the plastic multiplier $\Delta\lambda$ (one unknown).

Solving explicitly, the system problem is rather difficult (owing to the non-linearity). It is common to resort the formulation of an unbalance $\mathbf{G}[\mathbf{x}] = \mathbf{0}$. In view of the relations, \mathbf{G} is formulated as

$$\mathbf{G}[\mathbf{x}] = \begin{bmatrix} \mathbf{X}_i - {}^n\mathbf{X}_i - \Delta\lambda \left(\sqrt{\frac{2}{3}} C_i \frac{(\boldsymbol{\sigma}^{dev} - \mathbf{X})}{|\boldsymbol{\sigma}^{dev} - \mathbf{X}|} - \gamma_i \dot{\mathbf{X}}_i \right) \\ R - {}^nR - \Delta\lambda b(R_\infty - R) \\ \sqrt{\frac{3}{2}} |\boldsymbol{\sigma}^{dev} - \mathbf{X}| - (\sigma_{y0} + R) \end{bmatrix} = \begin{bmatrix} \mathbf{0} \\ 0 \\ 0 \end{bmatrix}, \mathbf{x} = \begin{bmatrix} \mathbf{X}_i \\ R \\ \Delta\lambda \end{bmatrix} \quad (6.41)$$

If only *one* backstress is considered, \mathbf{x} can be written as

$$\mathbf{x} = \begin{bmatrix} X_{xx} \\ X_{yy} \\ X_{zz} \\ X_{yz} \\ X_{xz} \\ X_{xy} \\ R \\ \Delta\lambda \end{bmatrix} \quad (6.42)$$

The solution \mathbf{x} is obtained as using Newton-Raphson iteration, so that $\{ {}^i\mathbf{x} \rightarrow {}^{i+1}\mathbf{x} \}_{i=1,2,\dots,n'}$ for i iterations. The procedure is drawn as

$$\mathbf{x} = \mathbf{x}^i + \boldsymbol{\xi} \quad \text{with} \quad \mathbf{J} \boldsymbol{\xi} = -\mathbf{G}[\mathbf{x}], \quad (6.43)$$

where \mathbf{J} is the Jacobian for $\mathbf{G}[\mathbf{x}]$

$$\mathbf{J} = \frac{d\mathbf{G}[\mathbf{x}]}{d\mathbf{x}} \quad (6.44)$$

The explicit expression of the Jacobian matrix, in case only one backstress is considered, is obtained as

$$\mathbf{J} = \begin{bmatrix} J_{11} & 0 & -\left(\sqrt{\frac{2}{3}} C \frac{(\boldsymbol{\sigma}^{dev} - \mathbf{X})}{|\boldsymbol{\sigma}^{dev} - \mathbf{X}|} - X_\gamma \right) \\ 0 & 1 + \Delta\lambda b & -b(R_\infty - R) \\ -\sqrt{\frac{3}{2}} \frac{(\boldsymbol{\sigma}^{dev} - \mathbf{X})}{|\boldsymbol{\sigma}^{dev} - \mathbf{X}|} & -1 & 0 \end{bmatrix} \quad (6.45)$$

where

$$J_{11} = \mathbf{I} - \Delta\lambda \left(-\sqrt{\frac{2}{3}} C \frac{1}{|\boldsymbol{\sigma}^{dev} - \mathbf{X}|} \left[\mathbf{I} - \frac{(\boldsymbol{\sigma}^{dev} - \mathbf{X}) \otimes (\boldsymbol{\sigma}^{dev} - \mathbf{X})}{|\boldsymbol{\sigma}^{dev} - \mathbf{X}|} \right] + \Delta\lambda \gamma \right) \quad (6.46)$$

The size dimension of the Jacobian is

Reminder:

\mathbf{I} is the 4th order identity tensor

\otimes is the symbol of the open tensorial product (it gives a tensor as a result, in this case a 4th rank tensor)

$$J = \begin{bmatrix} 6 \times 6 & 6 \times 1 & 6 \times 1 \\ 1 \times 6 & 1 \times 1 & 1 \times 1 \\ 1 \times 6 & 1 \times 1 & 1 \times 1 \end{bmatrix} \quad (6.47)$$

When *two backstresses* are considered the Jacobian is

$$J = \begin{bmatrix} J_{11} & J_{12} & 0 & -\left(\sqrt{\frac{2}{3}} C_1 \frac{(\sigma^{dev} - X)}{|\sigma^{dev} - X|} - X_1 \gamma_1\right) \\ J_{21} & J_{22} & 0 & -\left(\sqrt{\frac{2}{3}} C_2 \frac{(\sigma^{dev} - X)}{|\sigma^{dev} - X|} - X_2 \gamma_2\right) \\ 0 & 0 & 1 + \Delta\lambda b & -b(R_\infty - R) \\ -\sqrt{\frac{3}{2}} \frac{(\sigma^{dev} - X)}{|\sigma^{dev} - X|} & -\sqrt{\frac{3}{2}} \frac{(\sigma^{dev} - X)}{|\sigma^{dev} - X|} & -1 & 0 \end{bmatrix} \quad (6.48)$$

$$J_{ii} = I - \Delta\lambda \left(-\sqrt{\frac{2}{3}} C_i \frac{1}{|\sigma^{dev} - X|} \left[I - \frac{(\sigma^{dev} - X) \otimes (\sigma^{dev} - X)}{|\sigma^{dev} - X|^2} \right] + \gamma_i \right), \text{ with } i = 1, 2 \quad (6.49)$$

$$J_{ij} = -\Delta\lambda \left(-\sqrt{\frac{2}{3}} C_i \frac{1}{|\sigma^{dev} - X|} \left[I - \frac{(\sigma^{dev} - X) \otimes (\sigma^{dev} - X)}{|\sigma^{dev} - X|^2} \right] \right), \text{ with } i = 1, 2 \text{ and } i \neq j \quad (6.50)$$

Now, the size dimension of the Jacobian is

$$J = \begin{bmatrix} 6 \times 6 & 6 \times 6 & 6 \times 1 & 6 \times 1 \\ 6 \times 6 & 6 \times 6 & 6 \times 1 & 6 \times 1 \\ 1 \times 6 & 1 \times 6 & 1 \times 1 & 1 \times 1 \\ 1 \times 6 & 1 \times 6 & 1 \times 1 & 1 \times 1 \end{bmatrix} \quad (6.51)$$

Once the system is solved, the updated plastic strain is given by the associative flow rule written in BE formulation

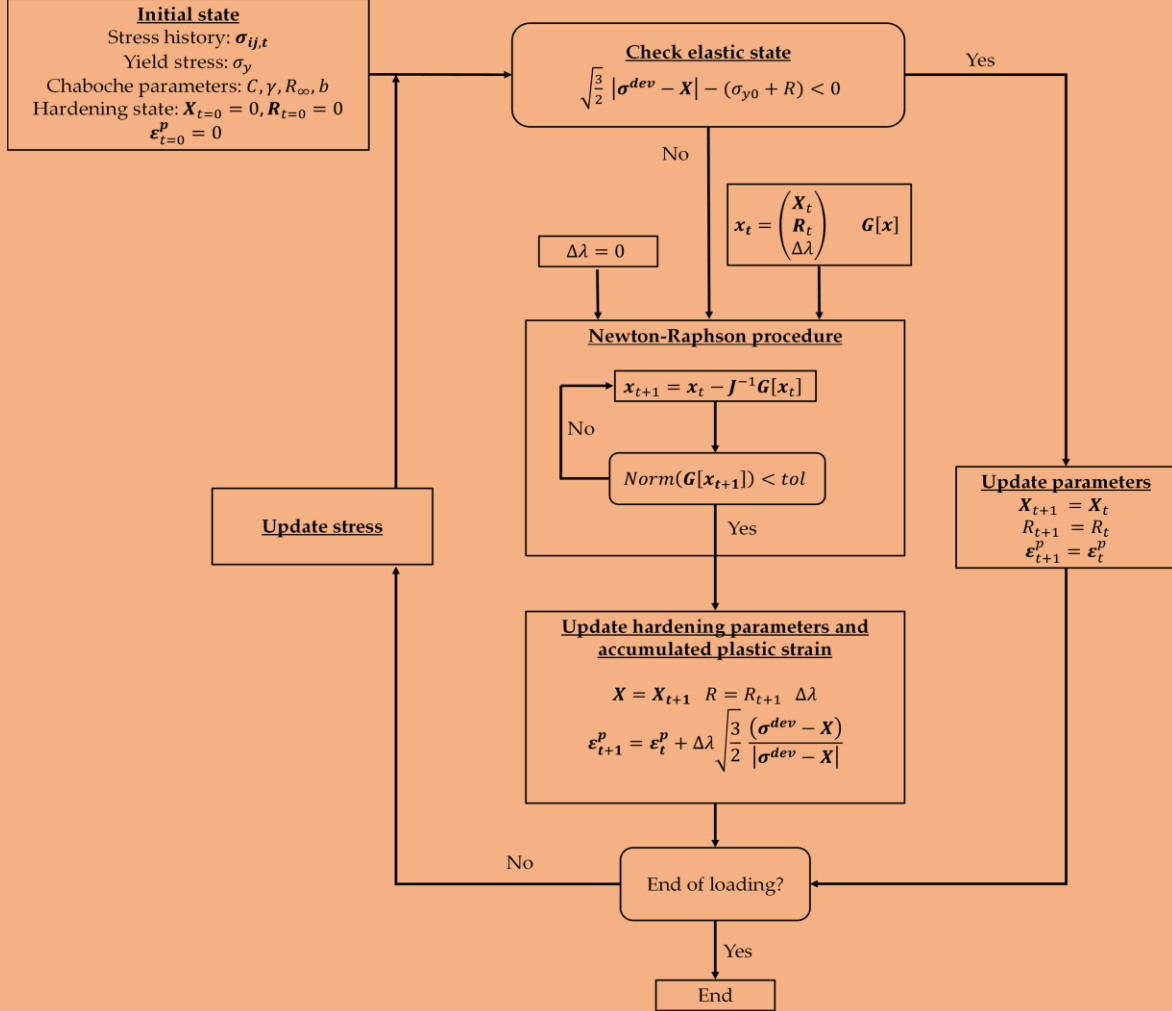
$$\epsilon^P = {}^n\epsilon^P + \Delta\lambda \sqrt{\frac{3}{2}} \frac{(\sigma^{dev} - X)}{|\sigma^{dev} - X|} \quad (6.52)$$

6.5 References

1. Gurtin ME, Fried E, Anand L. The mechanics and thermodynamics of continua. Cambridge University Press; 2010. <https://doi.org/10.1017/CBO9780511762956>.
2. Runesson K, Steinmann P, Ekh M, Menzel A. Constitutive modeling of engineering materials – theory and computation. Vol. I. 2006.
3. Runesson K. Constitutive Modeling of Engineering Materials – Theory and Computation. Chalmers University of Technology, Gteborg. 2006.
4. Niels Saabye Ottosen, Ristinmaa M. The mechanics of constitutive modelling. Elsevier; 2005. <https://doi.org/10.1016/B978-0-08-044606-6.X5000-0>.

5. Chaboche JL. A review of some plasticity and viscoplasticity constitutive theories. *Int J Plast.* 2008 Oct 1; 24(10):1642–93. <https://doi.org/10.1016/j.ijplas.2008.03.009>.
6. Chaboche JL. Constitutive equations for cyclic plasticity and cyclic viscoplasticity. *Int J Plast.* 1989; 5(3):247–302. [https://doi.org/10.1016/0749-6419\(89\)90015-6](https://doi.org/10.1016/0749-6419(89)90015-6).

PLASTIC STRAIN COMPUTATION



Total strain

Knowing the compliance matrix C of the material, the total strain ϵ can be obtained by adding the elastic strain ϵ^e to the plastic strain ϵ^p calculated through the above scheme

$$\epsilon_{ij} = \epsilon_{ij}^e + \epsilon_{ij}^p = (C_{ijkl} : \sigma_{kl}) + \epsilon_{ij}^p$$

Newton-Raphson method

Named after Isaac Newton and Joseph Raphson, it is also simply known as Newton's method. For more mathematical details about this method iteration, refer to (2). This is one of the most adopted iteration schemes to solve non-linear problems. We may summarise the main properties as follows:

1. This method works well both in loading and in unloading.
2. A fast convergence is provided.
3. Problem of convergence may occur close to peak points (the derivatives tend to zero).
4. Every iteration is costly in terms of time.

Multiaxial fatigue criteria

7

Contact mechanics produce a typical multiaxial problem with all the six Cauchy stress components involved. Multiaxial fatigue requires more attention to analyse than uniaxial fatigue. In the uniaxial condition, only the alternate stress amplitude is compared to the reduced fatigue limit (the fatigue limit corrected with the average stress, the stress concentration factors and so on). When more than one component is involved, the multiaxial state of stress is first related to the uniaxial fatigue limits. However, defining the middle value and the stress amplitude of six components is considerably more complicated.

7.1 High cycle fatigue criteria

High cycle fatigue (HCF) occurs under mostly elastic conditions. An initial elasto-plastic deformation may also occur, introducing residual stresses (elastic shakedown). Despite several HCF criteria that have been developed over decades of research, there is not yet a universally accepted approach. Different approaches were summarised by Papadopoulos et al. in (1). In the proposed code, two HCF criteria are implemented.

7.1.1 Crossland criterion

Crossland's approach (CR) (2), developed in 1956, is based on the stress invariants. For a general loading, it can be expressed as

$$\sigma_{eq,c} = \max_t \left[\sqrt{\frac{3}{2} \boldsymbol{\sigma}_a^{dev}(t) : \boldsymbol{\sigma}_a^{dev}(t)} \right] + c_c \max_t [\sigma_h(t)] < \sigma_{ec}, \quad (7.1)$$

where c_c and σ_{ec} are material parameters and σ_h is hydrostatic stress.

7.1.2 Dang Van criterion

The Dang Van (DV) criterion (3), developed in 1972, is a Tresca-type, which assumes that fatigue stems from damage induced at a critical plane. Also, it is one of the first criteria that addresses rotating principal stresses. For a general loading, this criterion can be formulated as

$$\sigma_{eq,DV} = \max_t \left[\sqrt{\frac{\sigma_{1,a}^{dev}(t) - \sigma_{3,a}^{dev}(t)}{2}} + c_{DV} \sigma_h(t) \right] < \sigma_{eDV} \quad (7.2)$$

where c_{DV} and σ_{eDV} are material parameters.

7.1.3 Deriving material parameters

A simple method to calibrate the material parameters in the equivalent stress criteria is using uniaxial fatigue data (fatigue limits in pulsating tension, alternating torsion and alternating bending). For example, one can write two equations, one for each uniaxial fatigue data chosen, and solve the system, whose unknowns will be c_C and σ_{eC} for Crossland or c_{DV} and σ_{eDV} for Dang Van.

However, neither of the criteria take volumetric or gradient effects into account. Therefore, the criteria will predict the same equivalent stresses for cases of alternating tension/compression as for alternating bending. Still, experimental tests reveal that $\sigma_{fl} \approx 0.8 \sigma_{flb}$, where σ_{fl} and σ_{flb} are the fatigue limit in tension/compression and in alternating bending, respectively. Therefore, the following suggestions can be adopted to account for the volumetric and gradient effects:

- If a large volume is subjected to a high equivalent stress, σ_{fl} and another uniaxial fatigue limit (the fatigue in pulsating tension σ_{flp} , for instance) are used.
- If only a small volume is subjected to high equivalent stresses, σ_{flb} and another fatigue (i.e. the pulsating bending fatigue) limit are employed.

In the literature (3–6), it is common to find the following results for the DV parameters:

$$c_{DV} = 3 \frac{\tau_{fl}}{\sigma_{flb}} - \frac{3}{2} \quad \sigma_{eDV} = \tau_{fl} \quad (7.3)$$

or

$$c_{DV} = \frac{3}{2} \frac{\sigma_{fl} - \sigma_{flp}}{\sigma_{flp} - \sigma_{fl}}, \quad (7.4)$$

where τ_{fl} is the fatigue life in torsion. For steels, c_{DV} is roughly equal to 1/3.

7.1.4 Mean and alternate stress in multiaxial case

Consider the stress tensor $\boldsymbol{\sigma}$ acting on an elementary volume of the body and a plane passing through the point of the volume being studied. We can denote \mathbf{t} as the stress vector acting on this plane:

$$\mathbf{t} = \boldsymbol{\sigma} \cdot \mathbf{n} \quad (7.5)$$

\mathbf{t} can be divided into two components: the normal stress σ_n and the shear stress $\boldsymbol{\tau}$. σ_n is the projection of \mathbf{t} on the normal vector to the plane and, for a time-dependent cyclic load, it is a scalar quantity. Therefore, the definition of the amplitude of σ_n is straightforward, both the mean and the maximum quantity. $\boldsymbol{\tau}$ is the orthogonal projection of \mathbf{t} on the plane (FIGURE 7.1).

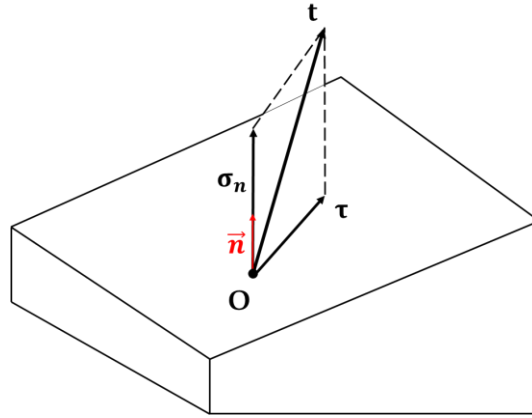


Figure 7.1 – Normal stress and shear stress acting on a material plane. O is the application point of the vector \mathbf{t}

The definition of the amplitude and the mean value of τ is a complex problem because both the amplitude and the direction of the shear stress vector vary with time. Ψ represents the path described by the tip of τ during a cyclic load. To define the amplitude and the mean stress, one must first construct the minimum circumscribed circle to the curve Ψ . The mean value of the shear stress is given by the length of the vector that defines the centre of the circle, while the radius of the circle defines the amplitude of the shear stress (FIGURE 7.2).

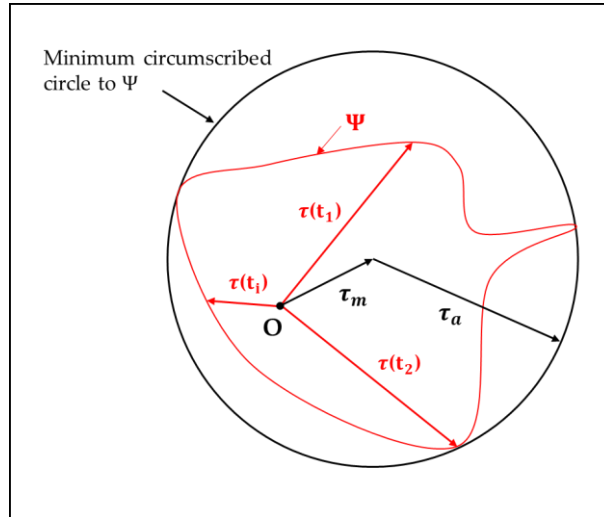


Figure 7.2 – Definition of shear strain amplitude through the construction of the minimum circumscribed circle to curve Ψ

7.1.5 HCF general procedure

The general approach to derive equivalent stresses is the following:

- I. In the material point studied, calculate the stress tensor at each instant in time.
- II. Derive the hydrostatic and the deviatoric part of the stress tensor.
- III. Derive the mean value of the deviatoric stress tensor. One way to find it is to apply an optimisation algorithm to the following min-max problem

$$\min \left\{ \max_t \left\| \sigma_{ij}^{dev}(t) - \sigma_{ij,mid}^{dev}(t) \right\| \right\} \quad (7.6)$$

A suitable choice is to take the norm $\|\cdot\|$ as the von Mises norm. Thus, the von Mises norm is calculated for every instant in time. $\sigma_{ij,mid}^{dev}(t)$ is obtained through an iteratively improved guess. The

algorithm will find the value of $\sigma_{ij,mid}^{dev}$ that makes the largest von Mises stress occurring during the period studied as small as possible. The main issue with this method is that it does not guarantee that $\sigma_{ij,mid}^{dev}$ is indeed deviatoric, but enforcing $\sigma_{kk,mid}^{dev} = -(\sigma_{ii,mid}^{dev} + \sigma_{jj,mid}^{dev})$ ensures this.

- IV. For every instant in time, calculate the amplitude of the deviatoric stress tensor

$$\sigma_{ij,a}^{dev} = \sigma_{ij}^{dev}(t) - \sigma_{ij,mid}^{dev} \quad (7.7)$$

- V. (DV) Calculate the amplitude of the Tresca shear stress for every instant in time

$$\tau_{Tr,a}(t) = \frac{\sigma_{1,a}^{dev} - \sigma_{3,a}^{dev}}{2}, \quad (7.8)$$

Where $\sigma_{1,a}^{dev}$ and $\sigma_{3,a}^{dev}$ are the smallest and the largest principal value of $\sigma_{ij,a}^{dev}$, respectively.

- (CR) Evaluate the von Mises stress for every instant in time

$$\sigma_{VM,a}(t) = \sqrt{\frac{3}{2} \boldsymbol{\sigma}_a^{dev}(t) : \boldsymbol{\sigma}_a^{dev}(t)} \quad (7.9)$$

- VI. Evaluate the equivalent stress

$$(DV) \quad \sigma_{eq,DV}(t) = \tau_{Tr,a}(t) + c_{DV} \sigma_h(t) \quad (7.10)$$

$$(CR) \quad \sigma_{eq,C}(t) = \sigma_{VM,a}(t) + c_C \sigma_{h,max} \quad (7.11)$$

- VII. The largest equivalent stress is employed, and fatigue initiation occurs if

$$(DV) \quad \sigma_{eq,DV} = \max_t [\sigma_{eq,DV}(t)] > \sigma_{eDV} \quad (7.12)$$

$$(CR) \quad \sigma_{eq,C} = \max_t [\sigma_{eq,C}(t)] > \sigma_{eC} \quad (7.13)$$

- VIII. Evaluate the safety factor

$$SF = \frac{\sigma_e}{\sigma_{eq}} \quad (7.14)$$

7.2 Low cycle fatigue criteria

Low cycle fatigue (LCF) is almost always limited to cases of limited fatigue life and is related to the amount of plastic flow accumulated during the loading cycles. The LCF criteria define fatigue life as a function of the strain. The most common uniaxial LCF criterion is given by the Manson-Coffin curve (6)

$$\varepsilon_a = \frac{\sigma_f'}{E} (2N_f)^b + \varepsilon_f' (2N_f)^c \quad (7.15)$$

where E is Young's modulus, and σ_f' , ε_f' , b and c are material parameters to be determined from fatigue tests. N_f is the estimated fatigue life.

7.2.1 Jiang-Sehitoglu criterion

The Jiang-Sehitoglu (JS) criterion (7) is a combination of an energy approach (such as Crossland) and critical plane approach. The JS parameter FP is identified as follows

$$FP = \left\langle \frac{\Delta \epsilon}{2} \sigma_{max} \right\rangle + c_{JS} \Delta \tau \Delta \gamma \quad (7.16)$$

The criterion is evaluated on any planes where σ_{max} is the maximum normal stress on the plane, $\Delta \epsilon$ is the range of the normal strain acting on the plane, and $\Delta \gamma$ and $\Delta \tau$ are the ranges of the (engineering) strain and shear stress, respectively. Note that the first term is the same as the SWT (Smith-Watson-Topper) parameter. The fatigue life is then evaluated from

$$(FP - FP_0)^d N_f = J, \quad (7.17)$$

where N_f is the fatigue life, and FP_0 , J and d are material parameters.

7.2.1 JS general procedure

- I. Evaluate stress and strain tensors at each instant in time for the time period to be studied.
- II. In each material point, loop through all planes of interest. In all planes, evaluate normal and shear stress and strain.
- III. For the normal component evaluate

$$\sigma_{max} = \max_t [\sigma_n(t)] \quad (7.18)$$

$$\Delta \epsilon = \max_t [\epsilon_n(t)] - \min_t [\epsilon_n(t)] \quad (7.19)$$

- IV. Evaluate $\Delta \gamma$ and $\Delta \tau$ according to FIGURE 7.3.

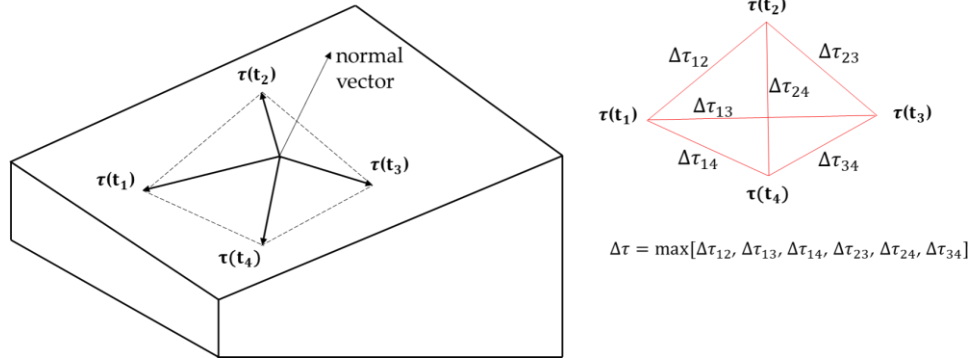


Figure 7.3 – Evaluation of shear stress range $\Delta \tau$. Example with stresses evaluated at four instants in time. The shear strain range is evaluated in the same way.

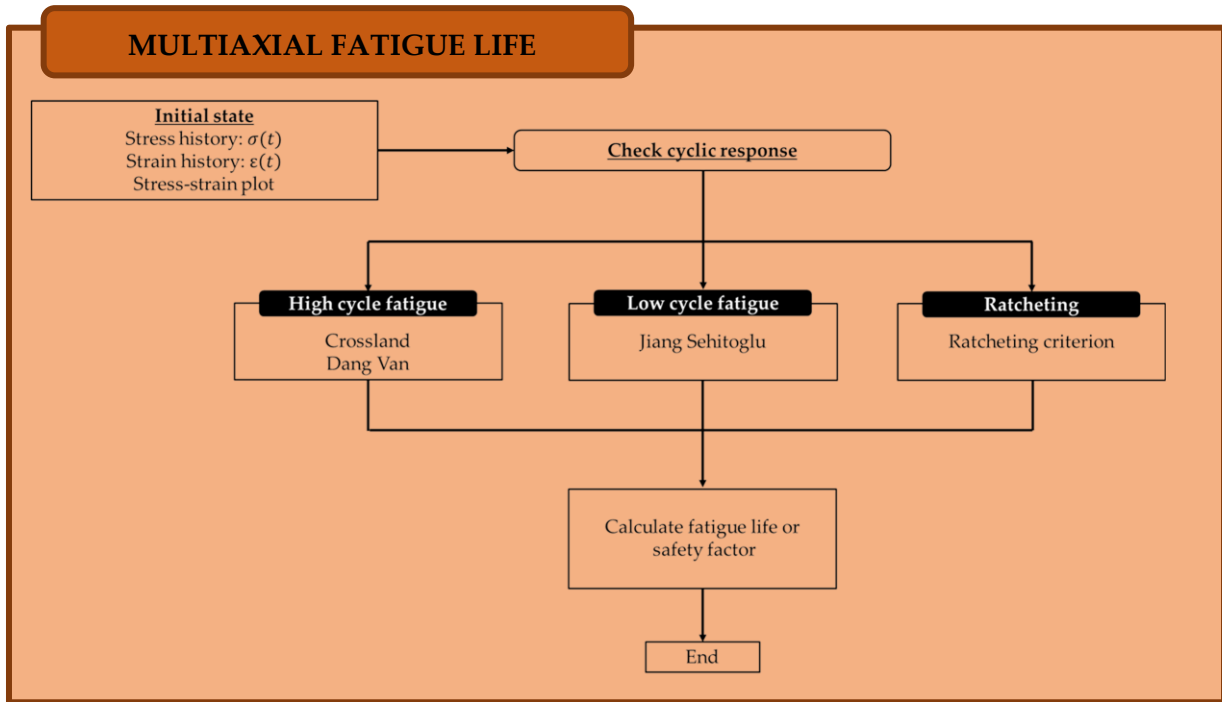
- V. Evaluate the JS parameter.
- VI. Evaluate the fatigue life N_f from the equation (7.17).

7.3 Ratcheting

If ratcheting is the dominating damage mechanism, the following criterion proposed by Kapoor (8) may be employed

$$\sum_i \varepsilon_i < \varepsilon_c, \quad (7.21)$$

where ε_i is the current strain increment, and ε_c is the fracture strain. ε_i needs to consider the multiaxial state of strain.



7.4 References

1. Papadopoulos I V., Davoli P, Gorla C, Filippini M, Bernasconi A. A comparative study of multiaxial high-cycle fatigue criteria for metals. *Int J Fatigue*. 1997 Mar 1; 19(3):219–35. [https://doi.org/ 10.1016/S0142-1123\(96\)00064-3](https://doi.org/10.1016/S0142-1123(96)00064-3).
2. Crossland B., in *Proc. Int. Conf. on Fatigue of Metals*, Institution of Mechanical Engineers, London, 1956, 138-139.
3. Dang Van K., *Sur la résistance à la fatigue des métaux*, Thèses de Doctorat ès Sciences, Sci. Techniq. l'Armement, 1973, 47, 647.
4. Desimone H, Bernasconi A, Beretta S. On the application of Dang Van criterion to rolling contact fatigue. *Wear*. 2006 Feb 24; 260(4–5):567–72. <https://doi.org/10.1016/j.wear.2005.03.007>.
5. Ekberg A. Rolling contact fatigue of railway wheels—a parametric study. *Wear*. 1997 Nov; 211(2):280–8. [https://doi.org/ 10.1016/S0043-1648\(97\)00106-3](https://doi.org/10.1016/S0043-1648(97)00106-3).

6. Ciavarella M, Monno F. A comparison of multiaxial fatigue criteria as applied to rolling contact fatigue. Tribol Int. 2010 Nov; 43(11):2139–44. <http://dx.doi.org/10.1016%2Fj.triboint.2010.06.003>.
7. Ciavarella M, Maitournam H. Letter to the Editor On the Ekberg , Kabo and Andersson calculation of the Dang Van high. Fatigue Fract E ngng Mater S truct. 2004; 523–8. <http://dx.doi.org/10.1111/j.1460-2695.2004.00772.x>.
8. Kapoor A. A re-evaluation of the life to rapture of ductile metals by cyclic plastic strain. Fatigue Fract E ngng Mater S truct. Feb 1994; 17-2. <https://doi.org/10.1111/j.1460-2695.1994.tb00801.x>

8

Wear

8.1 Modelling wear

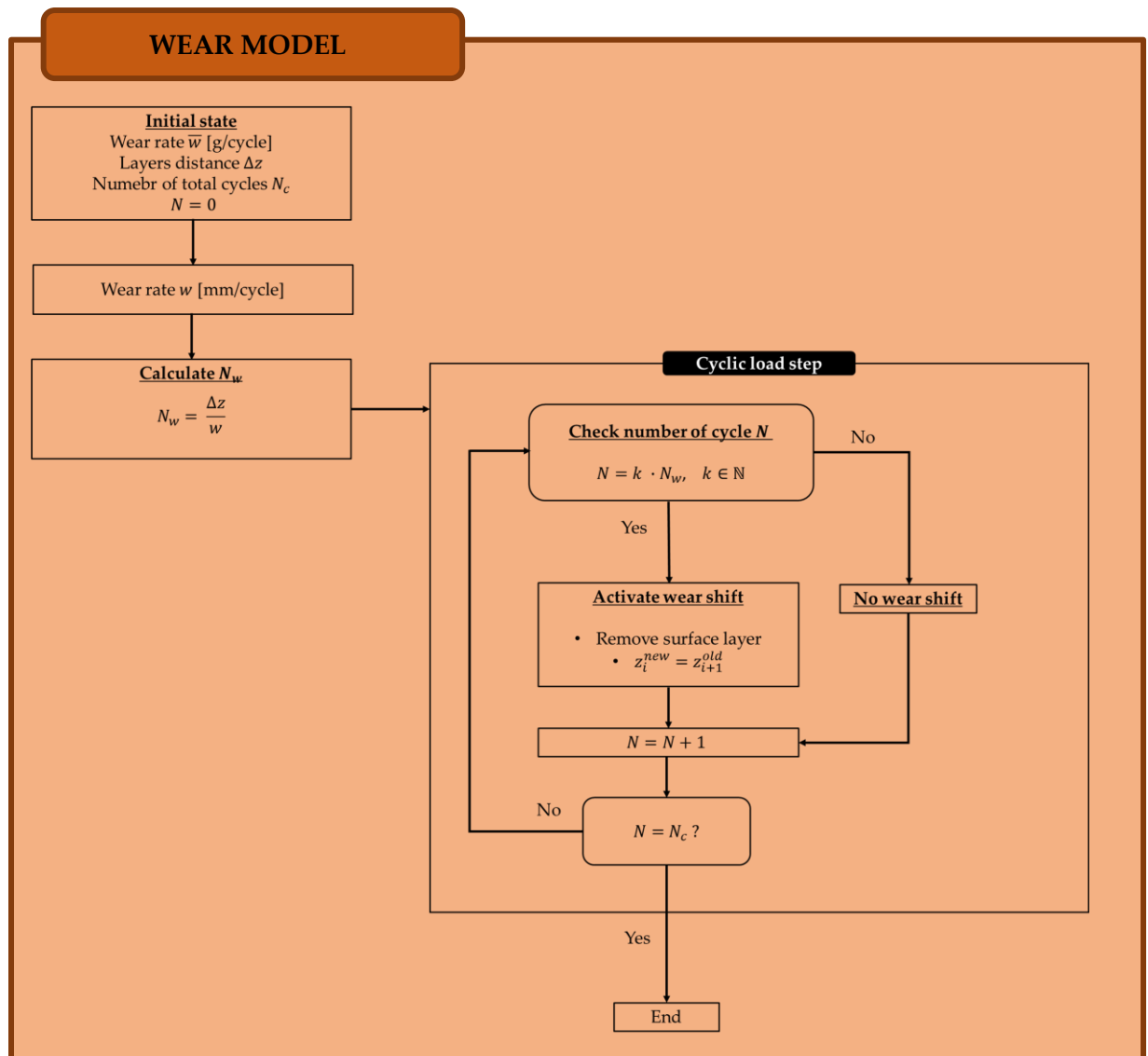
The wear phenomenon is already implemented in the cyclic plasticity code. The proposed wear model is very simple, and it should only be applied in the line contact (2D) case.

Wear is considered an independent phenomenon (1), which gradually removes layers of material from the surface and influences the plastic strain accumulation process. The wear rate w is a given in the problem and is supposed to be constant through all the simulations. Combined with the distance between the horizontal layers Δz , the wear rate allows us to calculate the number of cycles N_w necessary to remove the first layer, whose thickness is equal to the distance between two horizontal lines in the nodes grid. After the first layer is removed, all the layers below shift towards the surface (the second layer becomes the surface layer, the third layer the second one, and so on). At this point, the new surface layer has the plastic strain of the previous second layer, but it will undergo the cyclic load acting on the surface plane; the same reasoning is applied to the layers below.

The distance between two horizontal layers will play a fundamental role in the convergence of the problem since larger distances will predict smaller and smaller plastic deformations (the convergence problem will be assessed in the following chapter).

This approach has the following three issues:

- The wear rate must be known a priori, from experimental tests, for example.
- The wear rate is constant, which is not always true, although it applies to the cases in this investigation.
- This model is suitable for line contact problems, where the removal of material is roughly uniform over the contact body.



8.2 References

1. Mazzù A. A simplified non-linear kinematic hardening model for ratchetting and wear assessment in rolling contact. J Strain Anal Eng Des. 2008; 43(5):349–60. <https://doi.org/10.1243%2F03093247JSA405>.

9

Simulations

This chapter suggests solving some railway contact problems by means of the concepts introduced in the previous chapters. Before turning to the simulations, we remind that at this stage, the proposed solutions are only meant to understand the pros and cons of the semi-numerical model and not to obtain an exact solution of the problem.

9.1 Hertzian contact and elastic stress quantities

Both the full-scale and small-scale-bi-disk problems are proposed (see FIGURE 9.1 for the schematic of the models). TABLE 9.1 shows the geometrical and material parameters of the bodies in contact and the solution of the respective Hertzian problems. The two bodies are assumed to be the wheel and the rail.

For simplicity, we only show the results referring to the contact pressure 1100 MPa, but the same conclusions can be drawn for the higher pressure.

The trends of the contact pressure on the xz -plane and the yz -plane (the latter only for the general contact) are illustrated in FIGURE 9.2 and FIGURE 9.3. The tangential load is shown as well, which is calculated by assuming full-slip condition and applying different friction coefficients (0.1, 0.2, 0.3 and 0.5).

Once the pressure and the tangential load are found, we can move on the elastic stress computation problem. FIGURES 9.3-14 show the dimensionless stress quantities for the line and the general contact for friction set to 0, 0.3 and 0.5. The coordinates x and z are made dimensionless by dividing them by the semi-contact length a . As far as the general contact concerned, the results are shown for values of $z/a \gtrsim 0.18$, i.e. the area not affected by the singularity points in Boussinesq-Cerruti's equations.

Finally, FIGURE 9.16 and FIGURE 9.17 show the stress components near the surface ($z/a \approx 0.18$) and at the depth $z/a \approx 0.5$.

The out-of-plane shear components τ_{xy} and τ_{yz} are not represented in the figures because they are negligible in the rolling plane.

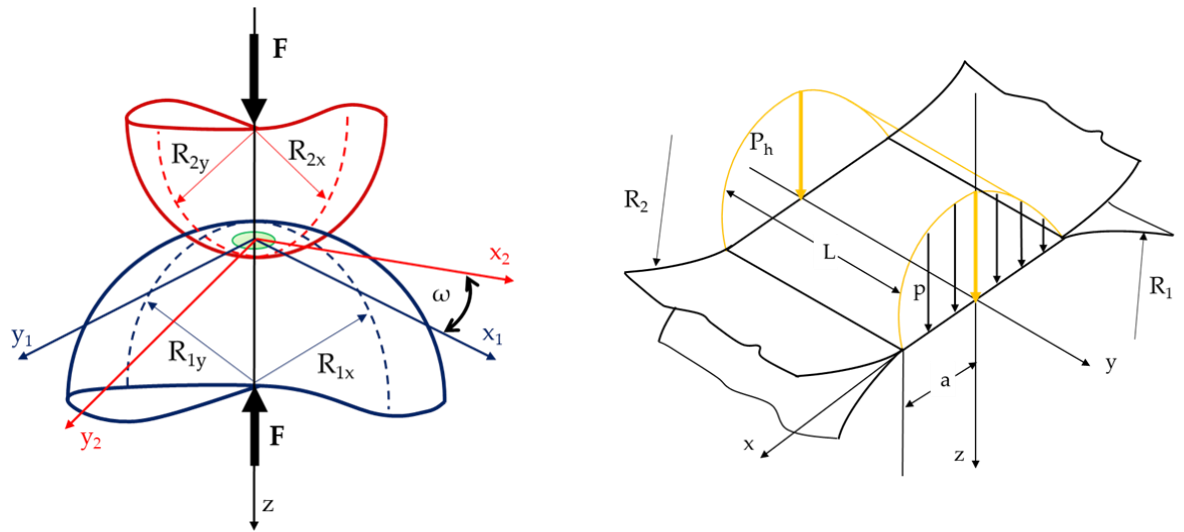


Figure 9.1 – Schematic representation of the general and the line contact

Table 9.1 – Geometrical properties of the adopted models, elastic properties and results of the Hertzian problem

SMALL-SCALE		FULL-SCALE	
Line contact		General contact	
R_{1x} [mm]	40	R_{1x} [mm]	440
R_{1y} [mm]	Inf	R_{1y} [mm]	Inf
R_{2x} [mm]	30	R_{2x} [mm]	Inf
R_{2y} [mm]	Inf	R_{2y} [mm]	300
L [mm]	15	ω [rad]	0
E [MPa]	206 000	E [MPa]	206 000
ν	0.3	ν	0.3
F [N]	6860	F [N]	70 000
a [mm]	0.33	a [mm]	6.26
c [mm]	7.50	c [mm]	4.85
p_H [MPa]	1100	p_H [MPa]	1100
F [N]	23 000		
a [mm]	0.55		
c [mm]	7.50		
p_H [MPa]	1800		

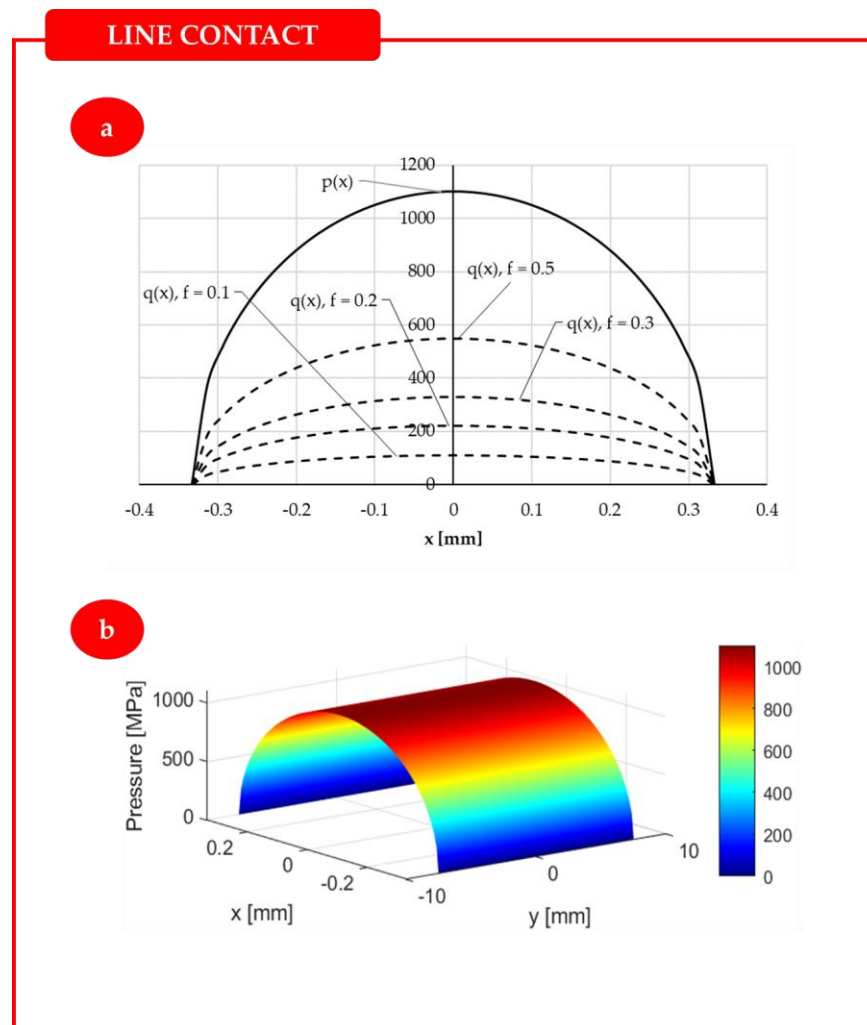


Figure 9.2 – Hertzian pressure distribution in the line contact problem

ELLIPTICAL CONTACT

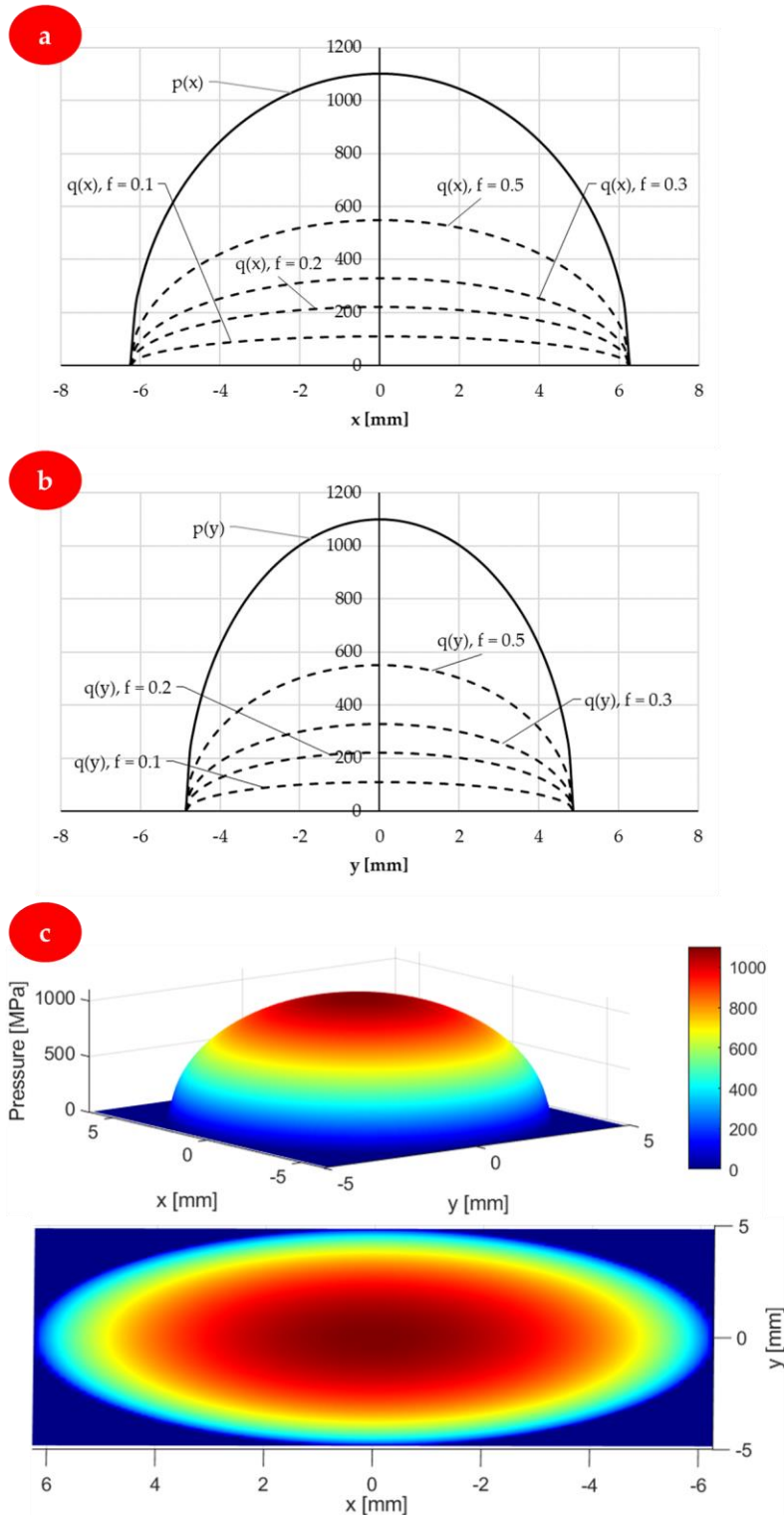


Figure 9.3 – Hertzian pressure distribution in the elliptical contact problem: (a) contact loading in direction x in MPa; (b) contact loading in direction y in MPa; (c) 3D pressure plot and contour plot.

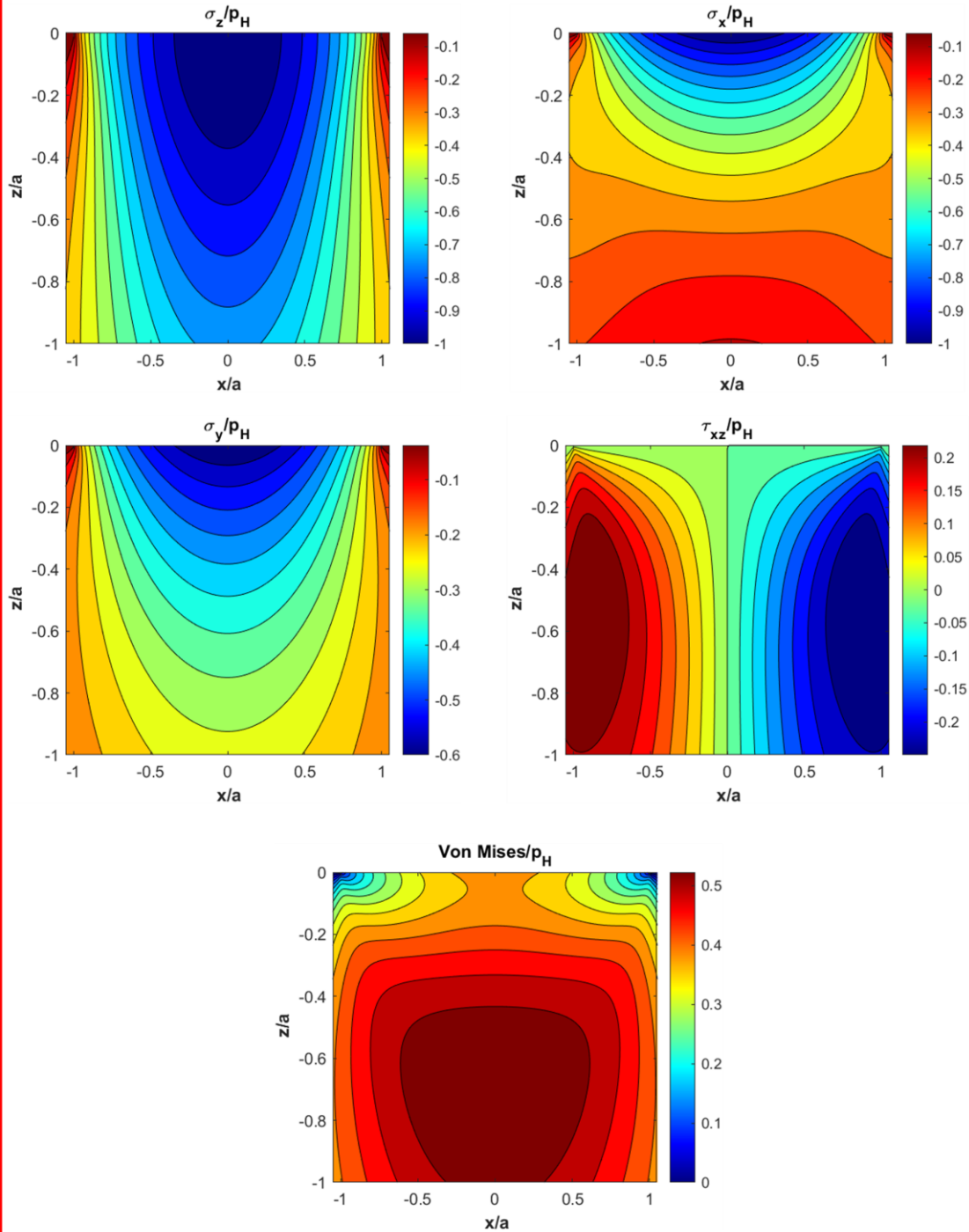
LINE CONTACT, FRICTION 0


Figure 9.4 – Elastic stresses and von Mises contours in the plane $y = 0$ (friction coefficient $f = 0$, $p_H = 1100$ MPa (line contact))

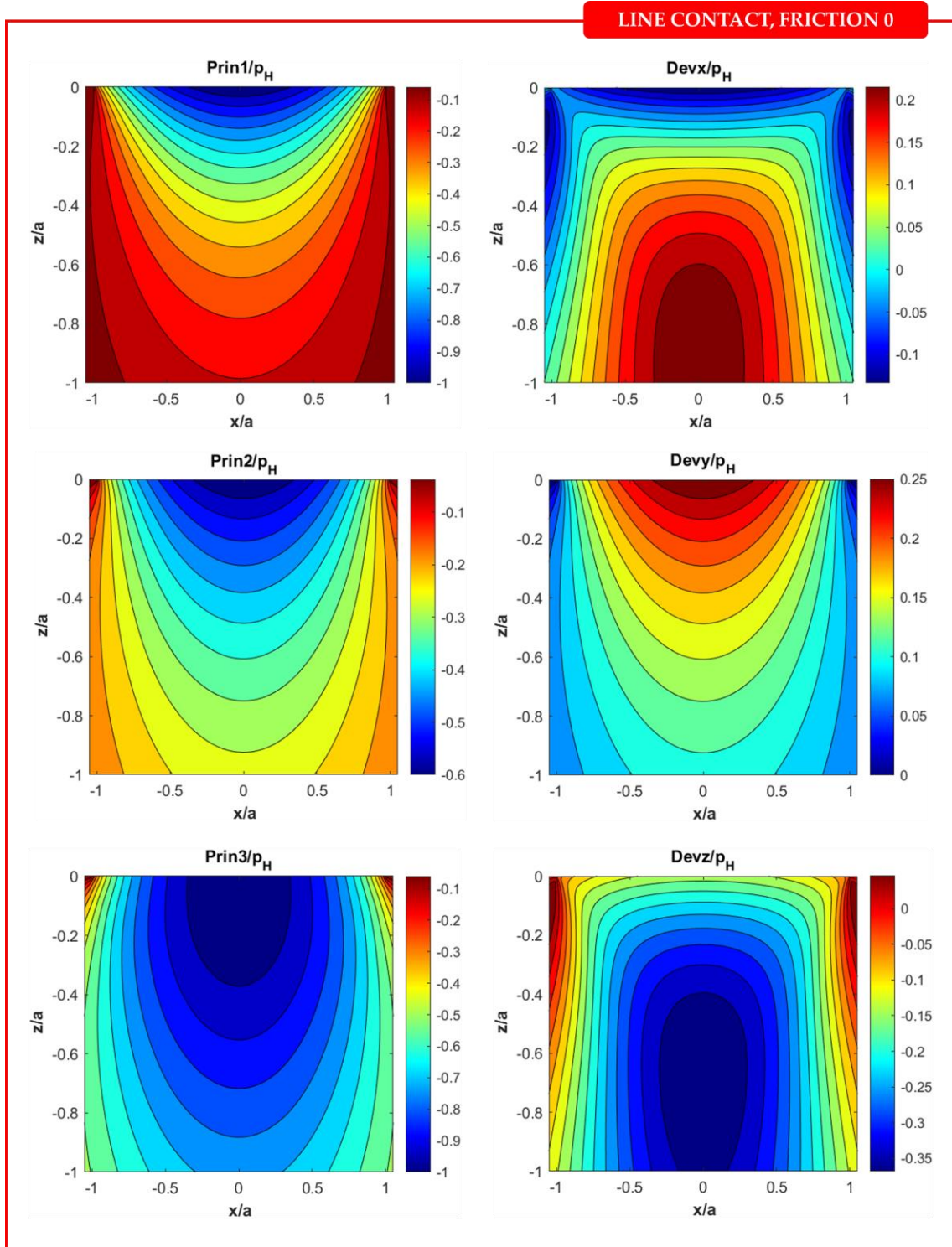


Figure 9.5 – Principal stresses and deviatoric stresses contours in the plane $y = 0$ (friction coefficient $f = 0$, $p_H = 1100$ MPa (line contact))

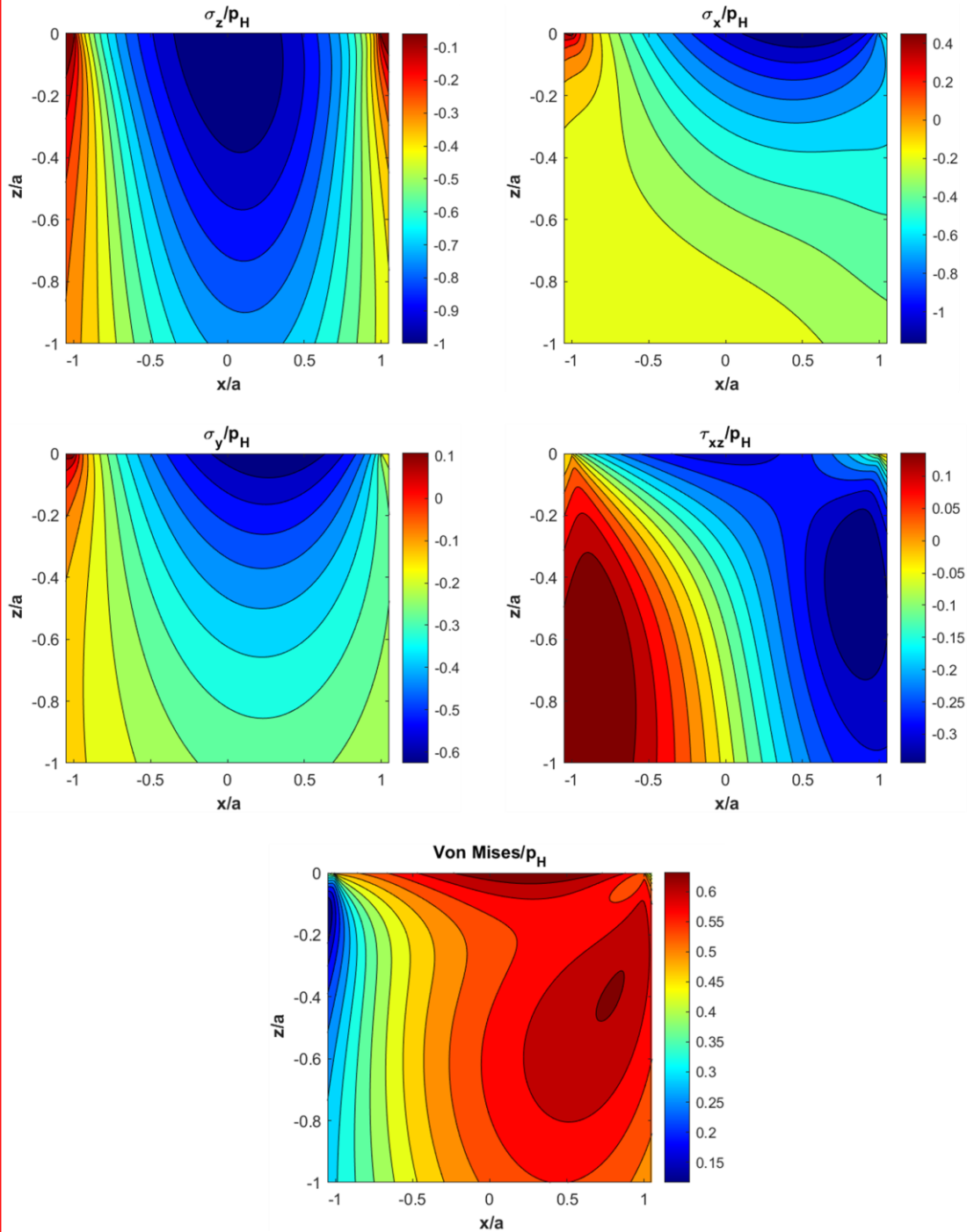
LINE CONTACT, FRICTION 0.3


Figure 9. 6 – Elastic stresses and von Mises contours in the plane $y = 0$ (friction coefficient $f = 0.3$, $p_H = 1100$ MPa (line contact))

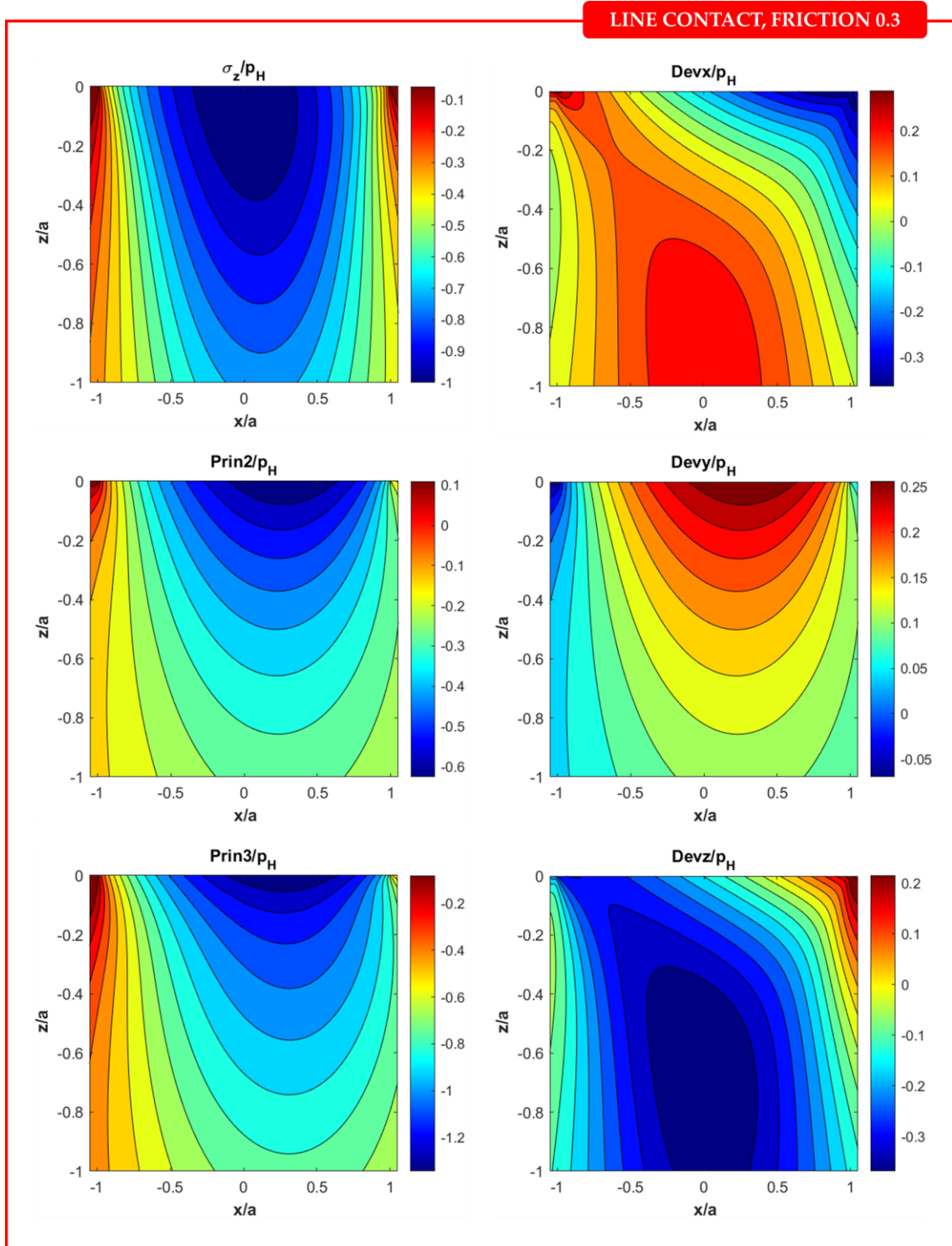


Figure 9.7 – Principal stresses and deviatoric stresses contours in the plane $y = 0$ (friction coefficient $f = 0.3$, $p_H = 1100$ MPa (line contact))

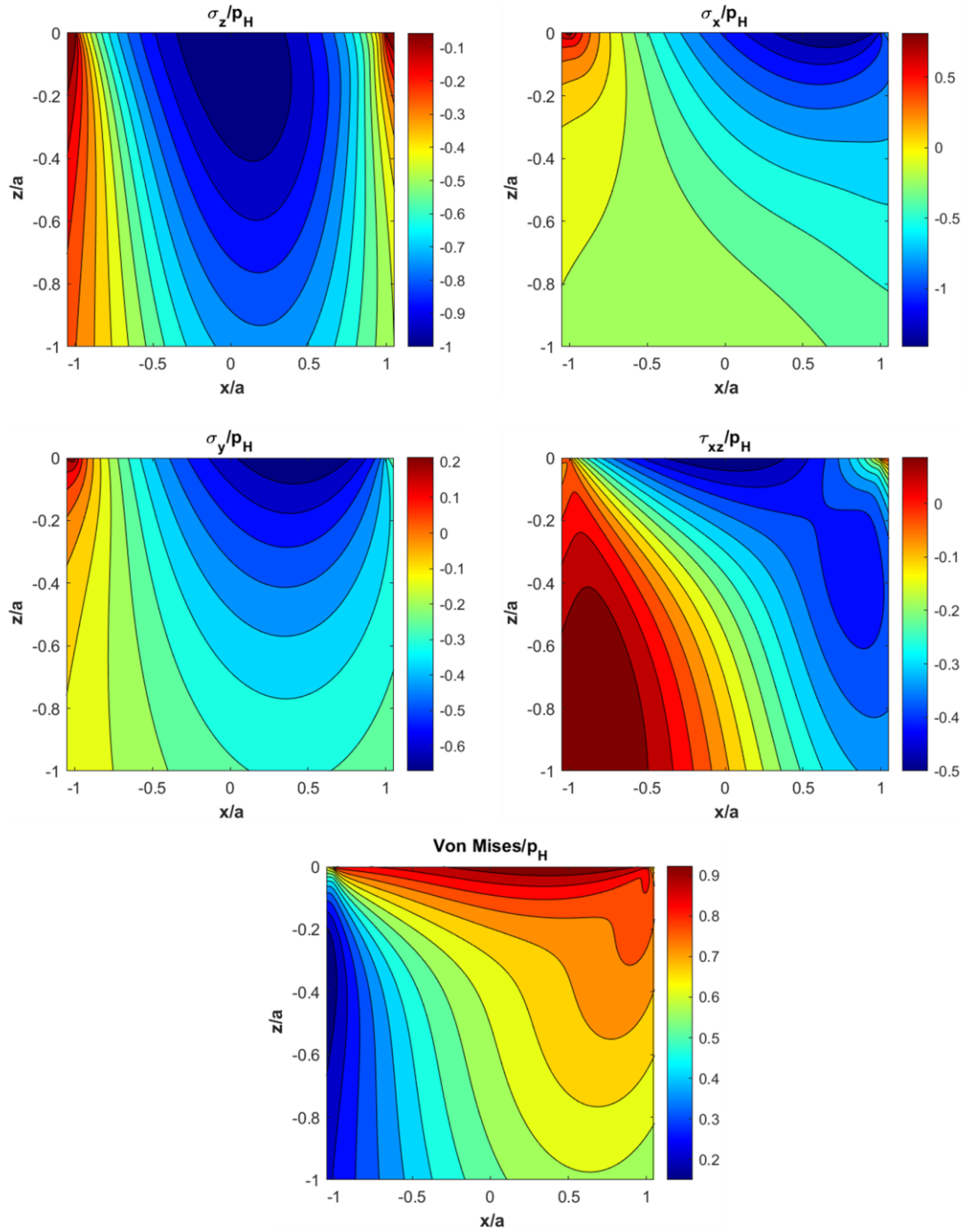
LINE CONTACT, FRICTION 0.5


Figure 9.8 – Elastic stresses and von Mises contours in the plane $y = 0$ (friction coefficient $f = 0.5$, $p_H = 1100$ MPa (line contact))

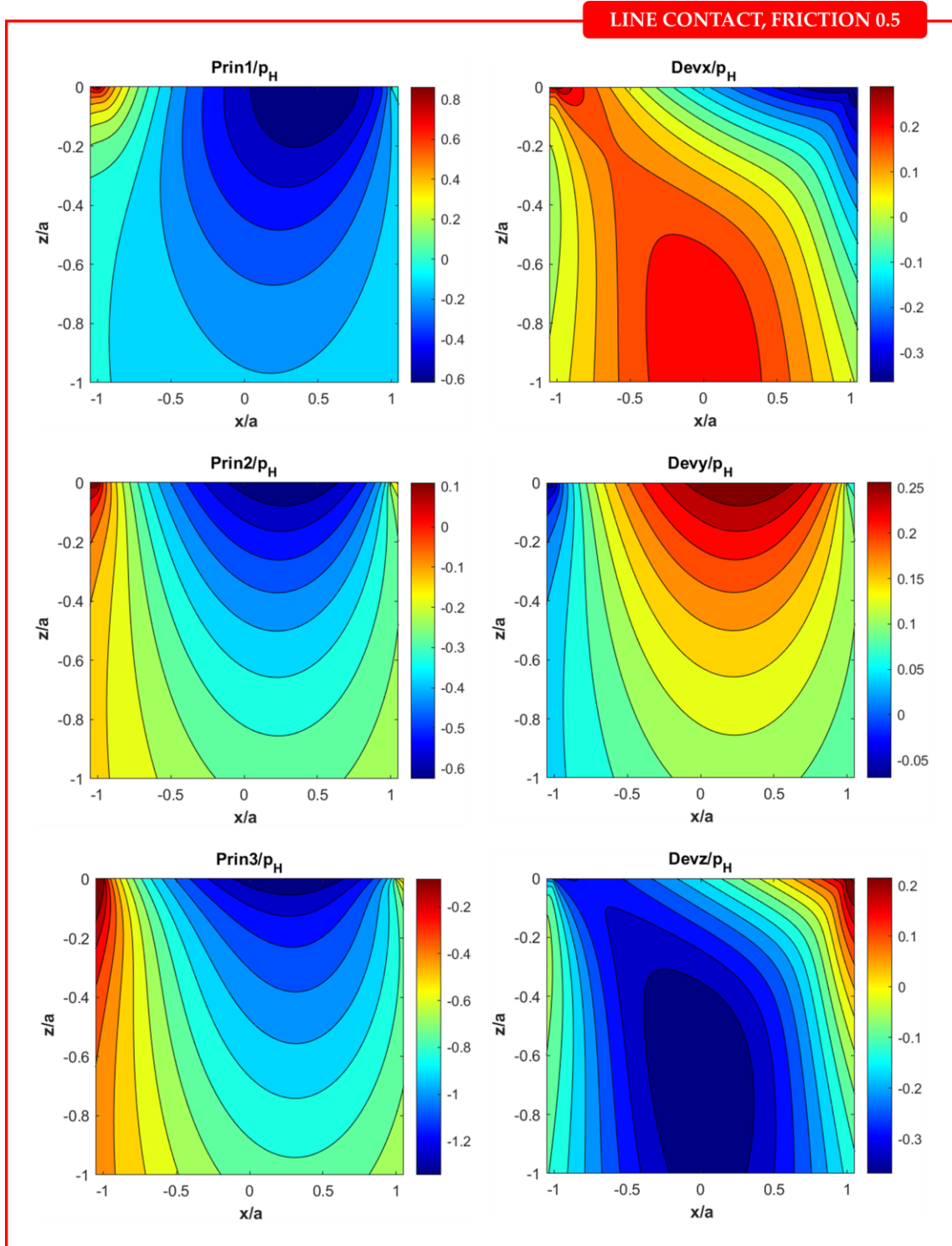


Figure 9.9 – Principal stresses and deviatoric stresses contours in the plane $y = 0$ (friction coefficient $f = 0.5$, $p_H = 1100$ MPa (line contact))

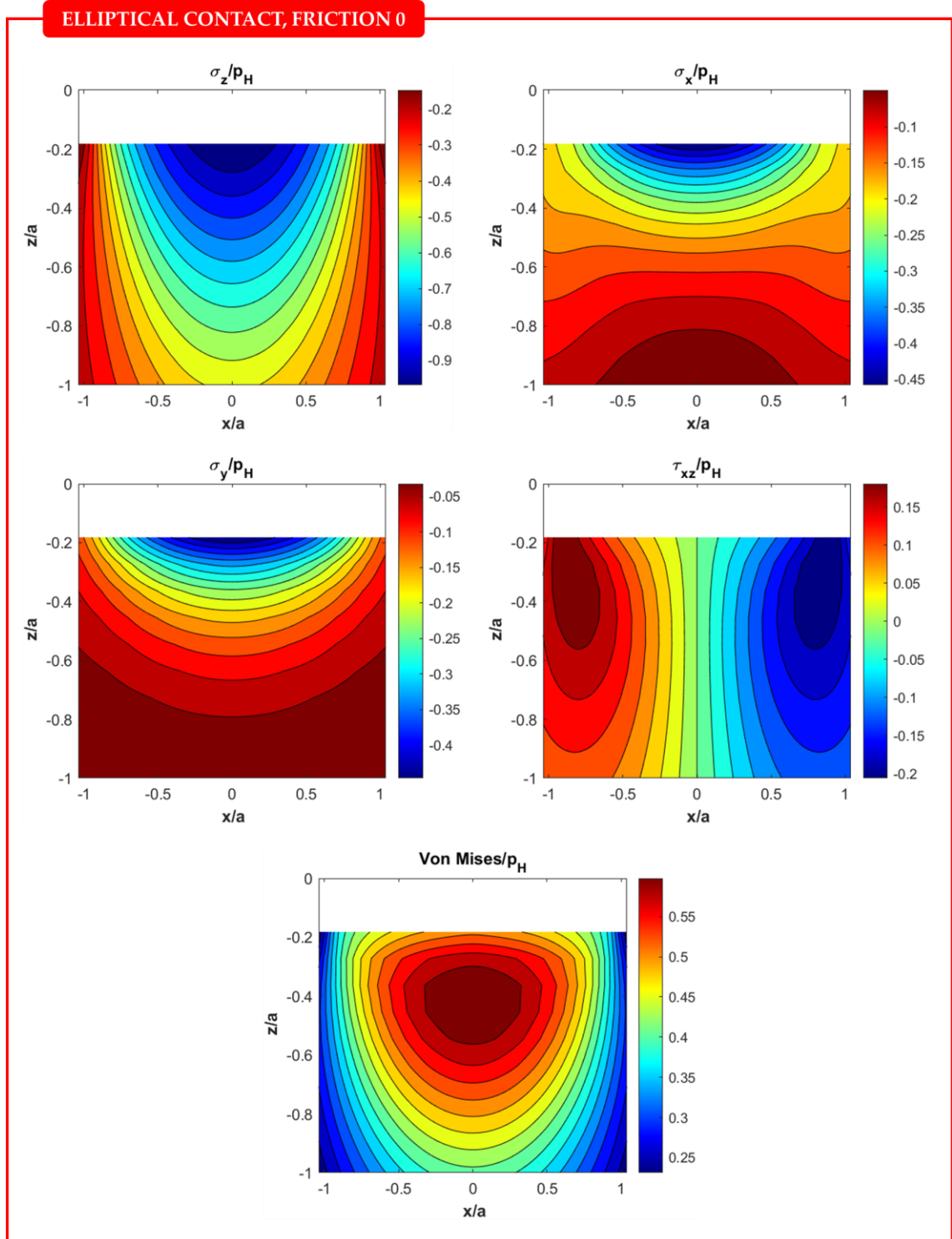


Figure 9.10 – Elastic stresses and von Mises contours in the plane $y = 0$ (friction coefficient $f = 0$, $p_H = 1100$ MPa (elliptical contact))

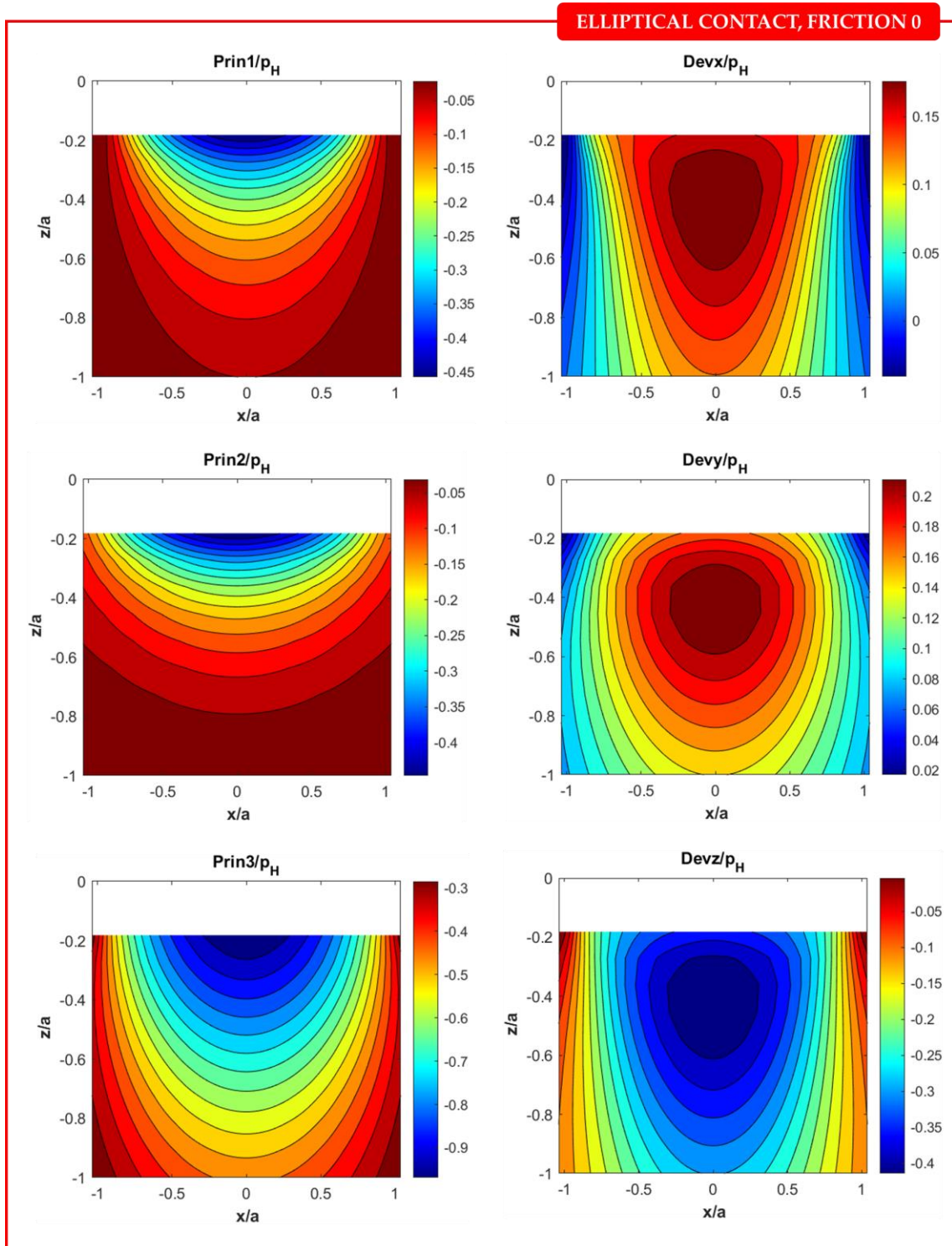


Figure 9.11 – Principal stresses and deviatoric stresses contours in the plane $y = 0$ (friction coefficient $f = 0$, $p_H = 1100$ MPa (elliptical contact))

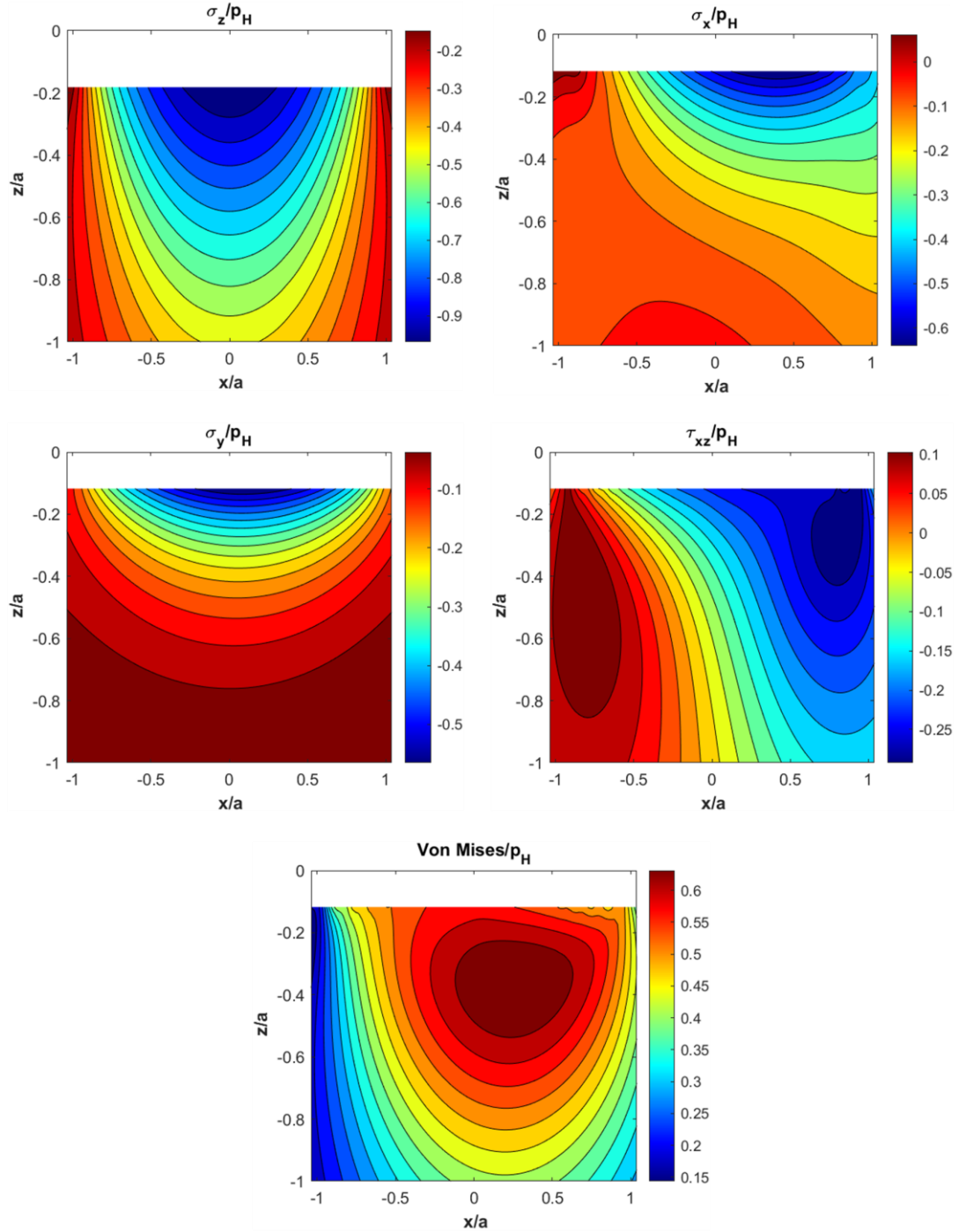
ELLIPTICAL CONTACT, FRICTION 0.3


Figure 9.12 – Elastic stresses and von Mises contours in the plane $y = 0$ (friction coefficient $f = 0.3$, $p_H = 1100$ MPa (elliptical contact))

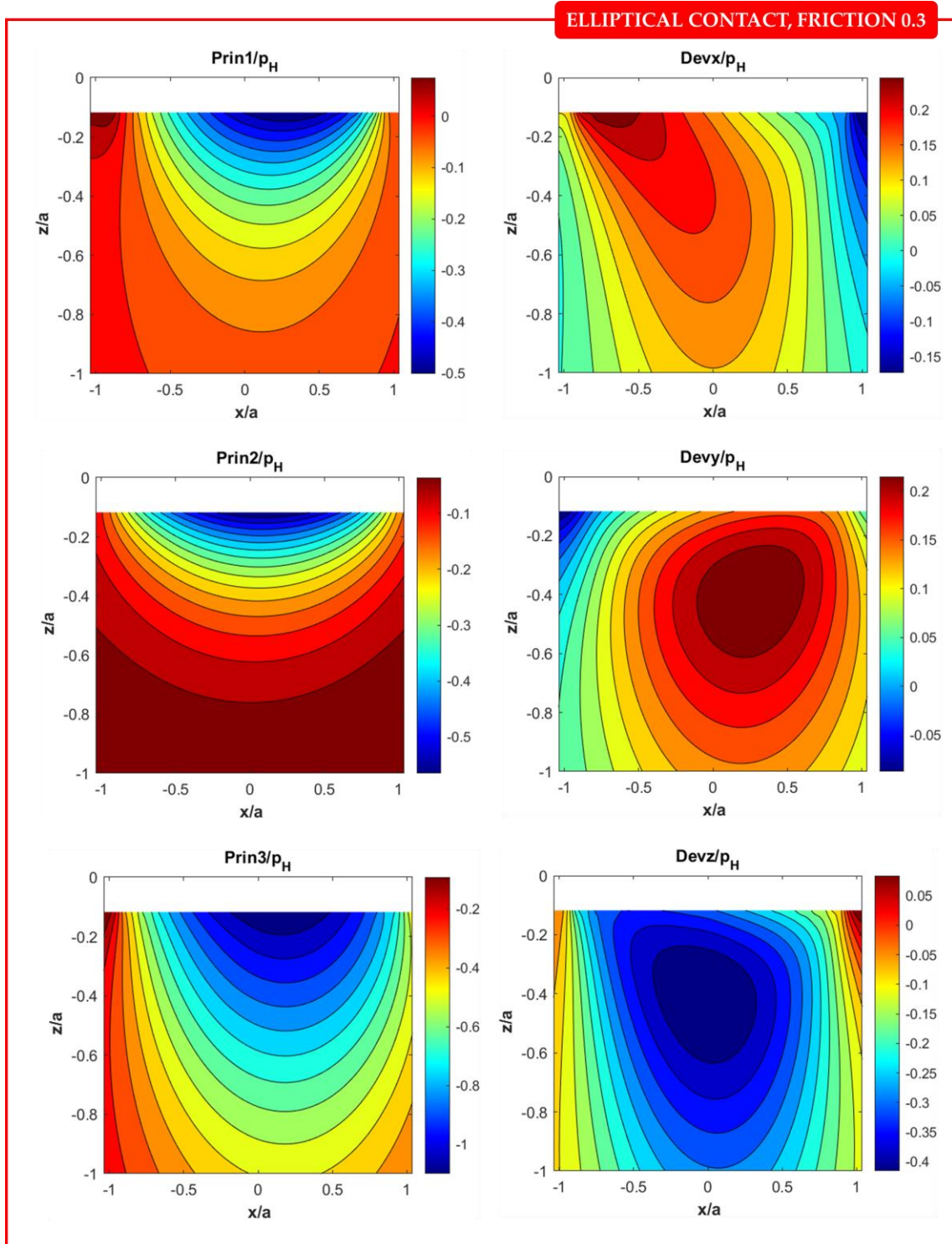


Figure 9.13 – Principal stresses and deviatoric stresses contours in the plane $y = 0$ (friction coefficient $f = 0.3$, $p_H = 1100$ MPa (elliptical contact))

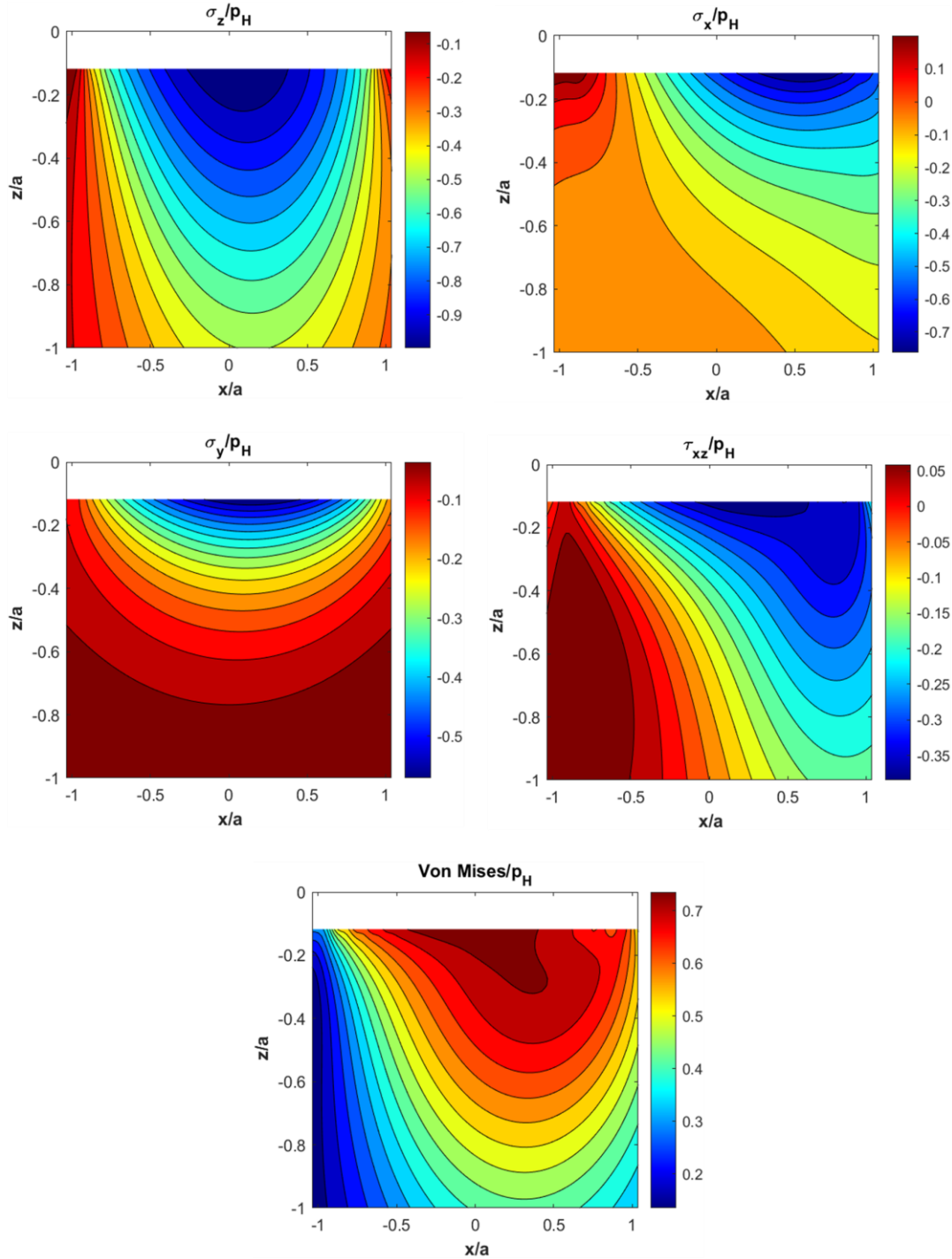
ELLIPTICAL CONTACT, FRICTION 0.5


Figure 9.14 – Elastic stresses and von Mises contours in the plane $y = 0$ (friction coefficient $f = 0.5$, $p_H = 1100$ MPa (elliptical contact))

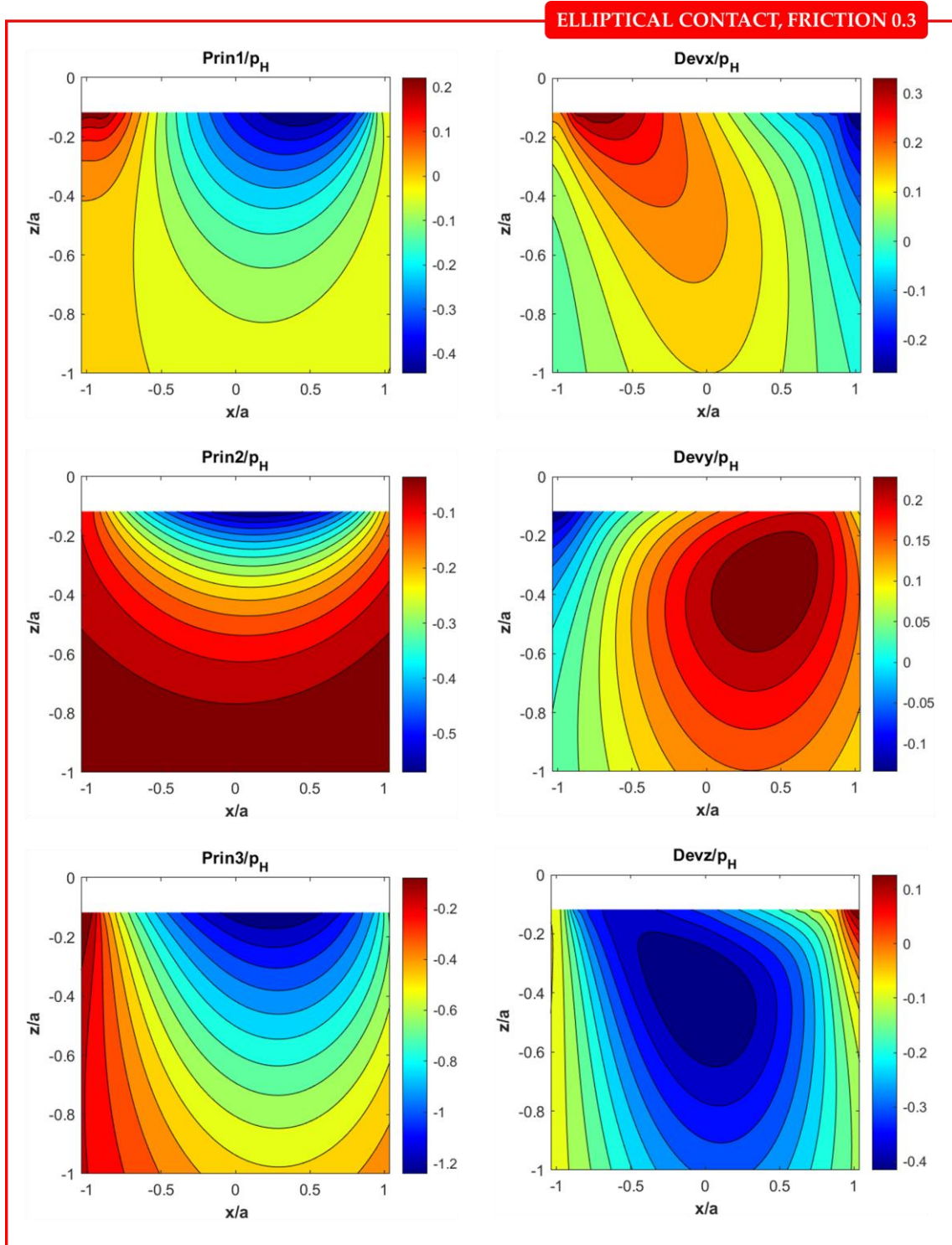


Figure 9.15 – Principal stresses and deviatoric stresses contours in the plane $y = 0$ (friction coefficient $f = 0.5$, $p_H = 1100$ MPa (elliptical contact))

LINE CONTACT

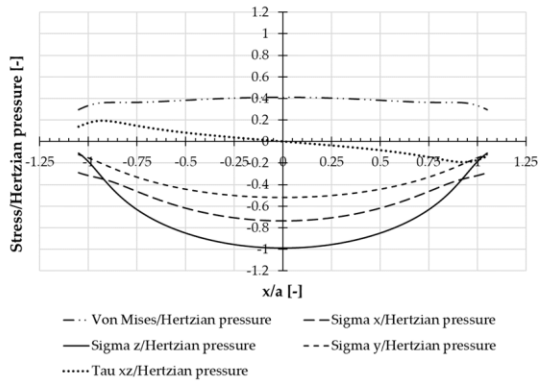
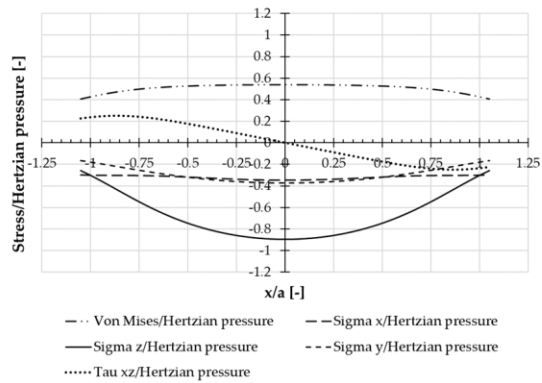
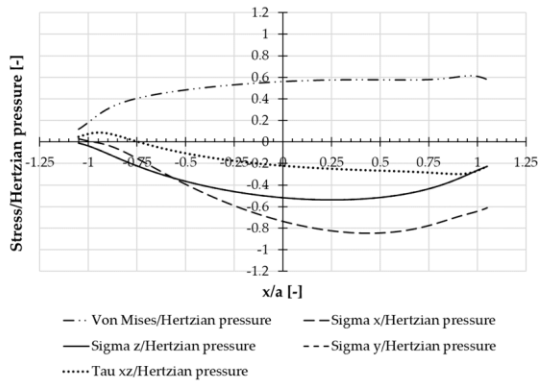
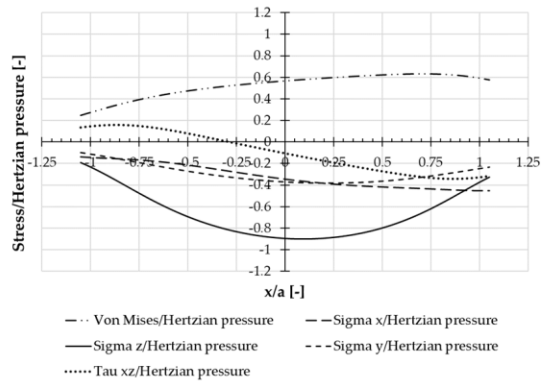
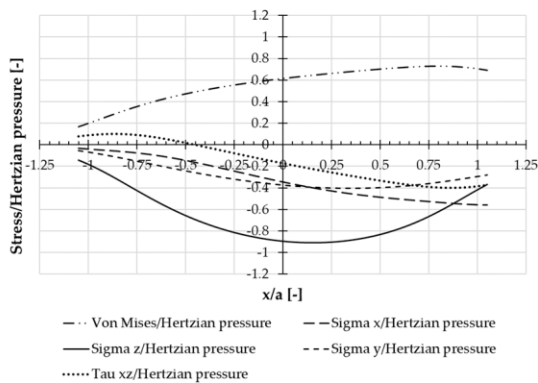
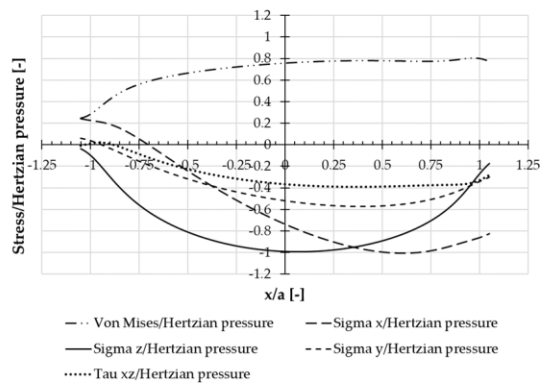
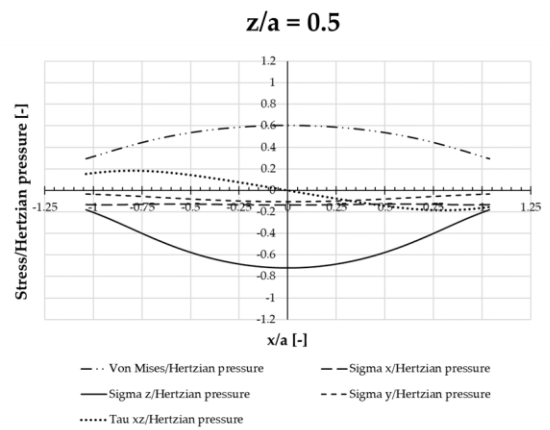
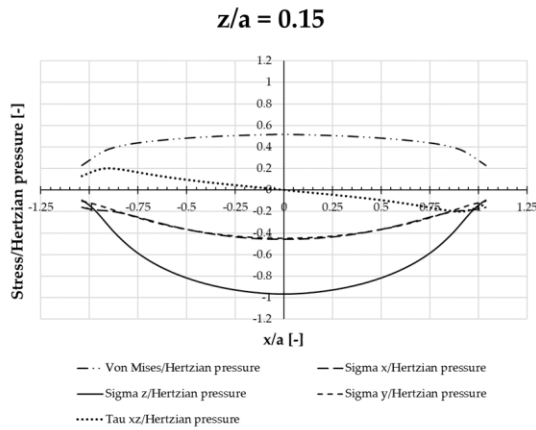
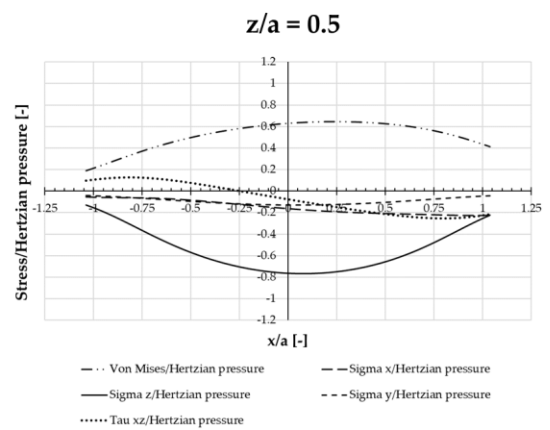
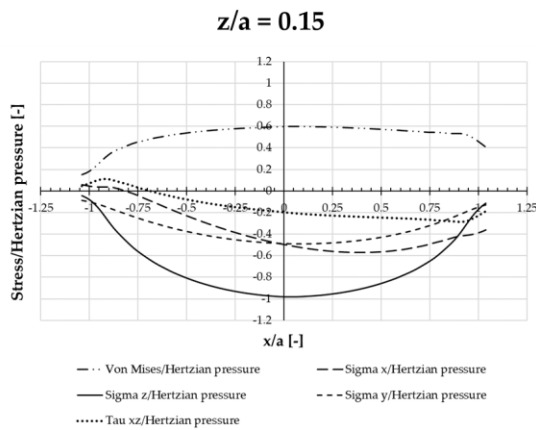
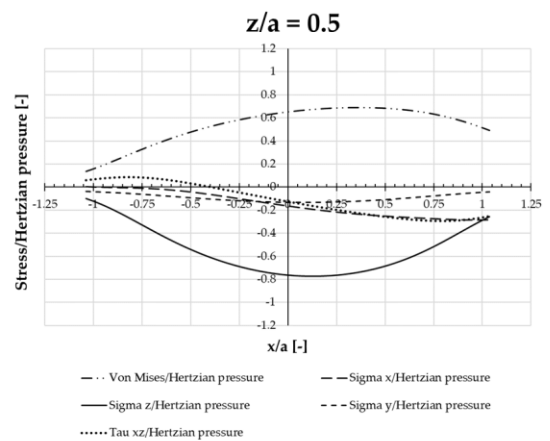
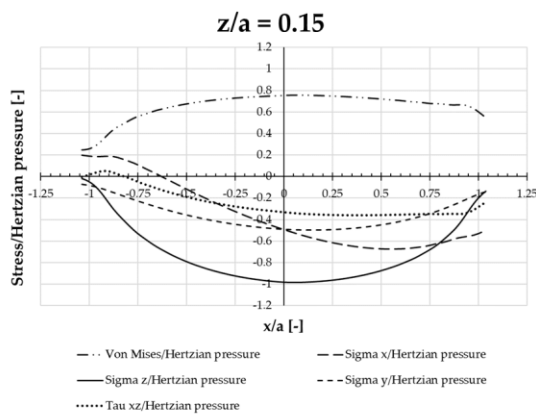
 $f = 0$ $z/a = 0.15$  $z/a = 0.5$  $f = 0.3$ $z/a = 0.15$  $z/a = 0.5$  $f = 0.5$ $z/a = 0.15$  $z/a = 0.5$ 

Figure 9.16 – Elastic stresses along the rolling direction x at $z/a = 0.15$ and $z/a = 0.5$ (line contact)

ELLIPTICAL CONTACT

 $f = 0$  $f = 0.3$  $f = 0.5$ Figure 9.17 – Elastic stresses along the rolling direction x at $z/a = 0.15$ and $z/a = 0.5$ (elliptical contact)

The most noticeable results are the following:

- All the stress quantities in frictionless contact are symmetric (or antisymmetric if we consider the shear stress); this is a direct consequence of the symmetry of the external pressure load. Moreover, all the normal components of the stress tensor are compressive.
- Once a depth is fixed, only the shear stress τ_{xz} shows an alternated trend in any cases. Nevertheless, by increasing the friction coefficient, σ_x shows an alternating trend near the surface as well, with values also higher than zero. Furthermore, the higher the friction, the higher the maximum σ_x . This evidence supports some models in the literature, which only consider the shear stress in the constitutive equations.
- The equivalent von Mises stress reaches the highest value in subsurface when frictionless contact is considered. When the friction coefficient is set to 0.3, the highest values are found in the subsurface and on the surface. When the friction coefficient is set to 0.5, the maximum occurs at the surface contact.
- In general contact, the stresses from the surface to the subsurface decrease more rapidly than in the line contact.

9.2 Cyclic plasticity

The cyclic plastic response of the material is investigated through the Chaboche non-linear hardening framework (see Chapter 6). The material properties are summarised in TABLE 9.2 (1). Only 300 cycles are simulated, but this number of cycles may provide us with an idea of the plastic evolution.

Table 9.2 - Plastic properties of the material
(1)

Material property	Value
σ_y [MPa]	315
C_1 [MPa]	33 900
γ_1	8.3
R_∞ [MPa]	271
b	0.52

In this section, the effects of the applied load, the friction coefficient, the contact model (cylindric vs elliptical) on the plastic strain evolution and wear are analysed. The results were studied considering the total shear strain on the rolling plane accumulated at the end of every cycle and the displacements. The shear strain was reported for the surface (only for cylindrical contact) and z/a equal to 0.04, 0.2 and 0.5. The shear-strain plotted versus the number of cycles is a useful tool since it provides an estimate for the ratcheting rate and, therefore, whether the material undergoes shakedown or plastic accumulation.

9.2.1 Effect of friction coefficient

Frictionless contact and friction set to 0.3 and 0.5 were analysed (FIGURE 9.18). The shear plastic strain illustrated in this figure and in the following ones is intended as the shear plastic strain accumulated considering the sum of all the cycles. As anticipated in the previous paragraph, the traction

generated from friction increases the alternating shear stress and shifts the most stressed areas towards the surface. FIGURE 9.18 shows all these aspects:

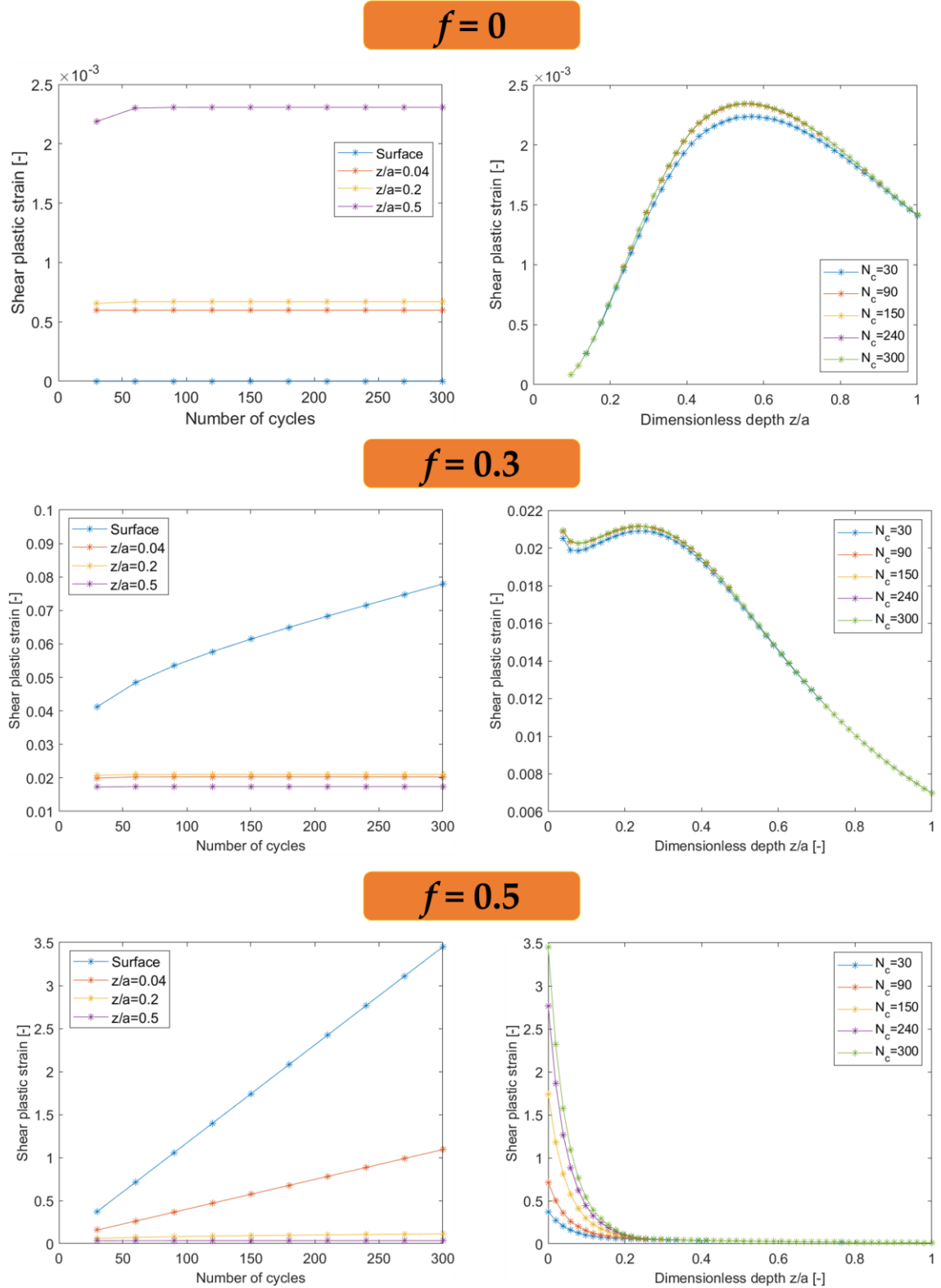


Figure 9.18 – Shear plastic strain versus number of cycles (left) and dimensionless depth z/a (right) according to the friction coefficient

- In frictionless contact, the surface layer does not even plasticise, while the other considered layers undergo shakedown after roughly 60 cycles. The total shear stress is one order of magnitude lower than the cases with friction. The layer set at $z/a = 0.5$ deformed more owing to the higher shear stress.
- Ratcheting phenomena were found for friction contact instead ($f = 0.3$ and 0.5). The estimated ratcheting rate was much higher for friction set to 0.5 and, in this case, the plasticised layer was also deeper.

9.2.2 Effect of contact geometry

FIGURE 9.19 shows the shear plastic strain when a contact Hertzian pressure of 1100 MPa is applied in cylindrical contact and elliptical contact. The surface layer was not considered for elliptical contact for the divergence problem previously explained. Despite the difference in the contact area and the pressure distribution in the two cases, the total shear strain accumulated near the surface on the rolling plane did not differ much. However, moving away from the surface, the discrepancy between the two cases higher (about 10%). This is a consequence of the elastic stress gradient along the depth.

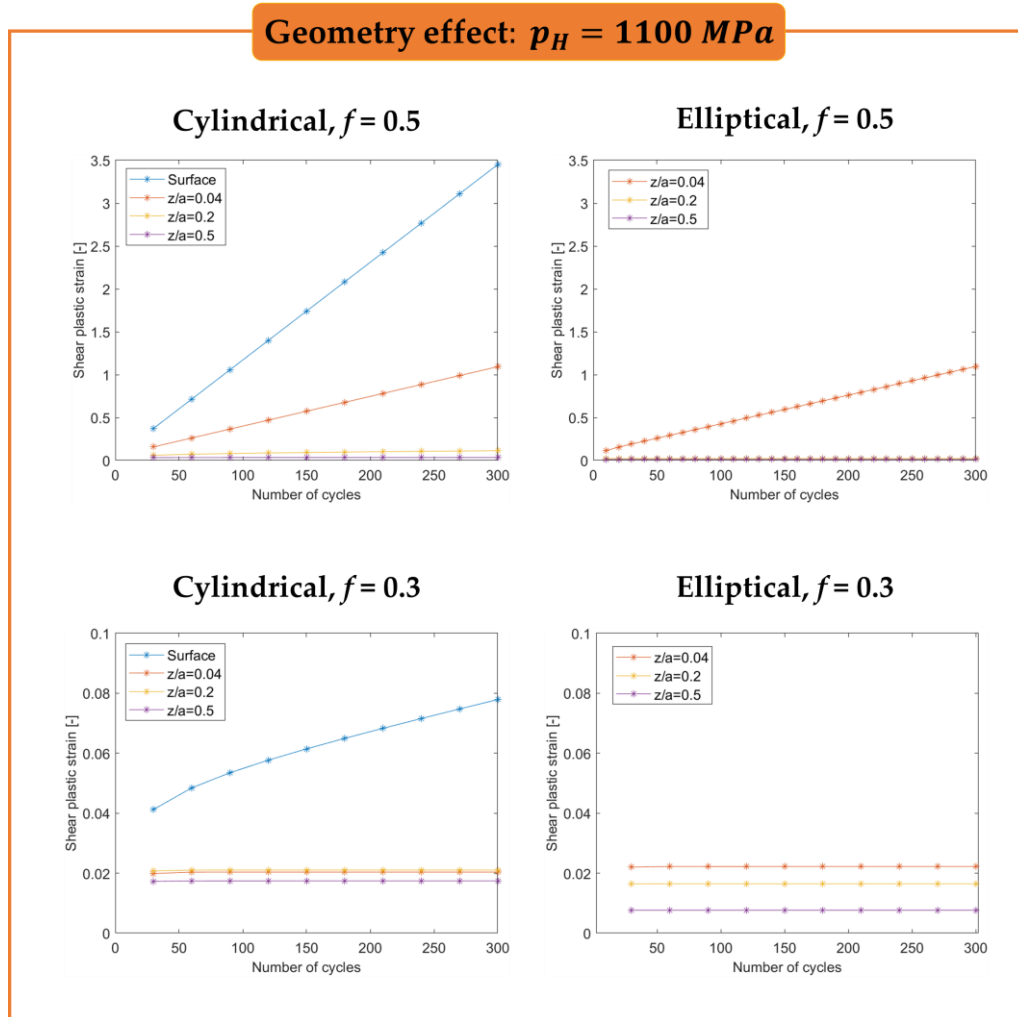


Figure 9.19 – Shear plastic stain versus number of cycles according to the geometry contact type

9.2.3 Effect of load

FIGURE 9.20 and FIGURE 9.21 illustrate the effect of changing contact pressure in the presence of friction. The two levels of pressure were 1100 MPa and 1800 MPa. The total plastic deformation accumulated in 300 cycles was one order of magnitude higher with 1800 MPa, and the ratcheting phenomena were more pronounced. Furthermore, the deformed area widened in the subsurface.

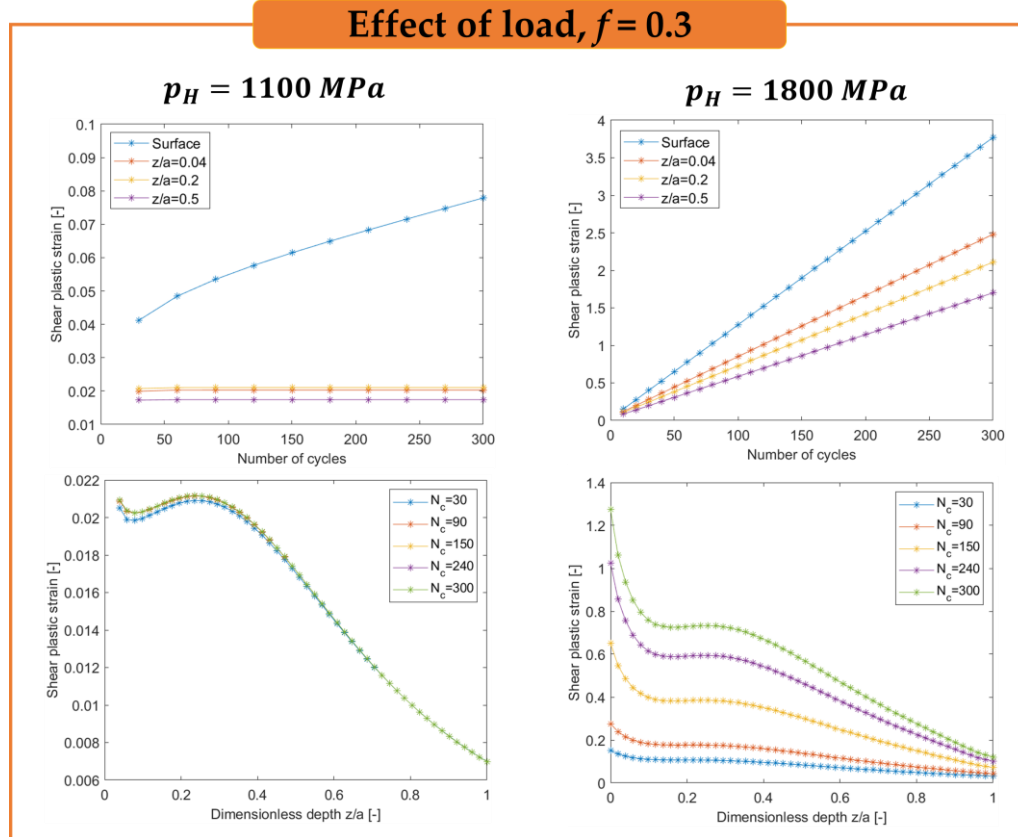


Figure 9.20 – Shear plastic strain versus number of cycles and dimensionless depth z/a according to the contact pressure (1100 MPa on the left, 1800 MPa on the right) when the friction coefficient is set to 0.3

Effect of load, $f = 0.5$

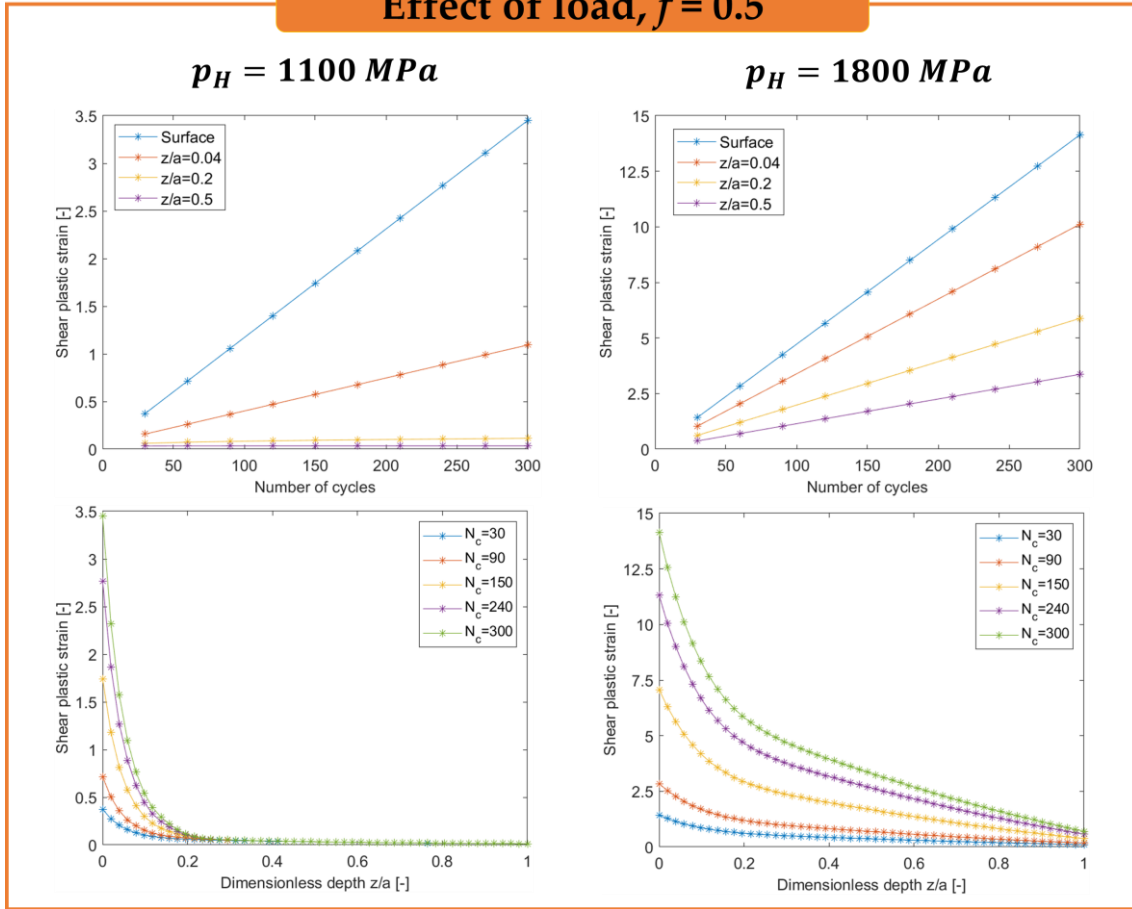


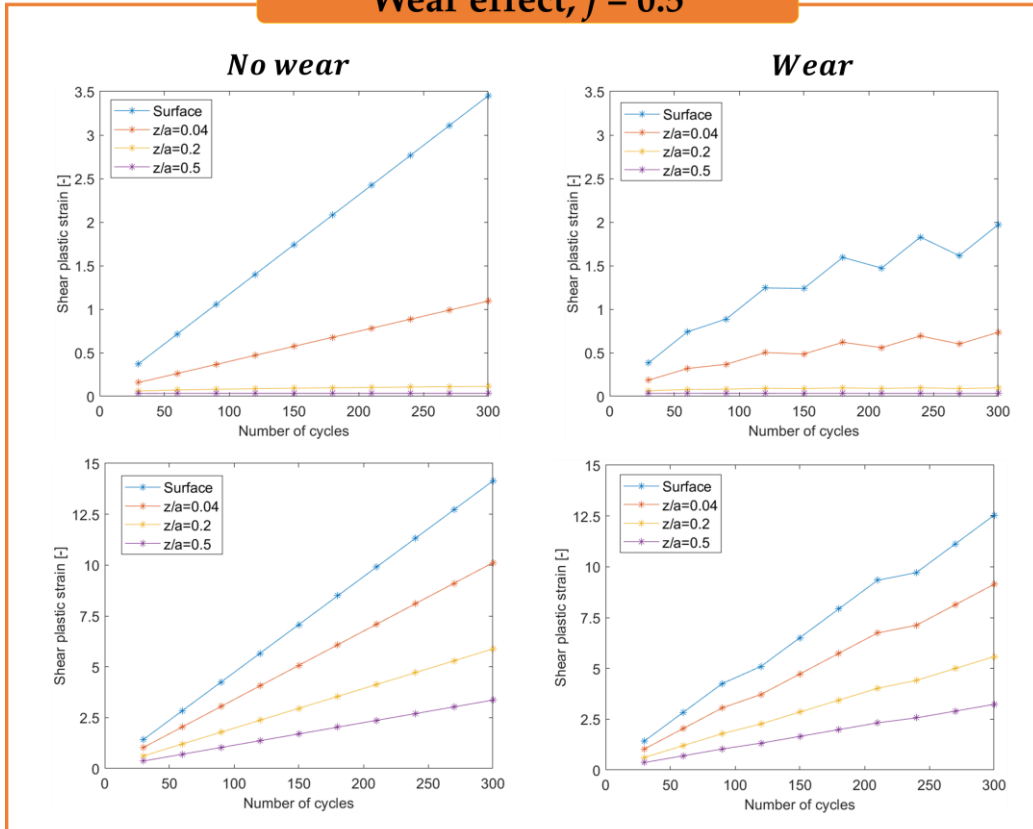
Figure 9.21 – Shear plastic strain versus number of cycles and dimensionless depth z/a according to the contact pressure (1100 MPa on the left, 1800 MPa on the right) when the friction coefficient is set to 0.5

9.2.4 Effect of wear

Wear was only coded for line contact (cylindrical contact); the model proposed in Chapter 8 cannot be applied for general contact problems; elliptical contact indeed requires more sophisticated models that consider the change of curvature of the contact bodies during the investigated time span.

In FIGURE 9.22, the results of the simulations with and without wear are illustrated; friction contact was considered, and two contact pressures were evaluated (in the first row, pressure is 1100 MPa; in the second row, pressure is 1800 MPa). Given the short time span (300 cycles), we needed to consider a wear rate higher than typically found in wheel–rail contact to see the effect of the material removal. Wear rate was set to 0.0001 mm/cycle (two orders of magnitudes higher than the wear rate in bi-disk tests (2,3)). As can be expected, simulations with wear estimated lower plastic strain after 300 cycles than in the case without wear. Except for $f=0.3$ and $p_H=1100 \text{ MPa}$, the plastic strain showed an increasing trend, meaning that the fatigue phenomenon was still dominating over wear. The “irregular” trend in presence of wear was justified by the low cycles sampling when plotting the graphs: if we simulated more loading cycles, we could adopt a higher cycles sampling and obtain an increasing trend in the plots.

Wear effect, $f = 0.5$



Wear effect, $f = 0.3$

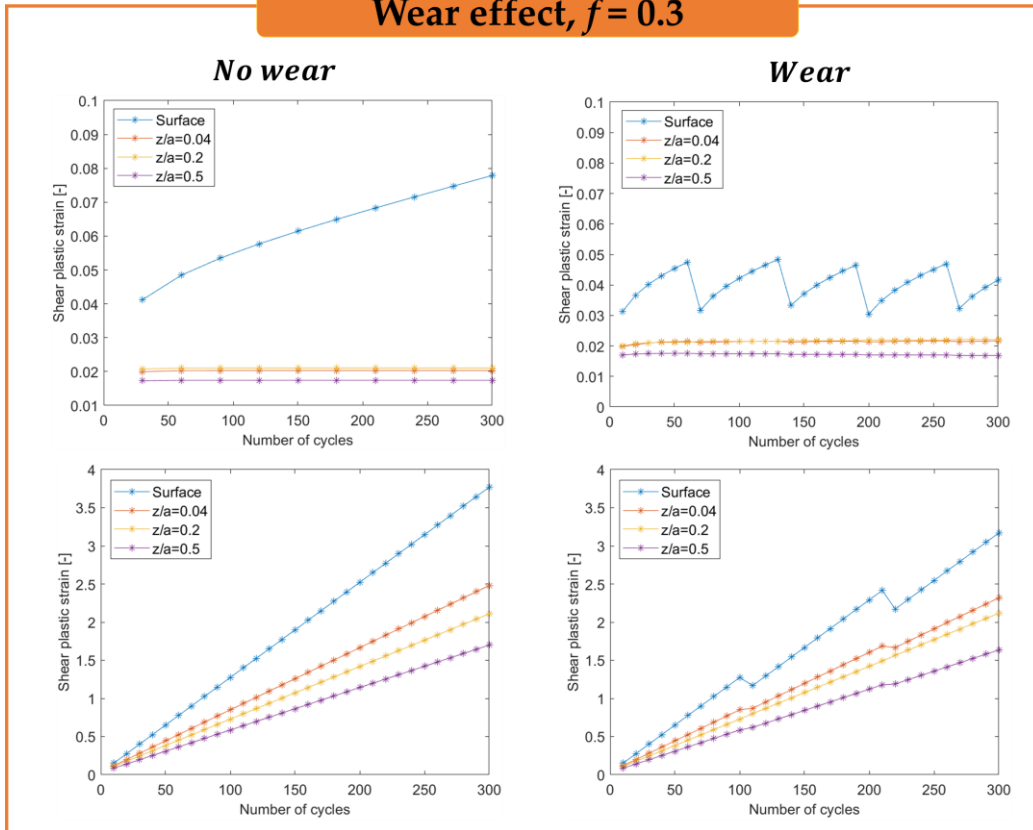


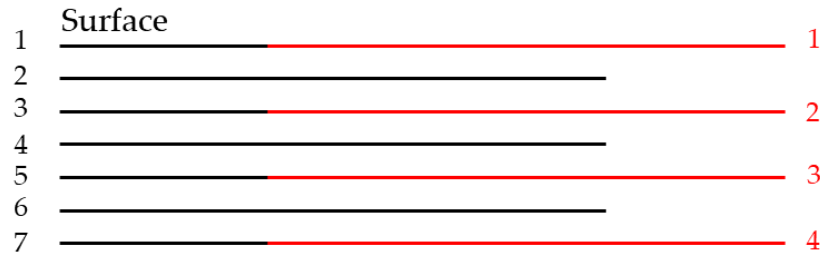
Figure 9.22 – Shear plastic strain versus number of with and without the effect of wear. The first row refers to contact pressure equal to 1100 MPa, the second one to 1800 MPa

9.3 Convergence in the wear model

As anticipated in Chapter 8, the wear model is based on the removal of the first layer after a fixed number of cycles. As a consequence, the distance between two layers (Δz) plays a fundamental role in determining the plastic strain accumulated throughout the simulations.

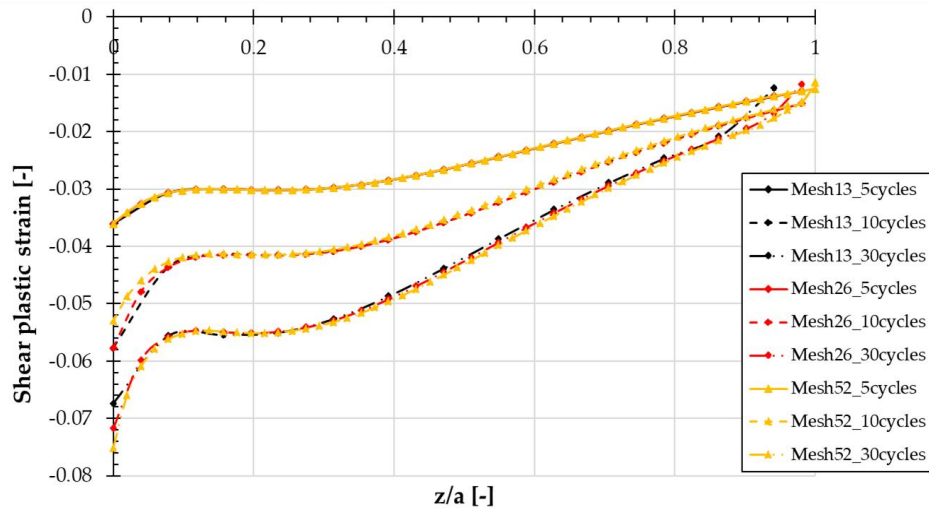
To better understand the influence of Δz , let us consider FIGURE 9.23. The black lines and the red lines represent the layers of the body in two different configurations; Δz of the black configuration is smaller than that of the red. When computing the plastic strain history with friction coefficients higher than 0.3, the second layer in the black reference will have a higher plastic strain than the second layer in the red frame of reference. Therefore, when the surface layers are worn out, and the layers below are shifted, the new surface layers will show different plastic strain according to how the semi-infinite space is discretised along the direction z . If Δz is too large, the results might be compromised since the model will predict smaller plastic strain.

Figure 9.23 –
Schematic
representation of the
layers



The proposed model was converged by considering different values of Δz and dividing the semi-infinite space into 102, 54, 26 and 13 layers. FIGURE 9.24 shows the shear plastic strain when 30 cycles are simulated. The solutions obtained with 102 layers are not shown since they are identical to those with 54 layers. However, the results tend to slightly diverge as the number of layers decreases, increasing Δz . With 26 layers the plastic strain at the surface is about 6% higher than with 102 layers, while, in the subsurface, the values differ less than 1%. With 13 layers, the plastic strain is at least 2% higher than with 54 layers almost at every depth.

Figure 9.24 – Shear
plastic strain along the
depth according to
different Δz size



9.4 Multiaxial fatigue: Dang Van and Crossland

This section seeks to investigate the multiaxial fatigue response, within high cycle regime. This hypothesis implies that the material undergoes elastic behaviour or, at most, elastic shakedown. However, for the elastic shakedown condition, we should also verify whether the material plastically collapses before reaching the elastic condition. For simplicity, we only consider the “pure” elastic response.

The simulated loading conditions were the following:

- Cylindrical and elliptical contact geometries as reported in TABLE 9.1
- Contact pressure set to 1100 MPa
- Five levels of friction coefficients: 0, 0.1, 0.2, 0.3 and 0.5.

Reminder:

Dang Van

$$\max_t \left[\sqrt{\frac{\sigma_{1,a}^{dev}(t) - \sigma_{3,a}^{dev}(t)}{2}} + c_{DV} \sigma_h(t) \right] < \sigma_{eDV}$$

Crossland

$$\max_t \left[\sqrt{\frac{3}{2} \sigma_a^{dev}(t) : \sigma_a^{dev}(t)} \right] + c_c \max_t [\sigma_h(t)] < \sigma_{ec}$$

DV and CR coefficients are reported in TABLE 9.3.

Dang Van		Crossland	
c_{DV}	0.33	c_c	0.6
σ_{eDV}	269 MPa	σ_{ec}	466 MPa

Table 9.3 – Multiaxial fatigue material parameters

From the shakedown maps, we can draw the yield strength that prevents the material from exceeding the elastic threshold. TABLE 9.4 illustrates the yield strengths according to von Mises yield criterion. These strengths are much higher than the shear yield stress considered in the previous simulations; indeed, plastic response was obtained.

Friction coefficient f	Von Mises shear stress threshold [MPa]	
	Cylindrical contact	Elliptical contact
0	~355	~305
0.1	~360	~323
0.2	~375	~379
0.3	~400	~440
0.5	~680	~647

Table 9.4 – Von Mises shear stress threshold for elastic response according to the shakedown maps

FIGURE 9.25 shows the CV and CR equivalent stress along the depth (dimensionless quantities are plotted; the stress is divided by the Hertzian pressure, and the depth by the semi-contact length a). The black lines indicate the thresholds for each criterion. The equivalent stresses were calculated for a plane parallel to the surface.

The threshold was exceeded in the surface layer for friction coefficients equal to 0.3 and 0.5. Surface crack initiations will be expected in these conditions provided elastic condition or elastic shakedown happen (if these two conditions are not verified, these criteria cannot be applied). It is also noteworthy that, according to the CR criterion, the material region that might fail is deeper than the one calculated using DV (at least twice as deep).

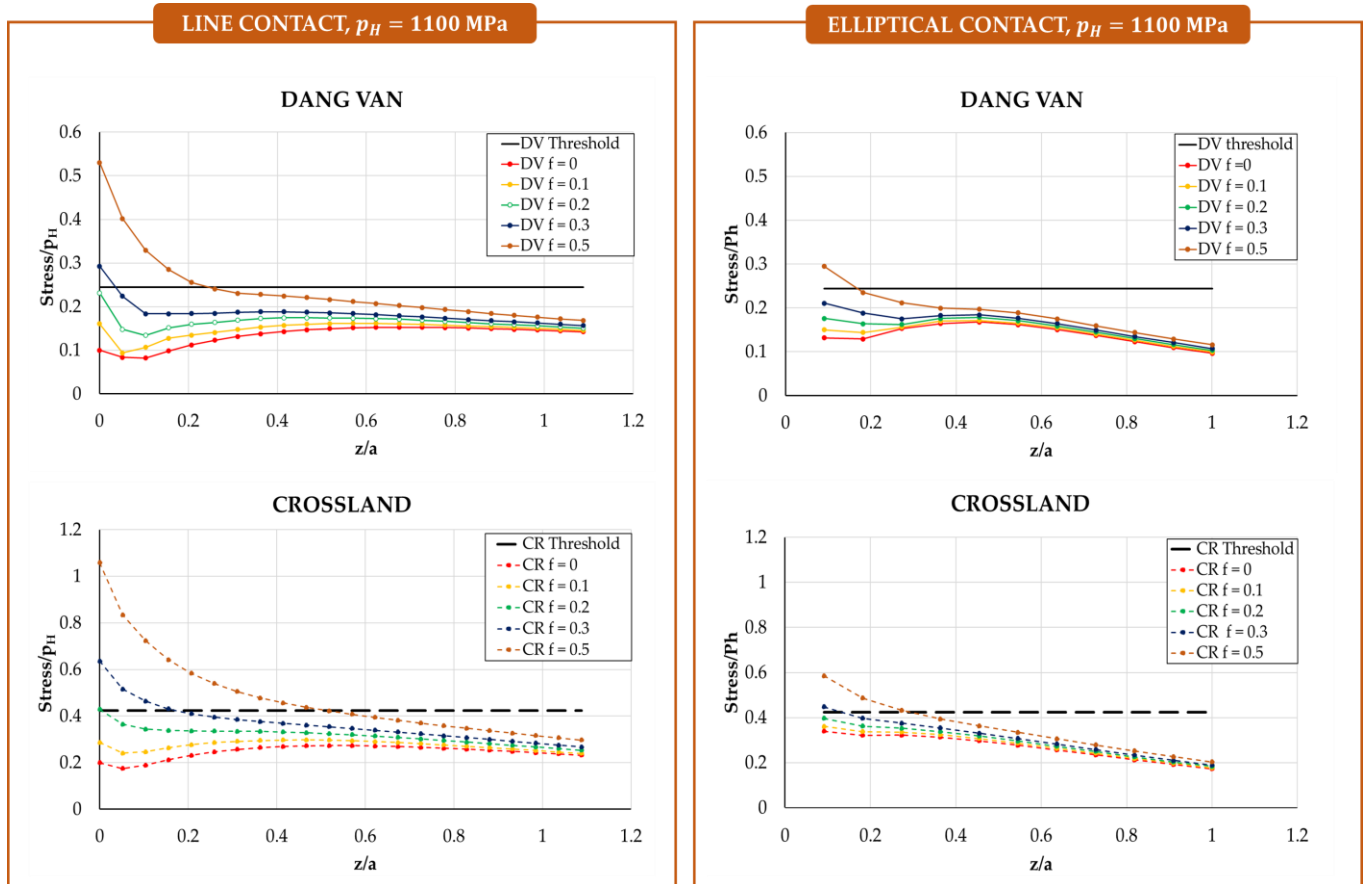


Figure 9.25 – Dang Van and Crossland equivalent stress according to the dimensionless depth z/a for line and elliptical contact

9.5 Multiaxial fatigue: Jiang-Sehitoglu

As already anticipated in this chapter, the JS criterion can be applied whenever plastic shakedown occurs. The following conditions were simulated to ensure that this criterion could be applied:

- Cylindrical contact (see TABLE 9.1 for the geometry)
- Contact pressure of 800 MPa, semi-contact length $a = 0.25$ mm
- Frictionless contact
- 100 cycles
- Yield strength of 230 MPa
- Kinematic hardening parameters C_1 and γ_1 of 30 000 MPa and 60, respectively
- Isotropic hardening R_∞ and b of 150 MPa and 3, respectively
- Wear was not considered.

The JS parameters from (4) were adopted:

$$FP_0 = 0.5 \text{ MPa} \quad d = 2.5 \quad c_{JS} = 0.32 \quad J = 1.5 \times 10^6 \text{ MPa}^d$$

The shear plastic strain history for the four depths is illustrated in FIGURE 9.26. The “history” is defined in terms of virtual time; the virtual time represents the total number of increments to simulate the behaviour of all the points in a layer in direction x (the rolling direction) during the 100 cycles. Since the nodes along x are 101, the total virtual time of the simulation is $101 \text{ nodes} \times 100 \text{ cycles} = 101000$. After roughly 92 cycles the plastic strain cycle stabilises, and no further deformation accumulated at $z/a = 0.5$; at $z/a = 0.2$, plastic shakedown occurs after about 38 cycles, instead. The surface layer remains in the elastic regime, while, just under the surface ($z/a = 0.04$), the material undergoes elastic shakedown. As a consequence, the JS approach should be applied only to the subsurface layers subjected to plastic shakedown and not to the surface layers. For the sake of completeness and to demonstrate the code capabilities, we applied the criterion in all the layers.

As a rule of thumb, a check is first performed on whether the material yields before the shakedown condition is reached. However, as a case study, we have only limited to study the stabilised stress-strain cycle.

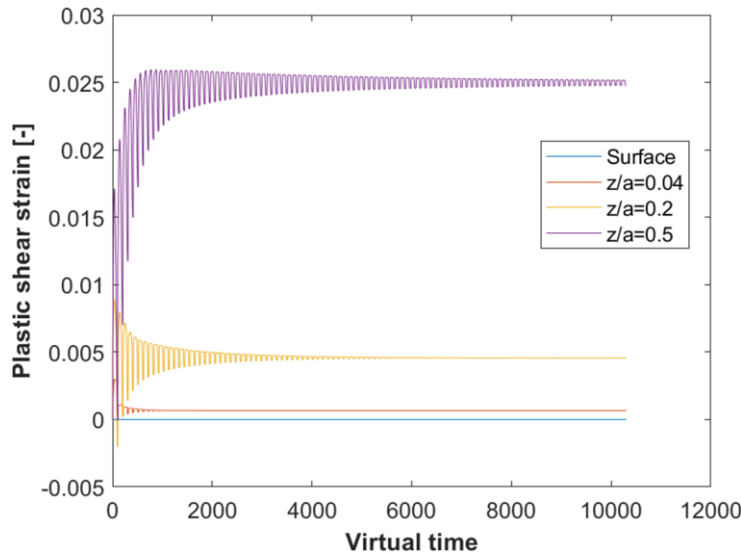


Figure 9.26 – Plastic shear strain evolution at four depths

Reminder:

Jiang-Sehitoglu

$$FP = \left\langle \frac{\Delta \epsilon}{2} \sigma_{max} \right\rangle + c_{JS} \Delta \tau \Delta \gamma$$

$$(FP - FP_0)^d N_f = J$$

The contribution due to the normal component $\langle \frac{\Delta \epsilon}{2} \sigma_{max} \rangle$ is zero regardless of the deformation since the normal stress is compressive and the normal strain is zero for equilibrium (8). This means that FP only depends on the shear strain and the shear stress and, in this case, FP is simply defined as

$$FP = c_{JS} \Delta \tau \Delta \gamma \quad (9.1)$$

FIGURE 9.27A and B show the shear stress and strain range according to the dimensionless depth when the xz -plane is rotated. For the sake of completeness, the parameters were evaluated for all the depths, even though some layers would not undergo plastic shakedown.

FIGURE 9.27C shows how FP varies according to the depth (represented as usual as the dimensionless quantity z/a). The maximum FP value (0.845) was estimated at $z/a = 0.5$ in the plane parallel to the surface.

From Equation (7.17), we can estimate the fatigue life

$$N_f = \frac{J}{(FP - FP_0)^d} = 21 \times 10^6 \text{ cycles} \quad (9.2)$$

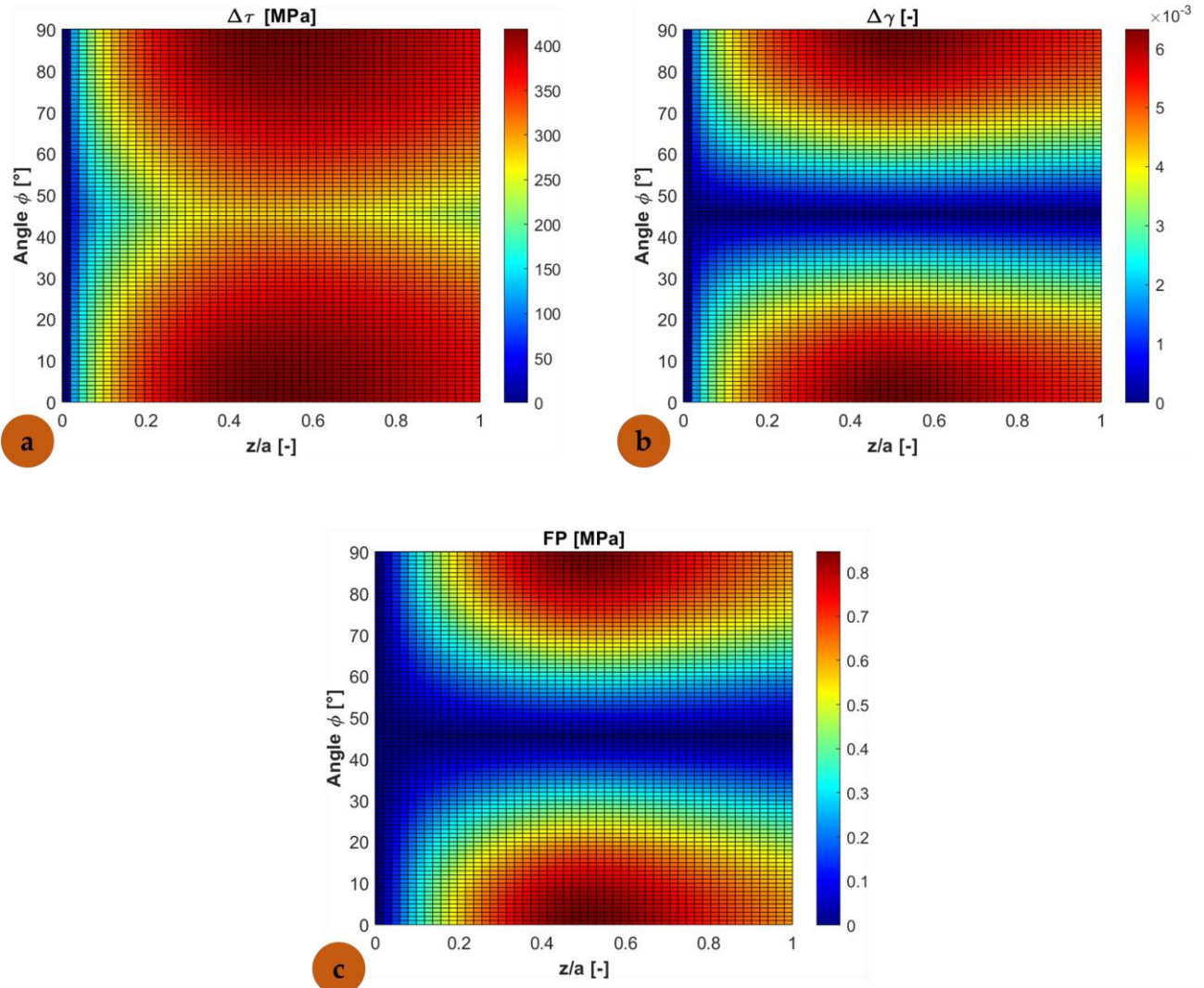


Figure 9.27 – $\Delta \tau$, $\Delta \gamma$ and FP parameter by varying the depth and the angle θ

9.6 Conclusions and ongoing activities

The current project has proposed a semi-numerical model to investigate cyclic non-conforming contact problems. This model enables the prediction of the material behaviour *more quickly* than numerical models; however, the computing time reduction is also a result of some simplifications with respect to reality.

The main assumptions that may be questioned are twofold:

- *Elastic stress framework and contact load.* The proposed model is stress-driven, and the stress history is directly calculated from the Boussinesq model and the Hertzian theory, whose hypothesis might be by far from the real wheel–rail working conditions. Because of plasticity, the real contact area is typically larger than that of the Hertzian, but the maximum contact pressure is lower. As a result, the stresses acting on the material should be lower than the those predicted by this model. However, according to Merwin and Johnson (5), Hearle and Johnson (6) and Bhargava et al. (7), the presumed error obtained by calculating the plastic field from the elastic stress is low.
- Another aspect related to the elastic stress is the choice of the *material parameters*; in fact, the stress (higher than actual) should not be higher than the saturation stress given by the constitutive law. Adopting a constitutive law with a high saturation level may make the convergence easier; alternately, a mixed hardening model with a linear isotropic hardening can be adopted. Furthermore, the combination of the normal pressure and the friction/traction force return an asymmetric contact load. However, as seen in Chapter 3, the distance between the location of the maximum pressure and the centre of the contact area may be considered negligible.
- *Residual stress.* The actual model, as it has been coded so far, predicts strain components that are not all compatible with the conditions of line contact. After the passage of the first load, stresses are zero, but there exists some residual strain (ε_x , ε_y and ε_z). Nevertheless, such normal strain is zero in reality. A relaxation procedure is then required to ensure this condition, yielding a rise in the stresses σ_x and σ_y (8), after which the next load can be applied.

Future activities

Further work is necessary to improve the model. Firstly, the aforementioned strain relaxation procedure should be implemented. Future research should then assess the impact of the viscous effect on the material, and viscoplasticity can be applied to study the effect of the high temperatures in shoe-braking conditions (3).

9.7 References

1. Mazzù A. A simplified non-linear kinematic hardening model for ratchetting and wear assessment in rolling contact. *J Strain Anal Eng Des.* 2008; 43(5):349–60. <https://doi.org/10.1243%2F03093247JSA405>.
2. Faccoli M, Petrogalli C, Lancini M, Ghidini A, Mazzù A. Effect of desert sand on wear and rolling contact fatigue behaviour of various railway wheel steels. *Wear.* 2018 Feb 15; 396–397:146–61. <https://doi.org/10.1016/j.wear.2017.05.012>.
3. Mazzù A, Provezza L, Zani N, Petrogalli C, Ghidini A, Faccoli M. Effect of shoe braking on wear and fatigue damage of various railway wheel steels for high speed applications. *Wear.* 2019 Sep; 434–435:203005. <https://doi.org/10.1016/j.wear.2019.203005>.
4. Onal O, Canadinc D, Sehitoglu H, Verzal K, Jiang Y. Investigation of rolling contact crack initiation in bainitic and pearlitic rail steels. *Fatigue Fract Eng Mater Struct.* 2012; 35(11):985–97. <https://doi.org/10.1111/j.1460-2695.2012.01686.x>.
5. Merwin JE, Johnson KL. An analysis of plastic deformation in rolling contact. 1966. <https://doi.org/10.1243%2F03093247JSA405> PROC 1963 177 052 02.
6. Hearle AD, Johnson KL. Cumulative Plastic Flow in Rolling and Sliding Line Contact. *J Appl Mech.* 1987; 54(1):1. <https://doi.org/10.1115/1.3172958>.
7. Bhargava V, Hahn GT, Rubin CA. An Elastic-Plastic Finite Element Model of Rolling Contact, Part 2: Analysis of Repeated Contacts. *J Appl Mech.* 1985; 52(1):75. <https://doi.org/10.1115/1.3169030>.
8. Foletti S, Desimone HJ. Application of shakedown maps under variable loads. *Eng Fract Mech.* 2007 Mar 1; 74(4):527–38. <https://doi.org/10.1016/j.engfracmech.2006.03.008>



Part V

Chapter 10 – Conclusion & Perspectives

Conclusion and Perspectives

10

10.1 Conclusion

The present research has proposed numerical and semi-analytical models for railway problems. Throughout the thesis, we addressed three main topics: the effect of solid contaminants in wheel–rail couplings, the presence of inhomogeneities in ferritic-pearlitic wheels and the plastic response of the wheel materials due to repeated loading cycles. These matters, though seemingly unrelated, indicated that the material parameters may be crucial when selecting the steel to adopt for a specific application.

The **presence of solid contaminants** at the wheel–rail interface (*CHAPTER 3*) produced a local strain field characterised by large plastic deformation, whose depth was roughly 2.5 times the radius of the particle. Furthermore, the addition of a deep layer comprising less intense plastic deformation was due to the overall contact between wheel and rail. The numerical results, as well as the experimental outcomes obtained from bi-disk tests, showed that *the cyclic yield strength* has a key role in improving the wheel and rail performance; increasing the cyclic yield strength of both components results in severe damage limited to a depth comparable to the particle size.

The microstructure depends on several factors, including the chemical composition and the thermal treatments and, in turn, influences the mechanical properties (tensile and yield strength, fracture toughness, etc.). The numerical and semi-analytical models simulating the **traces of bainite in the ferritic-pearlitic matrix** (*CHAPTER 4*) demonstrated how the microstructure may affect the plastic deformation. The bainitic spots, whose *cyclic yield strength* is higher than that of the ferritic-pearlitic material, deforms less, offering more resistance to rolling contact fatigue crack initiation. However, the differences of the *elastic properties* and *cyclic yield strength* between the bainitic spots and the matrix may generate localised deformations with increased intensity where the bainitic spots are densely spread.

Our **semi-analytical solver** (*CHAPTER 5–10*) offered the possibility to investigate non-conforming contact problems more quickly than the

traditional numerical solvers, like the finite element method. The model accurately predicted the response of the railway wheels (shakedown or ratcheting) occurring in the different layers of the materials within a reasonable time. The model may also be useful to optimise the wear (governed by the *wear rate*) with rolling contact fatigue (controlled by the *yield strength*), by determining the number of cycles necessary to balance the rate the material layers accumulate strain in the maximum stress region with the wear rate of these layers in this region.

10.2 Perspectives

Below are suggestions for future activities.

Contaminants at the wheel–rail interface – In this work, solid contaminants were the focus. Liquid contaminants also play a vital role in wheel–rail tribology and in-surface crack propagation. Liquid contaminants can be water or a lubricant, like frost or moisture. Water in the contact patch decreases friction and contributes to sliding; when the wheel slides, a significant amount of heat is generated, resulting in the formation of a thin, white layer of brittle-hard martensite. When martensite breaks, micro-cracks initiate, which can suddenly propagate when water fills in the crack. During the contact, the crack closes, compressed by the load, and water pressure increases, causing crack propagation. Finite element models can be useful in understanding this phenomenon by predicting how *stress intensity factor* (SIF) evolves during a loading cycle.

Influence of traces of bainite in ferritic-pearlitic wheels – Applying the fracture mechanics approach would help determine how the traces of bainite could affect the crack propagation in the matrix and whether the bainite stops or deviates the crack. The *extended finite element method* could be adopted; however, finding the fracture toughness of the single phases to implement in the numerical model will be the main challenge. Another solution consists of adopting the equations available in the literature, which link the displacements of the nodes near a pre-existing crack near the bainitic spots to the SIF to investigate how SIFs evolve during a loading cycle.

Semi-analytical model – The following features can further improve the efficiency of our solver:

- Addition of more constitutive laws to properly model viscoplastic and recovery phenomena occurring at high temperatures (braking condition, for example)
- Implementation a proper wear model for general contact problems, for example, possibly the Archard's model
- Application of a semi-numerical solver to solve the contact problem as an alternative to the Hertzian solution, also solving the conforming contact

*“When helping others, do not look for a reward;
If you are looking for a reward, don’t help others.”*

Chinese proverb

